Wetting and spreading of viscous droplets: a critical assessment of fluid and surface properties

Emily James

Submitted in accordance with the requirements for the degree of
Doctor of Philosophy

The University of Leeds
School of Chemical and Process Engineering

March 2018

The candidate confirms that the work submitted is her own, except where work which has formed part of jointly-authored publications has been included. The contribution of the candidate and the other authors to this work has been explicitly indicated below. The candidate confirms that appropriate credit has been given within the thesis where reference has been made to the work of others.

Published papers or manuscripts in review:

James, E.; Tangparitkul, S.; Brooker, A.; Amador, C.; Graydon, A.; Vaccaro, M.; Cayre, O.; Hunter, T.; Harbottle, D. Accelerated spreading of inviscid droplets prompted by the yielding of strongly elastic interfacial films. *Submitted to Colloids and Surfaces A: Physiochemical and Engineering Aspects.*

Acknowledgements

Firstly, I would like to express my deep gratitude to Dr David Harbottle for his guidance throughout this whole process and for introducing me to the world of research. David enabled me to develop my scientific debate and reasoning and assisted me in all my scientific adventures. I hope you have gained as much as I have from this project. I would like to offer special thanks to Dr Tim Hunter for providing pastoral advice and giving me the confidence and drive when things were not going well. Thank you for having patience and always providing a realistic view of the scientific challenges. I am also particularly grateful to Dr Olivier Cayre who provided not only the chemistry knowledge, but support and a sympathetic ear when problems arose.

I would also like to thank Dr Simon Cornell who provided both the equipment and technique for the AFM studies. I would like to thank the IT department in particular Margaret Gibson and Julie Webster, who have supported my IT needs throughout the project and who went the extra mile so that I could be mobile whilst writing up. I acknowledge the help and advice given from Ben Douglas, Suzanne Patel, Rob Harris and particularly Peter Dawson who have provided a huge amount of technical support to the project. I would also like to extend gratitude to Procter and Gamble for their financial aid and more importantly the support and advice from Anju Brooker, Mauro Vacarro, Sumanth Jamadagni, Andrew Graydon and Carlos Amador, who were able to provide technical information and who helped guide the project to utilise the knowledge to real-life applications.

I am indebted to Juliette, a true friend, with whom I have shared a great deal with over the past few years. I thank you not only for your companionship but for the help in the labs and the late night scientific debate. I would also like to thank other members of the group who have supported me throughout my time in Leeds including Kirsty, Mo, Calum, Andy, Huagui, Ian, Angela, Jaiyana, Wei and Chris.

To my other friends in Leeds, thank you for the downtime adventures, including David, Caroline, and Eloise and to those friends I have met through signing and St John. Particular thanks goes to James, Kim-Joy, Nabil and Siân who have kept me sane and supported me from further afield. Finally, this would not have been at all possible without the undying support and love from my family. Thank you all.

Abstract

The thesis examines the effects of various parameters on droplet spreading dynamics. A range of PDMS oils with viscosities from 9.9 – 12710 mPa·s were selected and spread on silicon wafers, and the spreading of the droplets were recorded on a pendant drop tensiometer. The droplet radius over time was then used to compare the different spreading dynamics. As expected, increasing droplet viscosity slowed droplet spreading dynamics, removing the viscosity by dividing time through by the oil viscosity created a master curve. The master curve showed that viscosity was the dominating force in droplet spreading. Regions of the curve which deviated from a $r \sim t^{0.1}$ spreading were those effected by droplet shape and kinetic energy. Additional kinetic energy showed an increase in spreading dynamics, however this was viscous dependant with a larger effect seen on low viscosity oils. Finally, the CH_3-terminated PDMS was compared to NH_2-terminated PDMS and it was found that the spreading dynamics for the NH_2-terminated PDMS was slower.

The spreading dynamics of the PDMS oils were also investigated under D_2O, where the viscous forces were also shown to affect droplet spreading dynamics but to a less extent compared to in-air observations. An induction time was also associated with droplet spreading. A thin liquid film (TLF) of water had to first drain and rupture before droplet spreading could take place. NH_2-terminated PDMS oils were shown to have a larger extent of wetting than the CH_3-terminated PDMS oils, but again had slower spreading dynamics. Silanisation of the surfaces (to display a water-in-air contact angle of 0, 30, 65 and 100°) enabled the effects of surface hydrophobicity to be studied, with a more hydrophobic surface exhibiting faster spreading dynamics and shorter induction times. The addition of a negatively charged surfactant SDS (sodium dodecyl sulphate) showed that with increasing concentration there was a decrease in spreading dynamics and an extension of the induction time, due to Marangoni effects. To explore the effect of surface roughness, cellulose coated wafers (RMS ~ 0.6) were also used, both the CH_3- and NH_2-terminated PDMS oils showed little spreading, highlighting the importance of surface roughness for droplet spreading.

The spreading of inviscid water droplets were also investigated. β-Aescin, a saponin, was found to partition at the air-water interface quickly; after 1 minute of ageing it showed strong interfacial elasticity (G'/G'' ~ 6). The effect of strong interfacial elasticity on droplet spreading dynamics was then studied for the first time. Droplet spreading dynamics of water, 5 wt % ethanol, 0.0015 wt% N-dodecyl β-D-glucopyranoside and xanthan gum were also studied, to ensure the spreading effects were not due to the solvent, surface tension, surfactant behaviour or bulk rheological properties. The four extra solutions were shown to spread according to a time-dependant power law of 0.5 then 0.1 (Tanner's law) as expected. However, the 0.01 wt % β-aescin droplets were shown to accelerate droplet spreading dynamics, with an initial power law of 1.05, then 0.61, then 0.1. The elastic film rupture promoted droplet spreading and also enhanced the dampening of oscillatory waves which followed after droplet detachment.

Table of Contents

List of Tables

List of Figures

List of Nomenclature

A	Droplet cross-sectional area, mm^2
A	Rheological exponent
A_{flat}	Area of a flat surface, mm^2
A_i	Area per molecules, nm^2
A_o	Initial droplet height, mm
A_{rough}	Area of a rough surface, mm^2
$A_{(t)}$	Droplet peak height, mm
Bo	Bond number
C	Bulk concentration, mol / L
C	Prefactor constant
Ca	Capillary number
Ca_f	Film capillary number
d	Flow consistency flow, $(Pa\cdot s^n)$
D	Drag coefficient
D_i	Droplet diameter on impact, mm
D_L	Largest droplet diameter when compressed, mm
D_s	Smallest droplet diameter when compressed, mm
f_1	Fraction of droplet with contact angle θ_1
g	Gravitational acceleration constant, m / s^2
G'	Elastic Moduli, $Pa\cdot m$
G''	Viscous moduli, $Pa\cdot m$
h	Droplet release height, mm
h	Thin film height, mm
H_o	Thin liquid film thickness, mm
K	Sommerfeld number
K_w	Quasi-equilibrium rate constant, s^{-1} (fitting parameter)
L	Characteristic length, mm
m	Mass of droplet, g
m	Power factor
m	Spreading exponential
n	Spreading exponential
N	Number of points

N_a	Avogadro’s number, mol^{-1}
Oh	Ohnesorg number ($\mathrm{Oh_c}$ – critical Ohnesorge number)
p	Spreading exponential
r	Droplet spreading radius, mm
r_o	Initial droplet spreading radius, mm
r_{eq}	Equilibrium droplet spreading radius, mm
R	Spherical droplet radius, mm
R	Universal gas constant, J / mol·K
R'	Surface roughness
R^2	Coefficient of determination
Re	Reynolds number ($\mathrm{Re_c}$ – critical Reynolds number)
R_f	Thin film radius, mm
R_L	Laplace radius, mm
S	Spreading coefficient
t	Time, s
t_{150}	Time when the droplet contact angle reaches 150°, s (similarly for t_{90}, t_{120})
t_c	Time at first droplet-surface contact, s
t_i	Induction time, s
T	Temperature, K
T_s	Time scale of surfactant diffusion, s
V	Volume, µL
V_d	Volume of spherical disk, µL
We	Weber number ($\mathrm{We_c}$ – critical Weber number)
$\check{Z}$	Average height, nm
Z_n	Height at point n, nm

α	Fitting parameter for Wang’s model
β	Dampening coefficient, s^{-1}
γ	Surface tension, mN / m
$\dot{y}$	Shear rate, s^{-1}
$\dot{y}_i$	Shear rate on impact, s^{-1}
γ_o	Surface tension of pure solvent, mN / m
γ_{ow}	Interfacial tension between oil (*o*) and water (*w*) (*s* = surface, *g* = gas, *l* = liquid, *d* = droplet), mN / m

Γ	Excess solute at the interface, mol / m^2
Γ_{max}	Maximum adsorption of solute at air-water interface, mol / m^2
ΔP	Disjoining Pressure / Driving force, N / m^2
ε_{δ}	Slip length to characteristic capillary length ratio (fitting parameter)
ζ	Friction coefficient (fitting parameter)
η	Dynamic viscosity, mPa·s
η_D	Droplet viscosity, mPa·s
η_S	Surrounding medium viscosity, mPa·s
θ	Contact angle, deg
θ_c	Cassie Baxter contact angle, deg
θ_d	Dynamic contact angle, deg
θ_e	Equilibrium contact angle, deg
θ_r'	Contact angle of a rough surface, deg
κ	Boltzmann constant, m^2 kg s^{-2} K^{-1}
κ^{-1}	Capillary length, mm
λ	Distance between adsorption and desorption sites, m
μ	Kinematic viscosity, m^2 / s
v	Velocity, mm / s
v_i	Impact velocity, mm / s
v_o	Characteristic velocity, mm / s
v_{Re}	Film drainage rate, m / s
v_t	Terminal velocity, mm / s
Π	Disjoining Pressure, N / m^2
Π_{el}	Electrostatic forces, N / m^2
Π_{vw}	Van der Waals forces, N / m^2
ρ	Density, kg / m^3
τ	Characteristic transition time from inertial to viscous regime, s
ψ	Phase shift, deg
ω	Frequency of oscillation, s^{-1}
Ω	Droplet volume, µL

Abbreviations

AFM: Atomic force microscopy

TLF: Thin liquid film

CA: Contact angle

CMC: Critical micelle concentration

CTAB: Cetyl trimethylammonium bromide

DG: N-Dodecyl β-D-glucopyranoside

DLVO: Derjaguin-Landau-Verwey-Overbeek Theory

DWR: Double wall ring

FPS: Frames per second

HDT: Hydrodynamic theory

LAOS: Large amplitude oscillatory strain

MKT: Molecular kinetic theory

PDMS: Polydimethylsiloxane

PEG400: Polyethylene glycol, 400 g/mol

RH: Relative humidity

RMS: Root mean squared (roughness)

SDS: Sodium dodecyl sulphate

SS: Stainless steel

TMSCellulose: Trimethylsilyl-cellulose

TPCL: Three phase contact line

TS: Trisiloxanes

XG: Xanthan gum

Chapter 1: Introduction

This chapter provides a brief introduction to droplets (the focus of this study) and how their interaction with surfaces is important in many different industrial applications. Subsequently, research novelty, research aims and objectives are highlighted. Finally, an outline of the thesis chapters is provided.

1.1 Droplets in industry

Droplet spreading dynamics on solid surfaces have been widely investigated,(1) there are numerous industrial applications wherein the application and performance of droplets interacting with surfaces can be improved by a greater understanding of the fundamental science. For instance; pesticide deposition,(2, 3) cosmetic applications,(4) adhesives,(5) printing(6) and cleaning products(7, 8) *etc.*, all shown in Figure 1.1.

Figure 1.1.a) Pesticide spreading,(9) b) Oil recovery,(10) c) Adhesives(11) and d) Cosmetics(12)

The agricultural sector commonly uses droplet science to apply pesticides and insecticides. The liquid formulation is applied by a spray coating onto the plant leaves, the droplets adhere to the leaves and spread, thereby covering the leaves. During this process the solvent evaporates, leaving the pesticide behind to be taken up by the plant.(2) A greater adherence of droplets with maximum droplet coverage increases the effectiveness of the pesticide.(13) It was found for example, that adding non-ionic surfactants enhances pesticide uptake,(14) smaller droplets also have improved retention and spread more efficiently.(15)

The ability for a droplet to spread also has a direct impact on the probability for the droplet to be retained on a surface. As the droplet contact area increases so does the droplet-substrate adhesion force, hence a greater force (shear, extensional, drag) is required to detach the droplet.(16) For example, in applications such as fabric conditioners in washing machines,(17) droplets need to attach and be retained on clothing during the wash cycle. The probability for droplet retention will be related to minimizing the droplet-fabric induction time and maximizing the droplet spreading speed. (18) It is these two aspects which are the primary focus of this study.

1.2 Research novelty and opportunities

To date most research has focused on the droplet spreading dynamics in air, with many parameters considered.(1, 19) However, there has been substantially less research focused on liquid-liquid systems.(20) This is surprising as there are numerous industrial applications for liquid-liquid systems such as emulsification,(21, 22) detergency,(7, 8) microfluidics(23, 24) and oil recovery.(25, 26) There is much room to study droplet spreading dynamics in water.(27) However, this leads to a host of new challenges, with thin liquid films preventing spontaneous wetting and possibly leading to lengthy induction times, droplets may ‘balloon’ if the droplet and liquid densities are similar, droplets preferentially wet dispensing surfaces leading to reduced experimental reliability; droplets may entrap air bubbles leading to incorrect behaviours.

More recently the influence of bulk rheological properties on the spreading dynamics of droplets has been investigated.(28, 29) However, to the author’s knowledge, interfacial rheological properties have not yet been considered, although the importance of the interface on droplet-substrate wetting and subsequent spreading is a fruitful area for exploration.

1.3 Research aim and objectives

Aim: The overall aim of this research is to better understand the conditions that promote rapid wetting and droplet spreading on surfaces. The fluid properties, surface properties and interfacial properties will all be considered. The project aim will be achieved by addressing the following objectives.

Objectives:

(1) Understand the effect of fluid properties (viscosity) on the spreading dynamics for droplets spreading in air.

(2) Develop a greater understanding of the key factors that influence droplet-substrate induction time and spreading rates for oil droplets spreading in water. The factors to

be considered include: oil viscosity, oil-terminating group, surfactant addition to the aqueous phase, surface wettability (hydrophilic to hydrophobic), and cellulose surface coatings.

(3) Better understand the role of interfacial shear rheology on the spreading dynamics of inviscid droplets. Previous research has considered the implications of surfactants and dilatational elasticity, but to date, studies have not considered the potential benefits of a strongly elastic film governed by the shear rheological property.

1.4 Thesis outline

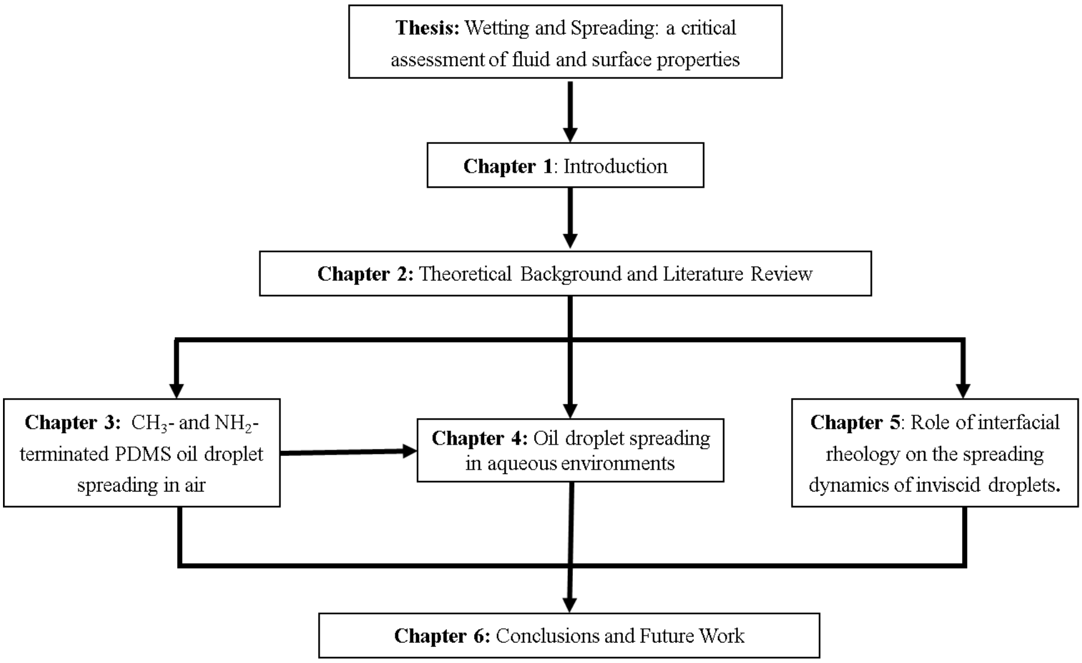

Figure 1.2. Flow chart of the thesis outline

A flow chart highlighting the main contribution of the thesis is shown in Figure 1.2, with Chapters 3-5 representing the results chapters. In Chapter 3, a range of viscosities (9.9 – 12720 mPa·s) of CH_3- and NH_2-terminated polydimethylsiloxane (PDMS) were selected and the droplet spreading dynamics investigated using a pendant drop analyser. The spreading dynamics were compared to three models; Seaver and Berg, de Gennes and Tanner. The Seaver and Berg model was shown to fit low viscosity droplets, presumably due to the model's assumption of a cylindrical disk being more appropriate, de Gennes and Tanner models were shown to fit higher viscosity droplets as they presume a spherical cap. The droplets were released from a height of 0.6, 3 and 6 cm in order to show the effect of additional inertia on the droplet spreading dynamics. For the lowest viscosity this surpassed the critical splashing threshold and the 9.9 mPa·s droplet showed a splashing outcome after being released from 6 cm. The terminating end group was varied from CH_3 to NH_2 where there was little difference in spreading. The studies presented in Chapter 3 provide the fundamental knowledge for complete wetting systems and describe spreading of droplets in air, which forms the foundation of Chapter 4.

In Chapter 4, the same oils are used to investigate the spreading droplet dynamics under water, the oil viscosity effects are also studied. Due to density similarities D_2O is used, this requires an inverted system. The effects of surface hydrophobicity is also investigated, by silanising silicon surfaces to vary water contact angles in air from 0 – 100°. The surface roughness is examined using cellulose coated silicon wafers, however, reduced spreading is also an effect of water retention and swelling of the cellulose fibres. The interfacial tension is explored by using a water soluble surfactant (SDS – sodium dodecyl sulphate) at various concentrations; 0, 0.25, 0.65 and 2.4 g/L. The effect of the NH_2-terminating group was shown to have a larger effect on spreading dynamics in water due to the polarizability.

Chapter 5 demonstrates the effect of interfacial rheology on the effects of droplet spreading dynamics. The interfacial shear rheology of saponin loaded water interface was first measured using a Discovery Hybrid Rheometer (TA Instruments, UK) and the concentration of 0.001 wt% chosen to minimise bulk effects whilst maximising interfacial shear elasticity. The droplets were then spread on silicon wafers, an increase in initial spreading dynamics was recorded due to the breaking of the film and the elastic energy promoting spreading dynamics.

Thesis conclusions are provided in Chapter 6. The research was aimed at understanding how different parameters affect spreading dynamics. It was found that increased viscosity of the spreading oil slowed dynamics, increasing the continuous phase viscosity also decreased spreading dynamics. Surfactant SDS (0 – 2.4 g/L) was added to decrease the interfacial tension, it was also found to increase the induction time due to Marangoni effects, the spreading dynamics were also slowed due to the surfactant. The hydrophobicity of the surface (water contact angle in air from 0 – 100^o) was also shown to slow the dynamics. Increasing the surface roughness using cellulose, however, prevented the droplet from spreading at all. The addition of saponin, which increases the interfacial shear elasticity also increased the early spreading dynamics of droplet spreading; as the film ruptured the elastic energy promoted quicker spreading dynamics.

It is important to note that a separate materials and methods section is provided for each chapter. Due to numerous techniques and slight adjustments to the technique this was considered the most appropriate way to present the information.

References A

1. VELLINGIRI, R., N. SAVVA and S. KALLIADASIS. Droplet spreading on chemically heterogeneous substrates. *Physical Review E*, 2011, **84**(3), p.036305.
2. ZHU, H., Y. YU, L. XU, H. OZKAN and C. KRAUSE. Evaporation Time and Spread Area of Adjuvant-amended Droplets on Waxy and Hairy Leaves. *In: ILASS-Americas 22nd Annual Conference on Liquid Atomization and Spray Systems, Cincinnati, OH*, 2010.
3. BERGERON, V., D. BONN, J.Y. MARTIN and L. VOVELLE. Controlling droplet deposition with polymer additives. *Nature*, 2000, **405**(6788), p.772.
4. BUTLER, H. *Poucher's Perfumes, Cosmetics and Soaps.* Springer Netherlands, 2013.
5. DE RUIJTER, M.J., J. DE CONINCK and G. OSHANIN. Droplet Spreading: Partial Wetting Regime Revisited. *Langmuir*, 1999, **15**(6), pp.2209-2216.
6. CAZABAT, A.-M. How does a droplet spread? *Contemporary Physics*, 1987, **28**(4), pp.347-364.
7. GILANI, M.N., H. DING and P.D. SPELT. Sliding, pinch-off and detachment of a drop on a wall in shear flow. *In: APS Division of Fluid Dynamics Meeting Abstracts*, 2008.
8. DING, H., M.N. GILANI and P.D. SPELT. Sliding, pinch-off and detachment of a droplet on a wall in shear flow. *Journal of Fluid Mechanics*, 2010, **644**, pp.217-244.
9. BURKE, M. *https://www.chemistryworld.com/news/pesticide-use-threatens-human-rights-un-advisers-say/2500546.article*, 2017.
10. FLURY, C., A. AFACAN, M. TAMIZ BAKHTIARI, J. SJOBLOM and Z. XU. Effect of Caustic Type on Bitumen Extraction from Canadian Oil Sands. *Energy & Fuels*, 2014, **28**(1), pp.431-438.
11. PATTERSON, E. https://www.rehabs.com/about/guide-inhalant-abuse-treatment/. 2018.
12. LUO, E.K. https://www.medicalnewstoday.com/articles/319867.php. 2018.
13. BASU, S., J. LUTHRA and K. NIGAM. The effects of surfactants on adhesion spreading and retention of herbicide droplet on the surface of the leaves and seeds. *Journal of Environmental Science and Health, Part B*, 2002, **37**(4), pp.331-344.
14. NALEWAJA, J.D. and R. MATYSIAK. Spray deposits from nicosulfuron with salts that affect efficacy. *Weed Technology*, 2000, **14**(4), pp.740-749.
15. BAUR, P. Impact of adjuvants on droplet spreading and droplet deposit area after spray application. *In: Pesticide Formulations & Delivery Systems, 26th Volume: Reassessing Pesticide Technologies*. ASTM International, 2008.
16. AL-SHARAFI, A., B.S. YILBAS, H. ALI and N. ALAQEELI. A Water Droplet Pinning and Heat Transfer Characteristics on an Inclined Hydrophobic Surface. *Scientific Reports*, 2018, **8**, p.3061.
17. MAC NAMARA, C., A. GABRIELE, C. AMADOR and S. BAKALIS. Dynamics of textile motion in a front-loading domestic washing machine. *Chemical Engineering Science*, 2012, **75**, pp.14-27.
18. MINTEER, S., I. ZHAROV and A. KHABIBULLIN. *The effect of sulfonic acid group content in pore-filled silica colloidal membranes on their proton conductivity and direct methanol fuel cell performance.* 2014.
19. BONN, D., J. EGGERS, J. INDEKEU, J. MEUNIER and E. ROLLEY. Wetting and spreading. *Reviews of modern physics*, 2009, **81**(2), p.739.
20. FETZER, R., M. RAMIASA and J. RALSTON. Dynamics of liquid− liquid displacement. *Langmuir*, 2009, **25**(14), pp.8069-8074.
21. KUMAR, D. and S.K. BISWAS. Effect of surfactant dispersed in oil on interaction force between an oil film and a steel substrate in water. *Colloids and Surfaces A: Physicochemical and Engineering Aspects*, 2011, **377**(1-3), pp.195-204.
22. LE FOLLOTEC, A., I. PEZRON, C. NOIK, C. DALMAZZONE and L. METLAS-KOMUNJER. Triblock copolymers as destabilizers of water-in-crude oil emulsions.

Colloids and Surfaces A: Physicochemical and Engineering Aspects, 2010, **365**(1-3), pp.162-170.

23. SPILDO, K. and J.S. BUCKLEY. Uniform and mixed wetting in square capillaries. *Journal of Petroleum Science and Engineering*, 1999, **24**(2-4), pp.145-154.
24. KOBAYASHI, I., M. NAKAJIMA and S. MUKATAKA. Preparation characteristics of oil-in-water emulsions using differently charged surfactants in straight-through microchannel emulsification. *Colloids and Surfaces A: Physicochemical and Engineering Aspects*, 2003, **229**(1-3), pp.33-41.
25. FREER, E., T. SVITOVA and C. RADKE. The role of interfacial rheology in reservoir mixed wettability. *Journal of Petroleum Science and Engineering*, 2003, **39**(1-2), pp.137-158.
26. ASSERSON, R.B., A.C. HOFFMANN, S. HØILAND and K.M. ASVIK. Interfacial tension measurement of freon hydrates by droplet deposition and contact angle measurements. *Journal of Petroleum Science and Engineering*, 2009, **68**(3-4), pp.209-217.
27. SEVENO, D., T. BLAKE, S. GOOSSENS and J. DE CONINCK. Predicting the wetting dynamics of a two-liquid system. *Langmuir*, 2011, **27**(24), pp.14958-14967.
28. WANG, X.D., D.J. LEE, X.F. PENG and J.Y. LAI. Spreading Dynamics and Dynamic Contact Angle of Non-Newtonian Fluids. *Langmuir*, 2007, **23**(15), pp.8042-8047.
29. LIANG, Z.-P., X.-D. WANG, D.-J. LEE, X.-F. PENG and A. SU. Spreading dynamics of power-law fluid droplets. *Journal of Physics: Condensed Matter*, 2009, **21**(46), p.464117.

Chapter 2: Theoretical Background and Literature Review

In this chapter, the current literature on droplet spreading dynamics will be summarised. Current methods to analyse droplet spreading experiments; including spreading models and the fitting laws for different spreading regimes will be discussed. The current research exploring the effects of surface roughness, surfactant and droplet rheology will also be highlighted. Where possible, the current research conducted in aqueous environments will also be described.

2.1 Surface-droplet interactions

Surface-droplet interactions affect the amount of wetting which can occur. Be it complete or partial wetting, the rate and dynamics of spreading are important for many industries and applications; such as printing, coatings, agriculture adhesives and detergency.(1) There has been a constant interest in the field, which as such, has led to a wide range of methods to analyse results and several theoretical models to describe spreading dynamics.(2, 3)

The first step of any droplet spreading on a surface is the droplet-substrate contact. A droplet impacting on a dry surface may not always spread, with a range of complicated flow patterns potentially occurring. This was comprehensively studied by Rioboo *et al.*(4-6), who identified at least six possible outcomes; i) deposition (spreading), ii) prompt splash, iii) corona splash, iv) receding break-up, v) partial rebound and vi) complete rebound as shown in Figure 2.1.

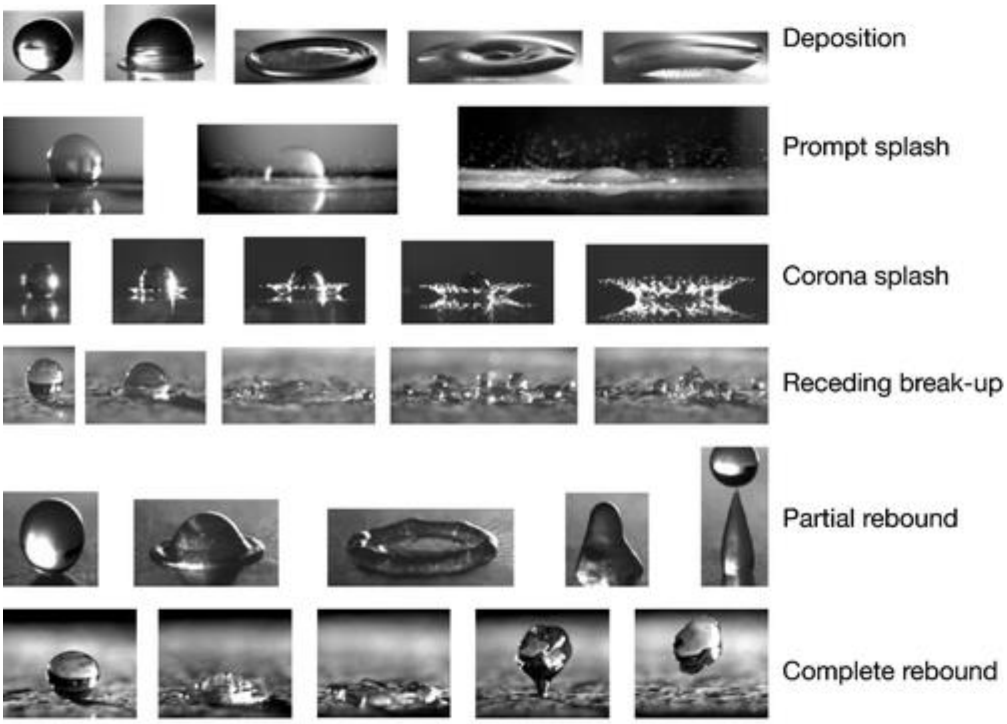

Figure 2.1. Six possible outcomes from a droplet impact on a dry surface.$^{(5)}$

There are many parameters which affect the spreading dynamics of a droplet.$^{(7\text{-}9)}$ For instance, droplet viscosity (μ), density (ρ), impact velocity (v_i), surface tension (γ) and compressibility, as well as droplet shape, size (r), volatility, surrounding medium density, droplet-surface wettability (θ_e),$^{(10)}$ surface roughness, surface film thickness or surface compressibility.$^{(6, 7)}$ Researchers have also studied other parameters such as temperature,$^{(11, 12)}$ and the influence of surfactants$^{(13\text{-}15)}$ or electrostatics.$^{(16, 17)}$

Often, the main parameters are grouped together to form dimensionless numbers, where forces can be more easily compared. As many parameters are dependent on one another, this enables a prediction of droplet impact morphologies to be made using only these dimensionless numbers. Dimensionless numbers are commonly used to predict the outcome of impacting droplets. Firstly, the Bond number (also known as the Eötvös number) shown in Eq. 2.1 compares surface tension and body forces, to determine the contributions from gravity, which is negligible when $Bo < 0.1^{(18)}$

$$Bo = \frac{\Delta\rho g L^2}{\gamma} \qquad (2.1)$$

where g is the gravitational acceleration, L the characteristic length, $\Delta\rho$ the density and γ the surface tension. The Bond number also reflects the droplet shape; if there is negligible gravitational effect then the droplet shape will be spherical, otherwise it may elongate and deform. (19) The Bond number is used to describe the droplets in motion, gravity may affect the droplets whilst they are falling, however this does not necessarily mean that gravity will have an impact on the droplet spreading dynamics. For small droplets surface and viscous forces will be dominant. Two other dimensionless numbers often used are the Weber (*We*) number shown in Eq. 2.2 and Reynolds (*Re*) number shown in Eq. 2.3:

$$We = \frac{\rho L v^2}{\gamma} \qquad (2.2)$$

$$Re = \frac{\rho L v}{\eta} \qquad (2.3)$$

where v is the velocity and η is the dynamic viscosity. The Weber number compares inertia to capillary effects. In terms of droplet spreading, inertia is comparable or less than capillary forces when $We < 10$. Similarly, Reynolds numbers compare inertia effects with viscous effects; this is normally used to infer a level of turbulence in flow dynamics.(20) In terms of droplet spreading, inertia is comparable or less than viscous forces when $Re < 10$.(18) Reynolds and Weber numbers can also be used to indicate the outcomes of substrate-droplet interactions and calculate critical values for splashing thresholds.

The Ohnesorge number (Oh) which is a function of both the Weber and Reynolds numbers as shown in Eq. 2.4, compares the capillary to viscous forces which are comparable when $Oh \approx 1$.(18)

$$Oh = \frac{\sqrt{We}}{Re} = \frac{\mu}{\sqrt{\rho \gamma L}} \tag{2.4}$$

Finally, the capillary number (Ca) is used to compare viscous and surface tension forces shown in Eq. 2.5;

$$Ca = \frac{\eta v}{\gamma} \tag{2.5}$$

where η is the dynamic viscosity. Many authors have used these dimensionless numbers to describe and compare droplet impact outcomes on solid surfaces, liquid interfaces and thin film surfaces.(21-24) Ohnesorge and Weber numbers are generally considered, for example a critical splash *We* or *Oh* number will indicate a point at which a droplet no longer spreads on a surface but instead splashes. (7)

Many authors have determined the critical Weber number for droplets splashing on solid surfaces. Pate *et al.* determined this condition to be $We \sim 100$,(25) Rein *et al.*, $We = 12$,(7) and Range and Feuillebois produced a range of critical *We* from 105 – 345(26) depending on surface roughness. As demonstrated, the critical splash condition as described by *We* is not consistent.

Some authors provide a critical splash number as a function of other dimensionless numbers, *e.g.* Hernandez *et al.* gives a critical Ohnesorge number as a function of the Reynolds number.(27) Other authors (6, 8, 28-30) also combined Weber and Reynolds numbers to form the Sommerfeld number $K = We^{0.5}Re^{0.25}$ (also $K = OhRe^{1.25}$), with the idea that using a single parameter simplifies the assessment and balances the two dimensionless numbers to create a single critical splash number. Yarin *et al.*(6) found K to be 57.7 for a flat smooth surface, however Lembach *et al.*(31) found K to be 87 on a nanofiber mat, again highlighting the strong effect of surface roughness.

Dimensionless numbers are regularly used to describe and compare droplet impact; however, they are not generally used in the case of spreading dynamics. One problem with using critical dimensionless numbers is that they often are not comparable; this is due to other parameters that affect droplet impact being undefined. Surface roughness has shown to have a large influence on whether a droplet spreads or splashes but is often not a given parameter. Dimensionless numbers are insensitive to surface roughness (both amplitude and wavelength) and surface wettability which also has a significant effect.(5, 6)

2.2 Droplet spreading

This report will focus on droplet spreading outcomes, i.e. on droplets that have low Reynolds and Weber numbers on impact (low kinetic energy). Droplets spread on surfaces due to molecular interactions. The molecular forces between the surface, droplet and surrounding medium such as van der Waals, electrostatics, hydrogen bonding affect the spreading and are encompassed within the surface forces.(32) Surface forces are generally split into two; cohesive forces – forces between like molecules – and adhesive forces – forces between unlike molecules. Stronger cohesive forces means a droplet will resist spreading and *vice versa*.(33) Other forces also affect the droplet spreading dynamics such as gravitational and buoyancy.(19, 34)

Different liquids interact differently with various surfaces, the chemistry of the surface, surrounding medium and droplet dictates what type of interactions occur and to what degree. For instance, the charge on the surface and droplet can be manipulated to alter the amount of wetting(35). It is easy to forget that the surrounding medium can also play an important role in droplet spreading, Figure 2.2 shows the same oil droplet spreading onto the same surface in air and water environments, note the large difference in contact angle.(36)

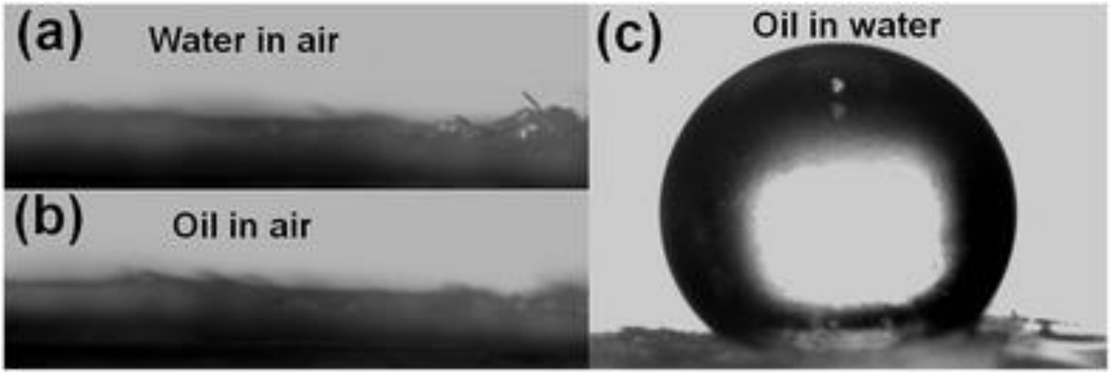

Figure 2.2. Effect of the surrounding medium on a) water droplet in air and b) oil droplet in air (both drops can be seen to completely wet). However in c) oil droplet underwater, a partially wetting, high contact angle droplet is seen. (36)

The wetting behaviour is frequently described by the equilibrium contact angle. A liquid which interacts favourably with a surface will spread thinly, leading to a contact angle well below 90°; whereas a droplet which interacts unfavourably with the surface will bead-up on the surface, resulting in a contact angle greater than 90°, these are depicted in Figure 2.3.

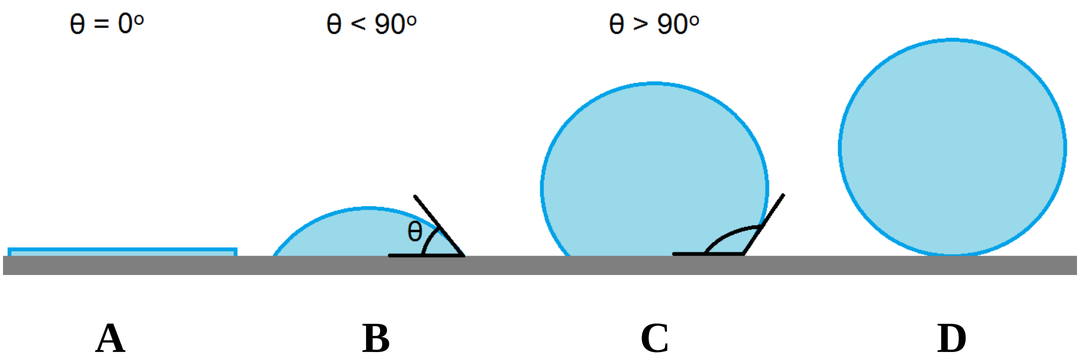

Figure 2.3. Equilibrium contact angles where the droplet-surface interactions are a) favourable to d) unfavourable (complete non-wetting).

A droplet on a surface can form an equilibrium shape which is A) completely wetting and the equilibrium contact angle, $\theta_e = 0$ or B) partially wetting (high wettability) and the equilibrium contact angle, $\theta_e < 90^o$ or C) partially wetting (low wettability) and the equilibrium contact angle, $\theta_e > 90^o$ or D) completely non-wetting where the droplet does not attach but rests on the surface. Minor deformations may be seen due to gravitational effects. Whether the droplet partially or completely wets a surface is determined by the interactions between the surface, droplet and surrounding medium, which can also affect the dynamics of spreading.(3, 37, 38) These surface interactions can be described by the contact angle θ. This results in the Young's equation shown in Eq. 2.6 which considers three interfacial tensions; γ_{sl} the solid-liquid, γ_{sv} the solid-vapour and γ_{lv} the liquid-vapour.(39)

$$cos\,\theta = \frac{\gamma_{sv} - \gamma_{sl}}{\gamma_{lv}} \tag{2.6}$$

Whether a droplet completely wets or only partially wets a surface can be determined by the spreading coefficient S shown in Eq. 2.7.(39)

$$S = \gamma_{sv} - (\gamma_{sl} + \gamma_{lv}) \tag{2.7}$$

If the interfacial tensions lead to $S > 0$, then the droplet will completely wet, if $S < 0$ then the droplet will only partially wet the surface. Combining both Eqs. 2.6 and 2.7 yields the Young-Dupré equation shown in Eq. 2.8, which describes the spreading coefficient given by the liquid-vapour surface tension and equilibrium contact angle.(39)

$$S = \gamma_{LV}(cos\,\theta - 1) \tag{2.8}$$

2.3 Droplet spreading models

There are two theoretical models used to represent the spreading of a droplet on a solid substrate; the hydrodynamic model (HDT) and molecular-kinetic model (MKT). The two models have caused controversy as they contradict one another. The hydrodynamic model describes viscous flow however it also follows the assumption of constant mass for liquids of constant density. The bulk viscous friction is the resisting force of spreading. The model splits the droplet into an inner and outer region (sometimes it also has a third intermediate region). The outer region is where the non-slip boundary is applied, *i.e.* the liquid at the solid substrate has zero velocity. The inner region is where slippage occurs and occurs within the first few layers of molecules near the substrate. The overall model gives the Eq. 2.9; (40-42)

$$(\theta_d)^3 = \left(\theta_{eq}\right)^3 \pm 9\frac{\eta V}{\gamma_{lg}} ln\left(\frac{L}{L_s}\right) \tag{2.9}$$

where L_s is in principle the fitting parameter or the slip factor, it represents the region where no-slip does not apply. The ± sign represents whether the dynamic contact angle is receding or advancing, θ_e is the equilibrium contact angle and θ_d the dynamic contact angle. The limitations of the model are that it does not take into account the characteristic of the solid surface or inertia.(40-42)

The second model is the molecular-kinetic theory (MKT) (40, 42, 43) which accounts for the surface characteristics but not the viscous dissipation. The hydrodynamic model is often thought as a macroscopic view, whereas MKT is seen as a microscopic point. Adsorption/desorption processes near the contact line dictates droplet spreading and can occur with no bulk liquid flow. As adsorption takes place, this shifts the equilibrium and the local surface tension, which drives the contact line forward and the droplet spreads. The relationship between dynamic contact angle and velocity are shown in Eq. 2.10;

$$cos\,\theta_d = cos\,\theta_{eq} \mp \frac{2kT}{\gamma_{lg}\lambda^2} arcsinh\left(\frac{V}{2K_w\lambda}\right) \tag{2.10}$$

where k is the Boltzmann constant, T the temperature, λ the distance between adsorption and desorption sites and K_w the quasi-equilibrium rate constant, K_w and λ are fitting parameters. These two models predict dynamic droplet spreading and are often said to work at different TPCL (Three Phase Contact Line) velocities. Blake and Haynes(44) found this model predicts fast spreading droplets; values for K_w and λ are around 10^6 s^{-1} and 1 nm, respectively.(40, 43, 45)

Studies have verified both MKT(46-48) and HDT(49-51) are applicable for a range of fluids. Others have shown that both models can be used to fit experimental data.(52-54) Certain systems have shown a better fit to one model, such as when liquid-liquid displacement occurs which tend to favour the MKT,(53) and for highly viscous fluids where the hydrodynamic model tends to better predict spreading dynamics.(53) Silicone oils are generally thought to be described by the hydrodynamic model. (40-42, 55, 56) However, several authors (57-59) have also suggested that MKT may be more prominent at early times where the contact angle is large and there is a crossover into hydrodynamic spreading. The crossover time will decrease with increasing viscosity.(57)

Even though the two models have been formed via two different perspectives; both are shown to be reasonably good in describing observed dynamic spreading behaviour.(53) A combined theory is now gaining much interest in that both models could better describe the evolution of a spreading droplet.(53) Combined models better represent the droplet spreading for a wider range of dynamics (which is dictated by several parameters such as viscosity, surface tension).(40, 57, 60, 61)

2.3.1 Spreading laws

Many droplet spreading laws use the droplet spreading radius and fit this to an exponent of time, with various parameters included in the coefficient. In its simplest form Eq. 2.11 describes droplet spreading:

$$r = Ct^n \tag{2.11}$$

where r is the spreading radius, t the spreading time, C a coefficient and n the fitted exponent. There are a wide range of spreading laws which have been theoretically derived with different forces applicable. For instance, models will use either gravity (gr) or surface tension (st) as the dominant force for spreading, which will generate different exponents. Whether the model is generated in two- (2D) or three- (3D) dimensions creates slightly different exponents; also whether the dynamics of the bulk of the droplet (vis) (where the viscosity dominates) or the moving contact line (cl) (where capillary forces dominates) is considered also generates different exponents. A few examples are shown in Table 2.1; (38)

Table 2.1. A list of examples of the exponents generated using different methods.(38)

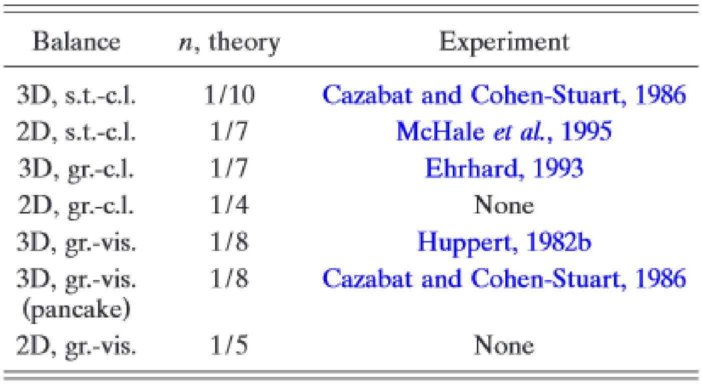

Balance	n, theory	Experiment
3D, s.t.-c.l.	1/10	Cazabat and Cohen-Stuart, 1986
2D, s.t.-c.l.	1/7	McHale *et al.*, 1995
3D, gr.-c.l.	1/7	Ehrhard, 1993
2D, gr.-c.l.	1/4	None
3D, gr.-vis.	1/8	Huppert, 1982b
3D, gr.-vis. (pancake)	1/8	Cazabat and Cohen-Stuart, 1986
2D, gr.-vis.	1/5	None

The difference in exponents results from the different principles used to derive them, but also the different approximations and conditions;(62) 1/8, 1/7 and 1/10 are the most common values published in the literature for long time spreading dynamics. It is believed that a droplet will follow Tanner's law (49) (value of 1/10) if the droplet size is below a capillary length. Gravity can affect the spreading dynamics of a droplet but the effect is negligible if the droplet radius is smaller than the capillary length (κ^{-1}), which is given by Eq. 2.12:

$$\kappa^{-1} = \sqrt{\frac{\gamma}{\rho g}} \qquad (2.12)$$

For droplets with a radius smaller than the capillary length, gravity is not considered to influence the spreading dynamics; however, as discussed earlier, gravity can affect the droplets. If the droplet has been released from height, this inertia can affect the outcome of the droplet's impact on the surface. As the droplet size increases the dynamics change due to increasing gravitational forces and the droplet spreading dynamics are said to follow either a value of 1/8 (Lopez *et al.*(63)) or a value of 1/7 (Ehrhard *et al.*(64)). A crossover from 1/10 to 1/8 has been shown by Cazabat *et al.*,(65) whereas a crossover to 1/7 has been shown by Ehrhard *et al.*,(62) although the experimental data used is not sufficiently accurate to distinguish between 1/7 and 1/8.(38)

For a non-volatile droplet (constant volume) where gravity effects are negligible (radius smaller than the capillary length) and the droplet exhibits complete wetting on a smooth flat surface, there are two commonly observed spreading regimes as shown in Figure 2.4. The first regime is the inertial regime (sometimes called the capillary regime), during which inertia controls the speed of spreading; inertia resists the capillary driven spreading. The inertial regime accounts for the fastest spreading dynamics, with the spreading radius r increasing with time t according to the power law $r = Ct^{0.5}$, where C is a prefactor constant. (66)

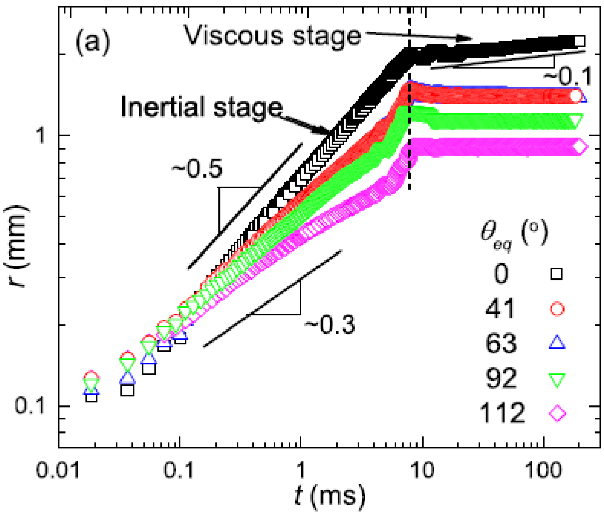

Figure 2.4. Water droplets on smooth glass substrates, silanised to form varying wettabilities. Droplet spreading dynamics occur via two spreading regimes, one with an exponent of 0.5 and the second with an exponent of 0.1. As shown the dependency is lessened for surfaces of partial wetting, θ_{eq}).(66)

The second regime follows a transitional stage when the droplet viscosity dominates the droplet spreading and is called the viscous regime. In the viscous regime the droplet spreading dynamic is comparatively slower with an exponent of 0.1, as described by Tanner. (67)

For completely wetting surfaces, as the droplet viscosity increases the effect of inertia diminishes as viscous forces dominate. The change is reflected in the inertial-viscous transition occurring earlier and less abruptly.(68, 69) At very high viscosities the two regimes cannot be distinguished, and the spreading dynamics are represented by a transient power law, beginning high and slowly decreasing with time towards n = 0.1.(70) The spreading exponent can be computed by Eq. 2.13;

$$n = \frac{\Delta \ln r}{\Delta \ln t} \tag{2.13}$$

where the short time dynamics the exponent can be between $0.5 < n < 1$, and the long-time dynamics anywhere between $0.1 < n < 0.2$. Eddi *et al.* (71) showed this effect for high viscosity oils with increasing fluid viscosity of water/glycerine mixtures spreading on glass substrates coated with fluoropolymers, shown in Figure 2.5a and b;

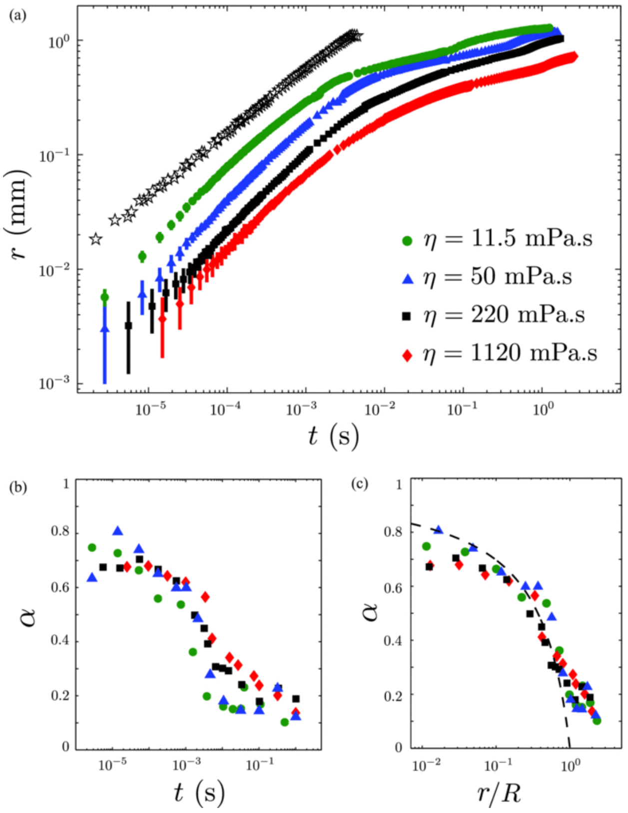

Figure 2.5. a) The spreading of different viscosity fluids on a partially wetting surface, b) the power exponent α (or n) as a function of the spreading time and c) the power exponent as a function of spreading radius.(71)

Figure 2.5a and b show the change in the spreading exponent n (or α) with time. The exponent starts at 0.8 and decreases to approximately 0.1.(71) The exponent of $n = 0.1$ is based on Tanner's model which was developed using the hydrodynamic model.(41) The spreading radius was theoretically derived and related to the droplet size, viscosity and surface tension. Tanner's model is shown in Eq. 2.14;(49)

$$r = R\left(\frac{\gamma}{\eta R}\right)^{\frac{1}{10}} t^{\frac{1}{10}} \tag{2.14}$$

where R is the spherical drop radius. Tanner first developed the model based on silicone oils over a viscosity range of 1.08 – 106 Pa·s, showing good agreement between the experimental data and model. Seaver and Berg(2) also produced a model where the fluid dynamics of a spreading spherical cap is approximated to a spreading cylindrical disk. For complete wetting, the authors formed a model described by Eq. 2.15 where r_o is the initial spreading radius, V_d is the volume of the spherical disk (constant):

$$r = r_o\left(1 + \frac{40\gamma V_d^3}{\pi^3 \mu r_o^{10}} t\right)^{\frac{1}{10}} \tag{2.15}$$

De Gennes(3) developed a spreading spherical cap geometry to describe droplet spreading, where the droplet dynamic contact angle is related to the spreading radius and volume (which is constant) as described by Eq. 2.16, where Ω is the drop volume, $n = 2/(3m+1)$ and $p = 2m/(3m+1)$ with the most probable value of $m = 3$:

$$r(t) = \sqrt{\frac{t^n \Omega^p}{\pi}} \tag{2.16}$$

All three models assume the driving force to be surface tension and the opposing force to be fluid viscosity,(72) and so are predominantly considering later stages of spreading, i.e. the viscous regime. Alteraifi *et al.*(73) are one of the few studies to compare all three models. Figure 2.6 shows the three models compared to the experimental results of a 100 cP silicone oil spreading on a glass surface.

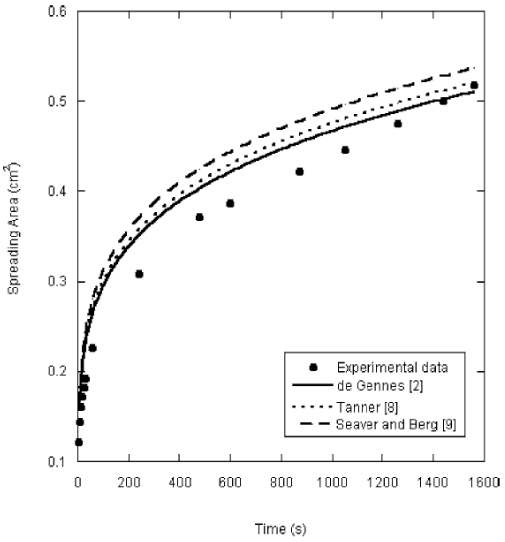

Figure 2.6. The spreading of a 100 cP silicone oil droplet and comparison to the spreading dynamics models as derived by de Gennes, Tanner, and Seaver and Berg.$^{(73)}$

As shown in Figure 2.6, all three models produce relatively good approximations to the spreading dynamics. Moet *et al.*$^{(73)}$ stated that such similarity in predictability of all three models does question the exclusivity of the assumptions used for each model. The authors also went further to discover that whilst these models were accurate in describing the spreading dynamics of silicone oils from 10 – 1000 cP, they were incapable of modelling spreading dynamics of other oils, most of which were low viscosity, but this also included the case of high viscosity oils, glycerine.

2.3.1.1 Partial wetting

Bird *et al.*$^{(74)}$ studied droplet spreading on partially wetting surfaces and found that the exponent was dependent on the surface wettability. Varying the wettability of the surface caused the spreading exponent to vary from $0.25 < n < 0.5$; these were similar results to what had been found by Drelich and Chibowska, $^{(75)}$ and was thought to be the inertial regime for the partial wetting surfaces. Eddi *et al.* $^{(69, 71)}$ showed that low viscosity droplets (water/glycerine) on surfaces of varying wettability always resulted in an initial spreading regime of $n = 0.5$, shown below in Figure 2.7, before exhibiting wettability effects at longer spreading times.

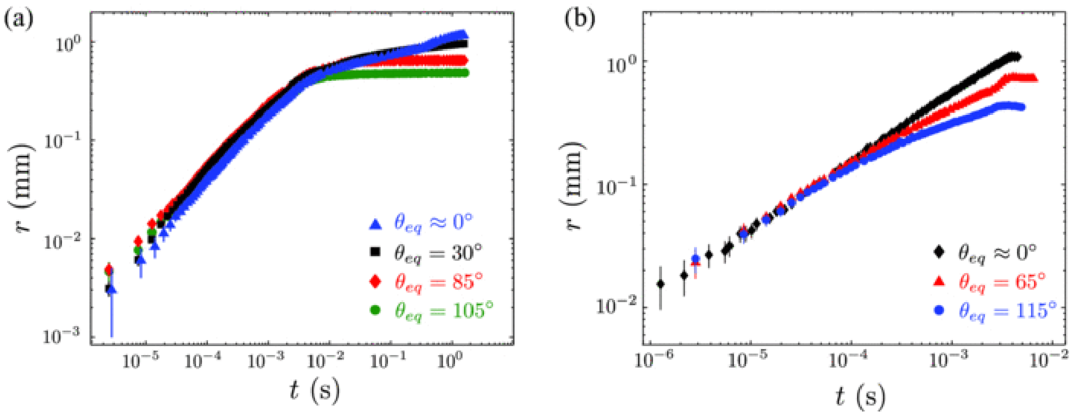

Figure 2.7. a) the spreading of a 50 mPa·s water/glycerine mixture on surfaces of varying wettability, b) the spreading of water on surfaces of varying wettability.(69, 71)

Figure 2.7a and b were obtained by the spreading of droplets on glass substrates of varying wettability, altered by fluorinating the surfaces. Figure 2.7a was obtained using a water/glycerine mixture with a viscosity of 50 mPa·s, whereas Figure 2.7b shows the spreading of pure water. As can be seen, the more hydrophobic the surface (the larger the equilibrium contact angle), the slower the droplet spreads, following the inertial regime of spreading, where droplets spread at $n = 0.5$. The dependence on surface wettability has also been shown by Stapelbroeck *et al.*(76). Eddi *et al*, (69, 71) believed that this was seen due to their optimised technique, where they gathered spreading data from below the droplet, which enabled them to record spreading data at earlier time scales.

In addition to the complete spreading model of Seaver and Berg(2) (Eq. 2.15), the model can be modified by including a correction factor to account for partial spreading of a droplet given by Eq. 2.17;(2)

$$\frac{dr}{dt} = \frac{4\gamma V_d^3}{\pi^3 \mu r^9} - \frac{\gamma \beta V_d}{2\pi \mu R r^3} \qquad (2.17)$$

where $\beta = 1 - \cos\theta_{eq}$. However, integrating Eq. 2.17 gives what the authors describe as an "unwieldly form", thus the equation has not been used to compare to experimental data. An empirical model has also been developed by Wang *et al.*(77) and is given by Eq. 2.18;

$$r = r_{eq}\left[1 - exp\left(-\frac{a}{r_{eq}} t^n\right)\right] \qquad (2.18)$$

As $r_{eq} \rightarrow \infty$, as for complete wetting, then $r = at^m$.(77) The model was originally derived by Lavi and Marmur,(10) but Wang *et al.*(77) showed the model can describe partially wetting droplets, as shown by Figure 2.8.

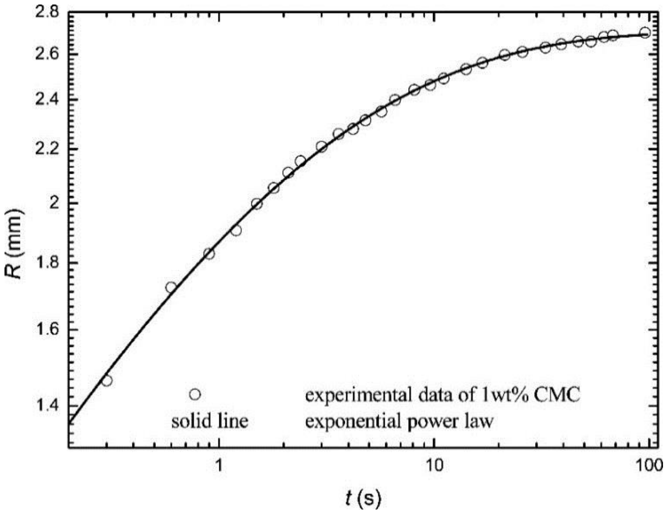

Figure 2.8. The spreading dynamics of a partially wetting droplet and the fit given by Eq. 2.18.(77)

2.4 Thin liquid films

Replacing the surrounding medium from air to water changes the spreading dynamics due to increased viscosity, from 1.818 x 10^{-5} Pa s (air)$^{(78)}$ to 1.002 x 10^{-3} Pa s (water)$^{(79)}$ at 20^{o}C, along with increased density from 1.204 kg/m^3 (air) to 998 kg/m^3 (water) at 20^{o}C. As the droplet approaches the surface, the droplet impact process follows several stages (see below).$^{(80)}$

I Approach
II Droplet interface deformation
III Drainage of thin liquid film (TLF)
IV Coalescence and wetting

As the droplet approaches the surface there is a deceleration in the approach velocity. Since the approach dynamic is greater than the time required for the liquid to drain from between the approaching droplet and spreading surface, a TLF is formed which cannot drain quickly enough. The effect of this is to deform the approaching droplet.$^{(81)}$ To 'wet' the substrate, the TLF must completely drain, described as the drainage time, such that the droplet contacts the substrate and spreads.$^{(82)}$ Rupture of the TLF occurs at a critical thickness when surface forces become strong and destabilize the TLF.$^{(83)}$ Following TLF rupture a hole appears in the TLF, with interfacial tension forces causing rapid expansion and displacement of the continuous phase.$^{(80)}$

For a TLF, the pressure is different from the bulk fluid due to the effect of surfaces forces.$^{(84)}$ The disjoining pressure becomes a function of i) molecular, ii) electrostatic and iii) structural forces. The structural force results from molecular orientation at the surface, while the electrostatic force is a function of the substrate and interfacial surface potentials and electrolyte concentration, influencing the magnitude of electrostatic repulsive force which can stabilize against van der Waals attractive forces.

When the attractive van der Waals forces acting between the droplet and substrate dominate, then an attractive pimple forms, (Figure 2.9) where the droplet is deformed towards the substrate. If electrostatic repulsion forces are strong, but the droplet inertia overcomes those forces, then a dimple in the droplet is observed.(85) The magnitude of the dimple formation can be characterised by the film capillary number $Ca_f = (\mu v_o/\gamma)(R_L/H_o)^2$, where v_o is the characteristic velocity, H_o the TLF thickness and R_L the Laplace radius.(86) A dimple forms a barrier rim, with the rate at which liquid flows past this rim often the rate limiting process to droplet wetting. Dimple and pimple formations are shown in Figure 2.9.(87)

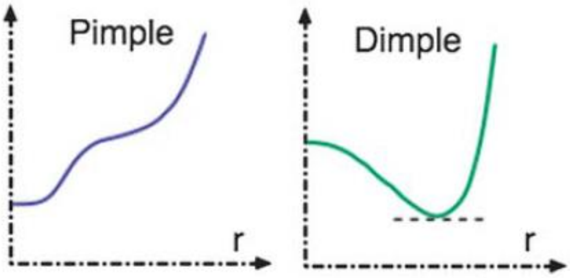

Figure 2.9. Commonly seen deformations for droplets approaching a surface, pimple and dimple.(85)

2.4.1 Film drainage and rupture

The Stefan-Reynolds drainage equation describes the liquid drainage between two parallel surfaces which are immobile, shown in Eq. 2.19.(88)

$$V_{Re} = -\frac{2h^3}{3\eta {R_f}^2}\Delta P \qquad (2.19)^{(88)}$$

where h is the TLF thickness, ΔP the difference between the capillary and disjoining pressure and R_f the film radius. If a dimple forms during droplet approach to a surface, film drainage at the centre of the TLF is much longer than at the edge of the TLF, thus film rupture often occurs off centre axis.(88)

The drainage time is a function of the droplet size,(82) with larger droplets requiring longer for the TLF to drain. Also, larger droplets are more deformable, thus again increasing the TLF drainage time.(80, 89) Drainage time is a function of the fluid viscosities, an increase in the continuous phase viscosity reduces the rate of TLF drainage thus increasing drainage time.(80) An increase in the continuous phase density can also increase drainage time, with increased buoyancy forces reducing the ΔP contribution. A comprehensive list of parameters affecting droplet-substrate interaction was summarized by Kamp *et al*,(82) shown in Figure 2.10.

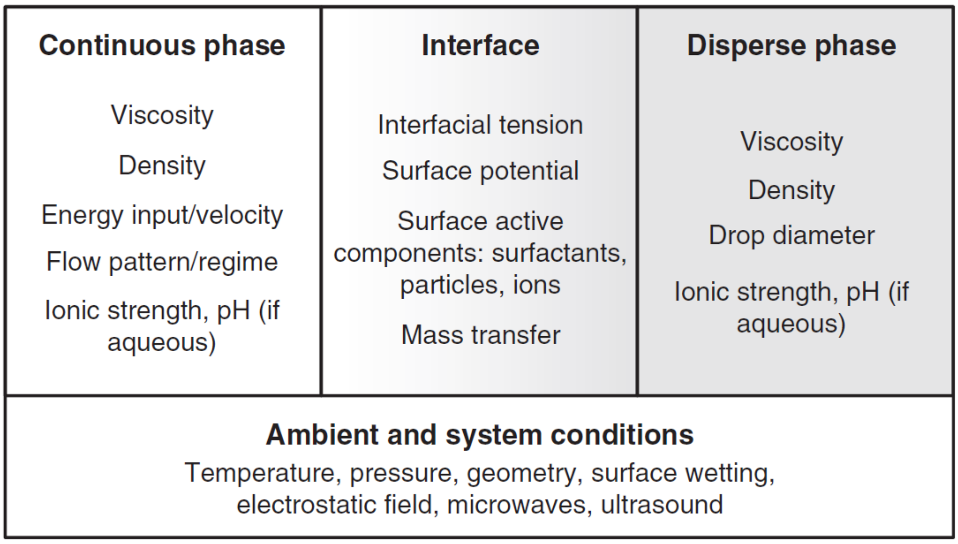

Continuous phase	Interface	Disperse phase
Viscosity Density Energy input/velocity Flow pattern/regime Ionic strength, pH (if aqueous)	Interfacial tension Surface potential Surface active components: surfactants, particles, ions Mass transfer	Viscosity Density Drop diameter Ionic strength, pH (if aqueous)

Ambient and system conditions

Temperature, pressure, geometry, surface wetting, electrostatic field, microwaves, ultrasound

Figure 2.10. Parameters affecting the droplet-substrate interaction process.(82)

2.5 Droplet spreading in water

There are relatively few studies considering droplet spreading in water, with most studies considering liquid-liquid displacement in capillary tubes or micro-channels.(90-95) Displacement dynamics are similar to spreading dynamics with displacement a function of $t^{0.1}$, (96) with the forces governing droplet spreading and displacement being consistent.

Foister(97) studied droplet spreading in water and showed that the dynamic viscosity ratio was most important to describe the change in spreading dynamics. The dynamic viscosity ratios considered were 5.9×10^{-3} to 3180. The larger the dynamic viscosity ratio, the closer the spreading dynamics resembled the spreading of a droplet in air. Foister (96) also showed that the droplet spreading dynamic was dependent on the droplet size, with increasing drop size from 0.0811 to 0.148 cm resulting in a slowing of the droplet spreading dynamics, which was attributed to a decrease in the slip length.

Fetzer *et al.*(95) studied spreading dynamics with two liquids of comparable viscosity, dodecane and water, hence the viscosity ratio was 1.5. For early time spreading dynamics (< 5 ms), the authors were able to fit the data using hydrodynamic models, however for later spreading times there was a clear deviation. The deviation was thought to be caused by local pinning and depinning of the liquid at the surface and so could thus be fitted to the MKT. The authors hypothesised two regimes, the first with higher TPCL velocities (and higher contact angles) could be modelled using the hydrodynamic theory shown in Figure 2.11, and a second regime with slower TPCL velocities (and lower contact angle) could be modelled by MKT.

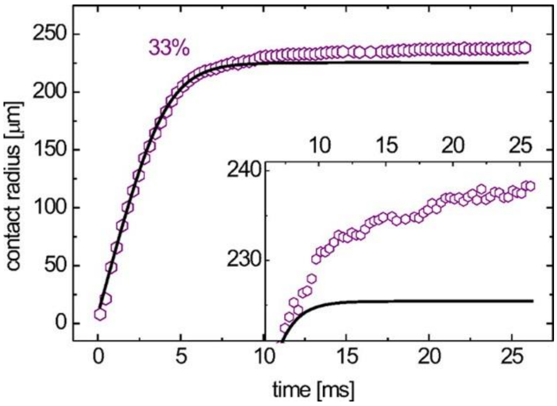

Figure 2.11. The spreading of a dodecane droplet in water on a 33% thiol coated gold surface, with an overlay of the hydrodynamic model.(95)

In a second study Fetzer *et al.* (98) showed that there was less contact line friction in liquid/liquid than in liquid/air systems. The authors also showed that the spreading dynamics of dodecane droplets increased with increased thiol (substrate more hydrophobic), this was observed in the hydrodynamic fittings along with the static contact angles which showed droplets to spread further on more hydrophobic surfaces.

Coninck *et al.*(47) studied the spreading of alkanes on silanised silicon wafers in water. The authors used a range of alkanes to vary the droplet viscosity and showed that more viscous droplets resulted in slower spreading dynamics in both air and water. The reduced spreading dynamics resulted from a linear increase in friction (resistance to motion) at the TPCL with increasing fluid viscosity. (47) The later stages of spreading could be fitted to the MKT. Spreading data for alkanes of varying viscosity are shown in Figure 2.12.

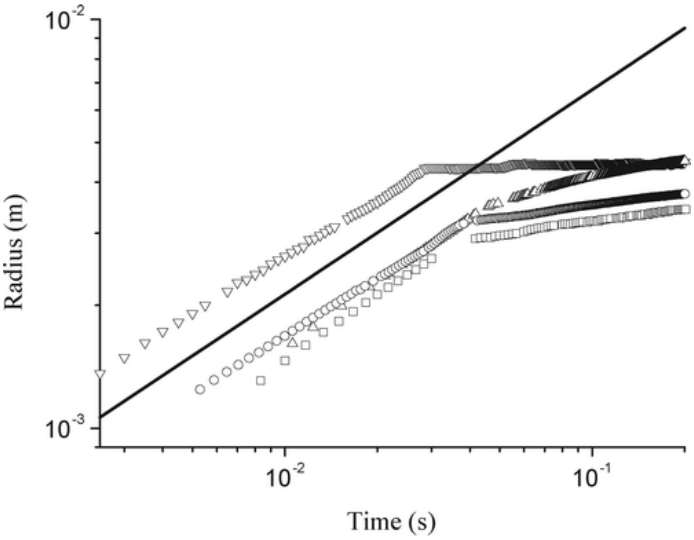

Figure 2.12. Spreading dynamics of droplets of hexane (▽), dodecane (□), hexadecane (○), and squalane (△) in water. The line represents a slope of $t^{0.5}$*, thus there is good agreement to the inertial spreading regime of* $t^{0.5}$ *for the low viscosity droplets spreading in water.*$^{(47)}$

Finally, Mitra *et al.*$^{(70)}$ considered the spreading of a laser oil (200 mPa·s) and dibutyl phthalate (DBP) (16 mPa·s) on a glass substrate in water. The authors discussed a second viscous regime that is observed at very early spreading times, before the inertial regime. The authors had also observed this behaviour for droplets spreading in air, as well as being reported for coalescing droplets.$^{(99)}$ The droplet spreading in both air and water and the associated spreading regimes are shown in Figure 2.13a and b.

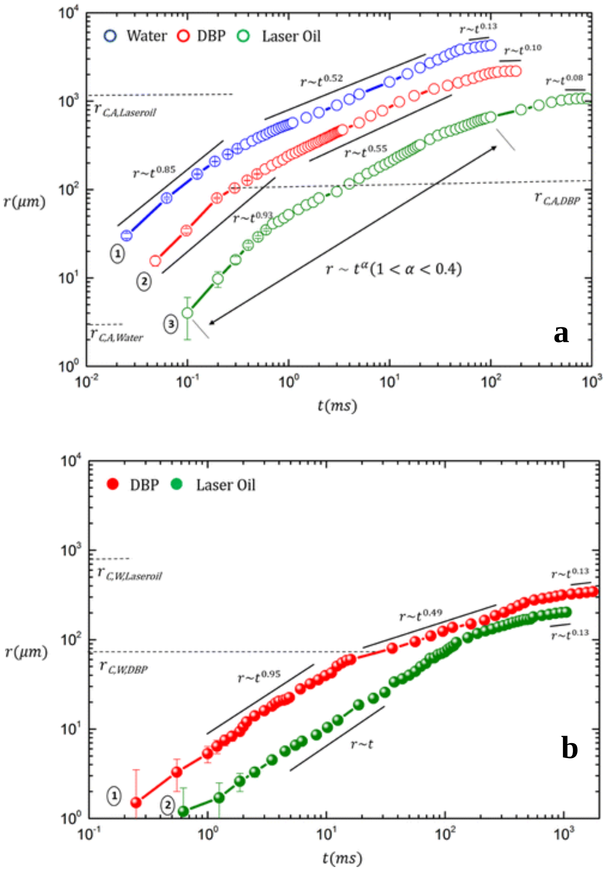

Figure 2.13. a) The spreading radius of water, DBP and laser oil in air, with water and DBP showing 3 regimes of spreading, while laser oil shows only 2 regimes. b) DBP and laser oil spreading in water, with DBP showing 3 regimes and laser oil showing 2.(70)

As stated by Mitra *et al.*(70) the droplet spreading in air is hard to confirm as this initial regime is only seen in the first few points, where the spreading speeds are at their fastest and where there is more error. The underwater spreading data in Figure 2.13b covers the same time range as Figure 2.12 where there is most definitely two regimes, this third regime is expected to only exist for intermediate viscosities 10 – 50 mPa·s (viscosity ratios from 550 – 3000). The data shows the initial viscous regime spreads at a rate close to unity ($r \sim t$) before spreading at $r \sim t^{0.5}$ in the inertial regime and approximately $r \sim t^{0.1}$ in Tanner's viscous regime.

2.6 Surface roughness

As previously discussed, the equilibrium wetting condition and the spreading dynamic of droplets can be altered by changing the surface wettability. Surface wettability can be modified by controlling the roughness of the surface. It has been shown that surface roughness affects droplet-surface interactions as rough surfaces require a lower critical Weber number to cause droplet splashing.(22, 100) Conventional wetting theories assume that the droplet is much larger than the characteristic scale of the surface roughness. As the droplet size to surface roughness ratio decreases, these assumptions become less valid, hence several studies have considered these limitations by investigating many local free energy minima on surfaces.(101-104)

For conventional wetting theories, the contribution from surface roughness is dependent on the substrate being either hydrophilic or hydrophobic. Firstly for a hydrophobic surface, increasing roughness decreases the amount of droplet spreading and the equilibrium contact increases. Such effect results from a rough surface having a larger contact area than a smooth surface of equivalent size. This leads to a greater net energy increase and thus the rough surface inhibits spreading, the drop becomes more spherical, (105) with the equilibrium droplet condition described by Wenzel wetting(106) as seen in Figure 2.14. A further increase in energy may lead to the Cassie-Baxter state(107); to further reduce the energy of the system air becomes trapped between the surface and droplet, reducing unfavourable surface-droplet interactions. The droplet is at rest on a mixed-surface composition, solid and air. The Cassie-Baxter state is more susceptible to rolling than the Wenzel state. Both wetting states are shown in Figure 2.14.

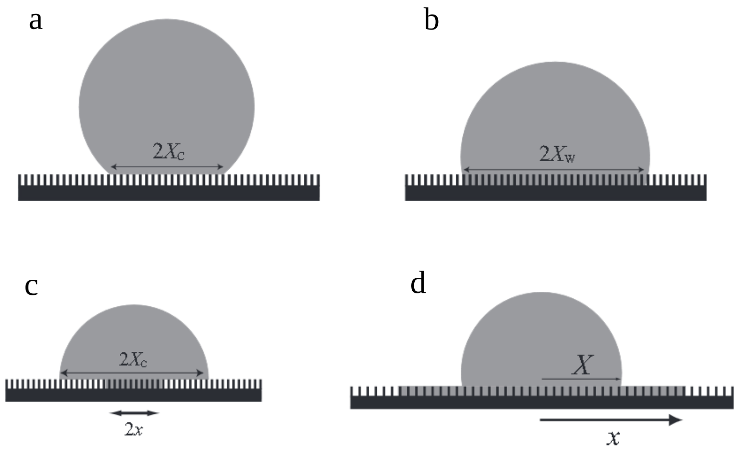

Figure 2.14. The droplet spreading states on rough surfaces a) Cassie-Baxter state, b) Wenzel state, c) Mushroom state and d) Penetration state (108)

There can be several different transition states between the Wenzel and Cassie-Baxter states. (108) The droplet can homogeneously spread more on the surface in the vertical direction, *i.e.* the droplet appears to sink towards the surface, with less air trapped between the droplet and surface.(109) Or the droplet can spread inhomogeneously, where a portion of the droplet spreads in a Wenzel manner from the droplet centre(110) – this is aptly named the mushroom state and is depicted in Figure 2.14c. Both transitions have been directly observed.(111)

For a hydrophilic surface, the water-solid interactions are favourable and so when the surface is roughened, the solid becomes more wetted by the spreading water droplet. As the contact angle is not necessarily measurable because of surface roughness, the contact angle is often referred to as the Wenzel contact angle.(112) Another interesting wetting state for hydrophilic surfaces is the liquid can spread ahead of the droplet in the grooves of the rough surface(113); this is known as hemi-wicking(112) or the penetration state, shown in Figure 2.14d.

The different states are also applicable to oil droplets in water, where the spreading of the droplet is due to the competition between the water-surface and the oil-surface energies. As rough surfaces are also susceptible to trapping air, there are also situations when multiphase heterogeneous Cassie-Baxter states are formed, where there is both water and air trapped between the droplet and surface, such as that shown in Figure 2.15.(114)

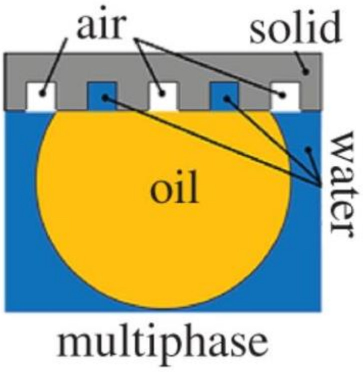

Figure 2.15. A multi-phase heterogeneous Cassie-Baxter state.(114)

There have been many studies (115-118) considering hydrophobic surfaces and how increasing surface roughness can make the surface more hydrophobic, 'Superhydrophobic'. However, this means that there are relatively few papers with spreading data, as the droplets simply do not spread. Nevertheless, the effects of surface roughness can be observed from the static equilibrium contact angles, as shown in Figure 2.16.(119)

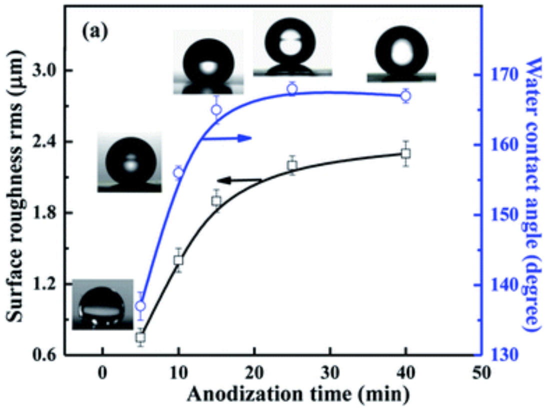

Figure 2.16. Water droplet contact angle as a function of surface roughness.(119)

Cazabat *et al.*$^{(65, 120)}$ used hydrophilic glass slides and polished the surfaces with various grades of abrasive powder (including sand blasting) to generate hydrophilic surfaces of varying surface roughness. The authors considered the spreading of a silicone droplet (0.02 Pas), shown in Figure 2.17.

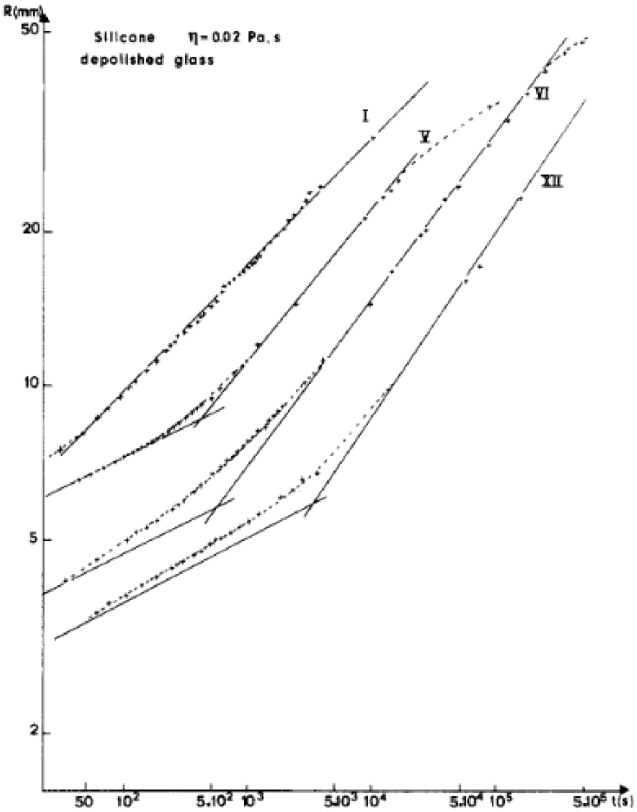

Figure 2.17. Spreading radius of a silicon droplet on different hydrophilic roughened surfaces, with roughness increasing from XII → I.$^{(120)}$

From XII to I the surfaces become rougher. As shown in Figure 2.17 the droplet spreads more on the rougher surfaces. The authors showed that a droplet spreading on a rough surface had four different spreading regimes. I (the smooth regime) where the droplet spreads at a rate of $r \sim t^{0.125}$, II (cap and foot regime) where the rate of spreading varies with $r \sim t^{0.25\text{-}0.5}$, III (flat drop regime) where $r \sim t^{0.25}$, and IV (film regime) where the droplet spreads at $r \sim t^{0.16}$. The spreading dynamics were not only affected by the average surface roughness but also the geometry of roughness. Bascom *et al.* (113) showed that horizontal scratches slowed down the spreading dynamics, whereas vertical scratches enhanced the spreading dynamics.

However, for droplets spreading on rough-hydrophilic surfaces the current understanding is still somewhat conflicted. Khan *et al.*(121) for instance published data that showed an increasing roughness decreased spreading rates. As with hydrophobic surfaces, roughness on different length scales can generate varying effects and whilst Khan *et al.* considered roughness effects at the nanometer scale, Cazabat *et al.*(51) had effects on the micrometer scale. Khan *et al.* also showed that these effects of roughness could be enhanced with increasing droplet viscosity.(121) Furthermore, Kandlikar *et al.*(122) showed that with increasing surface roughness the wettability would increase until a critical roughness was reached, whereby further roughness would decrease the wettability. More systematic studies on the scale of roughness, particularly on hydrophilic surfaces, are still required.

Research into droplets spreading in water is lacking, although from the few studies it tends to have outcomes similar to droplets spreading in air. For instance Sedev *et al.* (123) showed that hydrophilic surface wetting was enhanced by nano-roughness, and so with increasing roughness (in the form of silica nanoparticles) the contact angle of dodecane droplet decreased.

2.7 Surfactant effects on droplet spreading dynamics

From Tanner's law, it is known that a decrease in surface tension (γ_{lg}) will increase the droplet spreading dynamics on a surface.(121) Surfactants are amphiphilic molecules containing both a hydrophobic and hydrophilic part, which leads to structuring of the molecules at the liquid-gas interface, thus lowering the surface tension. Surfactants can also migrate along an interface resulting in concentration gradients that contribute to modifying the spreading dynamics of a droplet.

Firstly, there are two different surfactant types aptly named ’superspreaders’ (124) and ‘normal’(125) surfactants. The most common superspreaders are trisiloxane surfactants which can enhance the spreading dynamics from the expected $t^{0.1}$ (i.e. Tanner’s law) to much larger values ranging from 0.16 – 1.(125) The much increased spreading rates have been explained due to Marangoni flow aiding droplet spreading. (126) Normal surfactants are more commonly studied surfactants which can lead to an increase in the spreading dynamics up to $t^{0.16}$, however, this is unstable spreading dynamics (hydrophilic surfaces) and leads to droplet fingering. Normal surfactants tend to slow droplet spreading dynamics and exhibit viscous regimes exponents of $t^{0.1}$ or less. . These surfactants tend to be hydrocarbon based such as AOT, SDS, CTAB, *etc.*

Superspreaders are for example siloxanes surfactants which can lead to higher spreading dynamics of $t^{1.0}$. While superspreaders have been considered, their contribution will not be covered by this review. ’Normal’ surfactants have been considered for liquid-liquid systems and are interesting because the influence of the surfactant can be considered from both liquid phases; surfactant in either the displacing fluid (droplet) or the displaced fluid (continuous liquid phase).

2.7.1 Surfactants

The work discussed here has been focused on air-liquid studies, a severe lack of studies into the effects of surfactant on droplet spreading dynamics in liquid-liquid systems is evident. Surfactants not only change the droplet spreading dynamics but also the amount a droplet spreads on a surface. As the surfactant concentration increases the interfacial tension reduces until a critical surfactant concentration is reached where the bulk surfactant begins to form micelles and the interface is saturated with surfactant, this is known as the CMC or the critical micelle concentration. At concentrations greater than the CMC the interfacial tension plateaus.

Surfactants prefer to partition at an interface, hence during spreading surfactant moves to the new interface created at the three-phase contact line of a spreading droplet.(14) For hydrophobic surfaces, an aqueous droplet will not spread on the surface due to unfavourable surface energies. If the surfactant transfers to the solid-vapour interface ahead of the droplet it can also orient itself at this interface. The hydrophobic tail interacts with the hydrophobic surface, thus the hydrophilic head group is exposed to the spreading droplet,(14) making the surface more hydrophilic and allowing the droplet to spread further. The transfer of surfactant to the surface is relatively slow and limits the rate of droplet spreading, although the surfactant transfer leads to a local free energy increase the total free energy of the system decreases.(14)

Bonn *et al.* (125) used AOT aqueous solutions to spread over hydrophobic PET surfaces and showed that at concentrations below the CMC there was no spreading. At concentrations near to the CMC it was hard to distinguish if the droplet was spreading with small spreading exponents or not spreading at all. At higher concentrations well above the CMC the spreading dynamic was in agreement with Tanner’s exponent of 0.1. As the creation of new liquid-air interface is faster than the transport of surfactant molecules to the interface this slows the droplet dynamics.

Starov *et al.* (14) showed that as the surfactant concentration was increased up to the CMC, the droplet spreading rate increased along with the spreading diameter. As the surfactant concentration was increased from just below the CMC to just above the CMC the spreading dynamic increased further, until maximum spreading at Tanner's law with n = 0.1 was observed at 1 wt% (5 x CMC). The spreading dynamics for various concentrations above the CMC of SDS is shown in Figure 2.18.(14)

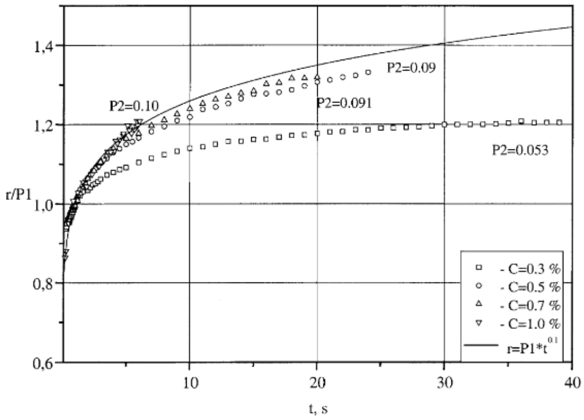

Figure 2.18. Spreading of droplets containing SDS concentrations above the CMC (0.2 wt%) on a polyethylene surface. Solid line is Tanner's law where n = 0.1. (14)

As shown in Figure 2.18, as the surfactant concentration increases so does the dynamics of droplet spreading, until 1.0 wt% SDS when the spreading reaches a maximum spreading exponent of 0.1. These findings were supported by Dutschk *et al.* (127), however the authors added that ionic surfactant solutions would only be able to spread on moderately hydrophobic surfaces, whereas non-ionic surfactant solutions would spread on moderately and highly hydrophobic surfaces.

The slower spreading dynamics at low surfactant concentrations has been observed several times. (128, 129) Starov *et al.*(14) found the exponent could be described by $\tau_s = 1/\alpha$ which is the time scale of surfactant transfer from the droplet to the solid-air interface ahead of the droplet. As the surfactants transfer to the surface-vapour interface it depletes the droplet-vapour interface, which leads to a local surface tension increase (they believed that the surfactant transfer comes predominantly from the liquid-vapour interface as opposed to the droplet bulk, or the droplet-surface interface). This process is relatively slow compared to the adsorption of surfactants to an interface from the bulk solution, due to a large energy barrier.

Although transport of surfactant molecules to the solid-air interface is generally accepted as one of the reasons for slower dynamics, there are other mechanisms that have been suggested which may work in conjunction. For instance, other diffusion controlled mechanisms; as the droplet spreads an increase in liquid-vapour surface area occurs; leading to an increase in the effective surface tension.(130) Slow diffusion of the surfactant from the bulk to the interface will also slow the spreading dynamics.(125, 128, 130)

2.7.2 Hydrophilic surfaces

To this point, how surfactants affect the spreading dynamics on hydrophobic surfaces has been described. First, surfactants adsorb to the interface and make the surface more hydrophilic. Surfactants are also able to adsorb onto hydrophilic surfaces. As the surface is hydrophilic the surfactant's polar head lays down on the surface with the hydrophobic tail oriented away from the surface. The surfactant orientation renders the surface more hydrophobic and is called 'autophobing' where a surfactant solution won't spread over its own monolayer.(131) This will build up a hydrophobic barrier, as the diffusion of the surfactant to the solid-air interface is controlled by the relative humidity (RH).(132) The surfactant on the surface ahead of the droplet has been directly observed.(133) Autophobing means that on hydrophilic surfaces the droplet spreads less, in some cases the droplet spreads to a maximum then slowly retracts in size as the surface is autophobed.(15)

For ‘Normal’ surfactants Cazabat *et al.*(132, 134)found that at low RH (where there is reduced surfactant adsorption at the liquid-air interface) and low surfactant concentration, no concentration gradient exists with the removal of surfactant from the drop to the surface. As no surface tension gradient exists this means that droplet spreading is observed at normal rates.(132) At high surfactant concentrations, no Marangoni flow can develop, any surfactant transportation to the liquid-solid interface actually builds up the hydrophobic barrier; slower spreading velocities occur, and the droplet will spread less.(15) However, the droplet still spreads symmetrically and uniformly.(132, 135)

At high RH and low surfactant concentration, surfactant readily adsorb at the liquid-air interface and a surface tension gradient develops. This increase gives rise to Marangoni flow and spreading velocities become much faster. Unlike superspreading surfactants on hydrophobic surfaces, the droplet spreads in a very ‘unstable’ way and forms fingering and dendrite patterns. Fingering has been seen in many studies (15, 132, 134, 135) as shown in Figure 2.19.

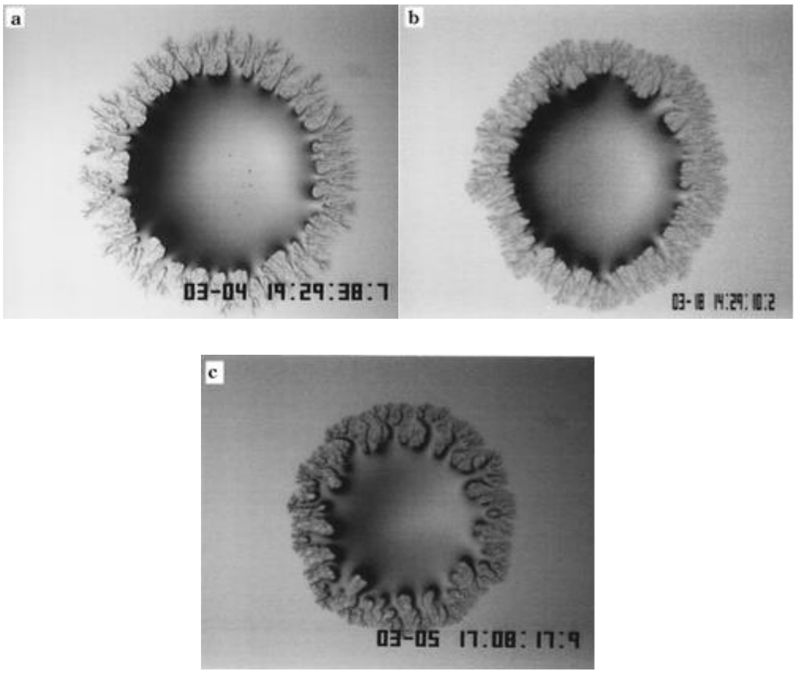

Figure 2.19. The fingering or the dendritic pattern that forms during droplet spreading with high RH and low surfactant concentrations.(132)

Frank and Garoff(136) showed that at low surfactant concentrations (< 0.45 CMC) for CTAB, the spreading dynamic shifted from the expected 0.5 exponent to 0.59, whereas at higher concentrations (> 0.45 CMC) the droplet spreading exponent was slightly lower at 0.49. Thereafter in most cases, a hydrophobic barrier occurs which means the droplet spreads following Tanner's law with exponent 0.1 or lower. One exceptional case is at low surfactant concentration and high RH, Marangoni flow is able to overcome the hydrophobic barrier and the droplet spreads quickly but unstably with fingering taking place;(134) a graphical summation is shown in Figure 2.20.

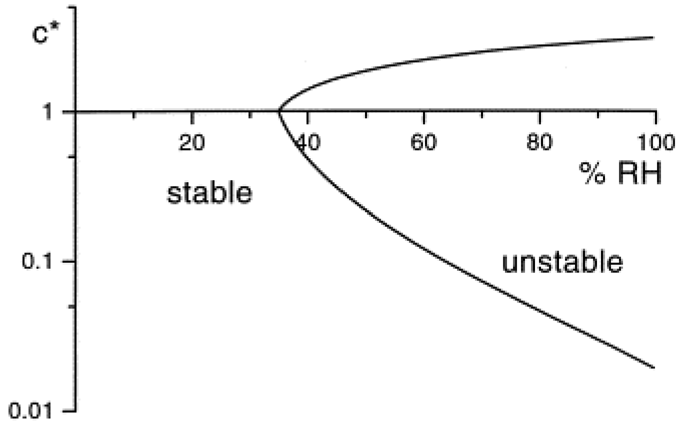

Figure 2.20. A graphical representative of the spreading of 'normal' surfactants on hydrophilic surface at different concentrations and RH. (134)

Stoebe *et al.*(13) studied surfactant effects on hydrophilic surfaces. The authors found SDS and CTAB solutions had very slow spreading velocities of < 2 mm/s, trisiloxane surfactants had faster spreading velocities from 4 - 7 mm/s, and non-ionic polyoxyethylene surfactants formed dendrite formations but spread at velocities between 5 - 15 mm/s.(13) Non-ionic polyoxyethylene surfactants were shown to have a spreading exponent of $n = 1$, this is generally the dendrite spreading regime, the bulk droplet spreading is still enhanced but with exponents of around $n = 0.25$.(137)

Frank and Garoff(138) also highlighted other parameters; for surfaces of silicon oxide (negatively charged), CTAB (cationic) solution showed autophobic behaviour and slow velocities, whereas SDS (anionic) resulted in superspreading with dendrites forming.(138) This was due to the negative nature of the surface, if the surface was replaced by a (positive) sapphire surface the reverse occurs; where CTAB exhibits fast dendritic spreading and SDS shows autophobic spreading; surface wettability can also be complicated by surface charge.(137, 138)

Spreading of surfactant solutions on surfaces is highly complex, with many parameters affecting the dynamics and spreading outcomes. In an attempt to simplify it, the main outcomes for spreading for ‘normal’ surfactants on surfaces of either hydrophilic or hydrophobic wettability have been summarised in Table 2.2.

Table 2.2. The spreading dynamics of normal surfactants on hydrophilic and hydrophobic surfaces, where n is the spreading exponent

Surface	
Hydrophilic	**Hydrophobic**
Mostly spreading is $n > 0.1$ due to autophobing Exception: High RH, low concentration – Superspreading by Marangoni (fingering occurs)	Increases spreading amount but rates are $n = 0.1$ or less

2.8 Summary

For low viscosity liquid droplets, there are two very abrupt regimes that can be easily distinguished, and the spreading dynamics described by two power law exponents.(66) For more viscous droplets the regimes cannot be visually distinguished and a slowing of dynamics over time is witnessed.(68, 70) There has been a general departure of research using models to fit and predict droplet spreading data, to using basic power laws to fit droplet spreading.(15) Yet there has been relatively very little research into the different models which may be able to provide a single exponent value for viscous droplet spreading.(73)

Research has shown the droplet-substrate interactions in liquid-liquid systems have an interesting side-effect in the formation of TLFs.(82) TLFs can lead to droplet deformations and long induction times due to slow TLF drainage and rupture. (80) However, there has been little research into spreading dynamics in liquid-liquid systems. The outcomes from air-liquid systems are predicted to be similarly displayed in liquid-liquid systems but with a decrease in spreading dynamics associated with the decrease in viscosity ratio.(96)

There have been interesting developments in droplet spreading dynamics, which can be both promoted and inhibited by surface modifiers.(125) Surfactants have been shown to affect both the extent of wetting and the spreading dynamics of droplets on hydrophobic and hydrophilic surfaces,(131) with dynamic surface tension gradients affecting spreading dynamics.(132) Bulk rheological properties have also been shown to increase spreading dynamics (shear thickening liquids) and decrease spreading dynamics (shear thinning liquids) with the change in dynamics associated with the droplet shape.(139)

2.9 References B

1. MARMUR, A. Equilibrium and spreading of liquids on solid surfaces. *Advances in Colloid and Interface Science*, 1983, **19**(1–2), pp.75-102.
2. SEAVER, A.E. and J.C. BERG. Spreading of a droplet on a solid surface. *Journal of applied polymer science*, 1994, **52**(3), pp.431-435.
3. DE GENNES, P.-G. Wetting: statics and dynamics. *Reviews of modern physics*, 1985, **57**(3), p.827.
4. RIOBOO, R., M. MARENGO and C. TROPEA. Time evolution of liquid drop impact onto solid, dry surfaces. *Experiments in Fluids*, 2002, **33**(1), pp.112-124.
5. RIOBOO, R., C. TROPEA and M. MARENGO. Outcomes from a drop impact on solid surfaces. *Atomization and Sprays*, 2001, **11**(2).
6. YARIN, A. Drop impact dynamics: splashing, spreading, receding, bouncing…. *Annu. Rev. Fluid Mech.*, 2006, **38**, pp.159-192.
7. REIN, M. and J.-P. DELPLANQUE. The role of air entrainment on the outcome of drop impact on a solid surface. *Acta mechanica*, 2008, **201**(1-4), pp.105-118.

8. MUNDO, C., M. SOMMERFELD and C. TROPEA. Droplet-wall collisions: Experimental studies of the deformation and breakup process. *International Journal of Multiphase Flow*, 1995, **21**(2), pp.151-173.
9. LIANG, G., Y. GUO, Y. YANG, N. ZHEN and S. SHEN. Spreading and splashing during a single drop impact on an inclined wetted surface. *Acta mechanica*, 2013, **224**(12), pp.2993-3004.
10. LAVI, B. and A. MARMUR. The exponential power law: partial wetting kinetics and dynamic contact angles. *Colloids and Surfaces A: Physicochemical and Engineering Aspects*, 2004, **250**(1), pp.409-414.
11. AZIZ, S.D. and S. CHANDRA. Impact, recoil and splashing of molten metal droplets. *International Journal of Heat and Mass Transfer*, 2000, **43**(16), pp.2841-2857.
12. SAMPATH, S. and X. JIANG. Splat formation and microstructure development during plasma spraying: deposition temperature effects. *Materials Science and Engineering: A*, 2001, **304–306**, pp.144-150.
13. STOEBE, T., Z. LIN, R.M. HILL, M.D. WARD and H.T. DAVIS. Surfactant-enhanced spreading. *Langmuir*, 1996, **12**(2), pp.337-344.
14. STAROV, V.M., S.R. KOSVINTSEV and M.G. VELARDE. Spreading of surfactant solutions over hydrophobic substrates. *Journal of colloid and interface science*, 2000, **227**(1), pp.185-190.
15. MARMUR, A. and M.D. LELAH. The spreading of aqueous surfactant solutions on glass. *Chemical Engineering Communications*, 1981, **13**(1-3), pp.133-143.
16. DECAMPS, C. and J. DE CONINCK. Dynamics of spontaneous spreading under electrowetting conditions. *Langmuir*, 2000, **16**(26), pp.10150-10153.
17. QUILLIET, C. and B. BERGE. Electrowetting: a recent outbreak. *Current Opinion in Colloid & Interface Science*, 2001, **6**(1), pp.34-39.
18. LI, R., N. ASHGRIZ and S. CHANDRA. Maximum Spread of Droplet on Solid Surface: Low Reynolds and Weber Numbers. *Journal of Fluids Engineering*, 2010, **132**(6), pp.061302-061302.
19. BASIT, A., K. KUSHAARI, T.H. TRINH and B. AZEEM. Spreading of Low Impact Velocity Droplet on Porous Surface. *International Journal of Chemical Engineering and Applications*, 2014, **5**(2), pp.95 - 99.
20. JONES, W.P. and B.E. LAUNDER. The prediction of laminarization with a two-equation model of turbulence. *International Journal of Heat and Mass Transfer*, 1972, **15**(2), pp.301-314.
21. SON, Y., C. KIM, D.H. YANG and D.J. AHN. Spreading of an Inkjet Droplet on a Solid Surface with a Controlled Contact Angle at Low Weber and Reynolds Numbers. *Langmuir*, 2008, **24**(6), pp.2900-2907.
22. ŠIKALO, Š., M. MARENGO, C. TROPEA and E.N. GANIĆ. Analysis of impact of droplets on horizontal surfaces. *Experimental Thermal and Fluid Science*, 2002, **25**(7), pp.503-510.
23. WAL, R.L.V., G.M. BERGER and S.D. MOZES. The splash/non-splash boundary upon a dry surface and thin fluid film. *Experiments in Fluids*, 2005, **40**(1), pp.53-59.
24. LAGUBEAU, G., M.A. FONTELOS, C. JOSSERAND, A. MAUREL, V. PAGNEUX and P. PETITJEANS. Spreading dynamics of drop impacts. *Journal of Fluid Mechanics*, 2012, **713**, pp.50-60.
25. COMEAU, D., K. LATOURETTE and J. PATE. The effect of Weber number and spread factor of a water droplet impinging on a super-hydrophobic substrate. *Applied mathematics*, 2007.
26. RANGE, K. and F. FEUILLEBOIS. Influence of Surface Roughness on Liquid Drop Impact. *Journal of colloid and interface science*, 1998, **203**(1), pp.16-30.
27. PALACIOS, J., P. GÓMEZ, C. ZANZI, J. LÓPEZ and J. HERNÁNDEZ. Experimental study on the splash/deposition limit in drop impact onto solid surfaces. *Proceedings of 23rd ILASS-2010, Brno, Czech Republic*, 2010.

28. ESCURE, C., M. VARDELLE and P. FAUCHAIS. Experimental and Theoretical Study of the Impact of Alumina Droplets on Cold and Hot Substrates. *Plasma Chemistry and Plasma Processing*, **23**(2), pp.185-221.
29. ZHANG, M.Y., H. ZHANG and L.L. ZHENG. Simulation of droplet spreading, splashing and solidification using smoothed particle hydrodynamics method. *International Journal of Heat and Mass Transfer*, 2008, **51**(13–14), pp.3410-3419.
30. ARMSTER, S., J.-P. DELPLANQUE, M. REIN and E. LAVERNIA. Thermo–fluid mechanisms controlling droplet based materials processes. *International materials reviews*, 2002, **47**(6), pp.265-301.
31. LEMBACH, A.N., H.-B. TAN, I.V. ROISMAN, T. GAMBARYAN-ROISMAN, Y. ZHANG, C. TROPEA and A.L. YARIN. Drop impact, spreading, splashing, and penetration into electrospun nanofiber mats. *Langmuir*, 2010, **26**(12), pp.9516-9523.
32. ISRAELACHVILI, J.N. *Intermolecular and surface forces: revised third edition.* Academic press, 2011.
33. PETRUCCI, R.H., W.S. HARWOOD and F. HERRING. General Chemistry, Principles and Modern Applications. *Journal of Chemical Education*, 1997, **74**(5), pp.491-491.
34. KOTIKALAPUDI, S. *Spreading of Initially Spherical Viscous Droplets.* 2000.
35. GHAZIAN, O., K. ADAMIAK and G.S.P. CASTLE. Spreading and retraction control of charged dielectric droplets. *Colloids and Surfaces A: Physicochemical and Engineering Aspects*, 2014, **448**(Supplement C), pp.23-33.
36. CHEN, Y., L. LIU, H.-J. CHUNG and J.A. NYCHKA. Selective oil/water filter paper via a scalable one-pot hydrothermal growth of ZnO nanowires. *RSC Advances*, 2015, **5**(110), pp.91001-91005.
37. CAZABAT, A.-M. How does a droplet spread? *Contemporary Physics*, 1987, **28**(4), pp.347-364.
38. BONN, D., J. EGGERS, J. INDEKEU, J. MEUNIER and E. ROLLEY. Wetting and spreading. *Reviews of modern physics*, 2009, **81**(2), p.739.
39. CHERRY, B.W. *Polymer surfaces.* CUP Archive, 1981.
40. RANABOTHU, S.R., C. KARNEZIS and L.L. DAI. Dynamic wetting: Hydrodynamic or molecular-kinetic? *Journal of colloid and interface science*, 2005, **288**(1), pp.213-221.
41. DAVIS, M.J. and S.H. DAVIS. Droplet spreading: Theory and experiments. *Comptes Rendus Physique*, 2013, **14**(7), pp.629-635.
42. ERAL, H. and J. OH. Contact angle hysteresis: a review of fundamentals and applications. *Colloid and polymer science*, 2013, **291**(2), pp.247-260.
43. CARLSON, A. Capillarity and dynamic wetting. 2012.
44. BLAKE, T.D. and J.M. HAYNES. Kinetics of liquidliquid displacement. *Journal of colloid and interface science*, 1969, **30**(3), pp.421-423.
45. SCHNEEMILCH, M., R.A. HAYES, J.G. PETROV and J. RALSTON. Dynamic Wetting and Dewetting of a Low-Energy Surface by Pure Liquids. *Langmuir*, 1998, **14**(24), pp.7047-7051.
46. YUAN, Q. and Y.-P. ZHAO. Multiscale dynamic wetting of a droplet on a lyophilic pillar-arrayed surface. *Journal of Fluid Mechanics*, 2013, **716**, pp.171-188.
47. GOOSSENS, S., D. SEVENO, R. RIOBOO, A. VAILLANT, J. CONTI and J. DE CONINCK. Can We Predict the Spreading of a Two-Liquid System from the Spreading of the Corresponding Liquid–Air Systems? *Langmuir*, 2011, **27**(16), pp.9866-9872.
48. HEINE, D.R., G.S. GREST and E.B. WEBB III. Spreading dynamics of polymer nanodroplets. *Physical Review E*, 2003, **68**(6), p.061603.
49. TANNER, L. The spreading of silicone oil drops on horizontal surfaces. *Journal of Physics D: Applied Physics*, 1979, **12**(9), p.1473.
50. CHEN, J. and N. WADA. *Edge profiles and dynamic contact angles of a spreading drop.* 1992.
51. CAZABAT, A. and M.C. STUART. Dynamics of wetting: effects of surface roughness. *J. Phys. Chem*, 1986, **90**(22), pp.5845-5849.

52. ZHANG, Y., C.A. FUENTES, R. KOEKOEKX, C. CLASEN, A.W. VAN VUURE, J. DE CONINCK and D. SEVENO. Spreading Dynamics of Molten Polymer Drops on Glass Substrates. *Langmuir*, 2017, **33**(34), pp.8447-8454.
53. BLAKE, T.D. The physics of moving wetting lines. *Journal of colloid and interface science*, 2006, **299**(1), pp.1-13.
54. BLAKE, T.D. and Y.D. SHIKHMURZAEV. Dynamic Wetting by Liquids of Different Viscosity. *Journal of colloid and interface science*, 2002, **253**(1), pp.196-202.
55. HOFFMAN, R.L. A study of the advancing interface. I. Interface shape in liquid—gas systems. *Journal of colloid and interface science*, 1975, **50**(2), pp.228-241.
56. REDON, C., F. BROCHARD-WYART and F. RONDELEZ. Dynamics of dewetting. *Physical review letters*, 1991, **66**(6), p.715.
57. DE RUIJTER, M.J., J. DE CONINCK and G. OSHANIN. Droplet Spreading: Partial Wetting Regime Revisited. *Langmuir*, 1999, **15**(6), pp.2209-2216.
58. DE RUIJTER, M.J., M. CHARLOT, M. VOUÉ and J. DE CONINCK. Experimental evidence of several time scales in drop spreading. *Langmuir*, 2000, **16**(5), pp.2363-2368.
59. LU, G., X.-D. WANG and Y.-Y. DUAN. A Critical Review of Dynamic Wetting by Complex Fluids: From Newtonian Fluids to Non-Newtonian Fluids and Nanofluids. *Advances in Colloid and Interface Science*, 2016, **236**(Supplement C), pp.43-62.
60. PETROV, P. and I. PETROV. A combined molecular-hydrodynamic approach to wetting kinetics. *Langmuir*, 1992, **8**(7), pp.1762-1767.
61. BROCHARD-WYART, F. and P.G. DE GENNES. Dynamics of partial wetting. *Advances in Colloid and Interface Science*, 1992, **39**(Supplement C), pp.1-11.
62. EHRHARD, P. Experiments on isothermal and non-isothermal spreading. *Journal of Fluid Mechanics*, 2006, **257**, pp.463-483.
63. LOPEZ, J., C.A. MILLER and E. RUCKENSTEIN. Spreading kinetics of liquid drops on solids. *Journal of colloid and interface science*, 1976, **56**(3), pp.460-468.
64. EHRHARD, P. and S.H. DAVIS. Non-isothermal spreading of liquid drops on horizontal plates. *Journal of Fluid Mechanics*, 2006, **229**, pp.365-388.
65. CAZABAT, A. and M.C. STUART. Dynamics of wetting: effects of surface roughness. *The Journal of Physical Chemistry*, 1986, **90**(22), pp.5845-5849.
66. CHEN, L. and E. BONACCURSO. Effects of surface wettability and liquid viscosity on the dynamic wetting of individual drops. *Physical Review E*, 2014, **90**(2), p.022401.
67. TANNER, L.H. The spreading of silicone oil drops on horizontal surfaces. *Journal of Physics D: Applied Physics*, 1979, **12**(9), p.1473.
68. BIANCE, A.-L., C. CLANET and D. QUÉRÉ. First steps in the spreading of a liquid droplet. *Physical Review E*, 2004, **69**(1), p.016301.
69. WINKELS, K.G., J.H. WEIJS, A. EDDI and J.H. SNOEIJER. Initial spreading of low-viscosity drops on partially wetting surfaces. *Physical Review E*, 2012, **85**(5), p.055301.
70. MITRA, S. and S.K. MITRA. Understanding the Early Regime of Drop Spreading. *Langmuir*, 2016, **32**(35), pp.8843-8848.
71. EDDI, A., K.G. WINKELS and J.H. SNOEIJER. Short time dynamics of viscous drop spreading. *Physics of Fluids*, 2013, **25**(1), p.013102.
72. LAURILA, T., V. VUORINEN, T. MATTILA, M. TURUNEN, M. PAULASTO-KRÖCKEL and J. KIVILAHTI. *Interfacial Compatibility in Microelectronics: Moving Away From the Trial And Error Approach.* 2012.
73. ALTERAIFI, A.M., D. SHERIF and A. MOET. Interfacial effects in the spreading kinetics of liquid droplets on solid substrates. *Journal of colloid and interface science*, 2003, **264**(1), pp.221-227.
74. BIRD, J.C., S. MANDRE and H.A. STONE. Short-Time Dynamics of Partial Wetting. *Physical review letters*, 2008, **100**(23), p.234501.

75. DRELICH, J. and D. CHIBOWSKA. Spreading Kinetics of Water Drops on Self-Assembled Monolayers of Thiols: Significance of Inertial Effects. *Langmuir*, 2005, **21**(17), pp.7733-7738.

76. STAPELBROEK, B.B.J., H.P. JANSEN, E.S. KOOIJ, J.H. SNOEIJER and A. EDDI. Universal spreading of water drops on complex surfaces. *Soft Matter*, 2014, **10**(15), pp.2641-2648.

77. WANG, X., Y. ZHANG, D. LEE and X. PENG. Spreading of completely wetting or partially wetting power-law fluid on solid surface. *Langmuir*, 2007, **23**(18), pp.9258-9262.

78. MONTGOMERY, R.B. Viscosity and thermal conductivity of air and diffusivity of water vapor in air. *Journal of Meteorology*, 1947, **4**(6), pp.193-196.

79. VENNARD, J.K. and R. STREET. Elementary Fluid Mechanics, John Wiley & Sons. *Inc*, 1954.

80. JEFFREYS, G.V. and G.A. DAVIES. CHAPTER 14 - Coalescence of Liquid Droplets and Liquid Dispersion A2 - HANSON, C. *In: Recent Advances in Liquid–Liquid Extraction*. Pergamon, 1971, pp.495-584.

81. BALDESSARI, F. and L.G. LEAL. Effect of overall drop deformation on flow-induced coalescence at low capillary numbers. *Physics of Fluids*, 2006, **18**(1), p.013602.

82. KAMP, J., J. VILLWOCK and M. KRAUME. Drop coalescence in technical liquid/liquid applications: a review on experimental techniques and modeling approaches. *Reviews in Chemical Engineering*, 2017, **33**(1), pp.1-47.

83. SHELUDKO, A. Thin liquid films. *Advances in colloid and interface science*, 1967, **1**(4), pp.391-464.

84. STAROV, V.M. Disjoining Pressure. *In:* D. LI, ed. *Encyclopedia of Microfluidics and Nanofluidics*. Boston, MA: Springer US, 2008, pp.380-385.

85. CHAN, D.Y., E. KLASEBOER and R. MANICA. Film drainage and coalescence between deformable drops and bubbles. *Soft Matter*, 2011, **7**(6), pp.2235-2264.

86. ---. Dynamic deformations and forces in soft matter. *Soft Matter*, 2009, **5**(15), pp.2858-2861.

87. CLASOHM, L.Y., J.N. CONNOR, O.I. VINOGRADOVA and R.G. HORN. The “Wimple”: Rippled Deformation of a Fluid Drop Caused by Hydrodynamic and Surface Forces during Thin Film Drainage. *Langmuir*, 2005, **21**(18), pp.8243-8249.

88. MANEV, E., S.V. SAZDANOVA and D. WASAN. *Emulsion and foam stability—The effect of film size on film drainage.* 1984.

89. BASHEVA, E.S., T.D. GURKOV, I.B. IVANOV, G.B. BANTCHEV, B. CAMPBELL and R.P. BORWANKAR. Size Dependence of the Stability of Emulsion Drops Pressed against a Large Interface. *Langmuir*, 1999, **15**(20), pp.6764-6769.

90. YANG, D., M. KRASOWSKA, C. PRIEST and J. RALSTON. Dynamics of capillary-driven liquid–liquid displacement in open microchannels. *Physical Chemistry Chemical Physics*, 2014, **16**(44), pp.24473-24478.

91. SOARES, E.J., M.S. CARVALHO and P.R.S. MENDES. Immiscible Liquid-Liquid Displacement in Capillary Tubes. *Journal of Fluids Engineering*, 2005, **127**(1), pp.24-31.

92. FERMIGIER, M. and P. JENFFER. An experimental investigation of the dynamic contact angle in liquid-liquid systems. *Journal of colloid and interface science,* 1991, **146**(1), pp.226-241.

93. VAN REMOORTERE, P. and P. JOOS. Spontaneous Liquid/Liquid Displacement in a Capillary. *Journal of colloid and interface science*, 1993, **160**(2), pp.397-404.

94. CHAN, W.K. and C. YANG. Surface-tension-driven liquid–liquid displacement in a capillary. *Journal of Micromechanics and Microengineering*, 2005, **15**(9), p.1722.

95. FETZER, R., M. RAMIASA and J. RALSTON. Dynamics of liquid− liquid displacement. *Langmuir,* 2009, **25**(14), pp.8069-8074.

96. FOISTER, R.T. The kinetics of displacement wetting in liquid/liquid/solid systems. *Journal of colloid and interface science*, 1990, **136**(1), pp.266-282.

97. FOISTER, R.T. Three-phase boundary expansion in thin liquid films. *Journal of colloid and interface science*, 1987, **116**(1), pp.109-128.
98. RAMIASA, M., J. RALSTON, R. FETZER and R. SEDEV. Contact Line Friction in Liquid–Liquid Displacement on Hydrophobic Surfaces. *The Journal of Physical Chemistry C*, 2011, **115**(50), pp.24975-24986.
99. PAULSEN, J.D., J.C. BURTON and S.R. NAGEL. Viscous to Inertial Crossover in Liquid Drop Coalescence. *Physical review letters*, 2011, **106**(11), p.114501.
100. ŠIKALO, Š., C. TROPEA, M. MARENGO and E. GANIĆ. Spreading of droplets on horizontal surfaces. *In: New and Renewable Technologies for Sustainable Development*. Springer, 2002, pp.683-692.
101. MARMUR, A. and E. BITTOUN. When Wenzel and Cassie Are Right: Reconciling Local and Global Considerations. *Langmuir*, 2009, **25**(3), pp.1277-1281.
102. SHAHRAZ, A., A. BORHAN and K.A. FICHTHORN. A Theory for the Morphological Dependence of Wetting on a Physically Patterned Solid Surface. *Langmuir*, 2012, **28**(40), pp.14227-14237.
103. WOLANSKY, G. and A. MARMUR. Apparent contact angles on rough surfaces: the Wenzel equation revisited. *Colloids and Surfaces A: Physicochemical and Engineering Aspects*, 1999, **156**(1), pp.381-388.
104. KIM, D., N.M. PUGNO and S. RYU. Wetting theory for small droplets on textured solid surfaces. *Scientific reports*, 2016, **6**, p.37813.
105. WENZEL, R.N. RESISTANCE OF SOLID SURFACES TO WETTING BY WATER. *Industrial & Engineering Chemistry*, 1936, **28**(8), pp.988-994.
106. MARMUR, A. Wetting on hydrophobic rough surfaces: to be heterogeneous or not to be? *Langmuir*, 2003, **19**(20), pp.8343-8348.
107. BICO, J., U. THIELE and D. QUÉRÉ. Wetting of textured surfaces. *Colloids and Surfaces A: Physicochemical and Engineering Aspects*, 2002, **206**(1), pp.41-46.
108. ISHINO, C. and K. OKUMURA. Wetting transitions on textured hydrophilic surfaces. *The European Physical Journal E: Soft Matter and Biological Physics*, 2008, **25**(4), pp.415-424.
109. ISHINO, C., K. OKUMURA and D. QUÉRÉ. Wetting transitions on rough surfaces. *EPL (Europhysics Letters)*, 2004, **68**(3), p.419.
110. ISHINO, C. and K. OKUMURA. Nucleation scenarios for wetting transition on textured surfaces: The effect of contact angle hysteresis. *EPL (Europhysics Letters)*, 2006, **76**(3), p.464.
111. MOULINET, S. and D. BARTOLO. Life and death of a fakir droplet: Impalement transitions on superhydrophobic surfaces. *The European Physical Journal E*, 2007, **24**(3), pp.251-260.
112. BICO, J., C. TORDEUX and D. QUÉRÉ. Rough wetting. *EPL (Europhysics Letters)*, 2001, **55**(2), p.214.
113. BASCOM, W.D., R.L. COTTINGTON and C.R. SINGLETERRY. Dynamic Surface Phenomena in the Spontaneous Spreading of Oils on Solids. *In: Contact Angle, Wettability, and Adhesion*. AMERICAN CHEMICAL SOCIETY, 1964, pp.355-379.
114. NOSONOVSKY, M. and B. BHUSHAN. Why re-entrant surface topography is needed for robust oleophobicity. *Phil. Trans. R. Soc. A*, 2016, **374**(2073), p.20160185.
115. MIWA, M., A. NAKAJIMA, A. FUJISHIMA, K. HASHIMOTO and T. WATANABE. Effects of the surface roughness on sliding angles of water droplets on superhydrophobic surfaces. *Langmuir*, 2000, **16**(13), pp.5754-5760.
116. MA, M. and R.M. HILL. Superhydrophobic surfaces. *Current Opinion in Colloid & Interface Science*, 2006, **11**(4), pp.193-202.
117. ZHANG, X., F. SHI, J. NIU, Y. JIANG and Z. WANG. Superhydrophobic surfaces: from structural control to functional application. *Journal of Materials Chemistry*, 2008, **18**(6), pp.621-633.
118. ERBIL, H.Y., A.L. DEMIREL, Y. AVCı and O. MERT. Transformation of a simple plastic into a superhydrophobic surface. *Science*, 2003, **299**(5611), pp.1377-1380.

119. XIAO, F., S. YUAN, B. LIANG, G. LI, S.O. PEHKONEN and T. ZHANG. Superhydrophobic CuO nanoneedle-covered copper surfaces for anticorrosion. *Journal of Materials Chemistry A*, 2015, **3**(8), pp.4374-4388.
120. CAZABAT, A. and M.C. STUART. Dynamics of wetting on smooth and rough surfaces. *In: Surface Forces and Surfactant Systems*. Springer, 1987, pp.69-75.
121. KHAN, M.I. and M.M. NASEF. Spreading behaviour of silicone oil and glycerol drops on coated papers. *Leonardo Journal of Sciences*, 2009, **8**, pp.18-30.
122. KANDLIKAR, S.G. and M.E. STEINKE. Contact angles and interface behavior during rapid evaporation of liquid on a heated surface. *International Journal of Heat and Mass Transfer*, 2002, **45**(18), pp.3771-3780.
123. RAMIASA, M., J. RALSTON, R. FETZER and R. SEDEV. Nanoroughness Impact on Liquid–Liquid Displacement. *The Journal of Physical Chemistry C*, 2012, **116**(20), pp.10934-10943.
124. THEODORAKIS, P.E., E.A. MÜLLER, R.V. CRASTER and O.K. MATAR. Insights into surfactant-assisted superspreading. *Current Opinion in Colloid & Interface Science*, 2014, **19**(4), pp.283-289.
125. RAFAÏ, S., D. SARKER, V. BERGERON, J. MEUNIER and D. BONN. Superspreading: Aqueous Surfactant Drops Spreading on Hydrophobic Surfaces. *Langmuir*, 2002, **18**(26), pp.10486-10488.
126. KOVALCHUK, N.M., O.K. MATAR, R.V. CRASTER, R. MILLER and V.M. STAROV. The effect of adsorption kinetics on the rate of surfactant-enhanced spreading. *Soft Matter*, 2016, **12**(4), pp.1009-1013.
127. DUTSCHK, V. and B. BREITZKE. Spreading characteristics of aqueous surfactant solutions on polymer surfaces. *Tenside Surfactants Detergents*, 2005, **42**(2), pp.82-87.
128. DUTSCHK, V., K.G. SABBATOVSKIY, M. STOLZ, K. GRUNDKE and V.M. RUDOY. Unusual wetting dynamics of aqueous surfactant solutions on polymer surfaces. *Journal of colloid and interface science*, 2003, **267**(2), pp.456-462.
129. VON BAHR, M., F. TIBERG and V. YAMINSKY. Spreading dynamics of liquids and surfactant solutions on partially wettable hydrophobic substrates. *Colloids and Surfaces A: Physicochemical and Engineering Aspects*, 2001, **193**(1), pp.85-96.
130. VON BAHR, M., F. TIBERG and B.V. ZHMUD. Spreading Dynamics of Surfactant Solutions. *Langmuir*, 1999, **15**(20), pp.7069-7075.
131. HILL, R.M. Superspreading. *Current Opinion in Colloid & Interface Science*, 1998, **3**(3), pp.247-254.
132. CACHILE, M. and A.M. CAZABAT. Spontaneous Spreading of Surfactant Solutions on Hydrophilic Surfaces: CnEm in Ethylene and Diethylene Glycol. *Langmuir*, 1999, **15**(4), pp.1515-1521.
133. NOVOTNY, V.J. and A. MARMUR. Wetting autophobicity. *Journal of colloid and interface science*, 1991, **145**(2), pp.355-361.
134. CACHILE, M., A.M. CAZABAT, S. BARDON, M.P. VALIGNAT and F. VANDENBROUCK. Spontaneous spreading of surfactant solutions on hydrophilic surfaces. *Colloids and Surfaces A: Physicochemical and Engineering Aspects*, 1999, **159**(1), pp.47-56.
135. TROIAN, S., X. WU and S. SAFRAN. Fingering instability in thin wetting films. *Physical review letters*, 1989, **62**(13), p.1496.
136. FRANK, B. and S. GAROFF. Surfactant self-assembly near contact lines: control of advancing surfactant solutions. *Colloids and Surfaces A: Physicochemical and Engineering Aspects*, 1996, **116**(1), pp.31-42.
137. BARDON, S., M. CACHILE, A.-M. CAZABAT, X. FANTON, M.-P. VALIGNAT and S. VILLETTE. Structure and dynamics of liquid films on solid surfaces. *Faraday Discussions*, 1996, **104**, pp.307-316.
138. FRANK, B. and S. GAROFF. Origins of the complex motion of advancing surfactant solutions. *Langmuir*, 1995, **11**(1), pp.87-93.

139. MIN, Q., Y.-Y. DUAN, X.-D. WANG, Z.-P. LIANG, D.-J. LEE and A. SU. Spreading of completely wetting, non-Newtonian fluids with non-power-law rheology. *Journal of colloid and interface science,* 2010, **348**(1), pp.250-254.

Chapter 3 Droplet spreading dynamics: CH_3- and NH_2-terminated PDMS oil droplet spreading in air

3.1 Summary

The spreading of silicone oils has for many decades attracted a significant amount of academic interest due to their use in many industrial applications such as lubrication, antifoaming, coatings, adhesives and cosmetic preparations. In this particular study, poly(dimethyl siloxane) oils (PDMS) was used to investigate the droplet spreading dynamics in air. A range of PDMS oils with viscosities ranging from 9.9 to 12720 mPa·s were chosen to explore the effects of viscosity on droplet spreading. It was shown that increasing the fluid viscosity decreased the droplet spreading rate. The spreading dynamics exhibited universal behaviour when the spreading time was normalized by the fluid viscosity; which enabled further elucidations of the initial spreading dynamics by increasing the fluid viscosity. This method can be used to predict spreading dynamics over the entire viscosity range, contrary to the current models developed by Seaver and Berg, de Gennes, and Tanner, which are applicable only for limited viscosity ranges. In addition, the droplet impact velocity was experimentally varied from 0.28 to 1.06 m/s and it was shown that increasing the droplet impact velocity led to enhanced spreading rates. Three very similar master curves were generated with a small shift towards higher spreading radii associated with the effect of increased impact velocity. Finally, the PDMS terminating group was substituted from CH_3 to NH_2 to test the influence of end-group chemistry of these oils on the spreading characteristics. This latter study demonstrated that the NH_2-terminated oils had slightly slower spreading dynamics, which was thought to be due

to increased structuring of the molecules at the air-droplet interface and surface-droplet interface.

3.2 Introduction

The rate of droplet spreading is important in many industrial applications, such as printing, coating, agriculture adhesives, oil recovery and detergency.(1) As a result, there has been a constant interest in droplet spreading, leading to the development of a wide range of data analysis methods and several theoretical models describing the spreading dynamics of droplets on surfaces such as Seaver and Berg, Tanner and de Gennes.(2, 3)

A non-volatile droplet (maintains constant volume), where gravity effects are considered negligible and the droplet completely wets a smooth flat surface, is considered in this Chapter. For such systems, there are usually two commonly observed spreading regimes, often fitted to a simple power law $r = Ct^n$, where C is a constant.(4) The first regime is the inertial regime, where droplet spreading is at its fastest and the spreading radius r increases with time t according to the power law(4) $r = Ct^{0.5}$. The second regime follows a transitional stage where the droplet viscosity inhibits the droplet spreading and is called the viscous spreading regime. This second regime is much slower and the droplet spreads at a speed of $r = Ct^{0.1}$, a relationship otherwise known as Tanner's law.(4) As the droplet viscosity increases the transition between the two regimes occurs earlier but the transitional stage is less defined as the two regimes appear to merge.(5) For highly viscous liquids, both the inertial and viscous regimes merge into an inertial-viscous regime, there is a gradual decrease in the spreading exponent over time. Indeed, the viscous dissipation becomes dominant at earlier stages and slows down the droplet spreading.

Spreading data is commonly fitted using the power law model to compare spreading behaviours.$^{(4-11)}$ However, this becomes complicated for viscous oils, where distinct regimes are not easily identified. Hence, a new equation has been suggested for viscous liquids to describe the spreading exponent over time as shown in Eq. 3.1:$^{(11)}$

$$n = \frac{\Delta \ln r}{\Delta \ln t}. \qquad (3.1)$$

n has been shown to equal ~ 0.8 (at 10^{-5} s) and to gradually decrease over time to 0.1 (at 10^{-2} s) predicted by Tanner's law.$^{(11)}$ Eddi *et al.* presented values of the inertial exponent to be much higher than the expected value of 0.5, for a droplet of viscosity 50 mPa·s. The authors believe this was due to an enhanced 'spatio-temporal resolution due to their bottom-view experimental method' which allowed them to record measurements from times as early as 10^{-5} s.$^{(11)}$ However, Alteraifi *et al.*$^{(12)}$ have shown that silicon oil droplets of intermediate viscosity (10 – 1000 mPa·s) can be reasonably well modelled by Tanner's (Eq. 3.2),$^{(13)}$ Seaver and Berg (Eq. 3.3),$^{(2)}$ and de Gennes (Eq.3.4) models.$^{(3)}$ These models provide only one exponent value to describe droplet spreading instead of a range of exponent values with time.

Tanner $$r = R\left(\frac{\gamma}{\mu R}\right)^{\frac{1}{10}} t^{\frac{1}{10}} \qquad (3.2)$$

Seaver and Berg $$r = r_o\left(1 + \frac{40\gamma V_d^3}{\pi^3 \mu r_o^{10}}\, t\right)^{\frac{1}{10}} \qquad (3.3)$$

De Gennes $$r = \sqrt{\frac{t^n \Omega^p}{\pi}} \qquad (3.4)$$

where R is the spherical drop radius, μ the dynamic viscosity of the drop, t the spreading time, r_o the initial spreading radius, V_d the volume of the spherical disk (constant), Ω the drop volume, $n = 2/(3m+1)$ and $p = 2m/(3m+1)$ where the most probable value of m is 3.(3)

For silicone oil droplets, Ogarev *et al.*(14) and Tanner were the first to study droplet spreading dynamics,(13) developing a model (Eq. 3.2) to describe the spreading behaviour. However, these researchers studied relatively high viscosity oils: Ogarev *et al.*(14) studied oils in the viscosity range 5.6 – 1,590,000 Pa·s, and Tanner(13) in a viscosity range of 1.08 – 106 Pa·s. Sawicki(15) conducted similar research but for lower viscosity oils in the range of 0.02 – 12 Pa·s spreading over a period of 3600 s. Sawicki commented that there was a departure from Tanner's model for lower viscosity oils. Sawicki also showed that the terminating groups of the silicone oil could influence the spreading dynamics, the PDMS-OH terminated silicon oils spread slower than the -CH_3 terminated silicon oils. Sawicki hypothesised that this was the result of more ordering at the oil-air interface. (15) This initiated some debate(16) but due to the limited amount of research on the terminating group effects on spreading dynamics, no agreement was achieved and the exact mechanism(s) remains unknown.

Alteraifi *et al.*(12) compared the three spreading models described by Eqs. 3.2-3.4, and showed that these equations were also useful to predict the spreading dynamics of low viscosity silicone oils (0.01 – 1 Pa·s) (also see Figure 2.9). Alteraifi *et al.*(12) found a dependence of the fitting parameter value on the droplet viscosity. It is important to note that due to slow spreading dynamics of viscous oils many studies have been conducted over long periods of time (e.g. 1600 s).

Viscous oils do not tend to show a defined inertial regime as viscous forces are dominating, this means the spreading exponent often slowly decreases to the expected Tanner's spreading exponent, 0.1. Spreading models are a unique way to fit the data of viscous oils and provide a single exponent value that can be used to compare the spreading dynamics of different droplets. This study will focus on the very early spreading dynamics ($t < 10$ s) and considers the dynamics of viscous silicone oils (10 – 12720 mPa·s) spreading on silicon substrates in air. The study considers the effect of oil viscosity, droplet impact velocity and oil terminating groups (CH_3 and NH_2).

3.3 Materials and Methods

3.3.1 Materials

Silicon wafers were used as the wetting substrate and were purchased from Silicon Valley Microelectronics (USA). The properties of the silicon wafers were: Type P, dopant: boron, orientation <100>, resistivity 10 – 20 ohm-cm and thickness 525 ± 25 μm. Ultrapure Milli-Q water was used in all experiments with a minimum resistivity of 18.2 MΩ·cm. Ethanol (purity 99.96% A.C.S. grade, VWR) and Decon90 (Fisher scientific) were used as cleaning agents.

Measured properties of the polydimethylsiloxane (PDMS) oils used in the current study are given in Table 3.1. Similar viscosity oils of different terminating groups (NH_2 and CH_3) were selected for comparison. The amino (NH_2) terminated PDMS oils were purchased from Gelest (USA), except the most viscous one, which was supplied by P&G (UK). The methyl (CH_3) terminated PDMS oils were purchased from Alfa Aesar (USA), all were used as received without further purification.

Table 3.1. Measured viscosities and surface tension of CH_3- and NH_2-terminated PDMS oils at 25°C.

CH_3 terminated PDMS		**NH_2 terminated PDMS**	
Viscosity (mPa·s)	**Surface tension (mN/m)**	**Viscosity (mPa·s)**	**Surface tension (mN/m)**
9.9 ± 0.4	20.9 ± 0.4	17.8 ± 0.4	22.3 ± 0.1
52.2 ± 0.2	21.1 ± 0.3	59.0 ± 0.3	20.5 ± 0.1
202 ± 1	21.1 ± 0.3	112.6 ± 0.5	20.3 ± 0.1
1000 ± 1	20.9 ± 0.4	941 ± 0.1	20.5 ± 0.4
12120 ± 90	18.1 ± 0.6	12710 ± 50	20.6 ± 1.1

3.3.2 Methods

The PDMS oil viscosity was measured using a Bohlin Gemini Rheometer (Malvern, UK). A 40 mm diameter, 4^o angle cone and plate geometry was used to measure the viscosity at 25 °C. The shear stress was varied logarithmically with the equilibration time set to 10 s and the averaging time set to 15 s. All the PDMS oils exhibited a Newtonian behaviour across the studied stress range, over which the viscosity values were averaged. These mean values are shown in Table 3.1 along with their associated error.

The PDMS oil surface tension was measured using a pendant droplet analyser (KSV Modular, CAM200, Sweden). The maximum droplet size was generated at the blunt-tip of a 22 G stainless steel (SS) needle. The surface tension of the droplet was determined from droplet shape analysis, with the CAM 200 software executing an edge-detection routine. For surface tension measurements the image capture rate was set to 2 fps. Measurements of 3 droplets were conducted and an averaged surface tension was obtained. Values of these averaged surface tensions are shown in Table 3.1. Prior to each measurement the SS needle was cleaned using ethanol and dried with nitrogen.

Droplet spreading dynamics were also visualised using the pendant drop apparatus. Silicon wafers were cleaned with ethanol, Decon90 and excess Milli-Q water before being dried with air. The needle was cleaned following the previously described method and the distance between the wafer and needle tip was then set using a calliper (verified by image capture). The needle tip was positioned 6, 3, or 0.6 cm from the spreading substrate, with the droplet apex (lower edge) approximately 5.8, 2.8 and 0.4 mm from the spreading substrate. Droplets of maximum volume were produced at the blunt-tip of a 22 G SS needle, with the image capture software triggered prior to the droplet detaching from the needle.

Droplets detached from the needle under gravity with a typical droplet radius of approximately 1 mm. The free droplet then impacted the substrate and began to spread. Droplet deposition and its spreading was recorded at 60 fps. For longer timescale (1 hr) studies, the frame rate was reduced to 1 fps. Figure 3.1 shows a series of images taken during a typical droplet spreading experiment, the quoted droplet radius was the time-dependent droplet spreading radius; which is used to compare the droplet spreading dynamics. The droplet contact angle, droplet height and spreading radius were all recorded and measured using the tensiometer software CAM200, which was initially calibrated using a 4 mm SS ball. For the initial phase of viscous droplet spreading, a significant portion of the droplet was deformed following detachment from the needle (discussed in Section 3.3.1). Therefore a spherical droplet shape was not captured and consequently the CAM200 software was unable to fit the droplet shape. These images were analysed using ImageJ software to measure the droplet spreading diameter as a function of time. The first image where the droplet was observed to be in contact with the silicon wafer was taken to be $t = 0$. However, due to the time resolution (image capture rate) of the camera, this was not necessarily a true representation of initial contact, and the very early stages of droplet wetting and spreading may not have been fully captured.

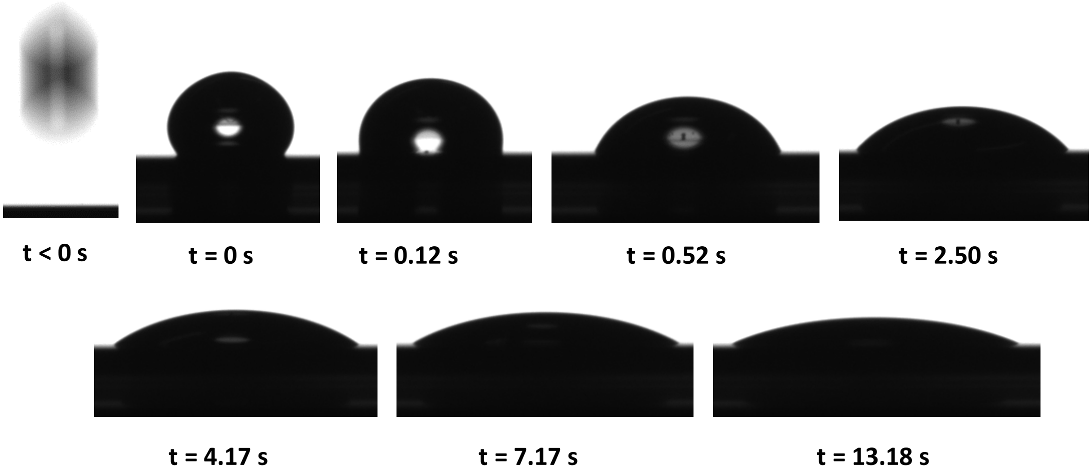

t < 0 s t = 0 s t = 0.12 s t = 0.52 s t = 2.50 s

t = 4.17 s t = 7.17 s t = 13.18 s

Figure 3.1. Digital images recorded with the pendant drop analyser showing a CH_3 *terminated oil droplet spreading. Oil viscosity is 1000 mPa·s and the droplet was released from a height of 3 cm above the spreading surface. Spreading time shown below each image.*

Higher frame rate studies were also conducted. The experimental conditions were kept constant and the data collected using the Theta T200 pendant droplet analyser (Biolin Scientific, Sweden), with frame rates of 200, 1250, 2315 fps. For bottom-view studies, all experimental parameters were kept constant, however the droplet spreading was recorded on a Zeiss Microscope. The droplet spreading radius was measured using ImageJ. Droplet spreading dynamics were an average of three droplets. To maintain clarity in the data presented no error bars were included. The first spreading radius measured always exhibited the largest error (due to inaccuracies in determining $t = 0$), and the measurement error then decreased with droplet spreading time. The lower the droplet viscosity the larger the measurement error (shown in Figure 3.8b). However, as the lower viscosity droplets spread faster, any slight error to determine $t = 0$ were not as significant. For any fluid viscosity tested, no measurement error (variability) exceeded 2%.

3.3.2.1 Droplet impact velocity

Due to blurring of the droplet (Figure 3.1) or a lack of sequential images with droplets in frame, the droplet impact velocity could not be measured accurately. As such, the droplet impact velocities were calculated for the different release heights. The density of the PDMS oil was 0.98 g cm^{-3}. To calculate the droplet impact velocity the droplet terminal velocity (v_t) was calculated using Eq.3.5:(17)

$$v_t = \sqrt{\frac{2mg}{D\rho A}} \qquad (3.5)$$

where m is the mass of the droplet, g the gravitational acceleration, ρ the continuous phase density, A the droplet cross-sectional area and D the drag coefficient, which for a sphere was taken to be 0.47.(18) With the droplet diameter taken to be 1 mm, the terminal velocity was calculated to be 9.2 m/s. The droplet impact velocity (v_i) can then be calculated by Eq. 3.6:

$$v_i = v_t\sqrt{1 - exp\left[\frac{-2gh}{v_t^2}\right]} \qquad (3.6)$$

where h is the droplet fall distance before impact. The calculated droplet impact velocities are summarized in Table 3.2.

Table 3.2. The calculated (approximate) droplet impact velocities based on Eq. 3.6 for droplets falling in air.

Droplet release height (cm)	**Impact velocity (m/s)**
6.0	1.06
3.0	0.74
0.6	0.28

3.3.2.2 Droplet evaporation during spreading

Although previous studies suggest that droplet evaporation during spreading has no effect,(19) Alteraifi *et al.*(12) applied a useful method to graphically verify whether evaporation affects droplet spreading. The authors used a spherical cap approximation given by Eq. 3.7:

$$r^3\theta = r_{eq}^3\theta_e \tag{3.7}$$

where r_{eq} and θ_e are the equilibrium contact radius and equilibrium contact angle, respectively. By subsequently plotting $\cos\theta$ versus $\cos(r_{eq}^3\theta_e/r^3)$, the authors demonstrated that a system where droplet volume is conserved (*i.e.* no evaporation) exhibits a slope of 1, and a slope less than 1 indicates droplet evaporation.(12) This method has been applied in the current study and the results for two oils of different viscosities are shown in Figure 3.2.

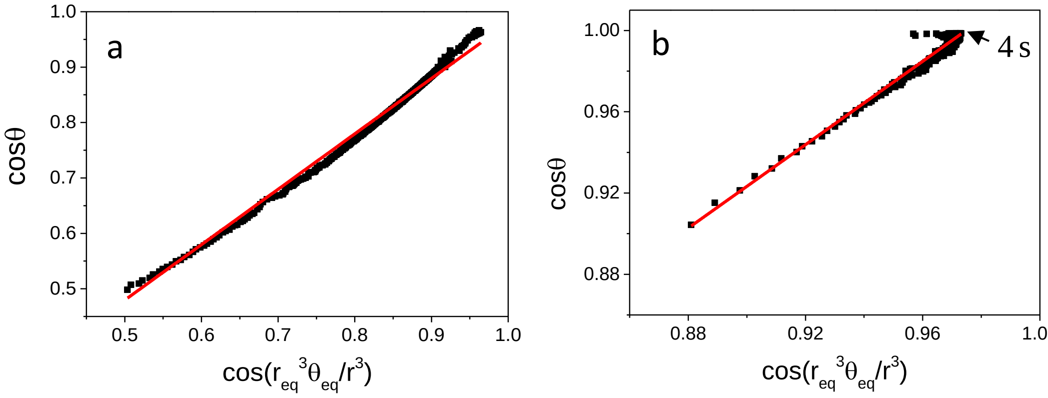

Figure 3.2. Assessment of volume conservation. A spreading droplet with a gradient of 1 shows constant volume with no evaporation. Droplet viscosity a: 1000 mPa·s over 10 s has a gradient of 1, and b: 9.9 mPa·s (lower viscosity oil) over 9 s has a gradient of 1.03, with volume deviations recorded after 4 s.

For the most viscous oil the line of best fit (red line) exhibits a slope of 1 ($R^2 = 0.9999$) (Figure 3.2a), hence there is negligible evaporation and the droplet volume during spreading is conserved (during the experiment). However, for the lower viscosity oil (μ = 9.9 mPa·s), the line of best fit has a slope of 1.03 ($R^2 = 0.9908$). The line of best fit is slightly above 1 and again suggests droplet spreading is not affected by evaporation, However, the measurement diverges from the line of best fit when the droplet contact angle is 4.5°, after 4.3 s of spreading (the droplet had approached a steady-state condition, see Figure 3.8a). When the droplet contact angle is very low the reliability of the data reduces. Reproducible data for contact angles less than 5° is difficult to measure with the tensiometer technique. Due to this divergence, an oil viscosity of 9.9 mPa·s was the minimum viscosity considered in the current study.

3.4 Results and Discussion

3.4.1 Observations of droplet impact and spreading

It was clearly observed that the lower viscosity oils spread faster, and the lowest viscosity oil (9.9 mPa·s) reached steady-state after just a few seconds. The time-dependent spreading of a slightly more viscous droplet (52.2 mPa·s) is shown in Figure 3.3. With higher viscous oils, the spreading dynamics are sufficiently slowed such that the interesting features of droplet impact and spreading can be observed.

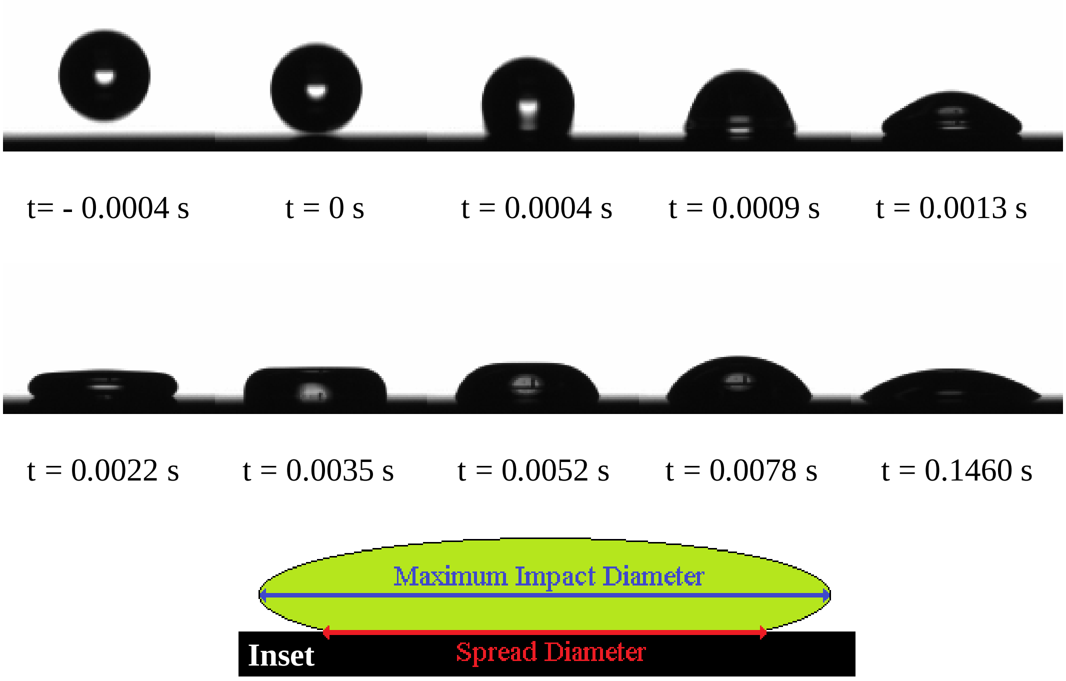

Figure 3.3. Sequence of digital images of 52.2 mPa·s CH_3 terminated PDMS oil droplet spreading on a silicone surface when released from a droplet height of 3 cm. Inset: The difference between the spread diameter and the maximum impact diameter.

Figure 3.3 shows the effect of the kinetic energy gained by a droplet released from a height of 3 cm. At time 0.0009 s, the droplet exhibits a rim; which is often seen when low viscosity droplets approach the splash threshold.(20) The high oil viscosity ensures sufficient viscous dissipation and the droplet does not splash. The droplet then quickly flattens (forming of a pancake) as seen at 0.0022 s. At this stage, the spreading radius is smaller than the maximum droplet radius (see Figure 3.3 inset) due to the balance of surface tension forces and kinetic energy of the droplet. Following the droplet flattening there is then a slight rebound that resulted in a lower energy spherical cap at $t = 0.0078$ s (Figure 3.3). The droplet rebound is due to the droplet kinetic energy dissipating and the surface forces minimising droplet surface area (droplet release height = 3 cm), with the kinetic energy dissipated at approximately 0.0078 s, and the droplet continuing to spread. Figure 3.4 shows the spreading of a 1000 mPa·s droplet.

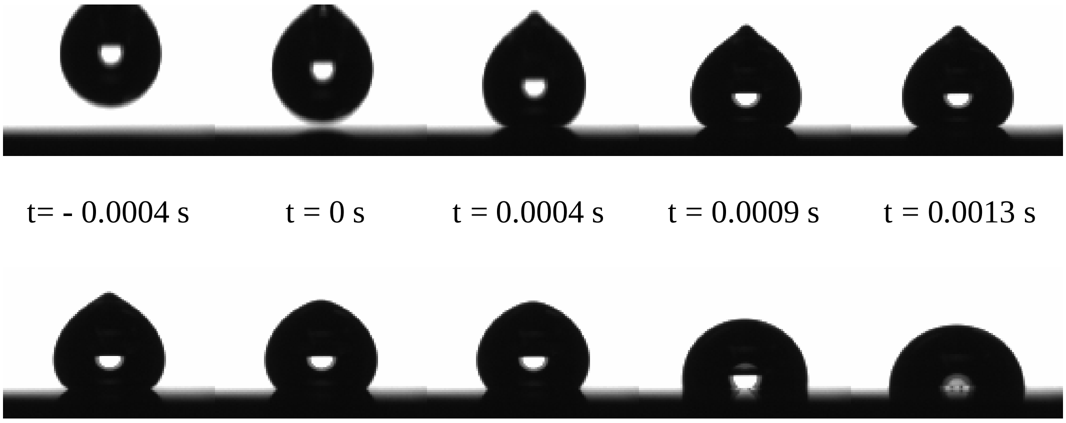

t= - 0.0004 s t = 0 s t = 0.0004 s t = 0.0009 s t = 0.0013 s

t = 0.0078 s t = 0.0207 s t = 0.0251 s t = 0.1546 s t = 0.2410 s

Figure 3.4. Sequence of digital images of 1000 mPa·s CH_3 *terminated PDMS oil droplet spreading on a silicone surface when released from a droplet height of 3 cm.*

For a higher viscosity oil droplet (μ = 1000 mPa·s, Figure 3.4) there is a marked difference when compared to the spreading behaviour of lower viscosity droplets. Here the droplet is less affected by the kinetic energy, i.e. there is no rim formation or flattening of the droplet, which instead maintains a spherical cap shape and spreading is noticeably slower. Another difference seen during initial spreading (from 0 – 0.0251 s) is that the droplet maintains a tear drop shape. Indeed, when a droplet detaches from the needle, surface tension forces enable a spherical droplet to form, minimising surface area, as seen in the first images of Figure 3.3 for a droplet with a viscosity of 52.2 mPa·s. However, for a more viscous droplet (μ = 1000 mPa·s) the spherical shape to minimize surface area is delayed due to competing effects of viscous and surface tension forces, leading to a small protrusion remaining on the droplet during initial spreading. This effect becomes more significant with increasing viscosity, as shown in Figure 3.5 for a CH_3 terminated droplet of viscosity 12120 mPa·s released from a 3 cm height.

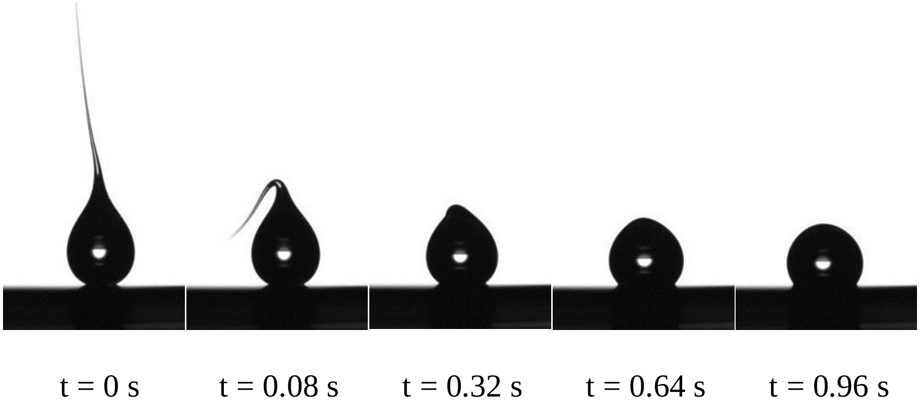

Figure 3.5. Sequence of digital images of 12120 mPa·s CH_3 *terminated PDMS oil droplet spreading on a silicone surface when released from a droplet height of 3 cm.*

As shown in Figure 3.5, the tail effect is more pronounced for extremely high viscosity oils. The tear drop shape is observed for at least 0.64 s. It is also worth noting that when the droplet is released from a lower height of 0.6 cm, the droplet remains in contact with both the needle and the spreading surface for a prolonged period of time (~ 0.6 s). These effects of droplet shape and the prolonged contact with the needle on the spreading dynamics will be discussed later.

3.4.2 Dimensionless numbers

Dimensionless numbers were first discussed in Chapter 2. The relevant dimensionless numbers used to describe droplet impact and spreading are given by Eqs. 3.8 – 3.12.

3.4.2.1 Gravitational effects

The bond number (*Bo*) (Eq. 3.8) compares the gravitational and surface tension forces. To calculate *Bo*, the droplet spherical diameter was used as the characteristic length *L*, the oil density was fixed at 0.98 g/cm^3 and the surface tensions are given in Table 3.1. The droplets had an average *Bo* of 1.8 ± 0.1. For falling droplets not to be influenced by gravity, *Bo* must be < 0.1;(21) hence gravitational effects are expected to influence the droplet behaviour during impact.(22)

$$Bo = \frac{\rho g L^2}{\gamma} \tag{3.8}$$

During droplet spreading the gravitational forces are thought to be negligible when the droplet diameter is smaller than the capillary length.(23) Using Eq. 3.9, the capillary length for the silicone oils was calculated to be 1.5 mm. The droplet radii were between 0.95-0.97 mm and thus below the capillary length, therefore, the spreading droplets should not be affected by gravity.

$$\kappa^{-1} = \sqrt{\frac{\gamma}{\rho g}} \tag{3.9}$$

3.4.2.2 Inertial effects

The ratio of inertial forces to surface tension and viscous forces can be calculated to better understand the behaviour of a droplet at impact (*i.e.* droplet splashing).

The Reynolds number (*Re*) compares the inertial to viscous forces and can be calculated using Eq. 3.10, with the impact velocities given in Table 3.2, and the droplet viscosities given in Table 3.1. The droplet *Re* was calculated for each droplet height and for each oil viscosity, see Figure 3.6. As shown, *Re* increases with the droplet release height, with the droplets having *Re* in the range of 0.04 - 210.

$$Re = \frac{\rho L v}{\mu_{drop}} \tag{3.10}$$

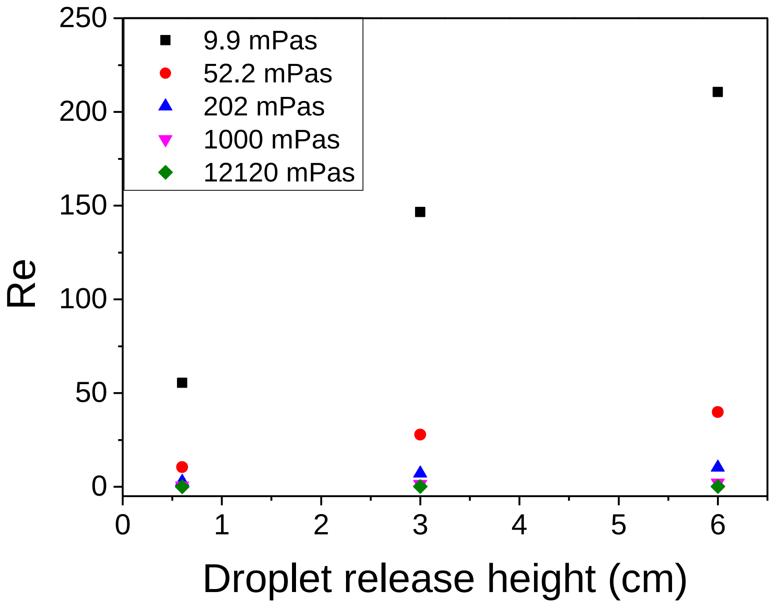

Figure 3.6. Reynolds number calculated for the PDMS oil droplets when they impact the surface after being released from a set height.

A critical Reynolds number (Re_c) can be determined; when *Re* is greater than Re_c simple spreading no longer occurs, and the droplet impact results in splashing. Authors have noted that the Re_c can be shifted due to influences of surface roughness.(24, 25) Keshavarz *et al.*(26) found that Re_c was approximately 350 for a smooth flat surface, similar to the silicon wafers used in the present study. The experiments should thus exhibit a deposition drop impact outcome; *i.e.* only spreading should occur.

The Weber number (*We*) compares inertial and surface tension forces with critical values used to describe splashing regimes. Like Re_c, the critical *We* (We_c) is affected by the surface roughness, (27, 28) with rougher surfaces leading to a decrease in the We_c. The *We* for this study have been calculated using Eq. 3.11 and are shown in Table 3.3.

$$We = \frac{\rho L V^2}{\gamma} \tag{3.11}$$

Table 3.3. Weber number as a function of droplet release height (impact velocity) for PDMS oil droplets.

Droplet release height / cm	***We***
6.0	102
3.0	50
0.6	7

The *We* increases with droplet impact velocity and inertia forces dominate behaviour during impact. The *We*, unlike the *Re*, is not affected by droplet viscosity. Many have sought the We_c for dry surfaces. Pate *et al.* estimated that We_c ~ 100,(29), Palacios *et al.*(30) found it to be approximately 300 and Range and Feuillebois recorded a range of We_c from 105 – 345(28) depending on surface roughness. These values (Table 3.3) indicate that the droplets released from 0.6 and 3 cm should exhibit spreading. The droplets released at 6 cm are closer to the literature We_c values, however, as the surfaces in this study are flat, with minimal roughness (RMS = 0.09 nm), the droplets released from 6 cm are likely to exhibit deposition outcomes too.

The surface tension, inertia and viscous forces can all be compared in one dimensionless number called the Ohnesorge number (*Oh*), which effectively combines the *Re* and *We* as seen in Eq. 3.12;

$$Oh = \frac{\sqrt{We}}{Re} = \frac{\mu}{\sqrt{\rho \gamma L}} \tag{3.12}$$

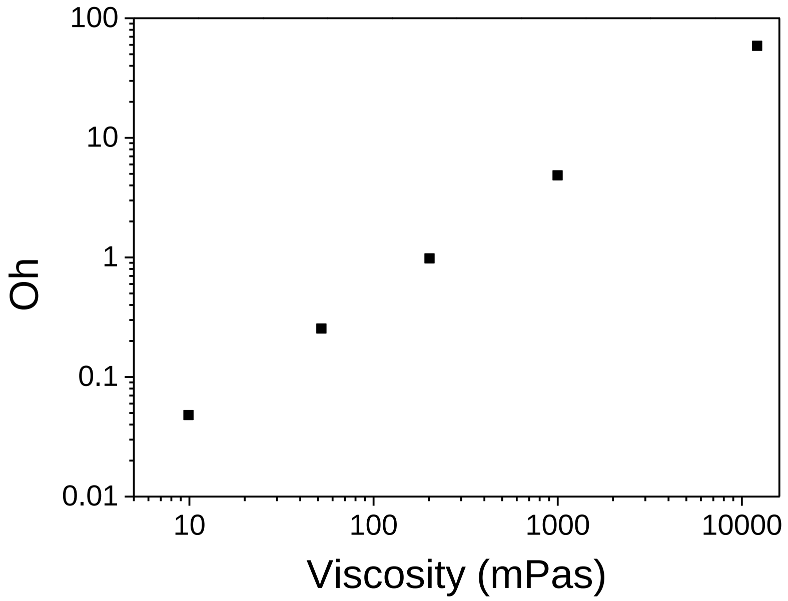

Figure 3.7. Change in Ohnesorge number with droplet viscosity.

The *Oh* was calculated to be 0.05 – 59. No change in *Oh* was seen due to the impact velocity; however, *Oh* is dependent on the oil viscosity as shown in Figure 3.7. Values much lower than 1 indicate surface tension forces dominate on impact (9.9 and 52.2 mPa·s droplets), however, as oil viscosity increases the *Oh* values are much larger than 1 and viscous forces dominate (1000 and 12120 mPa·s droplets). Critical Ohnesorge numbers (Oh_c) are usually never given alone but as a function of the *Re*. The Oh_c is inverse to the Re_c, when *Re* decreases, Oh_c increases, also the calculated *Oh* value must be below the Oh_c for splashing to occur. From the literature when the *Re* is 500 the Oh_c was around 0.04.(29, 30) The highest *Re* calculated for the present study is 210 as seen in Figure 3.6; so the *Oh* values calculated are higher than the literature Oh_c and so splashing should not occur. In this study the calculated *Re*, *We* and *Oh* all suggest that no splashing should occur, however, the likelihood increases with increasing impact velocity and decreasing oil viscosity.

3.4.3 Influence of oil viscosity on droplet spreading

Only the CH_3-terminated oils are considered in this section with comparisons to the NH_2-terminated oils provided in Section 3.3.5. The measured viscosities of the studied CH_3-terminated oils are provided in Table 3.1, together with their measured surface tensions. The evolution of the droplet spreading radius with time is shown in Figure 3.8a, and the presented data taken to be an average of 3 droplet spreading experiments.

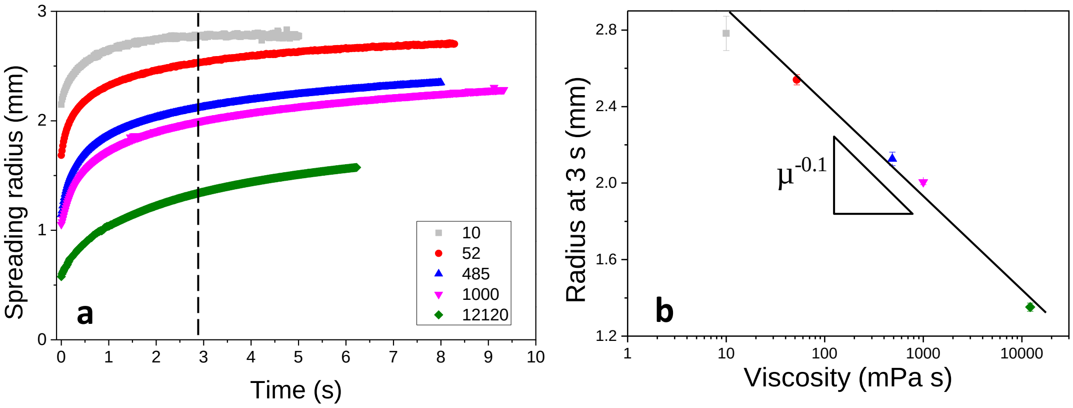

Figure 3.8a. The average spreading radius of 3 CH_3-terminated PDMS droplets of each oil viscosity. Droplet viscosity (mPa·s) provided in the figure legend, b: Droplet radius at 3 s for varying oil viscosities.

As shown in Figure 3.8a, the rate of droplet spreading decreases with increasing oil viscosity. With a frame rate capture of 60 fps the time difference between subsequent frames is 0.016 s. Hence, the first image at $t = 0$ can have an error of < 0.016 s, *i.e.* the incipient contact of droplet spreading time that could have been missed. The exact point of contact between the droplet and substrate is not identified.

Comparing the droplet radii at 3 s to the oil viscosity (Figure 3.8b**)**, it can be seen that the high viscosity oils spread less. On a semi-log plot, the dependence of spreading radius as a function of oil viscosity follows a linear behaviour, confirming the power law dependence. The characteristic behaviour gives an exponent of -0.10, in good agreement with Tanner's law (Eq. 3.2) and Seaver and Berg (Eq. 3.3).

Droplet spreading is often described by two regimes; i) inertial spreading, and ii) viscous spreading. The inertial to viscous spreading characteristic transition time, τ, can be calculated using Eq. 3.13,(5) with values for the current study provided in Table 3.4.

$$\tau \sim \left(\frac{\rho\gamma R}{\mu^2}\right)^{1/8}\sqrt{\frac{\rho R^3}{\gamma}} \tag{3.13}$$

Table 3.4. Inertial regime to viscous regime transition times, τ, calculated using Eq. 3.13 for the studied viscosities of the CH_3-terminated oils.

Viscosity (mPa·s)	**Inertial to viscous regime transition time (s)**
9.9	0.012
52	0.008
485	0.005
1000	0.004
12120	0.002

Table 3.4 confirms the increasing effect of inertial spreading for lower viscosity oils. However, it is worth mentioning that under the current set-up the transition time is shorter than the time between subsequent images, hence there is a possibility that the inertial spreading regime is missed. The data shown in Figure 3.8a predominantly represents viscous regime spreading.

As discussed, the droplet spreading dynamics in the viscous regime can be fitted using $r = Ct^n$.⁽⁴⁾ Figure 3.9 provides such fitting with the parameters n and C listed in Table 3.5.

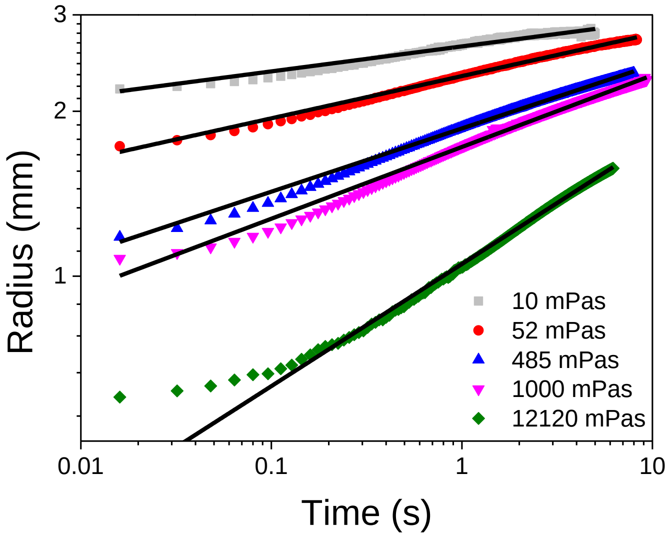

Figure 3.9. The spreading of CH₃-terminated PDMS droplets of varying oil viscosities. The solid black lines are the fits to a simple power law $r = Ct^n$. Time-dependent fittings have been considered in Figure 3.10.

Table 3.5. Constant exponential values after fitting the spreading data of the CH₃-terminated PDMS droplet of various viscosities with a typical power law.

Oil viscosity (mPa·s)	**Constant, *C***	**Exponent, *n***	***R*²**
10	5.25 ± 0.06	0.05 ± 0.010	0.938
52	4.64 ± 0.03	0.08 ± 0.002	0.994
485	3.75 ± 0.09	0.11 ± 0.007	0.996
1000	3.43 ± 0.04	0.13 ± 0.006	0.995
12120	2.16 ± 0.08	0.22 ± 0.002	0.995

The values reported in Table 3.5 were based on an average of 3 droplet spreading experiments (Figure 3.8a). As the viscosity increased the spreading constant decreased, and quite interestingly the spreading exponent, n, increased. From Tanner's law and proven by many, (4, 6-9, 11, 13) it would be expected that the spreading exponent should equal 0.1. However, in the current study this is true for an oil viscosity of 485 mPa·s. For less viscous oils, the exponent values were less than 0.1, whilst for more viscous oils, the spreading exponent was greater than 0.1. Similar variations in spreading gradients have been reported by Sawicki *et al.*(15), who studied oils over a similar viscosity range, 20 – 12000 mPa·s. Those experiments were performed over a much longer times of 60 or 150 min. However, the fitting values were below the 0.1 value for all viscosities, although the exponent approached 0.1 at higher viscosity.

Eddi *et al.*(11) showed that the spreading of viscous oils cannot be described by a single power law exponent but a transient exponent as described by Eq. 3.1. In their study, the exponent decreased from 0.8 to 0.1 with time. The same approach was adopted in the current study and the time-dependent exponents are reported in Figure 3.10. For each oil viscosity the first 5 data points were based on fitting 20 consecutive points to a simple power law $r = Ct^n$, *i.e.* points 1 – 20 from Figure 3.8a. Beyond the fifth point the presented data were based on fitting 50 consecutive points.

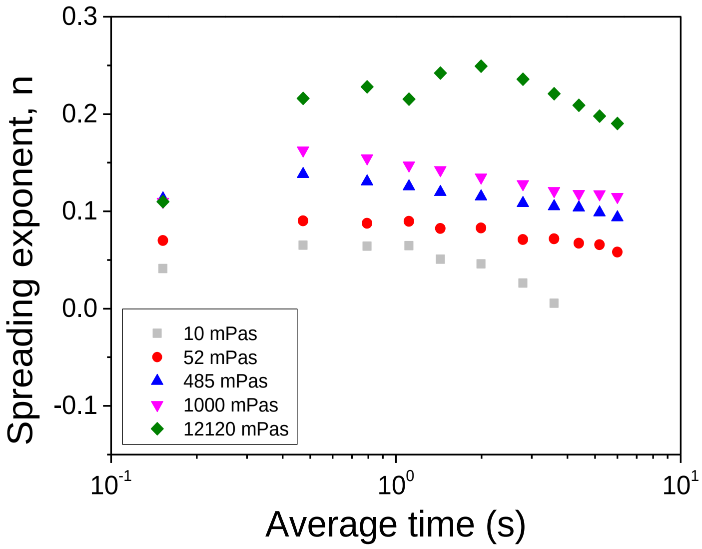

Figure 3.10. Exponent n value as a function of time for the different CH_3-terminated viscous oils, fitted to Eq. 3.1.

As shown in Figure 3.10, the exponents varied with spreading time, although the range was less than that reported by Eddi *et al.*(11), and was shown to depend on the oil viscosity. The discrepancy between our study and that by Eddi *et al.*(11) may result from their ability to measure spreading dynamics at shorter time intervals (t = 10^{-5} to 10^{1} s). As such, the exponents recorded in those studies decreased from n = 0.8 at t = 10^{-5} s to n = 0.2 at t = 10^{-2} s, after which the exponent gradually decreased, reminiscent of the current study (Figure 3.10).

In the current study most oils demonstrated a maximum in exponent values at an average time of 0.5 s and then slowly reduced. Indeed, the first few data points (initial spreading times) in Figure 3.9 showed little variation in the spreading radius, potentially an optical artefact of the experimental method, measuring the droplet spreading radius from a side view – this is then reflected by lower exponents of spreading, see Figure 3.10. Eddi *et al.* showed this phenomenon was observed for a water-glycerine droplet spreading on a glass substrate (as described in Section 2.3.2)(11).

The highest viscosity oil exhibits a more complex behaviour, with the spreading exponent increasing over a longer period of time. The oil has two differences in its droplet shape compared to the other oils i) there is a tail present until t = 0.8 s which slowly merges with the droplet bulk, ii) a spherical cap shape with a contact angle above 90° until t = 2.17 s. The droplet shape will affect the droplet spreading dynamics.

3.4.3.1 Master curve approach to droplet spreading

Figure 3.8b confirmed that the spreading radius could be described by $r = \mu^{-0.1}$, suggesting that the viscous forces dominate the droplet spreading dynamics. As such, the droplet spreading radius could be plotted against a viscosity normalised time (t/μ) to produce a master curve which describes the spreading dynamics of a droplet (Figure 3.11), and enables the incipient spreading dynamics to be captured by the high viscosity oils (although the short time deviation would need to be excluded).

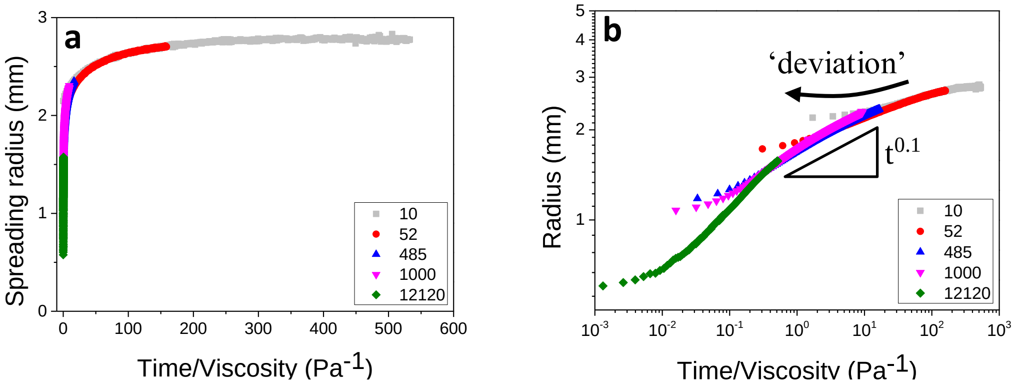

Figure 3.11. Spreading of CH_3-terminated PDMS oils at 3 cm height on a radius vs time/viscosity plot a: linear plot b: log-log plot.

As previously discussed, for all droplets the short time dynamics exhibit a behaviour that does not follow the master curve leading to some initial 'deviation' (Figure 11b). This deviation from master curve behaviour is more pronounced for higher viscosities, with the behaviour also reported by Mitra *et al.* (31) who viewed the spreading droplet from both below and side views. The authors showed the bottom view data to be of better quality at early spreading times due to enhanced spatial clarity. It should be noted that the region in which the spreading curves overlap to form the master curve has a power law gradient of 0.1. The early spreading dynamics of the most viscous oil (12120 mPa·s), and the extended spreading dynamics of the least viscous oil (9.9

mPa·s) indeed deviate from this power law of 0.1 due to shape/ tail effects and experimental limitations respectively, as previously discussed.

The uniqueness of a single spreading curve has several advantages, for example, the ability to predict the spreading dynamics of unknown oils, and the dynamics of high viscosity oils can be used to better understand the spreading dynamics of inviscid oils, where the spreading dynamics are too fast to capture.

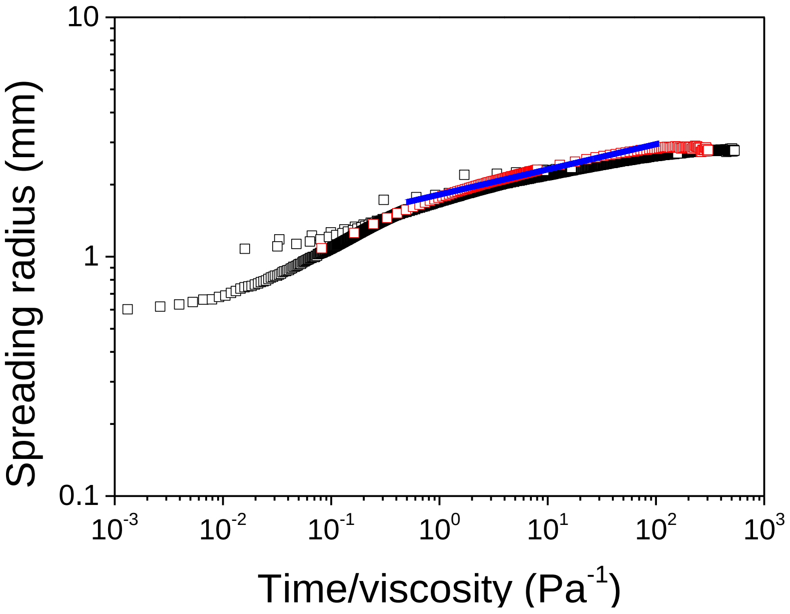

Figure 3.12. Spreading of CH_3*-terminated PDMS oil droplets of different viscosities released at a height of 3 cm. Black squares: master curve obtained from 10 s measurements (60 fps) performed on droplets of a wide range of viscosities. Red squares: spreading curve of the 12120 mPa·s oil droplet from a 1 h measurement (1 fps). Blue line: fit of* $(t/\eta)^{0.1}$.

The spreading dynamics of the most viscous oil (12120 mPa·s) was studied over 1 hr. As shown in Figure 3.12, the long-time spreading dynamics of the highest viscosity oil superimpose the master curve.

In Eddi *et al.*, deviation from single power law behaviour at short spreading times was said to be due to the side-on view recording of the droplet spreading. It is worth noting that those studies were conducted with no inertia, *i.e.* the droplet spontaneously detached from the needle after spreading on the surface. The 'deviation' effect occurred at times less than 10^{-3} s, whereas in the current study such effects were observed at later times ($t = 10^{-2}$ s). To see if the 'deviation' was indeed influenced by the experimental setup rather than the effect of inertia during spreading; droplet spreading experiments were conducted at higher frame rates (200, 1250 and 2315 fps) in an attempt to capture the fast spreading dynamics, see Figure 3.13.

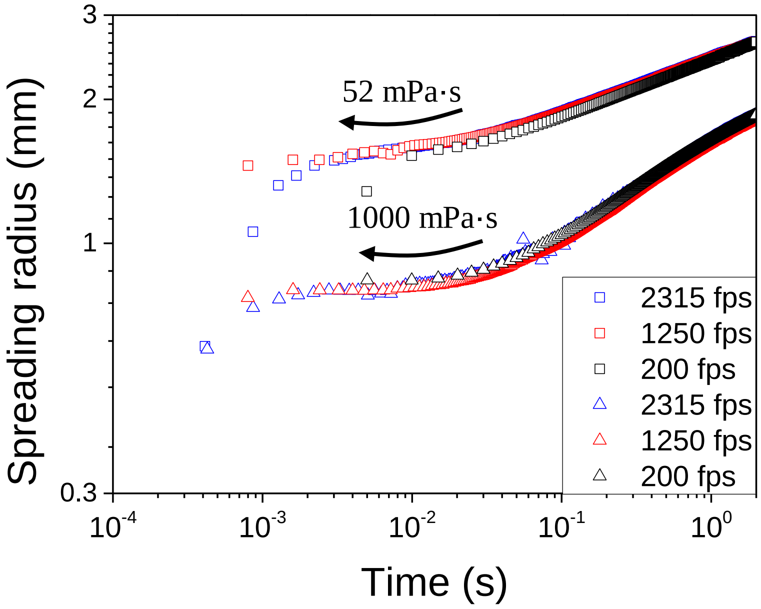

Figure 3.13. Droplet spreading rate of CH_3-terminated PDMS droplets released from 3 cm, for oils with a viscosity of 52 mPa·s (square symbols) and 1000 mPa·s (triangle symbols).

Increasing the frame rate from 200 to 1250 fps decreased the time between subsequent images from 0.005 s to 0.0008 s, and the period of negligible spreading radius was extended. At 2315 fps, the 'deviation' not only extended to shorter times but appeared to proceed at a faster spreading rate. This was more prominent for the lower viscosity oil.

Based on the spreading dynamics and the observations in Figures 3.3 and 3.4, it appears that the ‘deviation’ at early spreading times is a consequence of inertia and not the experimental set-up. For instance, the 52 mPa·s droplet flattens on impact with the spreading substrate, before recoiling (drop height increases) as the droplet begins to spread. It is hypothesized that, the early spreading data may not result from spreading but due to droplet deformation on impact. Unfortunately from visual assessment and a lack of discrimination by the software, the exact point of wetting and spreading could not be easily identified. Therefore some of the earlier spreading dynamic data may be a consequence of a non-wetting dynamic as the droplet elongates and recoils following impact on the substrate. It might be reasonable that simultaneous droplet recoil and spreading leads to an apparent negligible spreading rate.

In an attempt to better understand the initial spreading dynamics a bottom-view camera set-up was also considered. This data is compared to the side-on captured data for the same oil viscosity, see Figure 3.14, where the spreading radius (r) has been normalised by the initial captured radius (r_0). The insert shows an image obtained from the bottom-view set-up.

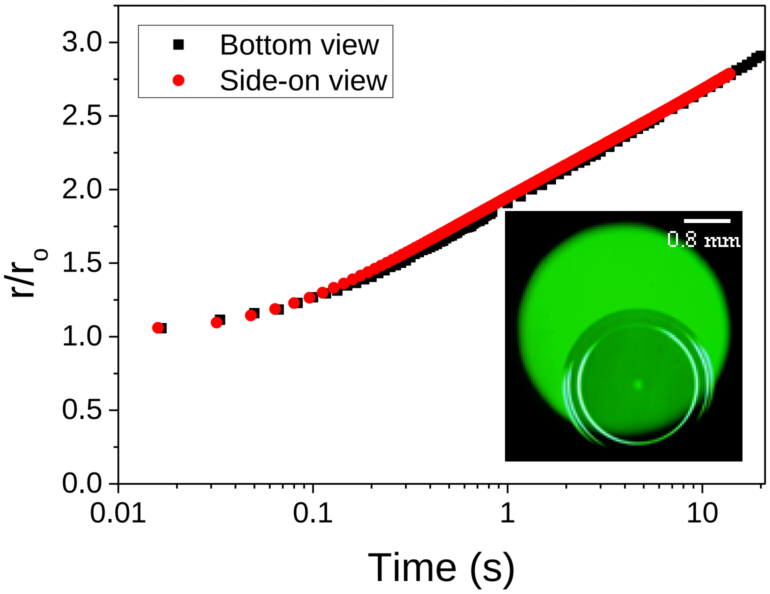

Figure 3.14. Experimental data from bottom and side views for a 1000 mPa·s viscosity CH_3-terminated oil droplet at an impact velocity of 0.74 m/s recorded at 200 fps. Insert: image of a droplet during spreading from the bottom-view experimental set-up, the green circle shows the field of view of the microscope, the darker circle represents the droplet which has an interference pattern at the edges.

Figure 3.14 shows little difference in the spreading dynamics as captured from the side-on and bottom-view perspectives. Such behaviour would confirm that the ‘deviation’ is a consequence of droplet inertia. When measured at a higher frame rate (2000 fps), the same result was observed (good agreement between side-on and bottom-view data), although the first few images did provide some interesting images as the droplet begins to interact with the spreading substrate, see Figure 3.15a-c.

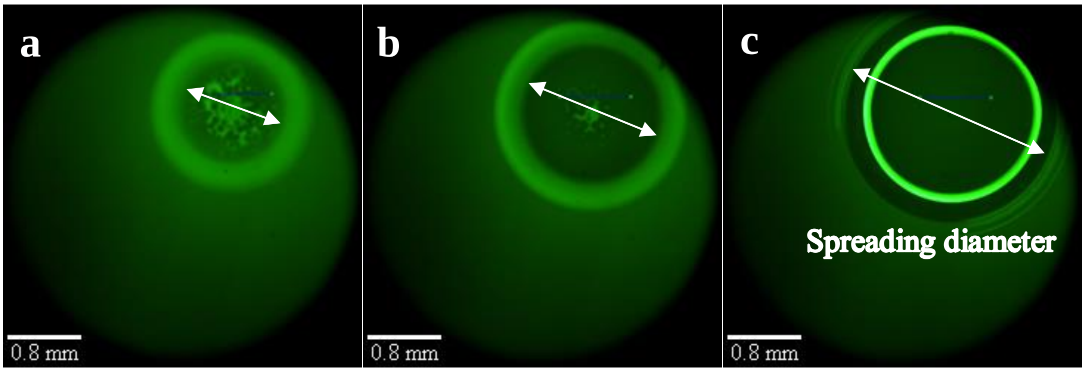

Figure 3.15. Bottom-view of a 1000 mPa·s viscosity oil droplet recorded at 2000 fps with droplets at t= a: 0.0005 s, b: 0.001 s, c: 0.08 s. The green area shows the microscopes field-of-view, the droplet is shown in top right hand side with the darker area showing where the droplet has wetted. In image a and b the mottled lighter areas show where there is a larger gap between droplet and surface, image c also shows an interference pattern at the droplet edge.

Figure 3.15a shows an approaching droplet with the image depicting several dark and light spots. This would indicate a deformed liquid interface which has not yet wetted the underlying glass substrate. As the droplet appears to expand over the substrate the extent of dark and light spot regions decreases (see Figure 3.15 b at t = 0.001 s), and such behaviour occurs in the region of 'deviation', i.e. negligible spreading. Once the droplet wets the substrate a clear interface is readily observed as the droplet proceeds to spread.

3.4.3.2 Comparison of spreading models

The spreading of non-volatile droplets has been theoretically described by Tanner,(13) Seaver and Berg,(2) and de Gennes,(32) models see Section 3.1. The spreading dynamics of the CH_3-terminated PDMS oils have been compared against each model.

Low (9.9 mPa·s), intermediate (1000 mPa·s) and high (12120 mPa·s) viscosity oils were considered, see Figure 3.16a-c.

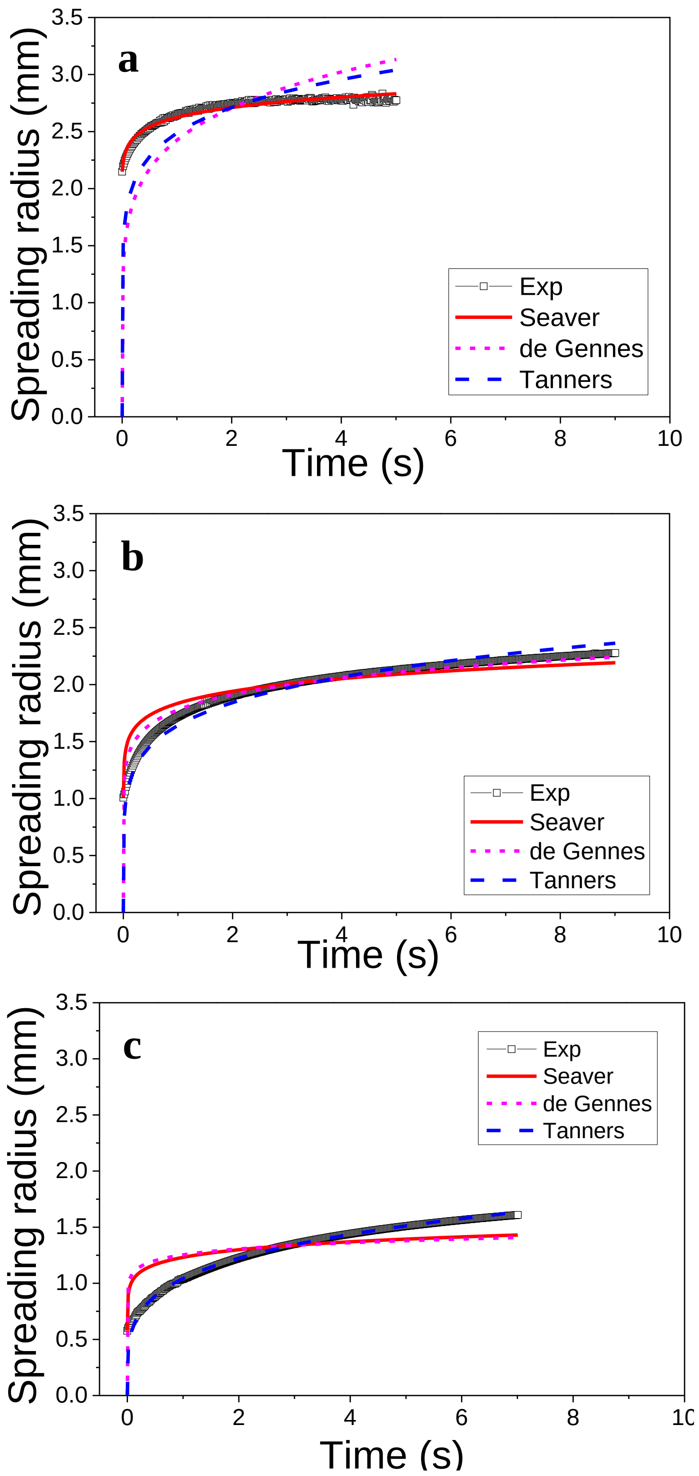

Figure 3.16. Fitting of the experimental data with the three models: Tanner, Seaver and Berg and de Gennes. CH_3-terminated PDMS oil droplets released from 3 cm and of viscosities a: 9.9 mPa·s, b: 1000 mPa·s and c: 12120 mPa·s.

Based on the models the spreading exponents (*n*) for Tanner, and Seaver and Berg are 0.1, and the exponent *m* for de Gennes is 3. If these exponents are fixed then there is clear deviation between the models and experimental data. To achieve the best fit, the values for *n* and *m* were varied and provided in Table 3.6. As shown in Figure 3.16, droplet spreading of the lowest viscosity oil (9.9 mPa·s) was in good agreement with Seaver and Berg. Tanner and de Gennes models provided equally poor fitting of the same data. The poor fitting was thought to result from the model assumptions where both Tanner and de Gennes models were based on a spherical cap approximation, unlike Seaver and Berg which assumes a cylindrical disk. Since the low viscosity oils spread quickly, a large percentage of the spreading regime is missed. Very low contact angles were measured in the first image, contact angle = 26°, becoming extremely low (< 4°) after 3 s of spreading (Figure 3.3). As such, the thin film spreading is better described by the cylindrical disk approximation.

For the intermediate viscosity oil (1000 mPa·s), see Figure 3.16b, all spreading models provide reasonable agreement to the experimental data. The model by Seaver and Berg does exhibit some deviation, especially at initial spreading times, where the droplet contact angle is high and the droplet retains a characteristic spherical cap shape and not a cylindrical disk as used as the basis for the model. Tanner's law, which assumes a spherical cap, shows slight deviation at longer spreading times when the contact angles are low and the droplet shape approaches a thin film (Figure 3.4).

For the highest viscosity oil (12,120 mPa·s) Tanner's model provided good agreement to the data, while both the Seaver and Berg and de Gennes models showed an equally poor fit. Again, such discrepancy is likely to result from the approximations of droplet shape, with the spreading droplet maintaining higher contact angles for extended spreading times. However, de Gennes does define a spherical cap approximation, but does not consider viscosity which clearly is a factor for the spreading dynamics of extremely high viscosity oils. This is potentially why the model significantly over predicts the spreading radius at short spreading times.

Table 3.6. Spreading exponents for the three models for all the CH_3-terminated oil droplets released at a height of 3 cm. In all cases, the spreading exponents increased with oil viscosity.

CH_3-terminated oil viscosities (mPa·s)	**Seaver and Berg, *n***	**de Gennes, *m***	**Tanner, *n***
9.9	0.048	1.76	0.125
52.2	0.065	2.07	0.134
481.5	0.075	2.70	0.150
1000	0.081	2.83	0.166
12120	0.077	5.26	0.231

The fitted spreading exponent of the Seaver and Berg model are below the expected value of 0.1, while the fittings to the Tanner model produce spreading exponents greater than 0.1. Quantitatively comparing the model exponents, in Table 3.5, and the exponents for the three values further highlight; the Seaver and Berg model successfully predicts low viscosity oils, Tanner predicts well high viscosity oils and de Gennes exponent, which is predicted to be 3 but has an acceptable range of 2.5 – 3.5(3), predicts the spreading of intermediate viscosity oils. This provides further support to Tanner's original work, as Tanner's law was developed and shown to work for silicon oils above 1.08 Pa·s.(13)

One study that compares these three models is that of Alteraifi *et al.*(12) The authors found that all three models were poor at predicting the spreading of liquid droplets except in the case of silicone oils. For 10 – 1000 mPa·s viscosity silicone oils, they found that all three models were good at predicting the spreading dynamics. However, they recorded spreading areas over a much longer time period of 1600 s. For their experiments, the models appear to overpredict spreading at early times but provide better agreement at longer times, at approximately 1200 s. The present study focuses on early spreading dynamics (t = 0 – 10 s), none of the three models are effective at modelling droplet spreading over all viscosity ranges, the master curve developed in this work could provide an alternative method to describe droplet spreading over a large range of viscosities.

3.4.4 Influence of impact velocity on droplet spreading

The impact velocity was varied for the different oil viscosities by varying the droplet release height. The distance between the needle tip and the surface was varied and set to 0.6, 3 and 6 cm, leading to impact velocities of 0.28, 0.74 and 1.06 m/s respectively (see Table 3.2 and Section 3.2.2.1 for details about velocity calculations). The raw data (spreading radius against time) of a high, intermediate and low viscosity oil are shown in Figure 3.17a-c.

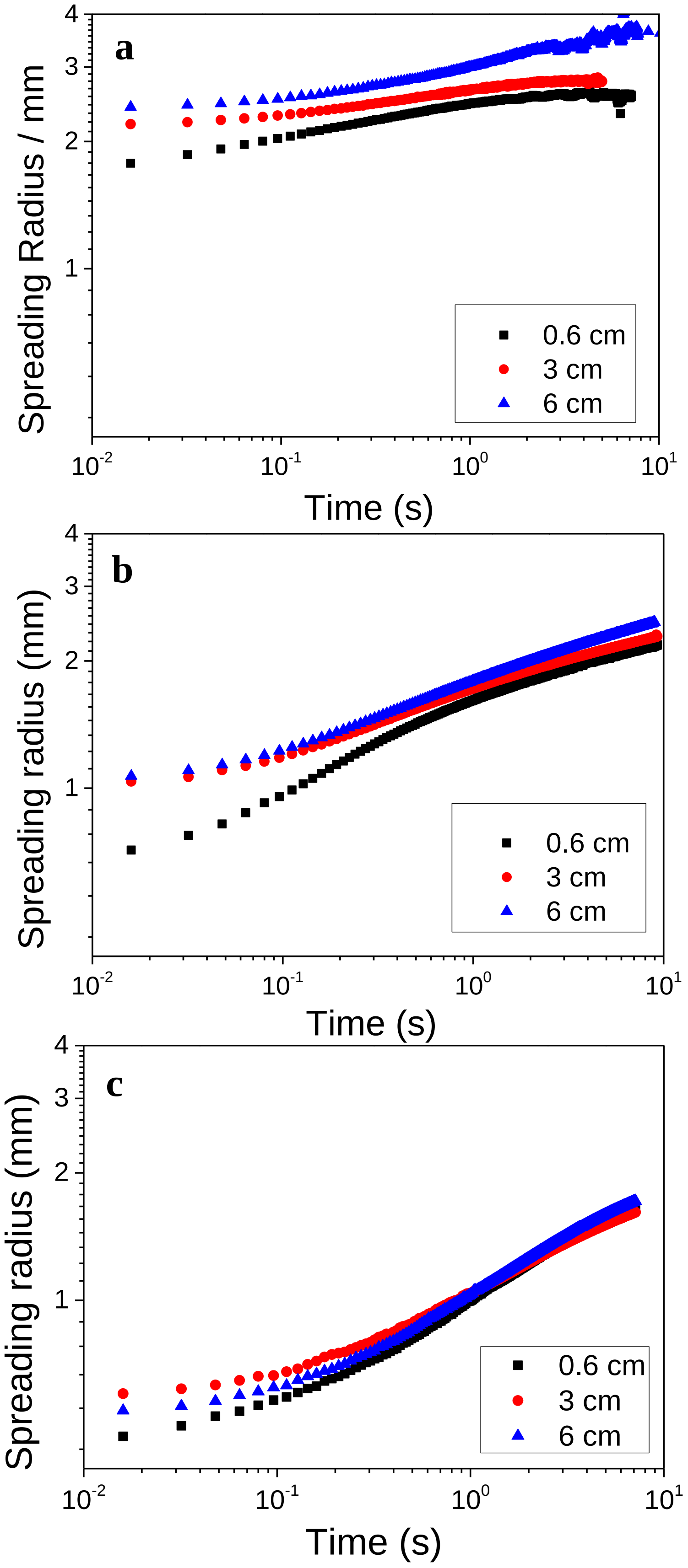

Figure 3.17. Raw spreading data for droplets released from three heights, 0.6, 3 and 6 cm, with oil viscosities of a: 9.9, b: 1000 and c: 12120 mPa·s.

The impact velocity has more effect on low viscosity oils, as seen from Figure 3.17a-c. For the 9.9 mPa·s oil (Figure 3.17a), at any given time there is an increase in spreading radius with impact velocity. For high viscosity oil droplets there is significantly less effect of impact velocity as the viscous dissipation increases and thus rapidly dissipates the kinetic energy from the system. This corroborates with what has been reported in the literature.(25, 33, 34)

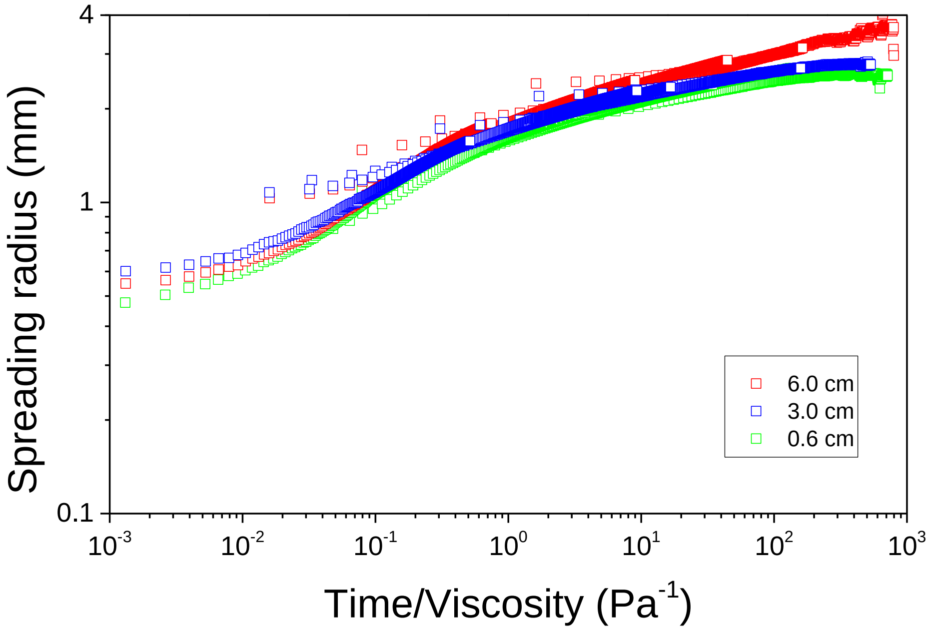

Figure 3.18. Master curves f (time/viscosity) versus droplet spreading radius shows the spreading behaviour of the CH$_3$*-terminated PDMS oils of different viscosities released from different heights.*

Figure 3.18 shows the three master curves (by normalising the spreading time by droplet viscosity) that was obtained for each impact velocity (the 3 cm master curve was also shown in Figure 3.11). All three impact velocities produced similar curves, with a slight upward shift with increasing impact velocity. Most of the data collapses onto the specific master curve, however, there are two discrepancies; 1) graphical ‘deviations’ are observed at the beginning of each droplet’s spreading data, 2) the spreading data of the lowest viscosity 9.9 mPa·s oil after being released from 6 cm, whose case is further discussed later.

Generally, the graphical ‘deviation’ exists over a longer period of time as the droplet impact velocity increases. Apart from the most viscous oil, the first measured radius increases with the droplet height (also shown in Figure 3.17a and c). Indeed, the kinetic energy is higher and causes the droplets to spread more during early spreading times (*i.e.* during the inertial regime which is not captured). The increase in the initial spreading radius (due to increased momentum) makes the data appear to have a more prominent ‘deviation’.

The second discrepancy is that the 9.9 mPa·s droplet released from 6 cm is not graphically similar to the 9.9 mPa·s droplets released at 3 and 0.6 cm. Lower viscosities and higher impact velocities bring the droplet closer to the critical splashing velocity as discussed in Section 3.4.2. Repeating the experiments provided an image of the droplet on impact as shown in Figure 3.19.

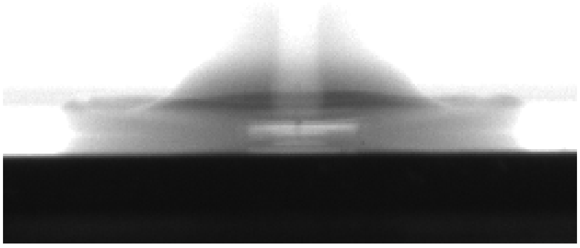

Figure 3.19. Captured image of a droplet impacting on the surface for the 9.9 mPa·s CH_3*-terminated PDMS oil released from a height of 6 cm.*

Figure 3.19 shows that the 9.9 mPa·s droplet released from a height of 6 cm belongs to the splashing regime,(35) and explains why the spreading data for this viscosity and height is different on the master curve. However, due to the low frame rate of 60 fps this was not routinely captured and as can be seen the image is blurred. This disagrees with the earlier calculation of the *Re* which led to the prediction that no splashing would occur. Indeed, the highest *Re* (210) was found to be below the value of the Re_c (300), above which splashing would occur. The simple *Re* calculations are not sensitive enough to correctly predict droplet-surface morphologies.

3.4.5 Influence of the oil terminating group on droplet spreading

A range of NH_2-terminated PDMS oils of viscosities closely matching the ones of the CH_3-terminated oils (see Table 3.1 for the measured viscosities) were investigated. Droplets of the NH_2-terminated PDMS oils were also released from 0.6 cm, 3 cm and 6 cm, the corresponding master curves are displayed in Figure 3.20.

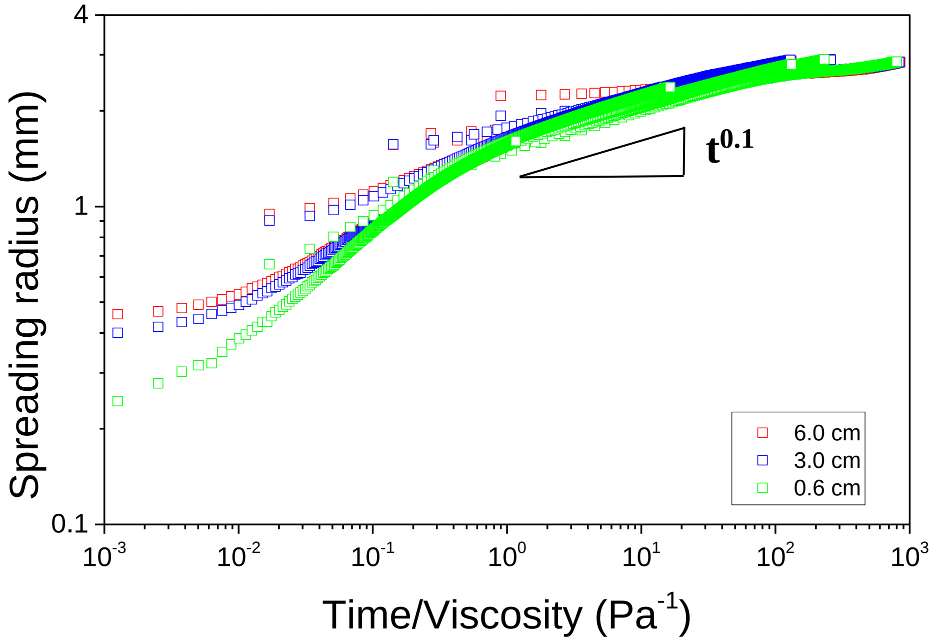

Figure 3.20. Master curves f (time/viscosity) versus droplet spreading radius showing the spreading behaviour of the NH_2-terminated PDMS oils of different viscosities from different release heights.

The master curves of the NH_2-terminated oils are similar to those obtained for the CH_3-terminated oils in Figure 3.18. Similar to the CH_3-terminated oils, there is a substantial region of the master curve which can be described by a power law with an exponent of 0.1. The NH_2-terminated oils also exhibit the graphical ‘deviations’ due to the droplet spreading but not wetting. Comparing the NH_2- to the CH_3-terminated PDMS master curves, the two main differences are: i) the spreading behaviour of the lowest viscosity oil at 6 cm and ii) the spreading behaviour of the most viscous oil.

Firstly, the lowest NH_2-terminated PDMS viscosity studied was 17.8 mPa·s, but 9.9 mPa·s for the CH_3-terminated PDMS oil. The slightly higher viscosity means the critical splashing velocity is not surpassed and hence all droplets released at 6, 3 and 0.6 cm are graphically similar. Secondly, the high viscosity NH_2-terminated oil droplets spreading behaviour does not align with that of the CH_3-terminated oil equivalents (clearly shown in Figure 3.21b), until late spreading times, although the spreading curves for the NH_2- and CH_3-terminated oils of low viscosity do superimpose (Figure 3.21a).

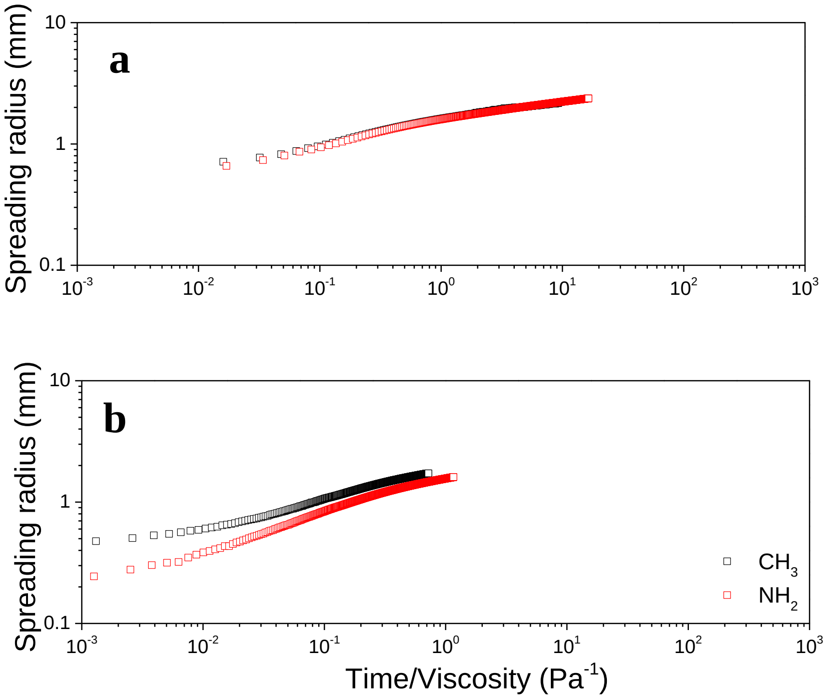

Figure 3.21. Comparison of the viscosity corrected spreading behaviour of NH_2-terminated and CH_3-terminated oil droplets released from a height of 0.6 cm for oil viscosities of a: 1000 and 941 mPa·s and b: 12120 and 12710 mPa·s.

As the time is normalised by the viscosity, the fact the spreading curves of the 12120 mPa·s CH_3-terminated and 12710 mPa·s NH_2-terminated oil do not superimpose should not, therefore be due to the viscosity difference. As discussed previously, the high viscosity oil droplets exhibit a tail at early spreading times, such as the one shown in Figure 3.5.

For a height of 0.6 cm, the tail of the CH_3-terminated oil lasts for approximately 1 s (corresponds to t/μ = 0.084 Pa^{-1} on the master curve), while the tail lasts longer, approximately 1.4 s (t/μ = 0.116 Pa^{-1}), for the NH_2-terminated oil. This is reproducible and due to the NH_2-terminated oil having a higher viscosity. The droplet shape (tail effect) affects the spreading dynamics and explains why the spreading of the 12710 mPa·s NH_2-terminated oil does not overlap with the 12120 mPa·s CH_3-terminated oil.

It is believed, the droplet shape alters the spreading dynamics, the droplet shape is a consequence of the viscosity but it is not the viscosity in itself that changes the droplet spreading dynamics.

The spreading data of the viscous NH_2-terminated oil droplet released at 0.6 cm shows a larger gradient deviation than that of 3 or 6 cm; with increased momentum, the tail is present for a shorter period of time. For instance, the 12710 mPa·s NH_2-terminated PDMS droplet forms a tail lasting for 1.4 s (t/μ = 0.116 Pa^{-1}) when released from 0.6 cm, 1.0 s from 3 cm (t/μ = 0.084 Pa^{-1}) and for 0.9 s from 6 cm (t/μ = 0.074 Pa^{-1}). With increased momentum, the tail is absorbed into the bulk of the droplet much faster and differences in spreading are thus less apparent.

The effect of terminating groups has been studied before, however, most studies have compared hydroxyl-terminating groups (OH) with CH_3-terminating groups. Differences in OH-terminated and CH_3-terminated PDMS oil spreading have been witnessed.(15, 36) Sawicki *et al.*(15) found that the OH-terminated oil droplets spread slower possibly due to a more ordered system at the air-liquid interface. Since then it has also been found that PDMS-OH is able to firmly anchor to silanol groups on the silicon substrate via hydrogen bonding, both polymer ends are able to anchor which creates a network close to the surface which reduces spreading dynamics.(37)

Sawicki also found that the data from the OH-terminated oils provided better fits with the Tanner model than the CH_3-terminated oils.(15) The spreading dynamics of NH_2-terminated molecules are expected to be in-between those of OH- and CH_3-terminated molecules;(36) this is because molecular properties such as proton affinity and polarizability of the NH_2 group are in-between that of CH_3 and OH.(38) The values of the exponents obtained from fitting the NH_2-terminated oil data to the models and to the power law ($r = Ct^n$) are shown below in Table 3.7.

Table 3.7. Exponent values obtained with the three fitting models and the simple power law fit ($r = Ct^n$) for all the studied NH_2-terminated oils released from a height of 3 cm.

NH_2-terminated oil viscosities (mPa·s)	**Seaver and Berg, *n***	**de Gennes, *m***	**Tanner, *n***	**Power law fit, *n***
17.8	0.046	2.291	0.106	0.020
59.0	0.065	2.258	0.126	0.041
112.6	0.074	2.215	0.140	0.072
941	0.081	2.960	0.152	0.113
12710	0.069	10.966	0.083	0.207

The comparison of the exponents obtained from the simple power law fit for both the CH_3- and NH_2-terminated PDMS oils (Table 3.5 and Table 3.7) quantitatively shows that NH_2-terminated oils spread slower. This is potentially due to the explanation given by Sawicki,(15) and Valignat *et al.*(37) with the ordering due to the polar NH_2 group able to interact with one another through hydrogen bonding. The Tanner's law exponents are much closer to the predicted value of 0.1 for the NH_2-terminated PDMS oils compared to those obtained for their CH_3-terminated equivalents; which is similar to what Sawicki(15) found.

3.5 Conclusions

The present study has demonstrated that viscosity has a large effect on the spreading dynamics. A viscosity range of 9.9 – 12710 mPa·s was investigated for a set of CH_3-terminated PDMS oils, and a similar range for NH_2-terminated oils. The Seaver and Berg, de Gennes and Tanner models were unable to model the entire viscosity range: the Seaver and Berg model was more appropriate for modelling the spreading behaviour of low viscosity oils, and the de Gennes and Tanner models were better at fitting higher viscosity oils. It was shown that the spreading dynamics of the oil viscosity range could be described by a master curve, which could enable the prediction of spreading dynamics of oils of other viscosities, *i.e.* the quick dynamics of low viscosity oils could also be predicted with spreading dynamics of more viscous oils using the master curve, and *vice versa*. The central part of the master curve was shown to have a power law gradient of 0.1, in agreement with the Tanner model. The spreading dynamics were shown to be faster with increased impact velocity. The spreading dynamics were also shown to be slower with a NH_2-terminated PDMS oil due to more ordering at the air-droplet and surface-droplet interfaces. The shape of the droplet was shown to affect the spreading dynamics; droplets from more viscous fluids would have a tail affecting the spreading dynamics.

3.6 References C

1. MARMUR, A. Equilibrium and spreading of liquids on solid surfaces. *Advances in Colloid and Interface Science*, 1983, **19**(1–2), pp.75-102.
2. SEAVER, A.E. and J.C. BERG. Spreading of a droplet on a solid surface. *Journal of applied polymer science*, 1994, **52**(3), pp.431-435.
3. DE GENNES, P.-G. Wetting: statics and dynamics. *Reviews of modern physics*, 1985, **57**(3), p.827.
4. CHEN, L. and E. BONACCURSO. Effects of surface wettability and liquid viscosity on the dynamic wetting of individual drops. *Physical Review E*, 2014, **90**(2), p.022401.
5. BIANCE, A.-L., C. CLANET and D. QUÉRÉ. First steps in the spreading of a liquid droplet. *Physical Review E*, 2004, **69**(1), p.016301.
6. CHEN, L., E. BONACCURSO and M.E.R. SHANAHAN. Inertial to Viscoelastic Transition in Early Drop Spreading on Soft Surfaces. *Langmuir*, 2013, **29**(6), pp.1893-1898.
7. WANG, X.D., Y. ZHANG, D.J. LEE and X.F. PENG. Spreading of Completely Wetting or Partially Wetting Power-Law Fluid on Solid Surface. *Langmuir*, 2007, **23**(18), pp.9258-9262.
8. LIANG, Z.-P., X.-D. WANG, D.-J. LEE, X.-F. PENG and A. SU. Spreading dynamics of power-law fluid droplets. *Journal of Physics: Condensed Matter*, 2009, **21**(46), p.464117.
9. MIN, Q., Y.-Y. DUAN, X.-D. WANG, Z.-P. LIANG, D.-J. LEE and A. SU. Spreading of completely wetting, non-Newtonian fluids with non-power-law rheology. *Journal of colloid and interface science*, 2010, **348**(1), pp.250-254.
10. WANG, X.D., D.J. LEE, X.F. PENG and J.Y. LAI. Spreading Dynamics and Dynamic Contact Angle of Non-Newtonian Fluids. *Langmuir*, 2007, **23**(15), pp.8042-8047.

11. EDDI, A., K.G. WINKELS and J.H. SNOEIJER. Short time dynamics of viscous drop spreading. *Physics of Fluids*, 2013, **25**(1), 013102-.
12. ALTERAIFI, A.M., D. SHERIF and A. MOET. Interfacial effects in the spreading kinetics of liquid droplets on solid substrates. *Journal of colloid and interface science*, 2003, **264**(1), pp.221-227.
13. TANNER, L. The spreading of silicone oil drops on horizontal surfaces. *Journal of Physics D: Applied Physics*, 1979, **12**(9), p.1473.
14. OGAREV, V., T. TIMONINA, V. ARSLANOV and A. TRAPEZNIKOV. Spreading of polydimethylsiloxane drops on solid horizontal surfaces. *The Journal of Adhesion*, 1974, **6**(4), pp.337-355.
15. SAWICKI, G. Dynamic surface phenomena associated with the spontaneous spreading of silicone fluids. *Wetting, Spreading and Adhesion*, 1978, pp.361-75.
16. SCOTT, J.C. Wetting, Spreading and Adhesion. Edited by J. F. PADDAY. Academic Press, 1978. 498 pp. £ 25.00. *Journal of Fluid Mechanics*, 2006, **94**(4), pp.794-795.
17. SERWAY, R.A. and J.W. JEWETT. *Physics for scientists and engineers: Raymond A. Serway, John W. Jewett, Jr.* Thomson-Brooks/Cole, 2004.
18. VOLKOV, R.S., G.V. KUZNETSOV, P. KUIBIN and P.A. STRIZHAK. The ranges of the aerodynamic drag coefficient of water droplets moving through typical gas media. *Journal of Engineering Thermophysics*, 2016, **25**(1), pp.32-44.
19. RAFAı¨, S. and D. BONN. Spreading of non-Newtonian fluids and surfactant solutions on solid surfaces. *Physica A: Statistical Mechanics and its Applications*, 2005, **358**(1), pp.58-67.
20. DE RUITER, J., R.E. PEPPER and H.A. STONE. Thickness of the rim of an expanding lamella near the splash threshold. *Physics of Fluids*, 2010, **22**(2), p.022104.
21. LI, R., N. ASHGRIZ and S. CHANDRA. Maximum Spread of Droplet on Solid Surface: Low Reynolds and Weber Numbers. *Journal of Fluids Engineering*, 2010, **132**(6), pp.061302-061302.
22. LUBARDA, V.A. and K.A. TALKE. Analysis of the equilibrium droplet shape based on an ellipsoidal droplet model. *Langmuir*, 2011, **27**(17), pp.10705-10713.
23. BONN, D., J. EGGERS, J. INDEKEU, J. MEUNIER and E. ROLLEY. Wetting and spreading. *Reviews of modern physics*, 2009, **81**(2), p.739.
24. RIOBOO, R., C. TROPEA and M. MARENGO. Outcomes from a drop impact on solid surfaces. *Atomization and Sprays*, 2001, **11**(2).
25. ŠIKALO, Š., C. TROPEA, M. MARENGO and E. GANIĆ. Spreading of droplets on horizontal surfaces. *In: New and Renewable Technologies for Sustainable Development*. Springer, 2002, pp.683-692.
26. KESHAVARZ, B., S. GREEN, M. DAVY and D. EADIE. *Newtonian Airless Liquid Jet Interaction with a High Speed Moving Surface.* 2018.
27. LAN, M., X. WANG, P. CHEN and X. ZHAO. *Effects of surface tension and wood surface roughness on impact splash of a pure and multi-component water drop.* 2016.
28. RANGE, K. and F. FEUILLEBOIS. Influence of Surface Roughness on Liquid Drop Impact. *Journal of colloid and interface science*, 1998, **203**(1), pp.16-30.
29. COMEAU, D., K. LATOURETTE and J. PATE. The effect of Weber number and spread factor of a water droplet impinging on a super-hydrophobic substrate. *Applied mathematics*, 2007.
30. PALACIOS, J., P. GÓMEZ, C. ZANZI, J. LÓPEZ and J. HERNÁNDEZ. Experimental study on the splash/deposition limit in drop impact onto solid surfaces. *Proceedings of 23rd ILASS-2010, Brno, Czech Republic*, 2010.
31. MITRA, S. and S.K. MITRA. Understanding the Early Regime of Drop Spreading. *Langmuir*, 2016, **32**(35), pp.8843-8848.
32. DE GENNES, P.G. Wetting: statics and dynamics. *Reviews of modern physics*, 1985, **57**(3), pp.827-863.
33. RIOBOO, R., M. MARENGO and C. TROPEA. Time evolution of liquid drop impact onto solid, dry surfaces. *Experiments in Fluids*, 2002, **33**(1), pp.112-124.

34. HULSE-SMITH, L., N. Z MEHDIZADEH and S. CHANDRA. *Deducing Drop Size and Impact Velocity from Circular Bloodstains.* 2005.
35. YARIN, A. Drop impact dynamics: splashing, spreading, receding, bouncing…. *Annu. Rev. Fluid Mech.*, 2006, **38**, pp.159-192.
36. RAMÉ, E., S. GAROFF and K.R. WILLSON. Characterizing the microscopic physics near moving contact lines using dynamic contact angle data. *Physical Review E*, 2004, **70**(3), p.031608.
37. VALIGNAT, M.P., N. FRAYSSE, A.M. CAZABAT and F. HESLOT. Molecular networks in the spreading of microdroplets. *Langmuir*, 1993, **9**(2), pp.601-603.
38. XU, Y. and C.B. MUSGRAVE. A DFT Study of the Al2O3 Atomic Layer Deposition on SAMs: Effect of SAM Termination. *Chemistry of Materials*, 2004, **16**(4), pp.646-653.

Chapter 4: Oil droplet spreading in aqueous environments

The complexity of droplets spreading on surfaces in water is of interest from the perspective of the personal care industry and others, although scientific understanding of this problem has been limited due to experimental challenges. In the current chapter it is shown that with the aid of an in-house built spreading cell these challenges can be somewhat overcome enabling a parametric study of oil droplets spreading on surfaces submerged in water. Silicon surfaces were silanised to form surfaces with a range of wettabilities, displaying a range of water droplet contact angles of 0, 30, 65 and 100°. It was shown that with an increase in hydrophobicity there was an increase in the extent of oil droplet spreading, increased spreading rate and a decrease in oil droplet-substrate induction time. The dynamics of oil droplet spreading were significantly hindered in the presence of surfactant, with reduced spreading (low surfactant concentrations) and increased induction times measured with increasing surfactant concentration due to the effects of Marangoni flow and charge-stabilization. Increasing the oil viscosity was also shown to decrease spreading dynamics. However, the oil droplet-substrate induction time decreased with increasing oil viscosity due to reduced droplet deformation (viscous resistance to deformation) as shown by the circularity ratio upon droplet-substrate impact. The oil droplet spreading dynamics were modelled using partial wetting laws, with the empirical model proposed by Wang *et al.*(1) providing a method to compare the spreading dynamics of droplets in different conditions. Finally, the spreading dynamics of CH_3 and NH_2 PDMS oils on cellulose surfaces were examined. These surfaces were shown to be hydrophilic (water contact angle = 35 °) and while the CH_3-

terminated PDMS oil did not spread on the cellulose (as expected), neither did the NH_2-terminated PDMS oil. The latter is quite interesting since the NH_2-terminated PDMS oil was observed to spread on almost all surfaces independent of the surface wettability. The lack of droplet spreading was attributed to enhanced surface hydrophilicity due to increased surface roughness and layer hydration.

4.1 Introduction

As previously stated in Chapter 3 droplet spreading dynamics are of interest to many industries, however, these processes are not solely applicable to spreading in air and are seen in a range of two-liquid systems. Liquid-liquid systems are relevant to many industries and topics such as emulsification,(2-5) detergency,(6-8) microfluidics,(5, 9) oil recovery,(10, 11) etc. While the spreading of a liquid droplet in a liquid environment is of interest, less is understood about these systems in comparison to droplet spreading in air.(12-21) Relatively few studies have considered droplet spreading in another liquid medium,(13, 22-24) although in the last few years there has been an increased interest. One of the main reasons is that liquid-liquid systems are widely encountered,(13) and the complexity of wetting and spreading increases due to other factors such as thin film liquid drainage, miscibility, closely matched liquid viscosities and densities.(13)

It has been shown that one dominant parameter in liquid-liquid systems is the viscosity ratio of the two liquids.(25, 26) The viscosity ratio is defined as η_D/η_S with η_D and η_S the viscosity of the droplet and the surrounding medium respectively. For viscous droplets spreading in air the droplet spreads entirely in the viscous regime, i.e. for silicone oils this would correspond to an oil viscosity above 100 mPa·s or a viscosity ratio of 5500, below this viscosity ratio an inertial regime would also be observed.(24)

When the viscosity ratio is significantly large, the droplet spreading dynamics can be treated using the same principles of droplets spreading in air, i.e. droplets should abide by Tanner's law.(25, 26) However, as the viscosity ratio approaches 1 there are significant deviations from dependence, an enhancement of spreading rates due to contact line instabilities.(27) Silicone oils of high viscosity, 201, 485 and 1000 mPa·s, correspond to viscosity (second liquid being D_2O; 1.25 mPa·s) ratios of 161, 389, 802 respectively, hence inertial and viscous regimes of spreading are expected to be observed. However, unlike oil spreading in air where the droplet completely wets the surface, in water there will be a wider range of equilibrium contact angles as the oil droplets display partial spreading behaviour on the various surface.

For partial wetting, Seaver and Berg(18) introduced a correction factor to their complete wetting model, but as discussed in Chapter 2.2 the model was "unwieldy" and is not widely used. De Gennes(28) showed there are three methods of dissipation, i) viscous dissipation, ii) dissipation in the precursor film and iii) dissipation in the droplet close to the three phase contact line.(29) Precursor films are yet to be observed in the case of partial wetting systems (and under water systems),(26) the first method is therefore described by the hydrodynamic model (HD), and the third method of dissipation described by the molecular kinetic theory (MKT). These models can be used to fit the data of a partial wetting droplet with the HD and MKT models described by Eq. 4.1 and Eq. 4.2 respectively:

$$\frac{d\theta_d}{dt} = \frac{\theta_d}{3R\,ln\left(\varepsilon_\delta^{-1}\right)} sin\,\theta_d \left[2 - sin\left(\frac{\pi}{2} - \theta_d\right)\right] \frac{\gamma_{ow}}{\eta_D} \left(cos\,\theta_e - cos\,\theta_d\right) \qquad (4.1)^{(30)}$$

$$\frac{d\theta_d}{dt} = \frac{1}{R} sin\, \theta_d \left[2 - sin\left(\frac{\pi}{2} - \theta_d\right)\right] \frac{\gamma_{ow}}{\zeta} (cos\, \theta_e - cos\, \theta_d) \qquad (4.2)^{(31)}$$

where θ_d is the dynamic contact angle, θ_e is the equilibrium contact angle, γ_{ow} is the interfacial tension between the oil and water, η_D is the droplet viscosity, R is the diameter, ε_δ is the slip length to characteristic capillary length ratio and the fitting parameter for the HD model, and ζ is the friction coefficient which is used as a fitting parameter for the MK model. In addition, a partial wetting model that is described empirically is given by Lavi and Mamur *et al.*,$^{(32)}$ but further refined by Wang *et al.*,$^{(1)}$ as described in Eq. 4.3 and 4.4;

$$r = r_{eq}\left[1 - exp\left(-\frac{a}{r_{eq}} t^m\right)\right] \qquad (4.3)$$

$$ln\left[-r_{eq} ln\left(1 - \frac{r}{r_{eq}}\right)\right] = ln\, a + m ln\, t \qquad (4.4)$$

where r is the spreading radius, r_{eq} is the droplet spreading radius once equilibrium is reached, t is time, a and m are fitting parameters - where m is a function of the droplet spreading velocity.

Ruijter *et al.* suggested that partial wetting should be divided into three stages; an initial stage where $r(t) \sim r_0 + at$, an intermediate stage which follows Tanner's law $r(t) \sim t^{0.1}$, and a final stage $\Delta r(t) \sim exp(-t/T)$, where T is a constant.$^{(16)}$ Droplets spreading in water will have lower impact and reduced spreading velocities compared to in air, this is beneficial in that impacting droplets may not splash and the slower spreading dynamics means that the early spreading dynamics can be readily observed. However, the viscosity of the surrounding water medium can lead to the droplet being more susceptible to “cushioning” and is more likely to be affected by rebound and/or rolling. Also surface forces are likely to influence the induction time as governed by the drainage and rupture of the thin liquid film (TLF) separating the oil from the spreading substrate.(33)

In the current chapter the effects of surface wettability, oil viscosity, surface tension, surface roughness and oil polarizability will be explored for PDMS oil droplets spreading in water. Silanised silicon surfaces were used to investigate surface wettability effects on spreading dynamics and induction times, spin coating surfaces with cellulose were also used to investigate surface roughness and film hydration effects. CH_3-terminated PDMS oil of different molecular weight (viscosity) were used to study the influence of droplet viscosity, while a similar NH_2-terminated PDMS oil was used to study the influence of oil polarizability. Finally, interfacial tension effects were studied by the addition of a water soluble surfactant, (sodium dodecyl sulphate) SDS, to the continuous water phase.

4.2 Materials

The amino (NH_2) terminated polydimethylsiloxane (PDMS) and methyl (CH_3) terminated oils were the same as used in Chapter 3, with the structure of the two PDMS oils shown below in Figure 4.1. Silicon wafers, ethanol and ultrapure Milli-Q water were used throughout this study as outlined in Chapter 3. Various solvents were used including; methanol (HPLC, Sigma Aldrich), Tetrahydrofuran (AR, Fisher

Scientific), D_2O (99.8 % - Fisher Scientific) and chloroform (HPLC, Acros Organics), with all solvents used as received without further purification. Hydrogen peroxide solution (30%+, Sigma Aldrich, UK), sulfuric acid (95%, Fisher Scientific, UK), cellulose - microcrystalline powder (Sigma Aldrich), lithium chloride (>98%, Alfa Aesar), N, N-dimethylacetamide (VWR), hexamethyldisilazane (Fluorochem), HCl (37%, Merck Millipore) sodium dodecyl sulphate (>92.5 %, Sigma Aldrich, UK), and dichloromethyl-n-octylsilane (98%, Alfa Aesar) were used as received without further purification.

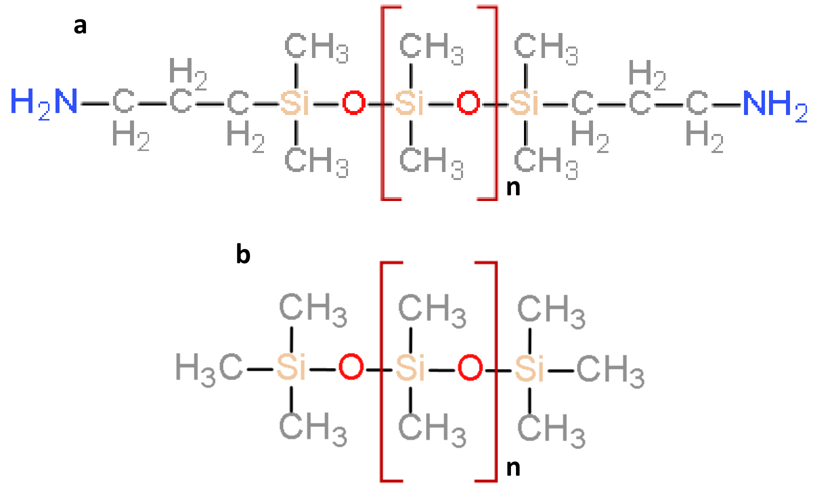

Figure 4.1. The molecular structure of a) NH_2*- and b)* CH_3*-terminated PDMS oils.*

4.3 Methods

4.3.1 Wafer preparation

Firstly, 9 g lithium chloride was dissolved overnight in 91 g N, N-dimethylacetamide at 80 °C, the solution was constantly stirred. 2 g of cellulose was then added and allowed to dissolve for 1 hour until the solution appeared white.(34) The solution was placed under a nitrogen atmosphere and heated to 150 °C and 20 mL hexamethyldisilazane added dropwise over a period of 2 hours, the solution became a light brown colour. The solution was then allowed to cool slowly to room temperature and then 40 mL methanol added to aid crystallization, this was left overnight. The solution was then filtered (filter diameter 90 mm, pore size 20-25 μm) which resulted in “toffee-like” globules as seen in Figure 4.2a with the residue then fully dissolved in 80 mL tetrahydrofuran which was then left overnight in 1 L methanol. This resulted in white crystals which then settled as seen in Figure 4.2b, the solution was filtered (filter diameter 90 mm, pore size 20-25 μm) and the residue washed with methanol and dried using a vacuum pump as shown in Figure 4.2c. Since cellulose swells and retains water, the residue was dried at 150 ^{o}C in a vacuum oven for 2 h. This is the trimethylsilyl-cellulose (TMSCellulose) and is shown in Figure 4.2d. 4.63 g of TMSCellulose was obtained. If complete conversion is assumed (each OH converted to $OSi(CH_3)_3$ – shown in Figure 4.3), that would correspond to a yield of 99 %. TMSCellulose was then dissolved in chloroform to a concentration of 15 g/L (Figure 4.2e).

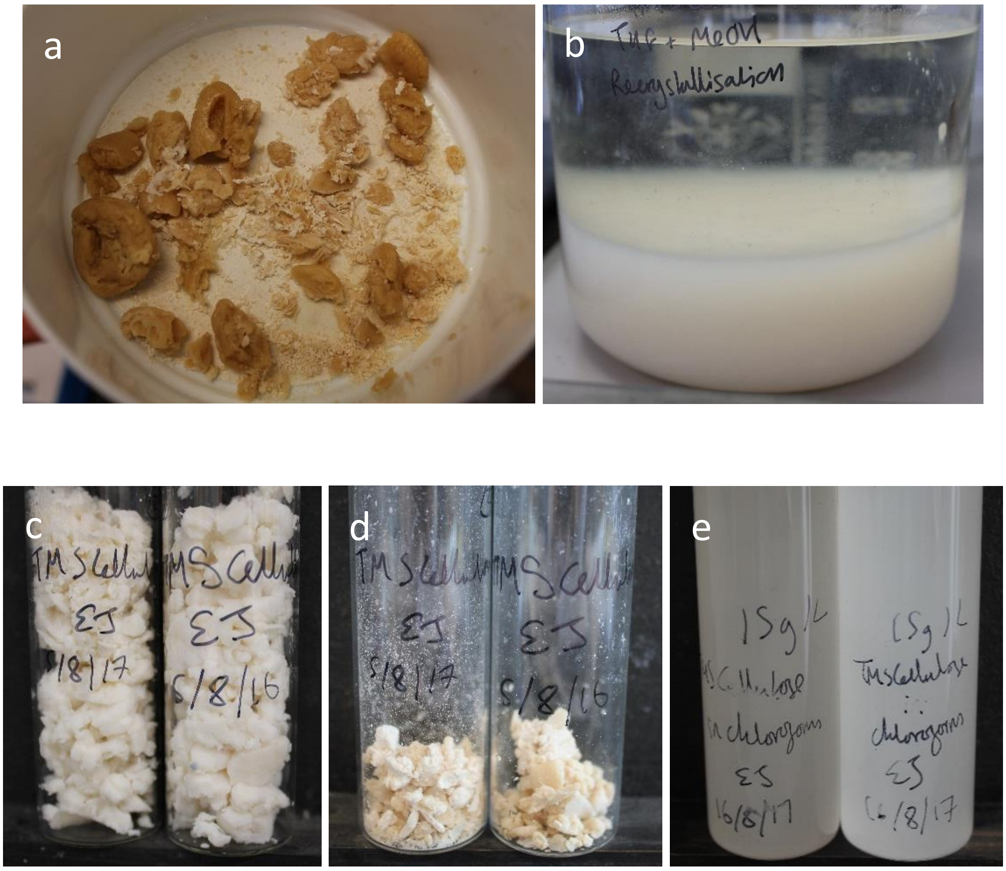

Figure 4.2. a) TMSCellulose globules after first filtration, b) sedimentation of the purer TMSCellulose in 1 L methanol, c) purified TMSCellulose after the second filtration, d) resulting TMSCellulose product after dehydration, e) 15 g/L TMSCellulose dissolved in chloroform.

Silicon wafers were soaked in a freshly prepared Piranha solution (1:2 Hydrogen peroxide: sulfuric acid) for 1 h, washed with Milli-Q water and dried with nitrogen before placing in a UV cleaner for 20 min, washed again with Milli-Q water and dried with nitrogen. The substrates were then spin coated at rates of 1000, 3000 and 6000 RPM. Approximately 1 mL of 15 g/L TMSCellulose in chloroform was slowly dripped onto the spinning wafer. The spin coated substrates were dried in a desiccator for 2 h with a beaker of 2 M HCl in the centre of the desiccator. Following the vapour phase acid hydrolysis, the wafers were cleaned with Milli-Q water and dried again in the vacuum oven. (35) A chemical scheme showing the conversion and reconversion is shown in Figure 4.3.(35)

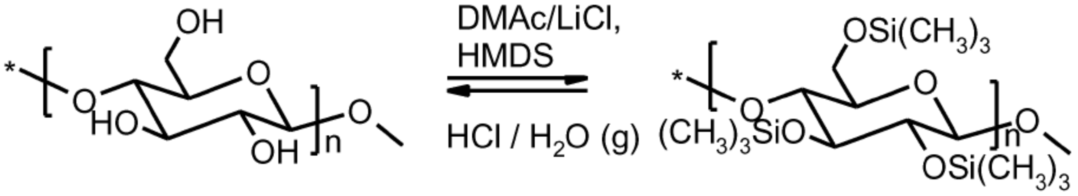

Figure 4.3. Scheme for the conversion of Cellulose to TMSCellulose and the reconversion step. (35)

To silanise the silicon wafers, the wafers were cleaned following the same procedure described above, then left in a desiccator with 1 mL of Dichloromethyl-n-octylsilane for a specific period of time, and finally washed with Milli-Q water before drying with nitrogen gas. The varying surface wettability (hydrophobicity) was measured by placing a Milli-Q water droplet on the wafer in air and measuring the contact angle using the pendant drop analyser. Surfaces with a water contact angle of ~0^o were freshly cleaned silicon wafers (no silanisation treatment) and measured contact angles < 3^o (the experimental limitation).

4.3.2 Wafer characterisation

Surface structure of the cellulose wafers was investigated by atomic force microscopy (AFM) (FastScan, Bruker, USA). Firstly the roughness (RMS) was measured in air and water, where the wafers were placed in water for 24 h before measuring the surface structure in water, to ensure the swelling (hydration) of the film had reached equilibrium. RMS roughness is given by Eq. 4.5.

$$RMS = \sqrt{\sum_{n=1}^{N} \frac{(Z_n - \check{Z})^2}{N}} \tag{4.5}$$

where Z_n is the height at point n, N is the number of points and $\check{Z}$ is the average height. The thickness of the film was also measured. A sharp clean scalpel was gently drawn across the wafer removing only the cellulose layer, such as that shown in Figure 4.4. The AFM was then used to measure the step-height of the cellulose layer in comparison to the smooth wafer. The scalpel was used to cut the cellulose film before hydrating in water. All film thicknesses were corrected to the depth calibration; using a 100 nm grating a value of 98.71 nm was recorded (within specifications), and cellulose thicknesses adjusted accordingly.

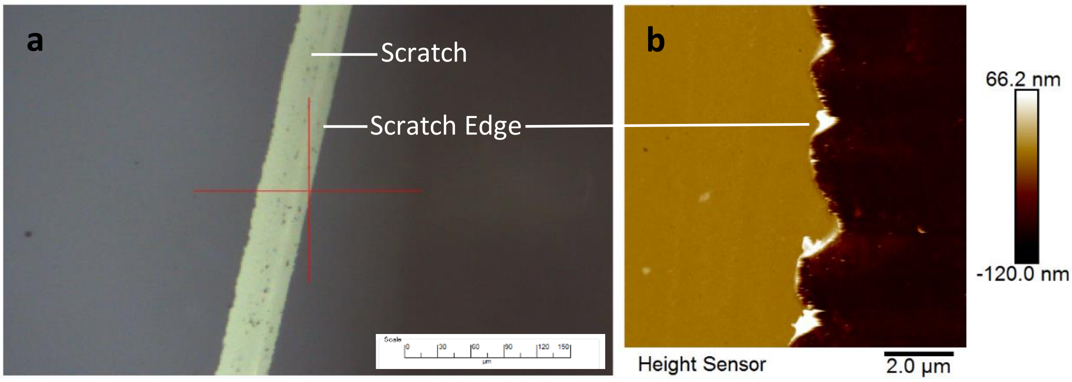

Figure 4.4. An image of the scratch on the cellulose surface viewed through a) the AFM camera and b) from the AFM measurement.

In order to study the effects of surface wettability (hydrophobicity) on the spreading dynamics of oil-in-water, an effective and reproducible method to change the surface hydrophobicity was needed. Using dichloromethyl-n-octylsilane, the hydrophobicity of the silicon wafers was changed by adjusting the amount of time the silicon wafers were exposed to the solvent vapour in the desiccator – i.e. vapour deposition (silanisation). The hydrophobicity of the cellulose-prepared, clean and silanised-prepared wafers were all measured using the pendant drop technique (Theta T200, Biolin Scientific, Sweden). A droplet of water was formed at the end of a 22 G stainless steel needle and allowed to deposit onto the surface forming a sessile droplet. Using the pendant drop software the contact angle of the droplet was then recorded at 2 FPS.

4.3.3 PDMS characterisation

The PDMS oil-water interfacial tensions were measured using a KSV pendant drop tensiometer (Cam 200, UK). A 2 cm by 1 cm quartz cuvette filled with D_2O and various sodium dodecyl sulphate (SDS) concentrations of 0, 0.05, 0.25, 0.45, 0.65 and 0.86 g/L were considered. The PDMS oil was placed in a gas-tight syringe connected to a hooked needle (22 G stainless steel needle). The oil was dispensed from the needle and the droplet volume increased to the maximum attached volume. This volume slightly varied due to the terminating group of the PDMS oil, viscosity and SDS concentration. The droplets were formed slowly and recorded at a rate of 2 FPS. Data from three repeat measurements is presented (averaged). Experiments were conducted at a temperature of 20^{o}C.

The solubility of the different viscosity oils (NH_2- and CH_3-terminated PDMS oils) was also investigated. 100 mL of D_2O was shaken for 2 min with 100 mL of PDMS oil in a 500 mL separating funnel. The solution was then left for 24 h, after which an aliquot of the less dense water phase was taken and the surface tension measured. Any deviation from the surface tension of water (72.8 mN/m) was attributed to the PDMS oil dissolving into the water phase and reducing the water surface tension.

4.3.4 Oil droplet spreading in water

The dynamic contact angle, droplet height and spreading diameter of PDMS oils spreading in D_2O was studied using the pendant drop tensiometer (Theta T200, Biolin Scientific, Sweden). It is conventional to provide the water contact angle, hence for an oil droplet spreading in water the water contact angle is 180-θ. However, it should be emphasized that in the current study the reported contact angle for an oil droplet spreading in water is the contact angle of oil and not water as shown in Figure 4.5. This allows comparison with the spreading contact angles measured in air (Chapter 3).

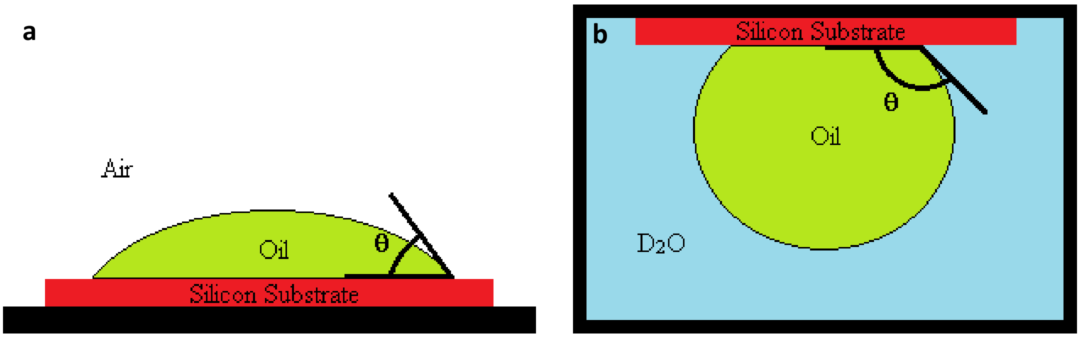

Figure 4.5. Schematic of the measured contact angle of a droplet a) in air and b) under water.

The experimental set-up for oil droplets spreading in water is shown in Figure 4.6. However, as the oil-in-water apparatus is unique to this project Appendix A.1 provides more details on the design and optimisation of these experiments. A droplet of maximum size was formed at the tip of a 27 G stainless steel needle. The droplet was approximately 1.5 mm from the spreading substrate to ensure the droplet fully detached from the needle, but minimized the impact velocity. The surface itself was inverted and held in place by two screws. The image capture software was triggered before droplet detachment from the needle. Once the droplet had reached the maximum volume it would detach (governed by the buoyancy force) and rise towards the surface. After an induction time the oil droplet would then spread on the surface. Since the initial droplet spreading was still fast (~ 4 mm/s), and in order to calculate an apparent induction time, the droplet was recorded at a rate of 200 FPS for 60 s and then recorded at 0.2 FPS for a further 1 h. The maximum oil droplet size at needle detachment did vary due to differences in oil viscosity, oil terminating group and surfactant concentration.

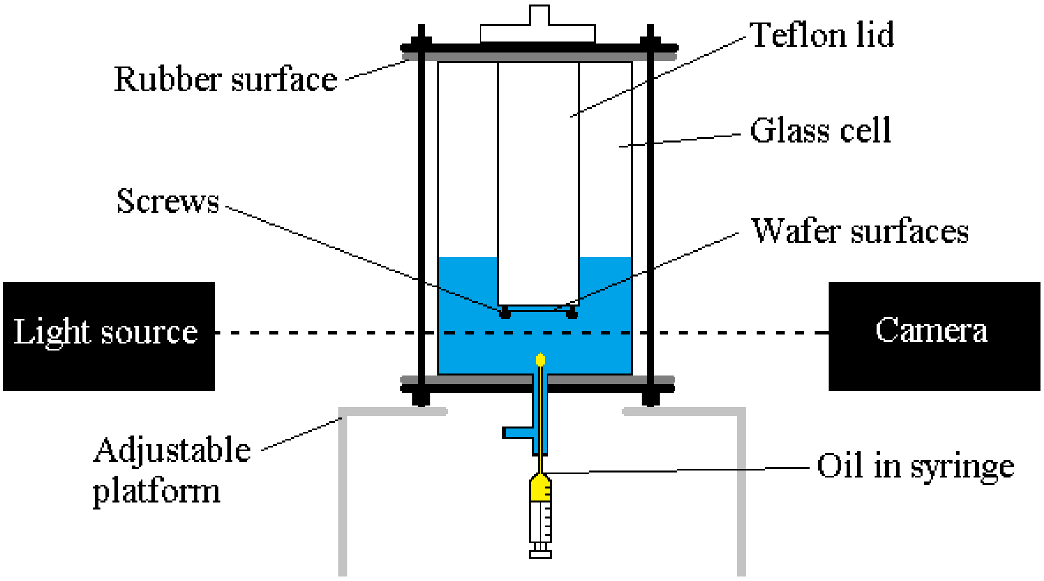

Figure 4.6. Set-up of the oil-in-water apparatus.

Precise reproducibility was difficult to achieve due to droplets impacting the substrate at different times (following triggering the software to capture the images), as can be seen in Figure 4.7a. There is also some variability associated with droplet induction time as shown in Figure 4.7b. Figure 4.7c shows the data from Figure 4.7b but represented in terms of the contact angle rather than the droplet radius. The onset of droplet spreading cannot be clearly identified, thus it is extremely difficult to accurately select $t = 0$ (onset of wetting). Also, for each experiment this may result in a different spreading diameter and contact angle, again increasing the difficulty to analyse and average the spreading dynamics of multiple droplets. As such, our approach was to set a condition for $t = 0$ which was specified when the droplet first reached a contact angle of 150^o. The contact angle 150^o was deemed suitable for all experimental systems. It was important that all droplets were analysed using the same method to enable comparisons of different assessed parameters. The apparent induction time was therefore determined from the first point of oil droplet – substrate contact (visual assessment) until the time it took for the droplet to attain a spreading contact angle of 150^o. When the droplet reached 150^o, the droplet spreading diameter at this point was recorded as the first diameter at $t = 0$ and the spreading dynamics compared from this point onwards. This method provided a means to compare data sets as shown in Figure 4.7d.

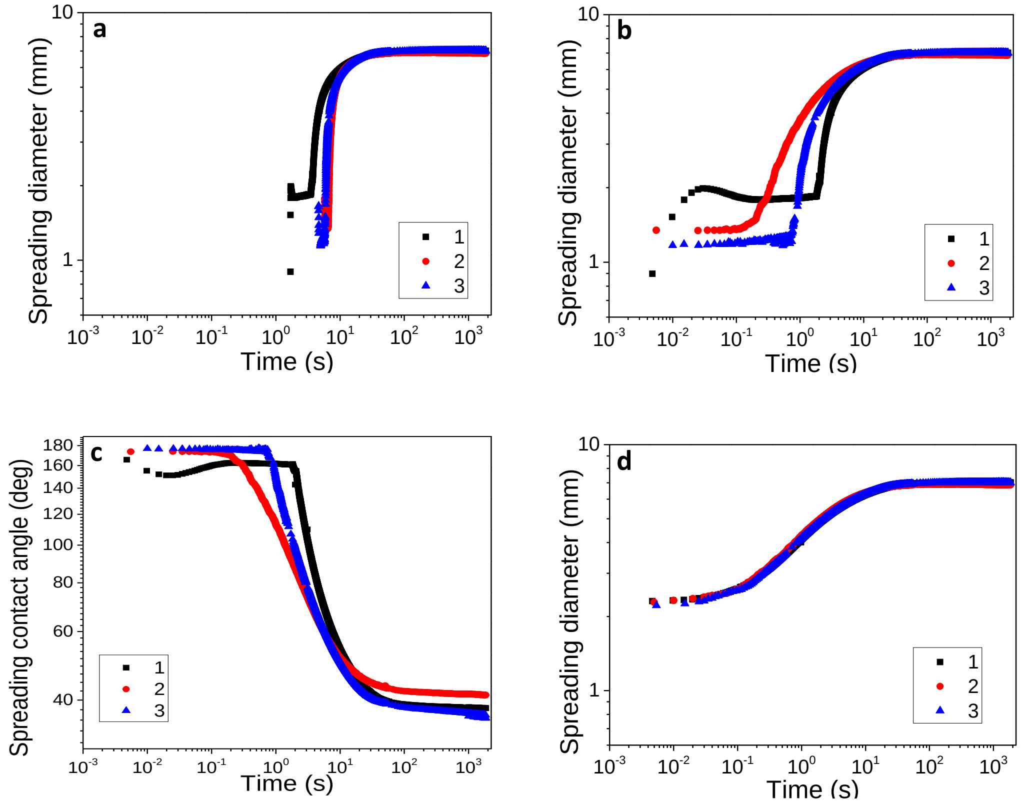

Figure 4.7.a) Raw data for 3 droplets spreading on a wafer (hydrophobicity 100^o), b) Same data corrected by the droplet impact set as t = 0 s, c) same data but with the contact angle shown as a function of time, d) Diameter data with t = 0 s set when the droplet contact angles is 150^o.

As can be seen from Figure 4.7a *and* b, both the first point of contact and the start of droplet spreading (following the real induction time) causes the data to appear unreproducible and cannot be easily analysed. By selecting 150° as the apparent induction time and setting $t = 0$ for the "start" of oil droplet spreading better aligns the data which then can be averaged for further analysis. The apparent induction time (t_i) is therefore calculated by Eq. 4.6 where t_c is the time of first contact (visual) and t_{150} is the time when the droplet contact angle reached 150°.

$$t_i = t_{150} - t_c \tag{4.6}$$

A 1000 mPa·s PDMS oil droplet spreading on a surface with a water contact angle of 100° is shown in Figure 4.8, with a visual representation of the initial droplet-substrate contact (Figure 4.8 b) and *t_{150}* (Figure 4.8 d)being shown.

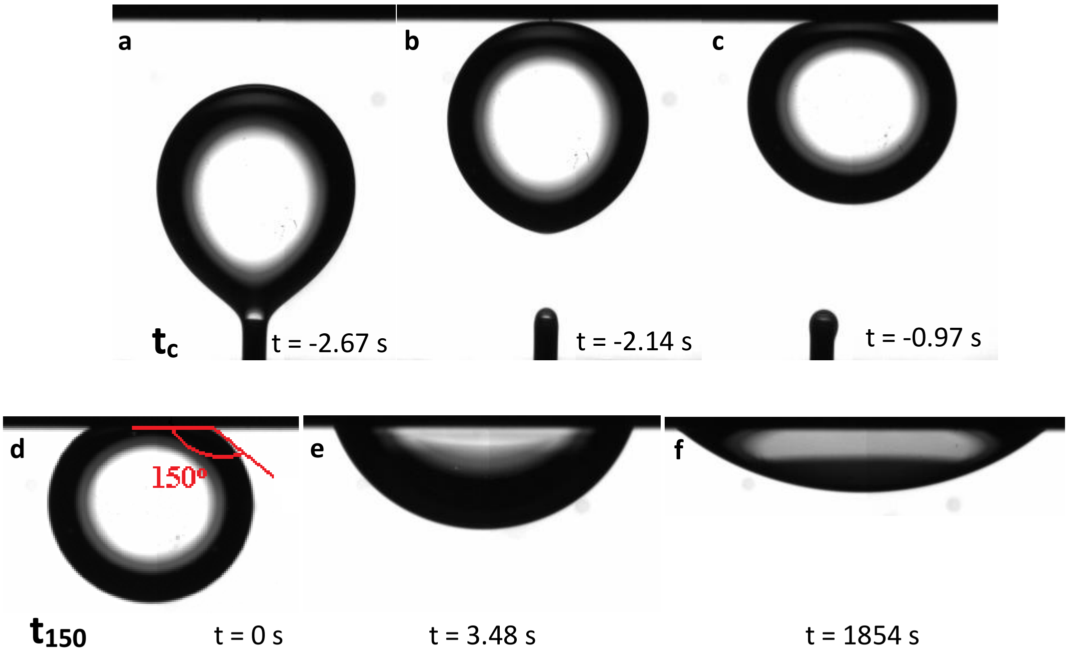

Figure 4.8. A 1000 mPa·s droplet spreading on a surface with a water contact angle of 100°, with a visual representation of t_c (visual droplet-substrate contact) and t_{150} a) the droplet reaches maximum size and detaches from the needle, b) the droplet first comes into contact at t_c and is fully detached from the needle, c) the droplet at rest at the surface during the induction time, d) the droplet has begun spreading and reached 150° (t_{150}), e) the droplet is now within the spreading period, f) the droplet has reached an equilibrium wetted state.

Although the apparent induction time may be influenced by the spreading rate (surfactant and viscosity effects – see below), such an approach was seen as a reasonable compromise since the real induction time could not be measured. The contact angle of 150° has been selected as it is a compromise between maximising the number of data points to be analysed (spreading dynamics), as well as ensuring the droplet is spreading and not just resting on the substrate. Droplets on all surfaces have been treated the same way to ensure comparisons can be made.

4.3.5 Droplet dewetting (preliminary investigation)

Dewetting of NH_2- and CH_3-terminated droplets that were first spread on silicon wafers in air, resulting in thin films (approaching the condition of complete wetting), were then dewet by injecting water into the measurement cell and measuring the receding contact angle as a function of time.

4.4 Results and Discussion

4.4.1 Surface characterisation

In order to study the effects of surface wettability (hydrophobicity) on the spreading dynamics of oil-in-water, an effective and reproducible method to change the surface wettability was needed. The wettability of the silicon wafers can be changed by altering the silanisation time. The average water contact angles for the various silanisation times are shown in Figure 4.9.

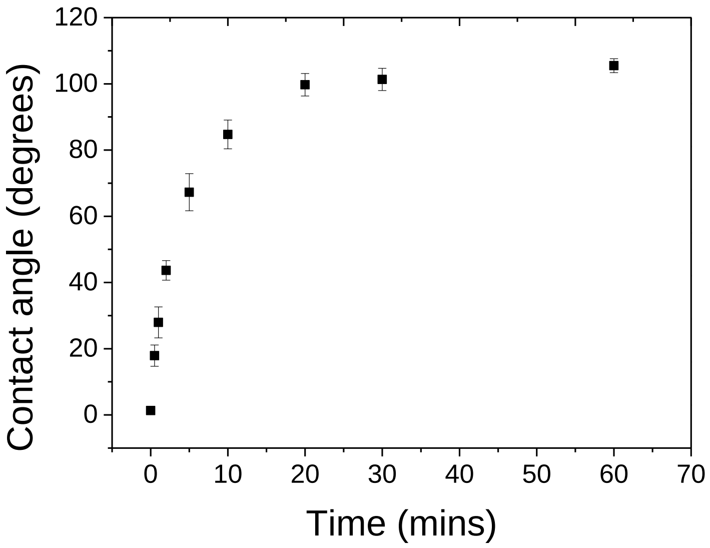

Figure 4.9. Milli-Q water contact angle on the silicon substrate after undergoing vapour deposition silanisation as a function of time.

Figure 4.9 shows a gradual increase in the water contact angle, or surface hydrophobicity, with increasing time of silanisation. This method does have challenges; the contact angle is very sensitive to the silanisation time with just a few seconds leading to a variation of approximately ± 5°. Also, vapour deposition results from the volatility of the silane compound, hence changes in the lab temperature may influence the vapour deposition rates. To improve accuracy, the experiments were conducted when the lab temperature was 23°C, and only wafers with the desired contact (within error see below) were considered for the spreading experiments. For the study, 4 different contact angles: 0° (un-silanised), 30°, 65°, 100° were considered. To ensure that the silanised silicon surfaces were consistent, only surfaces with a contact angle in the following ranges were considered 28 – 32°, 62 - 67° and 97 -102°.

To verify the successful completion of the spin coating and acid hydrolysis steps, the water contact angle on the modified surfaces was used to demonstrate the sequential changes in surface properties. Contact angle measurements were taken after cleaning the wafers (1), after spin coating on the TMSCellulose (2), after vapour acid hydrolysis (3) and after hydrating in water for 24 h (4), with the results shown in Figure 4.10.

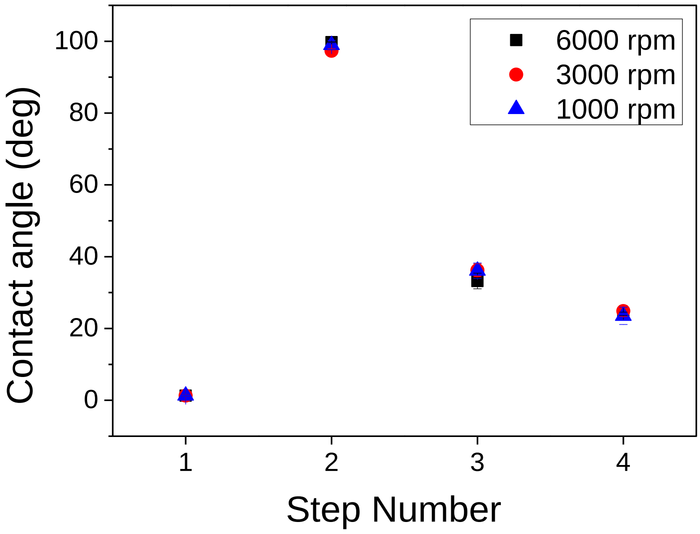

Figure 4.10. Milli-Q water contact angles on silicon substrates after various steps; 1) cleaned silicon wafer, 2) spin coated with TMSCellulose, 3) acid hydrolysis and 4) hydrated with water. Three different spin speeds 6000, 3000 and 1000 rpm are shown.

As shown in Figure 4.10, there are significant differences between each preparation step. For Step 1, cleaning the silicon substrates, it was difficult to measure accurate contact angles below 3° due to experimental limitations. Before cleaning, the silicon substrates had a contact angle of approximately 20°, after cleaning the contact angle was below 3°. The highest contact angle ~100° resulted from modification when TMSCellulose was spin coated onto the wafers. The high contact angle confirmed that a high substitution had been achieved, compared to literature data for TMSCellulose of approximately 80°.(36) Following vapour acid hydrolysis (Step 3) there was a significant decrease in contact angle to approximately 35°. This is comparable to literature which confirms the contact of cellulose to be in the region of 30°, but varies from approximately 15° to 45°.(37-40) This variation can be influenced by humidity,(37, 38) the cellulose source,(39, 40) the crystallinity of cellulose,(40) film thickness and roughness(40), and the measurement time (due to the cellulose adsorbing water)(37, 39). Step 4 was the resulting contact angle after the cellulose surfaces had been left for 24 h to fully hydrate in Milli-Q water. There was a small decrease in the contact angle as water absorbed into the cellulose layer creating a more hydrophilic surface.

The deposited cellulose surfaces were also analysed by AFM. The calibration for the AFM height measurements are discussed in Section 4.3.2. The AFM was used to measure the roughness of the cellulose layers (RMS roughness), and the thickness of the cellulose layers. The deposited surfaces were measured both in air and water, with the cellulose surfaces swelling in water. The FastScan AFM was utilized to minimize any time-dependent variation when the cellulose surfaces were submerged in an aqueous environment. The AFM images of the three different cellulose surfaces and the clean silicon surface are shown in Figure 4.11a-d, along with corresponding RMS values shown in Table 4.1.

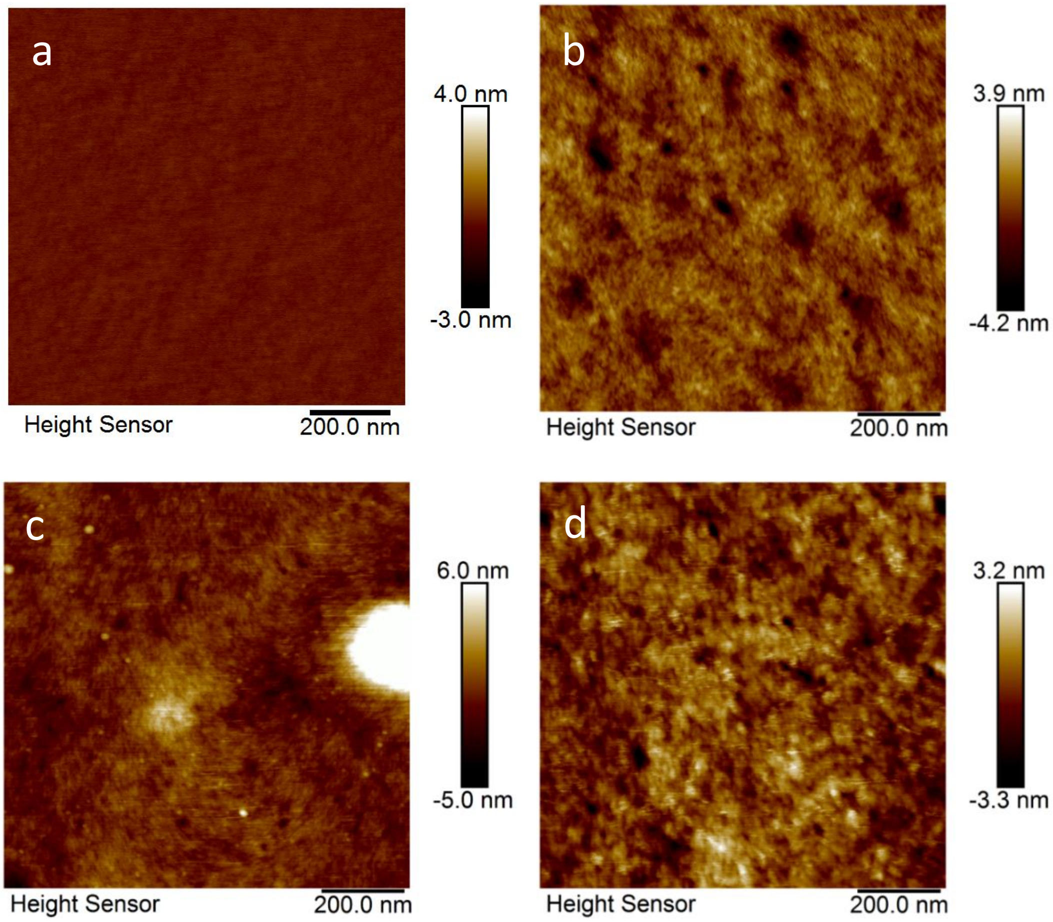

Figure 4.11. a) Clean silicon wafer, b) 6000 rpm cellulose surface, c) 3000 rpm cellulose surface, d) 1000 rpm cellulose surface in air.

Table 4.1. The RMS values and deposited cellulose thickness in both wet and dry environments.

Surface	**RMS (dry) (nm)**	**RMS (wet) (nm)**	**Thickness (dry) (nm)**	**Thickness (wet) (nm)**
Silicon surface	0.09	-	-	-
6000 rpm cellulose	0.55	1.46	84.9	97.3
3000 rpm cellulose	0.63	1.14	119.9	123.9
1000 rpm cellulose	0.60	1.63	179.4	202.6

As shown, the pure silicon surface exhibits a low root mean square (RMS) value and is comparable to literature values.(41, 42) Following spin coating of the silicon surface with TMSCellulose, it is readily observed that the substrate changes colour as shown in Figure 4.12. The 1000 rpm coated surface is a light blue, whereas the 3000 rpm appears as a darker blue/purple, and the 6000 rpm surface a deep blue/black. This difference likely results from changes in the thickness of the TMSCellulose at the three different spin speeds, with the thickness of the cellulose layer influenced by three main factors; the solvent used, the TMSCellulose concentration and the spin speed,(35, 43, 44) other factors such as temperature and humidity were constant. The colour of the deposited layer changed again following the vapour acid hydrolysis of the TMSCellulose, shown in Figure 4.12. All wafers (1000, 3000 and 6000 rpm) showed a darkening in colour which again can be associated to a change in the cellulose layer thickness. There has been previous research into the sequential steps as described by Konturri *et al.*, and the authors showed that the acid hydrolysis step leads to a reduction in the cellulose layer thickness by approximately 60 %.(45, 46) TMSCellulose has large silane groups inhibiting the tight packing of the molecule. Removing the large silane groups allows the layer to compress and pack more densely.(47) Removal of the silane group by hydrolysis produces hexamethyldisiloxane as a side-product , which is able to diffuse through the film and be removed due to its volatility.(47)

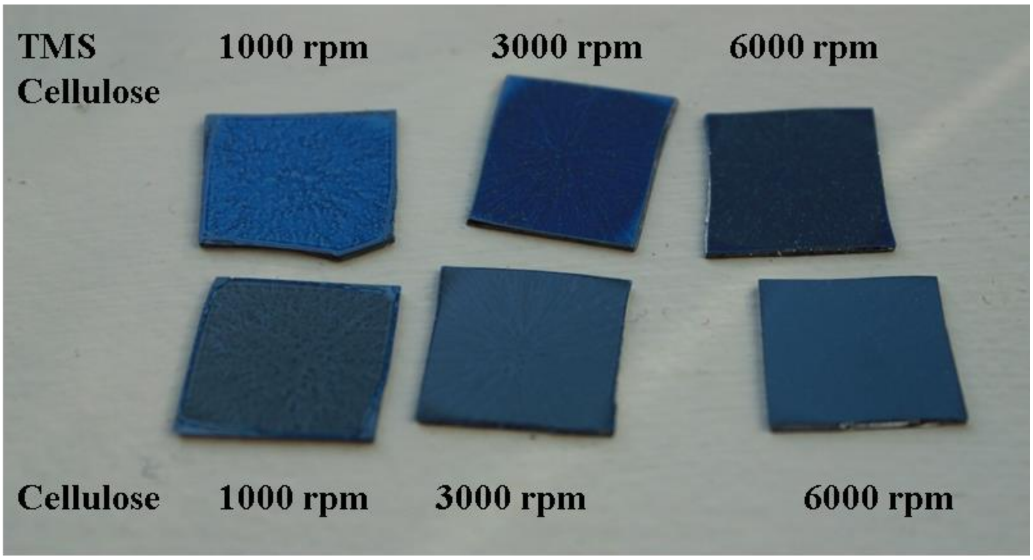

Figure 4.12. TMSCellulose samples spin coated at 1000, 3000 and 6000 rpm, and cellulose samples coated at 1000, 3000 and 6000 rpm after being hydrolysed.

Previous research suggested the use of toluene as a solvent could produce flatter surfaces, due to the lower volatility, producing thin surfaces of cellulose in the range of 20 – 40 nm.(35, 45, 48) However, the main objective of the current study was to produce thicker films that could swell and to ensure that the underlying substrate (silicon wafer) had no influence on the surface property, and so chloroform was used as the solvent. From the AFM data it can be seen that the RMS values for the cellulose surfaces were approximately six times larger than the pure silicon surface, but comparatively smaller (approximately 1 – 2 %) than the overall thickness of the deposited film.

The deposited surfaces were allowed to hydrate in Milli-Q water for 24 h to fully saturate the cellulose film. Similar AFM studies were conducted to measure the film thickness and roughness in an environment equivalent to those used in the droplet spreading studies. Figure 4.13 shows the AFM images with the corresponding film thickness and roughness values reported in Table 4.1.

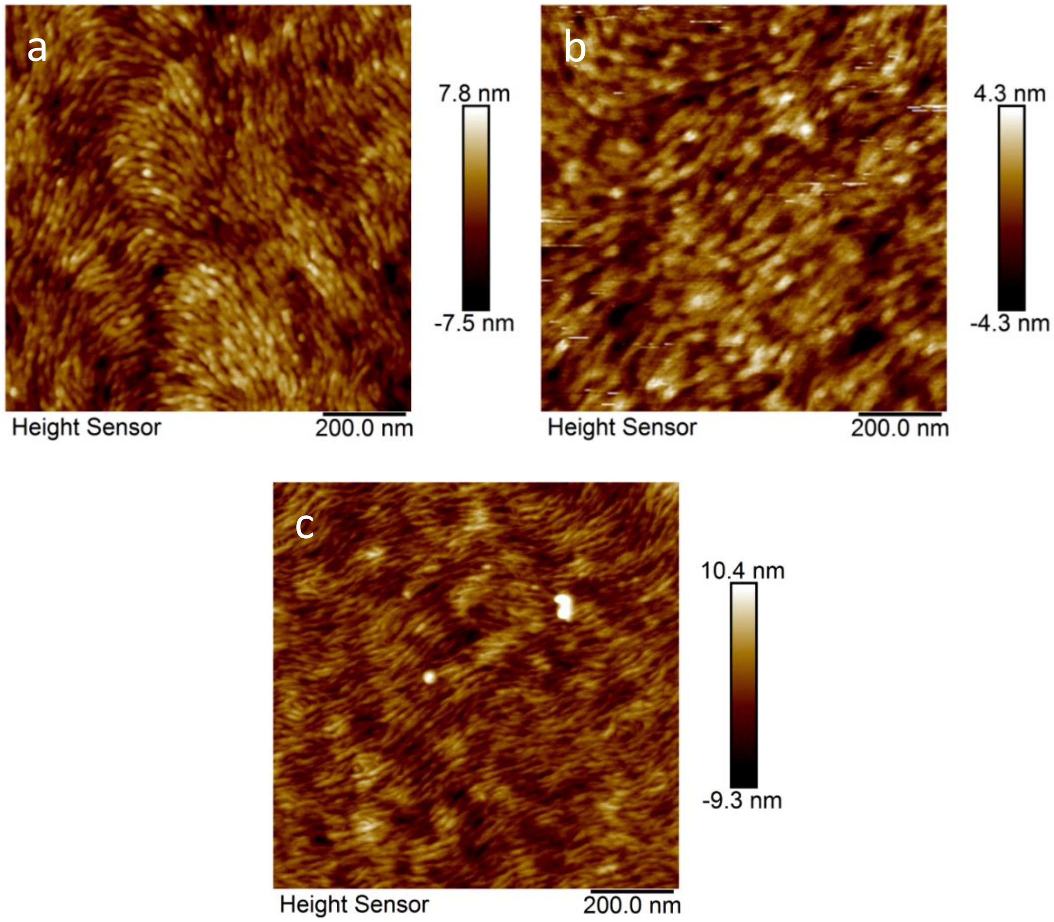

Figure 4.13. a) 6000 rpm, b) 3000 rpm, c) 1000 rpm deposited cellulose surfaces after hydration in Milli-Q water for 24 hours.

Comparing Figure 4.13 and Figure 4.11 it can be seen that the cellulose films appear more structured with the micro-fibrils easily observed due to their swelling in water. The swelling also leads to an increase in the film thickness, particularly for the 1000 and 6000 rpm deposited films. These films show an RMS increase of nearly 3 times compared to the dry films, whereas the 3000 rpm film has an increase of approximately 2 times. The 3000 rpm would be expected to show an increase in both thickness and RMS similar to that of the 1000 and 6000 rpm, with this slight deviation in behaviour most likely attributed to an inconsistency in the methodology. It should be noted that different surfaces were used to measure the RMS and film thickness values in both the dry and wet states. Experiments were later conducted using the 1000 rpm deposited film as it exhibited the largest film thickness.

4.4.2 Fluid characterisation

One of the parameters to be considered in this study was the interfacial tension effect on droplet spreading. Numerous studies on the spreading dynamics of droplets with surfactants have been reported,(49-52) however there are few studies which have added the surfactant to the bulk fluid (not the spreading droplet). It is known that increasing the surfactant concentration in the bulk fluid reduces the interfacial tension.(53) The interfacial tension of water-PDMS oils of varying viscosity and terminating groups as a function of the SDS concentration are shown in Figure 4.14.

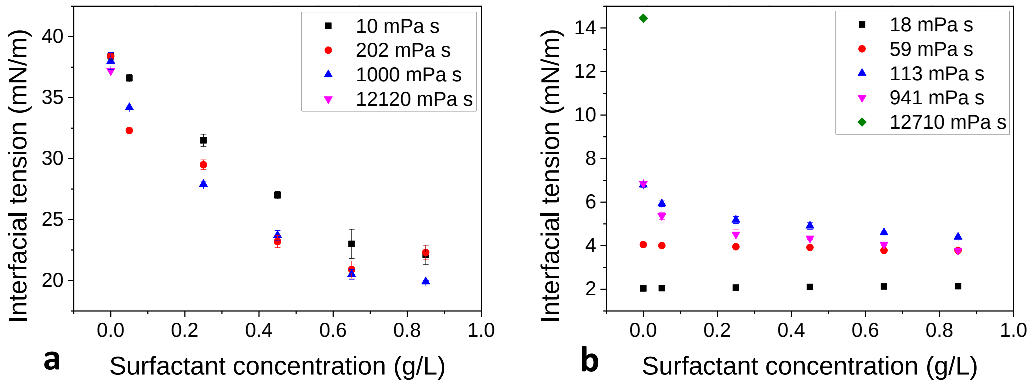

Figure 4.14. a) Interfacial tension of CH_3-terminated PDMS oils of varying viscosity in different SDS concentrations, the interfacial tension at the CMC 2.4 g/L is 5.4 mN/m, b) Interfacial tensions of NH_2-terminated PDMS oils of varying viscosity in different SDS concentrations.

The surface tensions of the PDMS oils were all very similar in the range of 21 mN/m, shown in Section 2.2. However, the interfacial tensions of the NH_2- and CH_3-terminated PDMS oils varied significantly in D_2O. Without addition of SDS, the CH_3-terminated PDMS oils exhibited an interfacial tension in the region of 38 mN/m, whereas the NH_2-terminated PDMS oils exhibited significantly lower interfacial tensions, with the interfacial tension dependent on the oil viscosity. The difference between the two oils results from the polarity of the oil. CH_3-terminated PDMS is non-polar, thus the interaction with the polar D_2O water molecules is negligible. However, the NH_2-terminated PDMS is polar and will favourably interact with D_2O, with hydrogen bonding between the NH_2 and OD groups. When varying the oil viscosity the chain length of the PDMS varies accordingly, meaning there is a higher percentage of surface NH_2 groups in NH_2-terminated PDMS oils of lower viscosity. A higher surface density of NH_2 groups results in a decreasing interfacial tension, with the 18 mPa·s NH_2-terminated oil showing an extremely low interfacial tension (2 mN/m) even in the absence SDS addition.

For most oils, increasing the SDS concentration leads to a gradual decrease in interfacial tension. Certainly the CH_3-terminated PDMS oil behaved conventionally, with a gradual decrease in interfacial tension with increasing SDS concentration. Such behaviour was less observed for the NH_2-terminated oil due to the extremely low and variable interfacial tensions as a function of the oil viscosity. The low interfacial tensions resulted in the oil streaming from the needle rather than forming a droplet. Such behaviour would limit the use of NH_2-terminated oils in further studies. Also, it is worth noting that the NH_2-terminated PDMS oil droplets produced solutions that appeared cloudy, with the droplet exhibiting diffuse trails as seen in Figure 4.15. These diffuse trails were also more vivid with increasing SDS concentrations.

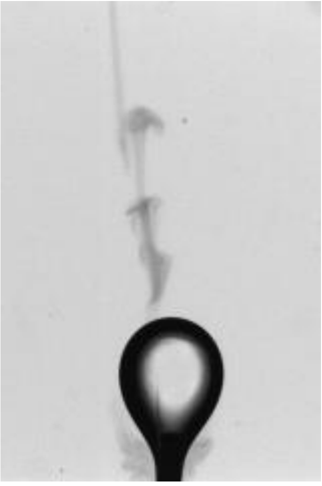

Figure 4.15. Picture of 18 mPa s NH_2-terminated PDMS oil in 0.25 g/L SDS in D_2O with 'diffuse' trails.

These diffuse trails only occurred for the NH_2-terminated PDMS oil and were more prominent at lower viscosities. It was hypothesised that the NH_2-terminated PDMS oil was partially miscible with the D_2O, the NH_2 group increasing the solubility of the PDMS in water.(54, 55) This would affect any droplet spreading dynamics experiments as the PDMS oil would solubilise in water, potentially pre-coating the spreading surface. In order to investigate whether the PDMS was soluble, a series of tests were conducted for all PDMS oils and the results shown in Figure 4.16.

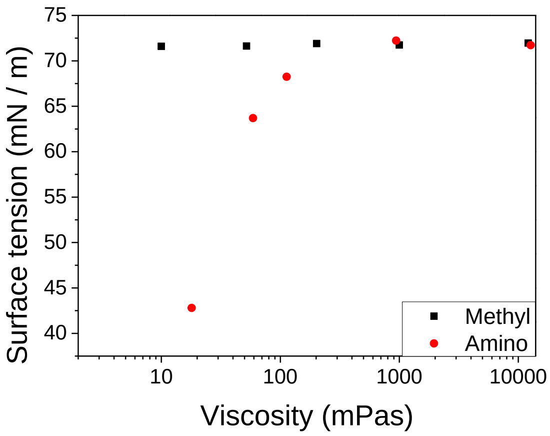

Figure 4.16. The surface tension of water after leaving in contact with the oils (NH_2-and CH_3-terminated of varying viscosity) for 24 hours.

As can be seen in Figure 4.16, the surface tension of pure water was approximately 72.5 mN/m. For the CH_3-terminated oils it was shown that the surface tension does not change (remains in the region of 72-73 mN/m), thus the oil and water can be considered completely immiscible. However, for the NH_2-terminated PDMS oil, the water surface tension varies and was shown to be a function of the oil viscosity, thus the oil can be considered partially miscible with water. For the lowest viscosity oil (18 mPa·s) the surface tension decreased by ~ 30 mN/m, with the magnitude of the decrease diminishing for higher viscosity oils. For 113 mPa·s the decrease was 5 mN/m, and for 941 mPa·s and higher there was no measurable change in surface tension. Again this effect is believed to be due to the polar NH_2 group. As the PDMS chain length increases (with increasing *n* in Figure 4.1), the viscosity also increases. The ratio of CH_3 groups along the PDMS backbone to the terminating NH_2 group increases with increasing viscosity and so the non-polar effect of the CH_3 groups decreases the solubility of the PDMS oil.

4.4.3 Oil droplet spreading dynamics in water

4.4.3.1 Effect of surface wettability

The effect of surface wettability (hydrophobicity) on the droplet spreading dynamics and the maximum droplet spreading diameter was studied using silicon wafers that were clean (0°) and silanised to increase the surface hydrophobicity: 30°, 65°, and 100°. These contact angles were obtained by measuring the contact angle of a water droplet at rest on the solid substrate in air, the resulting values were used as a reference name to identify the surface wettability. Ensuring that the spreading surfaces were flat (minimal roughness) was essential to clearly elucidate the effect of surface wettability. From literature it has been shown that oil droplets will spread more on hydrophobic surfaces,(56, 57) although there is little data on the dynamics of oil droplets spreading on such surfaces. The average spreading dynamics of three droplets per surface are shown in Figure 4.17.

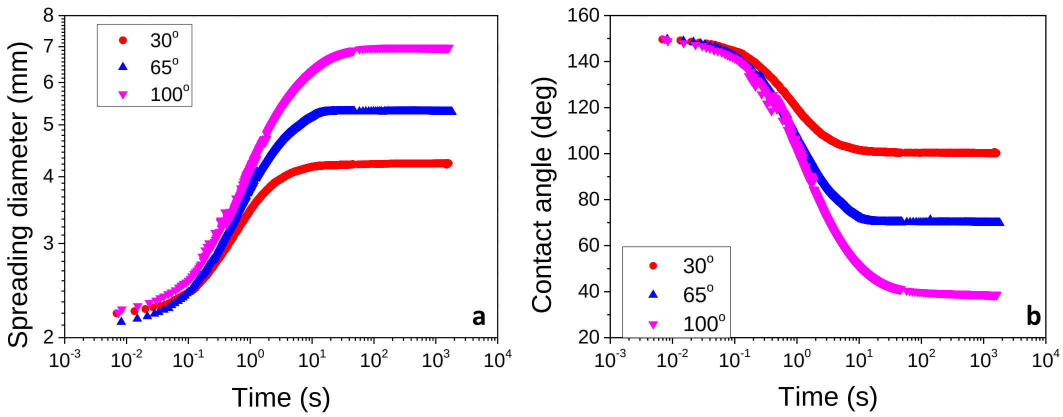

Figure 4.17. Averaged droplet spreading dynamics of 1000 mPa·s CH_3*-terminated PDMS on silicon wafers of different surface wettability – water-in-air contact angles; 30, 65 and 100°, a) droplet spreading diameter and b) droplet spreading contact angle.*

As previously discussed, to enable direct comparison of droplets spreading the conditions for the apparent induction time and the start of droplet spreading was set to a contact angle of 150°. CH_3-terminated PDMS oil droplets on 0° wetting surfaces did not reach the critical criteria of 150°, therefore no spreading data is reported in Figure 4.17. As can be seen in Figure 4.18, following 1 h undisturbed rest on the substrate, the 1000 mPa·s PDMS oil droplet on the 0° surface exhibited a very high contact angle of ~165°. As such, it is difficult to confirm whether or not the droplet had slightly wetted the surface, or the slight droplet deformation resulted from the buoyancy force acting on the droplet. However, clear evidence to confirm that the droplet did not wet the surface was shown by the droplet mobility following the 1 h undisturbed rest on the substrate, with the droplet able to roll when the surface was slightly tilted. Hence, the omission of this data from Figure 4.17 is correct.

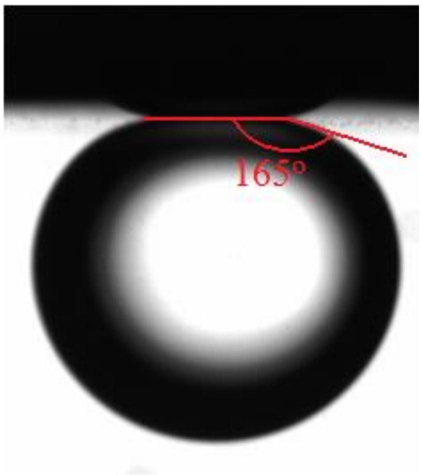

Figure 4.18. 1000 mPa·s CH_3-terminated droplets at rest on a silicon surface with a contact angle ~ 0°. This images were taken after 1 hour and confirm the non-wetting behaviour.

As shown in Figure 4.17, droplets spreading on the three surfaces of increased hydrophobicity reached an equilibrium contact angle within the hour. The extent of spreading was indicative of the surface wettability. The more hydrophobic the surface, the more the PDMS oil droplet spreads, which is due to the favourable intermolecular interactions. Since water is polar and the CH_3-terminated PDMS oil non-polar, a silicon surface that is very hydrophilic (0^{o}) is extremely favourable to water wetting but not oil wetting. As such, the droplet cannot overcome the disjoining pressure force that retains a thin-liquid layer of water between the oil and spreading substrate. The disjoining pressure is a force which acts between the surfaces, with the disjoining pressure (Π) given by the summation of van der Waals (Π_{vw}), and electrostatic forces (Π_{el}) in the form of Eq. 4.7(58);

$$\Pi(h) = \Pi_{vw} + \Pi_{el} \qquad (4.7)$$

In addition, many other forces can contribute to the disjoining pressure, such as steric, hydrophobic and gravitational forces, which are often considered to be summative terms. However, following silanisation the surfaces become more non-polar and hence more favourable for the non-polar PDMS oils to spread, with the degree of surface polarization reflecting the degree of droplet spreading. Such behaviour is quantitatively evidenced by the equilibrium contact angles of the droplet on the surface, with values shown in Table 4.2. A decrease in equilibrium PDMS contact angle with increasing hydrophobicity is readily observed.

Table 4.2. The average induction time and equilibrium contact angles for CH_3-terminated PDMS oil on surfaces of varying wettability. m and a represent the fitting parameters of the Wang et al.(1) model.

Contact angle in air (°)	**Induction time (s)**	**Equilibrium contact angle (°)**	***m***	***a***
0	> 60	165 ± 5.1	-	-
30	2.68 ± 0.46	99.6 ± 1.3	0.37	7.56
65	2.21 ± 0.25	69.8 ± 2.2	0.38	6.90
100	1.68 ±0.25	38.7 ± 2.4	0.39	6.33

Since the oil viscosity remains constant, the apparent influence of surface polarizability on the droplet induction time can be pseudo-quantitatively assessed as shown in Table 4.2. The more hydrophobic (non-polar) the surface the shorter the induction time. With stronger hydrophobic-hydrophobic interaction, between the increasingly hydrophobic surfaces and hydrophobic droplet, there is a reduction in the repulsive disjoining pressure (hydrophobic attractive force). With a diminishing disjoining pressure the thin water film continues to drain until a critical thickness is reached where the attractive forces promote destabilization of the thin film, leading to film rupture and oil droplet wetting of the spreading substrate. Thus the apparent induction time is observed to decrease with increased surface hydrophobicity.

To quantitatively compare the spreading dynamics, the Wang *et al.*(1) model given by Eq. 4.4 was fitted using two parameters *m* and *a*, with *m* a function of the droplet spreading rate. A typical example of the empirical model fitting for the varying surface wettabilities is shown in Figure 4.19, with the fitting parameters given in Table 4.2.

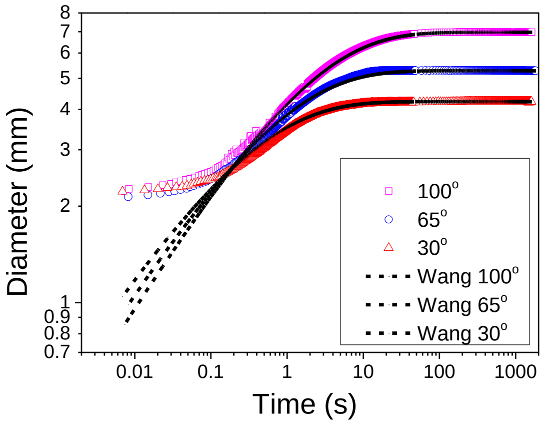

Figure 4.19. The raw data for CH$_3$*-terminated PDMS oil droplet spreading on 3 surfaces of increasing hydrophobicity (30, 65 and 100*^{o}*). Dashed lines are the empirical fit using the Wang et al.*$^{(1)}$ *model.*

As shown in Figure 4.19, the empirical model closely matched the spreading data for $t > 0.1$ s, with 0.1 s the shortest time interval considered by Wang *et al.*$^{(1)}$, thus those differences at shorter time intervals were not reported by Wang *et al.*$^{(1)}$. Such deviation at shorter times was similarly observed in Chapter 3 for silicone oils spreading in air. As was suggested by Winkels *et al.*, the tail at extremely short time intervals could be due to an optical illusion,$^{(59)}$ where the droplet appears to merge with its own reflection. As such, it is difficult to identify the first point of spreading (wetting), and the first few images show minimal changes in the spreading radius. This effect has also recently been reported for silicon oil droplets spreading in water.$^{(24)}$

From Figure 4.19 and the values of *m* reported in Table 4.2, it can be seen that the spreading dynamics of the CH$_3$-terminated PDMS oils slightly increase for droplets spreading on more hydrophobic surfaces. As there are more hydrophobic-hydrophobic interactions, which are thermodynamically favourable, the droplets spread more and spread comparatively faster. The viscosity ratio (oil viscosity η_D = 1000 mPa·s) $\eta_D/\eta_{S;}$ was 802, hence although large, the contribution from surface forces due to weakening viscous forces can begin to influence the spreading dynamics. Although small, there were measurable differences in spreading rates due to the influence of surface wettability as seen in Table 4.2.

4.4.3.2 Modelling of oil droplet spreading dynamics in water

The MKT and HD models are often seen as “contradictory models", with the driving force for spreading governed by the three-phase contact line in the MKT model, whereas it is the bulk fluid properties which influence the spreading dynamics in the HD model.(60) The HD model introduces an approximation for lubrication that suggests viscous dissipation retards droplet spreading, the model is generally said to be applicable when the droplet contact angle is small.(61) The MKT model is based on Eyring theory,(61) the bulk viscous dissipation is negligible and the wetting rate dictated by dissipation at the three-phase contact line. The MKT model describes a large number of identical adsorption sites on the solid surface, liquid molecules are able to adsorb and desorb on these sites, with adsorption causing the droplet to spread. The MKT model tends to apply when droplets have larger contact angles, as such a combined MKT-HD model is often proposed. (61) Both models given by Eqs. 4.1 and 4.2 were used to fit the spreading data of a 1000 mPa·s droplet spreading in D_2O on surfaces with a water contact angle of 100° and 30° as shown in Figure 4.20.

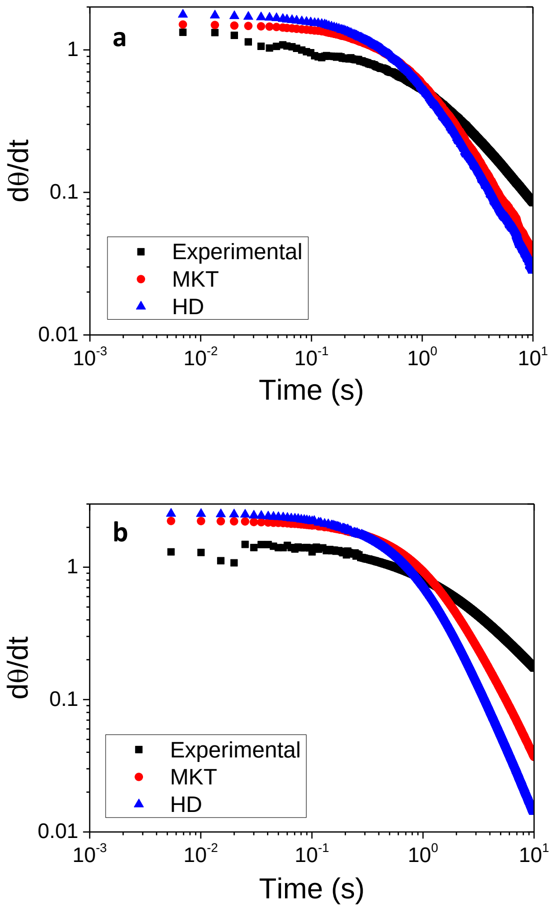

Figure 4.20. The relaxation of the contact angle during droplet spreading of a 1000 mPa·s CH_3*-terminated droplet on a silanised surface with a water contact angle of a) 30*^{o} *and b) 100*^{o}*, the experimental data is plotted alongside the MKT and HD model fits.*

As shown in Figure 4.20, although the two models (MKT and HD) have a different theoretical basis, they produce a similar level of accuracy when predicting the droplet spreading dynamics. The lack of agreement between theory and empirical data may be due to the partial wetting behaviour of the oils, where spreading laws often fail for droplet spreading on partial wetting surfaces.(61) While the model fits have been shown to be poor, the empirically derived Wang's model(1) shows a very close fit and will be used throughout this study to obtain a spreading rate (*m*) parameter which allows the spreading rates of droplets in different conditions to be directly compared.

4.4.3.3 Effect of oil viscosity

- The viscosity effect of the PDMS oil on the spreading dynamics was considered. To ensure a direct comparison, the spreading surface had a contact angle in water of 100°, *i.e.* the surface exposed for the longest silanisation time, thus providing the maximum spreading diameter for the oil droplets. Oil viscosities of 202, 485, and 1000 mPa·s were considered. A similar viscosity range to that described in Chapter 3 was initially considered, but difficulties with oil detachment for high viscosities and significant droplet deformation for low viscosities prevented other oils from being considered. The droplet spreading dynamics of different viscosity oils are shown in Figure 4.21.

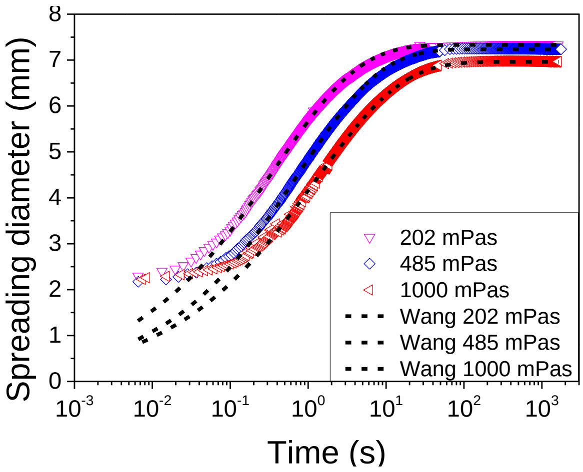

Figure 4.21. Spreading dynamics of three CH_3-terminated PDMS oils of varying viscosity; 202, 485 and 1000 mPa·s on a silanised surface with a water contact angle of 100°, the fitting of the Wang model⁽¹⁾ is also shown for each viscosity.

As shown in Figure 4.21, the oil droplets spread over approximately the same range (initial and final spreading diameters). The Young's equation (Eq. 4.8) describes the equilibrium contact angle as a function of the three interfacial tensions between the spreading surface, oil droplet and D_2O continuous fluid.

$$cos\,\theta = (\gamma_{sv} - \gamma_{sl})/\gamma_{lv} \tag{4.8}$$

where γ_{so} is the solid-oil, γ_{sw} the solid-water, γ_{ow} the oil-water interfacial tensions and θ is the oil droplet contact angle in water. Since the oils are molecularly equivalent, the viscosity difference results from changes in the polymer chain length or molecular weight. The interfacial tensions of the three considered oils were equivalent and equal to 38 mN/m (Figure 4.14). Hence, based on the Young's equation it would be expected that the droplets spread to the same extent as evidenced in Figure 4.21.

However, the oil viscosity does dictate the rate of spreading, with faster spreading observed for lower viscosity oils. Once the droplets had reached an equilibrium, the 1000 mPa·s droplet had a slightly smaller diameter than the other two droplets due to a slight variation in droplet sizes (see discussion below). While there should not be a change in droplet size, due to equivalent interfacial tensions, a variation can occur due to the droplet formation method. The droplets were formed manually using a threaded plunger syringe. The syringe is connected to the dispensing needle by tubing, but there is a delay to the droplet formation which leads to a pressure build-up in the syringe and tubing. The higher the oil viscosity the higher the build-up of pressure. As such, a 1000 mPa·s droplet required approximately 5 min to form and detach from the needle, with early detachment due to the pressure build-up. The method was reproducible for each viscosity, however there were size differences between viscosities; 27.2 µL, 26.7 µL and 24.7 µL droplet volume for 202, 485 and 1000 mPa·s oils, respectively. However, if the equilibrium contact angles are compared (Table 4.3), there is little difference between the equilibrium states of the three oils.

Table 4.3. The average induction time, equilibrium contact angle and spreading parameters m and a for 200, 500 and 1000 mPa·s oil droplets.

Oil viscosity (mPa·s)	**Induction times (s)**	**Equilibrium contact angle (°)**	**Droplet size (µL)**	***m***	***a***
1000	1.68 ± 0.25	38.7 ± 2.4	24.7 ± 1.2	0.39	6.33
485	3.91 ± 0.63	39.5 ± 1.2	26.7 ± 1.8	0.40	8.00
202	5.41 ± 1.10	38.8 ± 2.2	27.2 ± 1.3	0.41	10.99

Table 4.3 shows the fitting parameters of the empirical partial wetting model described by Wang *et al.*(1) The fitting parameters evidence that a decreasing oil viscosity increases the rate of droplet spreading. While the differences in *m* values are relatively small compared to those determined for oil droplets spreading in air, this reduced effect can be attributed to the smaller viscosity ratios in water: 802, 389 and 161 for the 1000, 485 and 202 mPa·s oils respectively. Also shown in Table 4.3 is the influence of oil viscosity on the droplet apparent induction time. While there is more variance with decreasing oil viscosity, overall the apparent induction time is observed to increase with decreasing oil viscosity. This observed trend results from the deformability/compressibility of the oil droplet on impact.

Figure 4.22a-c clearly shows that the impacting droplets deform but do not contact (wet) the spreading surface and remain separated by a thin-liquid film (TLF), identified by the thin white line between the droplet and spreading surface. As such, in order for the oil droplet to wet the surface, the thin-liquid film must drain to a critical rupture thickness. The drainage rate, which correlates to the real induction time can be described by the Stefan-Reynolds, Eq. 4.9: (62)

$$v_{Re} = -\frac{2h^3}{3\eta {R_f}^2}\Delta P \tag{4.9}$$ (62)

where v_{Re} is the velocity at which the film drains (*-dh/dt*), h is the film thickness, η the bulk viscosity of the film, R_f is the film radius and ΔP the pressure difference between the film and the spreading surface (disjoining pressure). Since the interfacial tension is constant for the three oils considered, the disjoining pressure contribution should be equivalent. Hence, the difference in film drainage time (*-dh/dt*) will result from differences in the radius (R_f) of the draining film, which is directly related to the degree of droplet deformation on impact.

With decreasing oil viscosity the droplets are able to compress more on impact which effectively increase R_f, with a larger R_f resulting in a greater volume of water to be drained to enable the oil droplet to wet the spreading surface. Since lower viscosity droplets are also more susceptible to dimple formation, this can also increase the amount of water trapped in the TLF, thus increasing the drainage time and real induction time. Figure 4.22 a-c compares the oil droplets (of increasing viscosity) at maximum compressibility (maximum deviation from circularity) immediately following droplet impact on the spreading surface, while images d- f show the oil droplets at rest (image prior to droplet wetting) on the spreading surface.

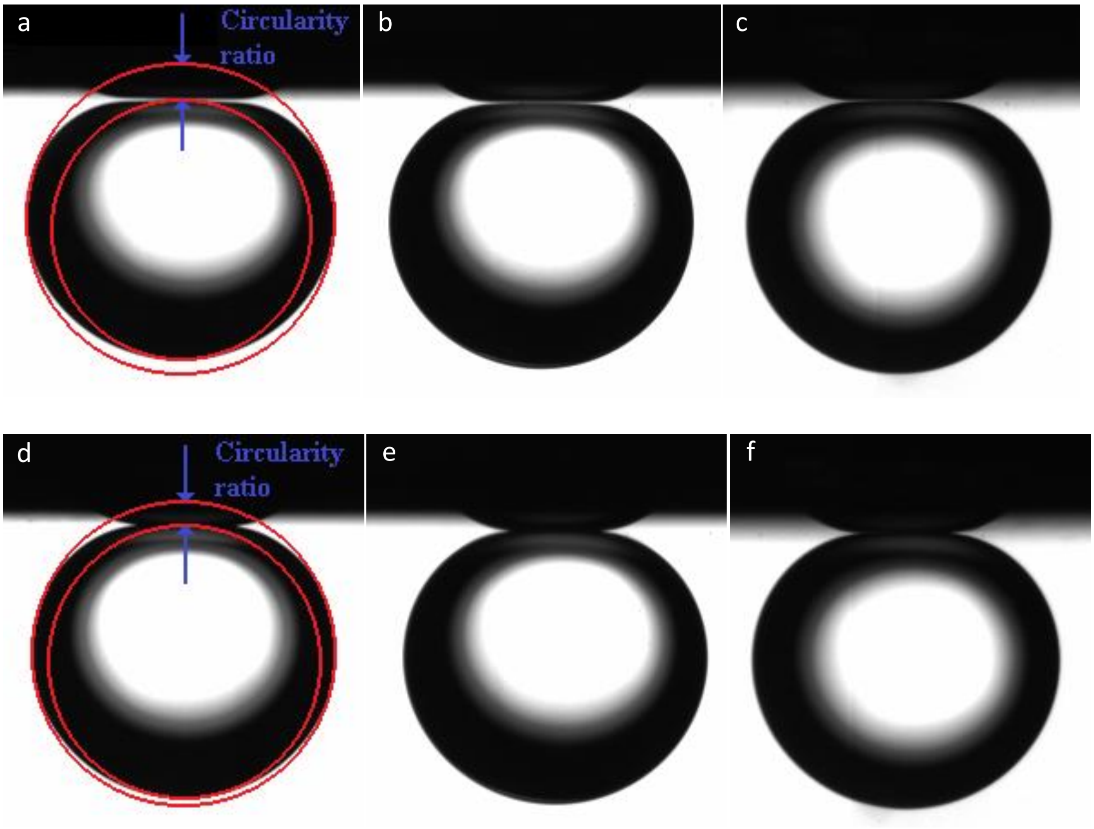

Figure 4.22. Maximum compression/deformation of the oil droplets immediately following impact with the spreading surface a) 202, b) 485, c) 1000 mPa·s, d-f) Same droplets at rest prior to wetting the spreading surface 202, 485 and 1000 mPa·s respectively.

To quantitatively describe the extent of droplet compressibility the smallest droplet diameter (D_S), taken as the droplet diameter in the direction perpendicular to the spreading surface, and the largest droplet diameter (D_L), taken to be the droplet diameter in the direction parallel to the spreading surface were measured. The circularity ratio was then calculated by D_S/D_L, with a smaller ratio confirming greater droplet deformation. The circularity ratio for droplets both at rest and at maximum compression (at impact) are shown in Table 4.4.

Table 4.4. The average circularity ratio of three droplets for the three different viscosities.

Viscosity (mPa·s)	**Circularity ratio for droplet at rest**	**Circularity ratio for droplet at maximum compression**
1000	0.895 ± 0.007	0.892 ± 0.008
485	0.895 ± 0.002	0.880 ± 0.006
202	0.895 ± 0.003	0.829 ± 0.010

As shown in Table 4.4, for droplets at rest (image prior to the oil droplet wetting the spreading surface) the circularity ratios were equivalent. However, for droplets at maximum compression the circularity ratios show a significant difference, with the circularity ratio increasing with decreasing oil viscosity. The 1000 mPa·s oil droplet exhibits the least compression (difference between the maximum and at rest deformations) with a circularity ratio difference of 0.003. For oil droplets with a viscosity of 458 and 202 mPa·s the circularity ratio difference increases, 0.015 and 0.066 respectively.

When considering the application of oil droplets wetting and spreading on fabrics, clearly there is an optimum viscosity to achieve the desired performance. While low viscosity oils are desirable for fast droplet spreading, the low oil viscosity also leads to significant droplet deformation on impact with the spreading surface and increased retention of trapped water which extends the overall apparent induction time.

The difference in spreading rates for these droplets is solely dependent on the oil viscosity. As previously mentioned, the apparent induction time is not the true induction time (although more appropriate for the current study) and is a function of the true induction time and partial spreading time. To ensure that the method is viable and not significantly influenced by the partial spreading time (time to θ = 150°), the apparent induction time was calculated as a function of different end-point conditions (critical contact angles; 90°, 120° and 150°). The resulting apparent induction times are shown in Table 4.5.

Table 4.5. The apparent induction times determined for different critical conditions - t_{150}, t_{120} and t_{90} for all three oil viscosities 200, 500 and 1000 mPa·s.

Viscosity (mPa·s)	**Apparent induction times (s)**		
	t_{150}	t_{120}	t_{90}
1000	1.68 ± 0.25	2.14 ± 0.25	3.21 ± 0.25
485	3.90 ± 0.63	4.14 ± 0.64	4.71 ± 0.63
202	5.25 ± 1.10	5.39 ± 1.10	5.74 ± 1.11

The apparent induction time is a function of the real induction time and partial spreading time. As the critical condition for the apparent induction time determination is changed (i.e. decreasing oil droplet contact angle), then the apparent induction time is observed to increase, a result of increased spreading diameter. Such an influence is shown in Table 4.5.

By extrapolating the apparent induction times at these three contact angles (90°, 120°, 150°) to a contact angle of 180°, it may be reasonable to indicate differences in the real induction times. The data was extrapolated using a power-law fit to represent the power-law dependency on spreading dynamics as shown in Figure 4.23, and the y-intercept may provide an assessment of the real induction times which were 1.29, 3.60 and 5.06 s for 1000, 485, 202 mPa·s respectively. While we have not measured the real induction time, our approach to providing some insight on the real induction time appears reasonable and illustrates that lower viscosity oils take longer to wet the substrate, an effect of droplet deformation upon impact with the spreading substrate as previously described.

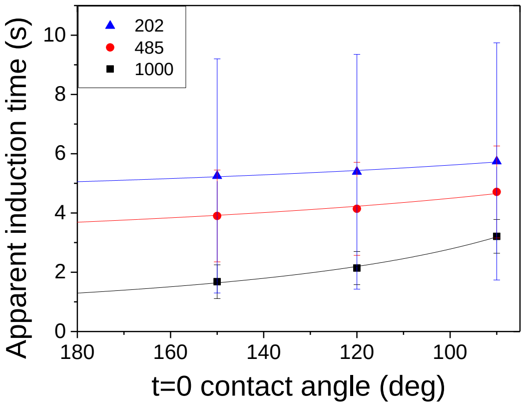

Figure 4.23. The apparent induction times determined for different critical conditions - t_{150}, t_{120} and t_{90} for all three oil viscosities 200, 500 and 1000 mPa·s, with a simple power law fit.

4.4.3.4 Effect of interfacial tension

The influence of oil-water interfacial tension on the droplet spreading dynamics was studied by increasing the concentration of SDS in the continuous aqueous phase. The surfactant concentration ranged from pure Milli-Q water (0 g/L SDS) to 2.4 g/L SDS, which is equivalent to the SDS critical micelle concentration (CMC). For comparison, only the 1000 mPa·s CH_3-terminated PDMS oil was considered, as shown in Figure 4.24. The experiments were once again conducted using a silanised surface with a water droplet contact angle in air of 100°.

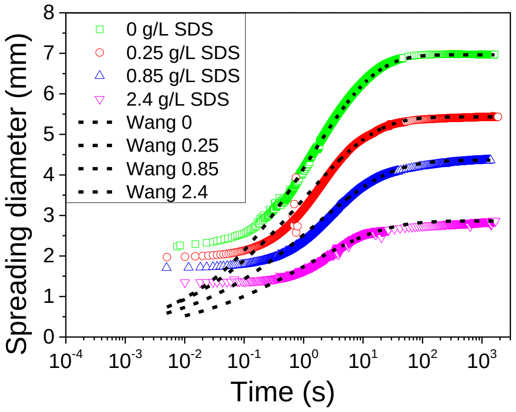

Figure 4.24. The spreading dynamics of 1000 mPa·s CH_3*-terminated PDMS oil droplets on a silanised surface with a water contact angle of 100° in an aqueous continuous fluid with varying SDS concentration.*

Unlike previous data the droplet spreading diameter (Figure 4.24) does not start at the same diameter (remembering that the first data point was taken when the spreading droplet reached a contact angle of 150°). As the surfactant concentration increased, the oil-water interfacial tension decreased; 38.0, 27.9, 19.9 and 5.4 mN/m for SDS concentrations of 0, 0.25, 0.85 and 2.4 g/L, respectively (Figure 4.14a). This reduction in interfacial tension leads to the formation of smaller droplets being released from the dispensing needle.

When a droplet is formed at the tip of a needle the contributions from buoyancy, pressure and interfacial tension forces will govern the minimum droplet size for detachment. A simple dimensionless correlation has been proposed where the volume of a detached droplet is given as a function of the Bond number (*Bo*) which accounts for the balance of gravitational (buoyancy) and interfacial tension forces: $Bo = \frac{r^2 \Delta \rho g}{\gamma}$. The volume (*V*) of a detached droplet is given by:$^{(63)}$

$$V = \left(\frac{3}{\left(\frac{Bo}{3.60}\right)^{1/2.81}} \right)^3 \tag{4.10}$$

Hence, a reduction in the interfacial tension increases Bo which reduces the volume of the detached droplet. The effect of interfacial tension on the detached droplet volumes are shown in Table 4.6. *N.b.* the reduced droplet volume naturally leads to a smaller droplet spreading diameter at θ = 150°.

Table 4.6. The apparent induction time, equilibrium contact angle and spreading parameters m and a for CH_3-terminated PDMS oil droplet in an aqueous continuous phase of different SDS concentrations.

Surfactant conc. (g/L)	**Induction times (s)**	**Equilibrium contact angle (°) – 1 h**	**Droplet volume (µL)**	***m***	***a***
0	1.68 ±0.25	38.7 ± 2.4	24.7 ± 1.2	0.39	6.33
0.25	2.84 ± 0.28	49.1 ± 0.6	15.6 ± 0.24	0.36	5.36
0.85	12.9 ± 2.00	59.0 ± 3.4	9.72 ± 0.51	0.34	3.77
2.40	> 60	77.1 ± 3.3	4.29 ± 0.68	0.33	2.67

The influence of interfacial tension (surfactant controlled) on droplet spreading is readily observed by the equilibrium contact angles (measured after 1 h) shown in Table 4.6. Oil droplets spreading in an aqueous fluid with a higher SDS concentration spread less, resulting in a larger equilibrium contact angle. The addition of SDS lowers the solid-water and oil-water interfacial tensions. The contact angles and oil-water interfacial tensions are given in Table 4.6. Using the Young's equation ($\cos\theta = (\gamma_{sw} - \gamma_{so})/\gamma_{ow}$), simultaneous equations of known values for the surfactant concentrations of 0 g/L and 2.4 g/L SDS showed that $\Delta\gamma_{sw} \approx 28.5$ mN/m, while the change in $\Delta\gamma_{ow}$ was 32.7 mN/m. Although both the numerator and denominator in the Young's equation are lowered with addition of surfactant, it has been calculated that the addition of surfactant has a more significant effect on the oil-water interfacial tension. The Young's equation predicts there is less droplet spreading with additional surfactant.

The surfactant molecules not only partition at the oil-water interface but will coat the hydrophobic spreading surface (water contact angle in air = 100°). Since the surfactants are amphiphilic (hydrophilic head and hydrophobic tail) the likely orientation of the surfactant molecules on the spreading surface is tail down (tail-surface interaction by hydrophobic forces), exposing the hydrophilic head group to the spreading oil droplet. As such, the apparent contact angle of the spreading substrate will decrease (become more hydrophilic) with increasing surfactant concentration, hence the hydrophobic droplet will spread less on the surface.

Fitting the spreading data with the partial wetting model of Wang *et al.*,(1) there is an apparent decrease in the spreading rate with increasing surfactant concentration. As shown in Figure 4.17, the surface wettability can have some influence on the overall spreading rate, with oil droplets spreading faster on more hydrophobic surfaces. However, for a contact angle change of 70° (30° and 100°) the spreading parameter m (an indicator of the spreading rate) only varied by 0.02. Hence, the measured changes in droplet spreading rates in the presence of SDS cannot solely be influenced by changes in surface wettability.

Secondly, the apparent induction time increases with increasing SDS concentration, even though the size of the impacting droplet reduced significantly. Such behaviour opposes our previous discussion regarding the Stefan-Reynolds drainage mechanics, where the rate of thin-liquid film drainage scales as a function of $1/R_f$, hence smaller droplets should exhibit a shorter real induction time. Therefore, the presence of surfactant at the oil-water interface significantly extends the droplet-substrate induction time.

The reason for an extended droplet-substrate induction time can be attributed to i) increased electrostatic repulsion between the negatively charged spreading surface and the negatively charged surfactant-stabilized droplet (SDS – anionic), and ii) increased Marangoni flow contribution.(64)

The Marangoni flow contribution can be thought of as a flow opposing the drainage of water from the thin-liquid film. As the oil droplet approaches the spreading substrate the surfactant molecules at the oil-water interface become mobilized, depleting the surfactant concentration at the interface of closest approach to the spreading surface. As such, a concentration gradient is established with the surfactant molecules seeking a more energetically favourable condition (equal concentration around the droplet interface). To rebalance the interfacial concentration the surfactant molecules move to oppose the direction of water drainage (counter-current flow), thus increasing the overall drainage time, as shown in Figure 4.25.(65) With increasing SDS concentration a larger concentration gradient can be formed, and hence the Marangoni flow contribution becomes stronger increasing the drainage time of the thin liquid film. (64) However, as the SDS concentration approaches the CMC the concentration gradient reduces, the interfacial surfactant mobility is reduced, thus the Marangoni flow contribution diminishes.

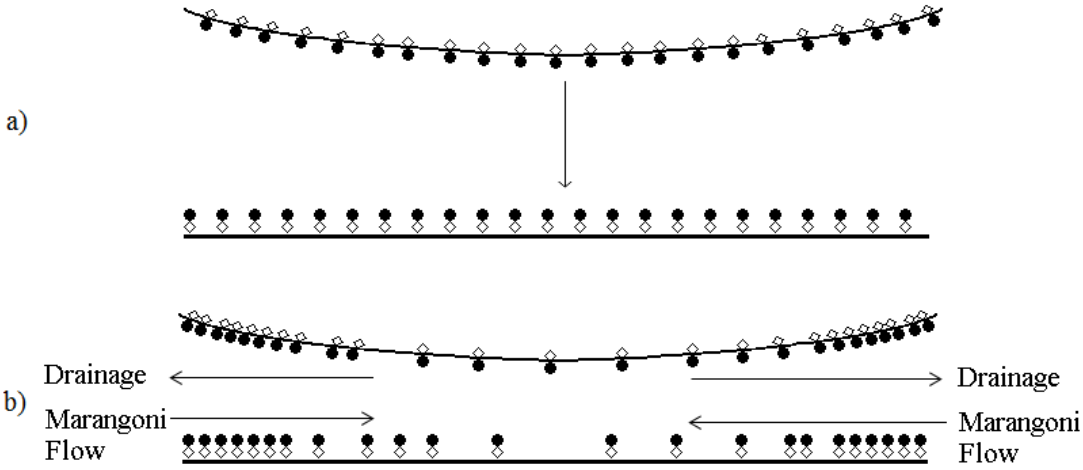

Figure 4.25. Visual representation of surfactant distributions leading to interfacial tension gradients to result in Marangoni flows.

One way to estimate the Marangoni flow contribution is to calculate the Marangoni number. This dimensionless number compares the viscous and interfacial forces that are associated with the Marangoni flow. There are several different methods to calculate the Marangoni number (*Ma*), many associated with differences in temperature. One method given by Hudson *et al.*(66) describes *Ma* as a function of the Capillary number (*Ca*) given by;

$$Ca = \frac{\eta_s \dot{\gamma} r}{\gamma} \tag{4.11}$$

$$Ma \approx \frac{\gamma_0 - \gamma}{\gamma_0 Ca} \tag{4.12}$$

where η_s is the surrounding medium viscosity, $\dot{\gamma}$ the shear rate (1/s) which is given by the radius normalized impact velocity, r the droplet radius, γ the interfacial tension and γ_0 the interfacial tension in the absence of surfactant. For the current experimental conditions, *Ca* and *Ma* were calculated and shown in Table 4.7.

Table 4.7. Capillary and Marangoni numbers for 1000 mPa·s CH_3-terminated PDMS oil in an aqueous fluid of increasing SDS concentration.

SDS conc. (g/L)	***Ca***	***Ma***
0	2.01×10^{-4}	0
0.25	3.47×10^{-4}	767
0.85	4.89×10^{-4}	974
2.40	1.75×10^{-3}	489

As shown in Table 4.7, while *Ca* increases with increasing surfactant concentration, for *Ma* the dependence on surfactant concentration clearly demonstrates a maximum contribution at a surfactant concentration less than the CMC. Initially, *Ma* scaled with the surfactant concentration,(67, 68) however as the CMC is approached, the oil-water interface becomes more densely packed by surfactant molecules, reducing surfactant mobility.$^{(69)}$ Above the CMC, due to higher number of surfactant molecules, the surface tension gradients occur over longer ranges and so the Marangoni forces are weaker,$^{(70)}$ until eventually there is no surface tension gradient and therefore no Marangoni flow contribution to influence the thin film drainage dynamics.$^{(71)}$

4.4.3.5 Effect of PDMS oil terminating group – NH_2

Since the NH_2-terminated PDMS oil is more polar than the CH_3-terminated PDMS oil, the oil polarity effect on the spreading dynamics could be studied. Two surfaces were chosen to compare the NH_2- and CH_3-terminated PDMS oils spreading on flat surfaces of different wettabilities: θ = 30° and 100° (water contact angles in air). The spreading dynamics of NH_2-terminated PDMS oil are shown in Figure 4.26a.

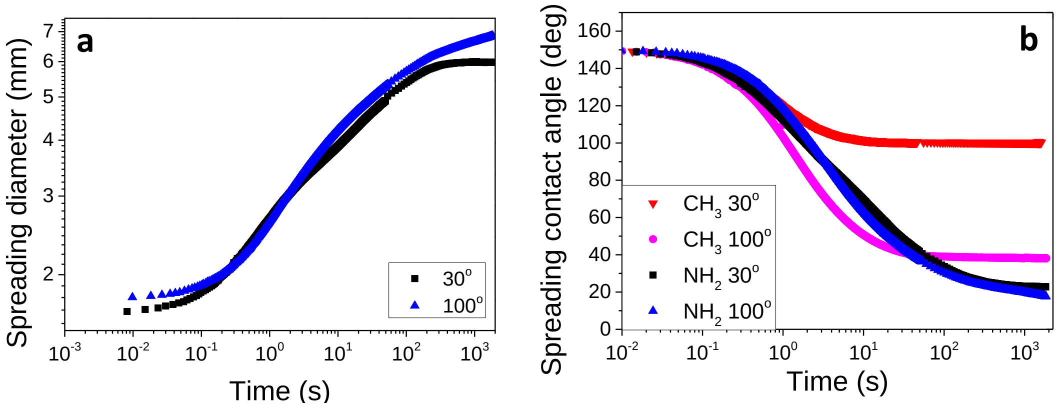

Figure 4.26. The spreading dynamics of 941 mPa·s NH_2-terminated PDMS oil droplets on surfaces of different wettabilities (water droplet contact angles shown inset) a) droplet spreading diameter and b) droplet spreading contact angle also including the 1000 mPa·s CH_3-terminated PDMS oils.

From Figure 4.26a it can be seen that the NH_2-terminated PDMS oil spreads at a similar rate on both surfaces of contrasting contact angles, 30° (hydrophilic) and 100° (hydrophobic). While the equilibrium wetting state of the oil droplet on the 30° surface reaches ~ 6 mm spreading diameter, on the 100° surface the droplet continues to progressively wet beyond the time-limit of the experiment (1 h). The droplet spreading rates, apparent induction times and "equilibrium" contact angles are shown in Table 4.8.

Table 4.8. The apparent induction time, equilibrium contact angle and the spreading parameters m and a for the 941 mPa·s NH_2-terminated PDMS oil droplets on surfaces of different wettabilities.

Silanised Surface	**PDMS oil**	**Apparent induction times (s)**	**Contact angle at 1 hr (°)**	**Droplet Size (µL)**	***m***	***a***
30°	NH_2	1.95 ± 0.74	22.8 ± 4.0	9.8 ± 0.9	0.27	3.48
100°	NH_2	2.62 ± 0.83	17.7 ± 1.8	9.8 ± 0.9	0.28	3.39
30°	CH_3	2.68 ± 0.79	99.6 ± 1.3	24.7 ± 1.2	0.37	7.56
100°	CH_3	1.68 ± 0.57	38.7 ± 2.4	24.7 ± 1.2	0.39	6.33

It should be noted that the NH_2-terminated droplets were prone to streaming, likely due to the lower interfacial tension of ~ 7 mN/m (Figure 4.14a). As such, droplets were generated at a much slower rate in an attempt to produce droplets of a similar size. While the 1000 mPa·s CH_3-terminated droplets were approximately 24.7 µL, the NH_2-terminated droplets were 9.8 µL (detached droplet volume described by Eq. 4.10). From the equilibrium contact angles it is clearly shown that the NH_2-terminated PDMS oil droplets preferentially wet both the 30° and 100° surfaces unlike the CH_3-terminated PDMS oils which showed a dependency on the surface wettability (Figure

4.17). Such wettability independence (NH_2) likely results from the polarity of the NH_2-terminated PDMS oil and lower interfacial tension (~7 mN/m for NH_2- compared to ~37 mN/m for CH_3-terminated oil), providing favourable conditions for the oil to spread. In water the positively charged NH_2 surface groups will interact with the negatively charged spreading surface, potentially diminishing the hydrophilic nature of the spreading surface.

This increased affinity for hydrophilic surfaces can be observed by conducting a simple dewetting experiment. Both NH_2- and CH_3-terminated PDMS oils were first deposited on a silanised spreading surface ($\theta = 30^{o}$) in air and allowed to completely wet the substrate. Then water was added to the quartz cuvette to flood the cell and monitor the dewetting dynamics of the two oils, see Figure 4.27. As expected following water flooding, the CH_3-terminated oil receded to an oil contact angle approaching 90^{o}, with the equilibrium contact angle partially influenced by the small air bubble retained in the oil. This effect seemed unavoidable and related to the deposition of oil on the dry spreading surface. However, for the NH_2-terminated PDMS oil the strong affinity for the hydrophilic surface was once again observed. Following water flooding the oil droplet did not dewet the hydrophilic surface, retaining a very low equilibrium contact angle.

For droplets to spontaneously dewet, the spreading coefficient, S, must be less than zero. Using the spreading coefficient equation, $S = \gamma_{ow}(cos\theta - 1)$, S for CH_3- and NH_2-terminated oils was -0.04 and -4×10^{-4}, respectively, indicating an increased dewetting potential by the CH_3-terminated PDMS oil.

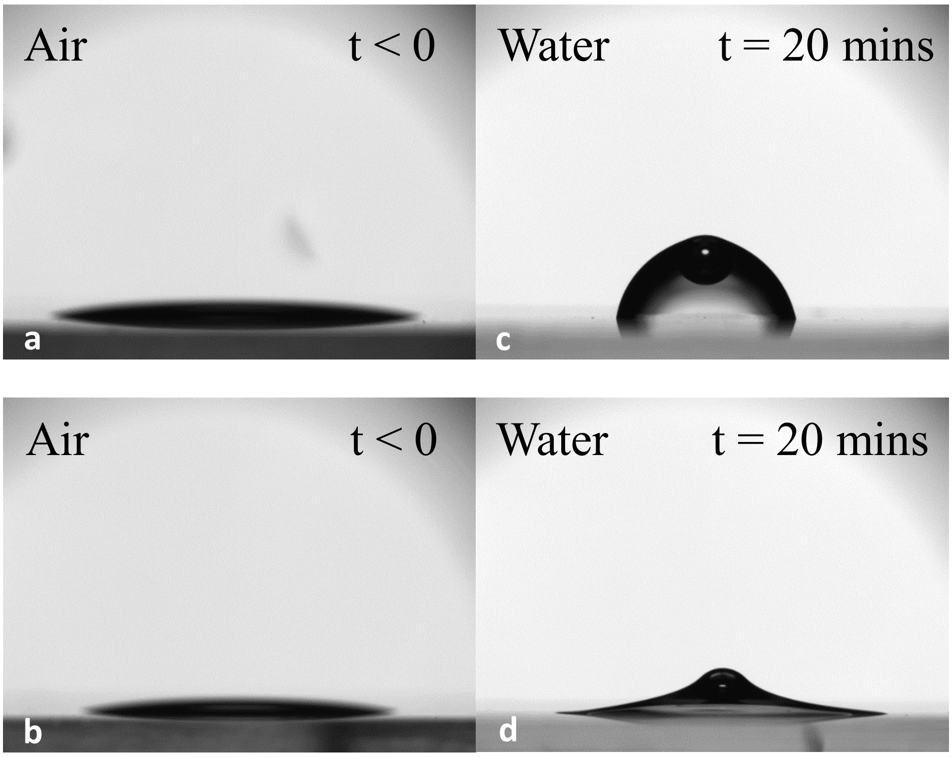

Figure 4.27. A PDMS droplet on a 30° silicon wafer in air a) CH_3*-terminated, b)* NH_2*-terminated, and the droplet after water is added to the system to dewet the droplet, c)* CH_3*-terminated and d)* NH_2*-terminated.*

4.4.3.6 Effect of cellulose coating (surface roughness)

The effect of the cellulose coating on the oil spreading dynamics was considered. Since the cellulose was hydrophilic comparisons were made to silanised hydrophilic surfaces (θ = 30°) which were considered to be smooth unlike the rougher cellulose substrates (see RMS values Table 4.1). All three cellulose coatings (deposition rpm) were considered to ensure no influence from the underlying silicon surface. The cellulose substrate had a water-in-air contact angle of ~35°. The apparent induction times and equilibrium contact angles are summarized in Table 4.9.

Table 4.9. The apparent induction time and equilibrium contact angles for CH_3- and NH_2-terminated PDMS oil droplets on various cellulose surfaces.

PDMS oil	**Surface coating (rpm)**	**Apparent induction time (s)**	**Equilibrium contact angle (°) – 1 h**
CH_3	Cellulose (6000)	> 60s	170 ± 2.7
CH_3	Cellulose (3000)	> 60s	170 ± 0.2
CH_3	Cellulose (1000)	> 60s	170 ± 1.2
NH_2	Cellulose (1000)	> 60s	161 ± 3.6

As shown in Table 4.9 the CH_3-terminated PDMS oil does not spread on any cellulose surface, with an equilibrium contact angle greater than our upper limit of 150° (criterion to confirm wetting). Hence, the induction times were reported as being greater than 60 s (self-imposed limit for comparison, *i.e.* non-wetting). In fact, the oil droplet contact angle did not surpass 150° within 1 h, with the equilibrium contact angles reported in Table 4.9 measured at 1 h. Figure 4.28 shows that the oil droplets did not spread on the surfaces, and was visually evidenced by droplets rolling when the surface was slightly tilted.

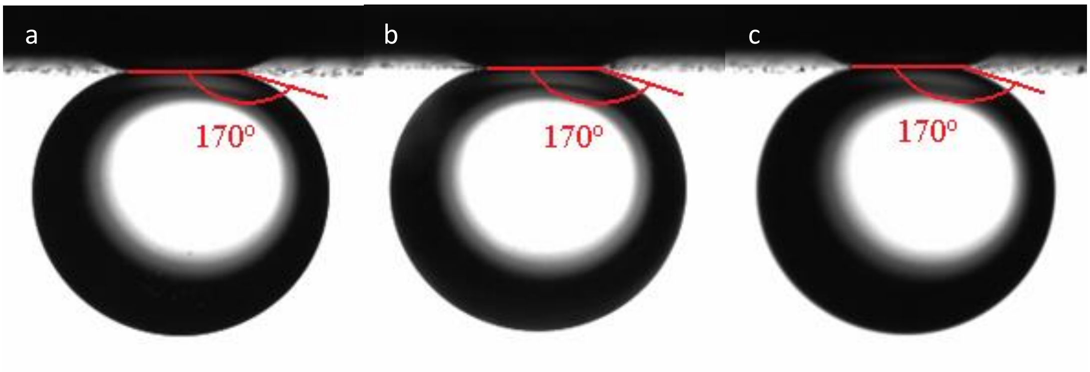

Figure 4.28. 1000 mPa·s CH_3-terminated PDMS oil droplets after 1 hour at rest on the cellulose surface; a) 1000 rpm, b) 3000 rpm, c) 6000 rpm (spin-coating conditions).

The cellulose surface can be compared to the 30^{o} silanised surface, however the non-wetting condition is more representative of the strongly hydrophilic 0^{o} silicon surface. Since the contact angles are almost equivalent (~ 30^{o}), the difference in wetting and non-wetting behaviour may be attributed to the increased roughness of the cellulose surface.

Wenzel(72) demonstrated that micro and nano surface structures can modify the wetting properties of the solid surface. The roughness modifies the overall contact area, with the roughness R' quantified by $R' = A_{rough}/A_{flat}$, and R' always greater than 1. Substituting R' in the Young's equation (Eq. 4.8) the relation between the contact angle on a smooth surface, θ, and the contact angle on a rough surface, $\theta_{R'}$, is given by:

$$cos\theta_{R'} = R' \cos\theta \qquad (4.13)$$

This equation is valid when the droplet size is substantially larger that the apparent roughness, and is based on the liquid completely penetrating into the roughness voids on the spreading surface. The larger the roughness (R') the more hydrophilic the surface becomes, similarly a hydrophobic surfaces becomes more hydrophobic.

A second wetting state is described by the Cassie model,(73) where the composite interface for spreading is composed of both solid-oil and water-oil interfaces, *i.e.* the drop lies on a mixture of water and solid. The Cassie model for the apparent contact angle on a composite surface is given by:

$$cos\theta_c = f_1 cos\theta_1 + f_2 cos\theta_2 \tag{4.14}$$

where f_1 is the fractional area of the surface with contact angle θ_1, f_2 is the fractional area of the surface with contact angle θ_2, and θ_c is the Cassie contact angle. The equation can be reduced to:

$$cos\theta_c = f_1 cos\theta_1 + f_2 \tag{4.15}$$

since θ_2 = 0° (as water). The Cassie equation can be viewed as a weighted mean of the Young's equation and Eq. 4.15 essentially means that the droplet will have a higher apparent contact angle if less droplet area is in contact with the solid substrate. Therefore, for the experimental case presented, the effect of surface roughness is to increase the apparent hydrophilicity of the wetting surface, thus decreasing the affinity for the CH_3-terminated PDMS oil to wet the cellulose layer. Since the deposited droplets were susceptible to rolling, it is thought that the Cassie wetting mechanism influences the overall behaviour. The cellulose films were also hydrated for 24 h prior to the spreading experiments, thus the cellulose layer (fibres and voids) will become completely hydrated and prevent the oil droplet from wetting the surface. (74) This increase in surface hydrophilicity following the hydration (swelling) of a layer has been previously reported.(39, 75, 76) Both effects of roughness and layer hydration are likely the cause of the observed non-wetting state.

Quite interestingly the super-wetting NH_2-terminated PDMS oil did not wet the cellulose surfaces. While this oil showed great affinity for both hydrophilic and hydrophobic surfaces, the rougher cellulose surface appears to inhibit droplet spreading. Unlike the CH_3-terminated PDMS oil the NH_2 oil did interact with the cellulose layer as evidenced by the droplet remaining stationary when the spreading surface was slightly tilted. The measured contact angle after 1 h was measured to be 161° (Figure 4.29), slightly lower than the CH_3-terminated PDMS oil. While the exact mechanism for this apparent non-wetting state is not currently known, it is thought to relate to the increased hydrophilicity of the cellulose layer which results from the increased surface roughness and layer hydration.

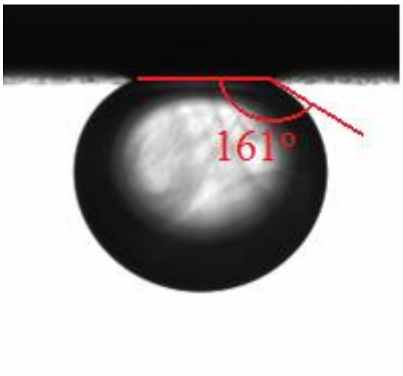

Figure 4.29. 941 mPa·s NH_2-terminated PDMS oil droplets at rest on the cellulose surface following partial wetting.

4.5 Conclusion

In the current study, PDMS droplets were spread on modified silicon surfaces under water. The surfaces were silanised to form a range of hydrophobicities, displaying a range of water contact angles of 0, 30, 65 and 100^{o}. The increased hydrophobicity allowed the CH_3-terminated PDMS to spread more, at quicker spreading rates and with a smaller induction time due to the increase in hydrophobic-hydrophobic interactions possible with increasingly hydrophobic surfaces. The spreading dynamics were shown to fit MKT and HD wetting laws well, with a slight preference to the MKT, however the empirical Wang model(1) showed a better fit and allowed comparisons of droplet spreading to be compared with higher accuracy. The spreading of the CH_3-terminated PDMS droplet became increasingly slower in an aqueous surfactant solution due to the surfactant reducing the effective hydrophobicity of the surfaces, the surfactant also lead to increased induction times due to Marangoni flow effects. Increasing viscosity effects were also shown to decrease spreading dynamics, however there was a decrease in induction times due to a decrease in droplet deformation as shown by the circularity ratio differences. The circularity ratio of the 202 mPa·s oil was 0.83 and lead to an induction time of 5.41 s, whereas the more viscous 1000 mPa·s oil had a smaller deformation with a circularity ratio of 0.89 which exhibited an induction time of 1.68 s. Finally, it was shown that rough cellulose surfaces with an RMS value of approximately 0.6 nm were able to prevent wetting by both the CH_3-terminated PDMS oil and the more polarizable NH_2-terminated PDMS. The prevention of oil wetting was due to both roughness effect increasing the hydrophilicity of the surface and also the hydrophilicity increasing with the cellulose fibres absorbing water and causing a chemical effect. Although NH_2-terminated oils exhibited a larger extent of spreading on silicon surfaces they showed little increased spreading with rough cellulose surfaces.

4.6 References

1. WANG, X.D., Y. ZHANG, D.J. LEE and X.F. PENG. Spreading of Completely Wetting or Partially Wetting Power-Law Fluid on Solid Surface. *Langmuir*, 2007, **23**(18), pp.9258-9262.
2. KUMAR, D. and S.K. BISWAS. Effect of surfactant dispersed in oil on interaction force between an oil film and a steel substrate in water. *Colloids and Surfaces A: Physicochemical and Engineering Aspects*, 2011, **377**(1–3), pp.195-204.
3. LE FOLLOTEC, A., I. PEZRON, C. NOIK, C. DALMAZZONE and L. METLAS-KOMUNJER. Triblock copolymers as destabilizers of water-in-crude oil emulsions. *Colloids and Surfaces A: Physicochemical and Engineering Aspects*, 2010, **365**(1–3), pp.162-170.
4. CAMBIELLA, Á., J.M. BENITO, C. PAZOS and J. COCA. Interfacial properties of oil-in-water emulsions designed to be used as metalworking fluids. *Colloids and Surfaces A: Physicochemical and Engineering Aspects*, 2007, **305**(1–3), pp.112-119.
5. KOBAYASHI, I., M. NAKAJIMA and S. MUKATAKA. Preparation characteristics of oil-in-water emulsions using differently charged surfactants in straight-through microchannel emulsification. *Colloids and Surfaces A: Physicochemical and Engineering Aspects*, 2003, **229**(1–3), pp.33-41.
6. PERWUELZ, A., T. NOVAIS DE OLIVERA and C. CAZE. Study of wetting at the silicone oil/water/fibre interface. *Colloids and Surfaces A: Physicochemical and Engineering Aspects*, 1999, **147**(3), pp.317-329.
7. DING, H., M.N. GILANI and P.D. SPELT. Sliding, pinch-off and detachment of a droplet on a wall in shear flow. *Journal of Fluid Mechanics*, 2010, **644**, pp.217-244.
8. DING, H. and P.D. SPELT. Onset of motion of a three-dimensional droplet on a wall in shear flow at moderate Reynolds numbers. *Journal of Fluid Mechanics*, 2008, **599**, pp.341-362.
9. SPILDO, K. and J.S. BUCKLEY. Uniform and mixed wetting in square capillaries. *Journal of Petroleum Science and Engineering*, 1999, **24**(2–4), pp.145-154.
10. ASSERSON, R.B., A.C. HOFFMANN, S. HØILAND and K.M. ASVIK. Interfacial tension measurement of freon hydrates by droplet deposition and contact angle measurements. *Journal of Petroleum Science and Engineering*, 2009, **68**(3–4), pp.209-217.
11. FREER, E.M., T. SVITOVA and C.J. RADKE. The role of interfacial rheology in reservoir mixed wettability. *Journal of Petroleum Science and Engineering*, 2003, **39**(1–2), pp.137-158.
12. FETZER, R., M. RAMIASA and J. RALSTON. Dynamics of liquid− liquid displacement. *Langmuir*, 2009, **25**(14), pp.8069-8074.
13. SEVENO, D., T. BLAKE, S. GOOSSENS and J. DE CONINCK. Predicting the wetting dynamics of a two-liquid system. *Langmuir*, 2011, **27**(24), pp.14958-14967.
14. DE RUIJTER, M.J., M. CHARLOT, M. VOUÉ and J. DE CONINCK. Experimental Evidence of Several Time Scales in Drop Spreading. *Langmuir*, 2000, **16**(5), pp.2363-2368.
15. DE RUIJTER, M.J., J. DE CONINCK, T.D. BLAKE, A. CLARKE and A. RANKIN. Contact Angle Relaxation during the Spreading of Partially Wetting Drops. *Langmuir*, 1997, **13**(26), pp.7293-7298.

16. DE RUIJTER, M.J., J. DE CONINCK and G. OSHANIN. Droplet Spreading: Partial Wetting Regime Revisited. *Langmuir*, 1999, **15**(6), pp.2209-2216.
17. CAZABAT, A.M., S. GERDES, M.P. VALIGNAT and S. VILLETTE. Dynamics of Wetting: From Theory to Experiment. *Interface Science*, 1997, **5**(2), pp.129-139.
18. SEAVER, A.E. and J.C. BERG. Spreading of a droplet on a solid surface. *Journal of Applied Polymer Science*, 1994, **52**(3), pp.431-435.
19. BROCHARD-WYART, F. and P.G. DE GENNES. Spreading of a Drop between a Solid and a Viscous Polymer. *Langmuir*, 1994, **10**(7), pp.2440-2443.
20. TANNER, L.H. The spreading of silicone oil drops on horizontal surfaces. *Journal of Physics D: Applied Physics*, 1979, **12**(9), p.1473.
21. OGAREV, V.A., T.N. TIMONINA, V.V. ARSLANOV and A.A. TRAPEZNIKOV. Spreading of Polydimethylsiloxane Drops on Solid Horizontal Surfaces. *The Journal of Adhesion*, 1974, **6**(4), pp.337-355.
22. GOOSSENS, S., D. SEVENO, R. RIOBOO, A. VAILLANT, J. CONTI and J. DE CONINCK. Can We Predict the Spreading of a Two-Liquid System from the Spreading of the Corresponding Liquid–Air Systems? *Langmuir*, 2011, **27**(16), pp.9866-9872.
23. RAMIASA, M., J. RALSTON, R. FETZER and R. SEDEV. Contact Line Friction in Liquid–Liquid Displacement on Hydrophobic Surfaces. *The Journal of Physical Chemistry C*, 2011, **115**(50), pp.24975-24986.
24. MITRA, S. and S.K. MITRA. Understanding the Early Regime of Drop Spreading. *Langmuir*, 2016, **32**(35), pp.8843-8848.
25. MITRA, S. Under Liquid Wetting Dynamics. 2016.
26. FOISTER, R.T. The kinetics of displacement wetting in liquid/liquid/solid systems. *Journal of colloid and interface science*, 1990, **136**(1), pp.266-282.
27. LIN, C.-M., P. NEOGI and R. YBARRA. Wetting kinetics of a drop on a horizontal solid surface under a viscous ambient liquid. *Industrial & engineering chemistry research*, 1998, **37**(1), pp.66-70.
28. DE GENNES, P.-G. Wetting: statics and dynamics. *Reviews of modern physics*, 1985, **57**(3), p.827.
29. SEVENO, D., A. VAILLANT, R. RIOBOO, H. ADÃO, J. CONTI and J. DE CONINCK. Dynamics of Wetting Revisited. *Langmuir*, 2009, **25**(22), pp.13034-13044.
30. BASU, S., K. NANDAKUMAR and J.H. MASLIYAH. A study of oil displacement on model surfaces. *Journal of Colloid and Interface Science*, 1996, **182**(1), pp.82-94.
31. BLAKE, T. and J. HAYNES. Kinetics of liquidliquid displacement. *Journal of Colloid and Interface Science*, 1969, **30**(3), pp.421-423.
32. LAVI, B. and A. MARMUR. The exponential power law: partial wetting kinetics and dynamic contact angles. *Colloids and Surfaces A: Physicochemical and Engineering Aspects*, 2004, **250**(1), pp.409-414.
33. CHURAEV, N.V. Surface forces in wetting films. *Advances in Colloid and Interface Science*, 2003, **103**(3), pp.197-218.
34. MCCORMICK, C.L., P.A. CALLAIS and B.H. HUTCHINSON JR. Solution studies of cellulose in lithium chloride and N, N-dimethylacetamide. *Macromolecules*, 1985, **18**(12), pp.2394-2401.
35. KONTTURI, E., P. THÜNE and J. NIEMANTSVERDRIET. Novel method for preparing cellulose model surfaces by spin coating. *Polymer*, 2003, **44**(13), pp.3621-3625.
36. RANKL, M., S. LAIB and S. SEEGER. Surface tension properties of surface-coatings for application in biodiagnostics determined by contact angle measurements. *Colloids and Surfaces B: Biointerfaces*, 2003, **30**(3), pp.177-186.
37. FERRIS, J.L. *The wettability of cellulose film as affected by vapor-phase adsorption of amphipathic molecules*. thesis, Georgia Institute of Technology, 1974.

38. LUNER, P. and M. SANDELL. The wetting of cellulose and wood hemicelluloses. *Journal of Polymer Science Part C: Polymer Symposia*, 1969, **28**(1), pp.115-142.
39. LIUKKONEN, A. Contact angle of water on paper components: Sessile drops versus environmental scanning electron microscope measurements. *Scanning*, 1997, **19**(6), pp.411-415.
40. DANKOVICH, T.A. and D.G. GRAY. Contact Angle Measurements on Smooth Nanocrystalline Cellulose (I) Thin Films. *Journal of Adhesion Science and Technology*, 2011, **25**(6-7), pp.699-708.
41. AKIYAMA. S, N. KOBAYASHI, Method for heat-treating silicon wafer, 2002
42. WIEGAND, M., M. REICHE, U. GÖSELE, K. GUTJAHR, D. STOLZE, R. LONGWITZ and E. HILLER. Wafer bonding of silicon wafers covered with various surface layers. *Sensors and Actuators A: Physical*, 2000, **86**(1), pp.91-95.
43. SUKANEK, P.C. Dependence of film thickness on speed in spin coating. *Journal of The Electrochemical Society*, 1991, **138**(6), pp.1712-1719.
44. SKROBIS, K.J., D.D. DENTON and A.V. SKROBIS. Effect of early solvent evaporation on the mechanism of the spin-coating of polymeric solutions. *Polymer Engineering & Science*, 1990, **30**(3), pp.193-196.
45. KONTTURI, E., P.C. THÜNE and J. NIEMANTSVERDRIET. Cellulose model surfaces simplified preparation by spin coating and characterization by X-ray photoelectron spectroscopy, infrared spectroscopy, and atomic force microscopy. *Langmuir*, 2003, **19**(14), pp.5735-5741.
46. SCHAUB, M., G. WENZ, G. WEGNER, A. STEIN and D. KLEMM. Ultrathin films of cellulose on silicon wafers. *Advanced Materials*, 1993, **5**(12), pp.919-922.
47. KONTTURI, E., T. TAMMELIN and M. ÖSTERBERG. Cellulose—model films and the fundamental approach. *Chemical Society Reviews*, 2006, **35**(12), pp.1287-1304.
48. KONTURRI, E. Surface chemistry of cellulose: from natural fibres to model surfaces. Academic Dissertation, Technische Universiteit Eindhoven, Niedereland, 2005. 145 p. 2005.
49. VON BAHR, M., F. TIBERG and V. YAMINSKY. Spreading dynamics of liquids and surfactant solutions on partially wettable hydrophobic substrates. *Colloids and Surfaces A: Physicochemical and Engineering Aspects*, 2001, **193**(1), pp.85-96.
50. VON BAHR, M., F. TIBERG and B.V. ZHMUD. Spreading Dynamics of Surfactant Solutions. *Langmuir*, 1999, **15**(20), pp.7069-7075.
51. DUTSCHK, V., K.G. SABBATOVSKIY, M. STOLZ, K. GRUNDKE and V.M. RUDOY. Unusual wetting dynamics of aqueous surfactant solutions on polymer surfaces. *Journal of colloid and interface science*, 2003, **267**(2), pp.456-462.
52. MATAR, O. and R. CRASTER. Dynamics of surfactant-assisted spreading. *Soft Matter*, 2009, **5**(20), pp.3801-3809.
53. NEUMANN, B., B. VINCENT, R. KRUSTEV and H.-J. MÜLLER. Stability of Various Silicone Oil/Water Emulsion Films as a Function of Surfactant and Salt Concentration. *Langmuir*, 2004, **20**(11), pp.4336-4344.
54. LASSEN, C., C.L. HANSEN, S.H. MIKKELSEN and J. MAAG. Siloxanes-consumption, toxicity and alternatives. *Environmental project*, 2005, **1031**, pp.1-111.
55. ŁUBKOWSKA, M. and W. STAŃCZYK. Aminoalkyl functionalized siloxanes. *Polimery*, 2014, **59**.
56. CREMALDI, J.C., T. KHOSLA, K. JIN, D. CUTTING, K. WOLLMAN and N. PESIKA. Interaction of Oil Drops with Surfaces of Different Interfacial Energy and Topography. *Langmuir*, 2015, **31**(11), pp.3385-3390.
57. GRATE, J.W., K.J. DEHOFF, M.G. WARNER, J.W. PITTMAN, T.W. WIETSMA, C. ZHANG and M. OOSTROM. Correlation of Oil–Water and Air–Water Contact Angles of Diverse Silanized Surfaces and Relationship to Fluid Interfacial Tensions. *Langmuir*, 2012, **28**(18), pp.7182-7188.

58. TADROS, T. Colloids and Interface Science Series, Vol. 1, Colloid Stability: The Role of Surface Forces, Part I. *Willey-VCH Verlag GmbH & Co. KGaA, Weinheim*, 2007.
59. WINKELS, K.G., J.H. WEIJS, A. EDDI and J.H. SNOEIJER. Initial spreading of low-viscosity drops on partially wetting surfaces. *Physical Review E*, 2012, **85**(5), p.055301.
60. PRIMKULOV, B.K. Bitumen Liberation Dynamics. 2015.
61. LU, G. *Dynamic Wetting by Nanofluids.* Springer Berlin Heidelberg, 2015.
62. MANEV, E., S. SAZDANOVA and D. WASAN. Emulsion and foam stability-the effect of film size on film drainage. *J. Colloid Interface Sci.;(United States)*, 1984, **97**(2).
63. LEE, B.-B., P. RAVINDRA and E.-S. CHAN. New drop weight analysis for surface tension determination of liquids. *Colloids and Surfaces A: Physicochemical and Engineering Aspects*, 2009, **332**(2-3), pp.112-120.
64. SESEN, M., T. ALAN and A. NEILD. Droplet Control Technologies for Microfluidic High Throughput Screening (μHTS). *Lab on a Chip*, 2017.
65. BARET, J.-C. Surfactants in droplet-based microfluidics. *Lab on a Chip*, 2012, **12**(3), pp.422-433.
66. HUDSON, S.D., A.M. JAMIESON and B.E. BURKHART. The effect of surfactant on the efficiency of shear-induced drop coalescence. *Journal of Colloid and Interface Science*, 2003, **265**(2), pp.409-421.
67. GIRIBABU, K. and P. GHOSH. Adsorption of nonionic surfactants at fluid–fluid interfaces: importance in the coalescence of bubbles and drops. *Chemical engineering science*, 2007, **62**(11), pp.3057-3067.
68. MITRA, T. and P. GHOSH. Binary coalescence of water drops in organic media in presence of ionic surfactants and salts. *Journal of Dispersion Science and Technology*, 2007, **28**(5), pp.785-792.
69. DELACOTTE, J., L. MONTEL, F. RESTAGNO, B. SCHEID, B. DOLLET, H.A. STONE, D. LANGEVIN and E. RIO. Plate coating: influence of concentrated surfactants on the film thickness. *Langmuir*, 2012, **28**(8), pp.3821-3830.
70. KOCH, K., B. DEW, T.E. CORCORAN, T.M. PRZYBYCIEN, R.D. TILTON and S. GAROFF. Surface tension gradient driven spreading on aqueous mucin solutions: a possible route to enhanced pulmonary drug delivery. *Molecular pharmaceutics*, 2011, **8**(2), pp.387-394.
71. MYERS, D. *Surfactant Science and Technology.* Wiley, 2005.
72. WENZEL, R.N. RESISTANCE OF SOLID SURFACES TO WETTING BY WATER. *Industrial & Engineering Chemistry*, 1936, **28**(8), pp.988-994.
73. CASSIE, A.B.D. and S. BAXTER. Wettability of porous surfaces. *Transactions of the Faraday Society*, 1944, **40**(0), pp.546-551.
74. NOSONOVSKY, M. and B. BHUSHAN. Why re-entrant surface topography is needed for robust oleophobicity. *Phil. Trans. R. Soc. A*, 2016, **374**(2073), p.20160185.
75. HÄNNI-CIUNEL, K., G.H. FINDENEGG and R. VON KLITZING. Water Contact Angle On Polyelectrolyte-Coated Surfaces: Effects of Film Swelling and Droplet Evaporation. *Soft materials*, 2007, **5**(2-3), pp.61-73.
76. SEDEV, R., J. PETROV and A. NEUMANN. Effect of swelling of a polymer surface on advancing and receding contact angles. *Journal of Colloid and Interface Science*, 1996, **180**(1), pp.36-42.

Chapter 5: Accelerated spreading of inviscid droplets prompted by the yielding of strongly elastic interfacial films

The complexity associated with droplets spreading on surfaces has attracted significant interest for several decades. Sustained activity results from the many natural and manufactured systems that are reliant on droplet-substrate interactions and spreading. Interfacial shear rheology and its influence on the dynamics of droplet spreading has to date received little attention. In the current study, saponin β-aescin was used as an interfacial shear rheology modifier, partitioning at the air-water interface to form a strongly elastic interface ($G'/G'' \sim 6$) within 1 min aging. The droplet spreading dynamics of Newtonian (water, 5 wt% ethanol, 0.0015 wt% N-dodecyl β-D-glucopyranoside) and non-Newtonian (xanthan gum) fluids were shown to proceed with a time-dependent power-law dependence of ~ 0.50 and ~ 0.10 (Tanner's law) in the inertial and viscous regimes of spreading, respectively. However, water droplets stabilized by saponin β-aescin were shown to accelerate droplet spreading in the inertial regime with a depreciating time-dependent power-law of 1.05 and 0.61, eventually exhibiting a power-law dependence of ~ 0.10 in the viscous regime of spreading. The accelerated rate of spreading is attributed to the potential energy as the interfacial film yields and relaxation of the buckled interfacial film during spreading. Even though the strongly elastic film ruptures to promote droplet spreading, interfacial elasticity is retained enhancing the dampening of droplet oscillations following detachment from the dispensing capillary.

5.1 Introduction

Spreading droplets are important in many industries including paints, coatings, agrochemicals and lubrication to name just a few.(1) The energy associated with a droplet spreading on a solid in air is given by, Equation 5.1, where (γ_{xy}) is the interfacial tension between three phases, S = solid, L = liquid and G = gas. When combined with the well-known Young's equation (Eq. 5.2), the energy associated with droplet spreading yields Eq. 5.3.

$$\frac{dG}{dA} = \gamma_{SG} - (\gamma_{SL} + \gamma_{LG}) \tag{5.1}$$

$$\cos\theta = \frac{\gamma_{SG} - \gamma_{SL}}{\gamma_{LG}} \tag{5.2}$$

$$-\frac{dG}{dA} = \gamma_{LG}(\cos\theta - 1) \geq 0 \tag{5.3}$$

Droplet spreading in air has been extensively studied(2) and several models including Tanner (Eq. 5.4)(3), Seaver and Berg(4), and de Gennes(5) have been proposed to describe the droplet spreading dynamics. Tanner's spreading theory is widely reported for viscous liquids spreading on hydrophilic surfaces, with the hydrodynamic spreading radius (r) dependent on the initial droplet radius r_o, the surface tension γ, the fluid viscosity μ, and the spreading time t (3, 6)

$$\frac{r}{r_o} \sim \left(\frac{\gamma t}{\mu r_o}\right)^{1/10} \qquad (5.4)$$

While most fluids can be reasonably described by Tanner's law, Sawicki *et al.* showed discrepancies for low viscosity poly(dimethyl siloxane) (PDMS) oils.(7) Such divergence was suggested to relate to the interfacial viscosity being significantly lower than the bulk fluid viscosity, resulting from differences in the molecular orientation at the interface.

The dynamics of inviscid droplet spreading exhibits two distinct regimes; the first phase of spreading is commonly termed inertial spreading and progresses at a rate of $r \sim t^{0.5}$,(8, 9) while the second phase is described as viscous spreading and the three-phase contact line moves as a function of $r \sim t^{0.1}$, i.e. Tanner's law. The viscous regime is limited by the droplet viscosity(9), with the characteristic time of spreading (Eq. 5.5) used to describe the transition from inertial to viscous spreading(10)

$$\tau \sim \left(\frac{\rho\gamma r}{\mu^2}\right)^{1/8} \sqrt{\frac{\rho r^3}{\gamma}} \qquad (5.5)$$

where ρ is the droplet density.

Table 5.1 summarizes the effect of several fluid and surface properties on the spreading dynamics of mostly inviscid droplets. In addition to those commonly studied parameters, there are many other factors that have been shown to influence spreading dynamics including drop shape(11), surface roughness(12), temperature(13, 14), complex and soft surfaces(15, 16), electro-wetting(17, 18) and droplet impact velocity.(19)

Table 5.1. The effect of physicochemical properties on the spreading dynamics of droplets. The spreading exponents in the inertial and viscous regimes are represented as n' and n'', respectively.

Parameter	**Impact on spreading**	**Spreading exponent**
Fluid viscosity (droplet)	General observation: *Increased viscosity decreases the droplet spreading rate.*	$n'' \sim 0.15$, $\mu = 11.5 - 1120$ mPa.s (9) $n' \sim 0.5$, $\mu = 1 - 10.7$ mPa.s (20) $n' \sim 0.5$ then $n'' \sim 0.1$, $\mu = 1 - 1000$ mPa.s (10) $0.3 < n' < 0.5$ then $0.1 < n'' < 0.125$, $\mu = 1 - 60.1$ mPa.s (21) $0.1 < n'' < 0.2$, $\mu = 35.5 - 109$ mPa.s (19) $n' \sim 0.5$ then $n'' \sim 0.1$, $\mu = 1 - 1412$ mPa.s (22) $0.12 < n'' < 0.18$, $\mu = 1.34 - 50000$ mPa.s (23) $0.030 < n' < 0.085$ then $0.073 < n'' < 0.109$, $\mu = 20 - 1150$ mPa.s (24)
Surface wettability	General observation: *Aqueous droplets on hydrophilic surfaces – decrease in the substrate hydrophilicity decreases the droplet spreading rate.*	$n' = 0.5$, $\theta = 0 - 115^o$ (9) $n' \sim 0.5$ then $0.06 < n'' < 0.1$, $\theta = 0 - 50^o$ (13) $0.25 < n' < 0.5$, $\theta = 30 - 180^o$, $3 - 180^o$ (20) $0.3 < n' < 0.5$ then $n'' \sim 0.1$, $\theta = 0 - 112^o$ (21) $n' \sim 0.5$, $\theta = 0 - 115^o$ (25) $0.1437 < n' < 0.2785$, $\theta = 0 - 36.8^o$ (26)
Initial drop size	General observation: *Droplets with a size below the capillary length spread at a rate $n'' \sim 0.1$.* R = Droplet radius	$0.5 < n' < 1$ then $0.1 < n'' < 0.2$, R 0.37 – 0.82 mm (9) $n' \sim 0.5$, R 0.22 – 0.78 mm (20) $n' \sim 0.5$ then $n'' \sim 0.1$, R 1.2 – 2.7 mm (10) $0.44 < n' < 0.53$, R 0.5 – 1.2 mm (21) $0.14 < n'' < 0.2$, R 10 µm – 2.5 mm (19) $0.073 < n'' < 0.141$, R 1.24 – 1.34 mm (24) $0.1 < n'' < 0.13$, R 0.57 – 1.51 mm (12)
Surface tension	General observation: *Decrease in surface tension increases the droplet spreading rate.* *Using surfactants either:* *a) increase spreading dynamics (trisiloxanes (TS)) or b) decrease spreading dynamics (docusate (AOT), CTAB, SDS).*	TS $0.16 < n'' < 1$, AOT $n'' \sim 0.1$ (27) $0.001 < n'' < 0.06$ (28) $0.053 < n'' < 0.09$ (29) pure liquids $n' \sim 0.5$ then $n'' \sim 0.1$, (22) surfactant $n' \sim 0.5$ then $n'' < 0.1$ (22) $0.053 < n'' < 0.1$ (30) TS $0.015 < n' < 0.23$ then $0.38 < n'' < 0.58$ (23) $0.099 < n'' < 0.137$ (24)

Of particular interest in the current study is the contribution of surface elasticity which can be influenced by surface active species partitioning at the liquid-liquid interface.(31-34) To the author’s knowledge, interfacial effects on the spreading dynamics of droplets are rarely explored except for surfactant systems, with particular focus given to changes in surface tension. Generally, surfactants reduce the equilibrium three-phase contact angle and increase the solid-liquid contact area. However, the rate of droplet spreading is slightly retarded as the creation of new interfacial area is much faster than the diffusion transport of surfactants to the interface,(35) hence surface tension gradients are established during droplet spreading leading to Marangoni flows.(36)

However, few studies have considered the influence of surface shear elasticity on droplet wetting dynamics. Leiske *et al.* considered the contribution of surface elasticity on the mobility of droplets residing on a sliding substrate.(37) The authors selected four insoluble surfactants to produce varying degrees of surface elasticity, as the insoluble nature of these surfactants was a determinant property to generate surface shear elasticity. The authors evidenced that the motion of a droplet on a sliding substrate was influenced by the surface shear elasticity, and not solely by the surface tension. For the most rigid interface the authors observed compression of the droplet interface and the formation of an interfacial skin which eventually ruptured to promote droplet spreading.

To advance our understanding of the effects of interfacial rheology on droplet spreading dynamics, in the current study, β-aescin was chosen as an interfacial rheology modifier. The molecular structure of β-aescin (Figure 5.1) is highly polycyclic and favors the formation of strongly elastic films at the air-water interface.(38) The research objective was to assess the contribution of interfacial shear elasticity on the droplet spreading dynamics of inviscid fluids.

5.2 Materials and Experimental Methods

5.2.1 Materials

Saponin *β*-aescin (purity 95 %, Mw 1101.2 g/mol) a triterpenoid monodesmosidic glycoside, was purchased from MP Biomedicals (UK). A non-ionic surfactant, N-Dodecyl *β*-D-glucopyranoside (DG) (purity 98 %, Mw 320 g/mol), and xanthan gum (XG) (Mw 4.5MDa) were purchased from Sigma Aldrich (UK). Silicon wafers were used as the wetting substrate and were purchased from Silicon Valley Microelectronics (USA). The properties of the silicon wafers were: Type P, dopant: boron, orientation <100>, resistivity 10 – 20 ohm.cm and thickness 525 ± 25 µm. Ultrapure Milli-Q water was used in all experiments with a minimum resistivity of 18.2 MΩ·cm. Ethanol (purity 99.96% A.C.S. grade, VWR) and PDMS (Alfa Aesar, USA) with a nominal viscosity of 1000 mPa·s were used as received.

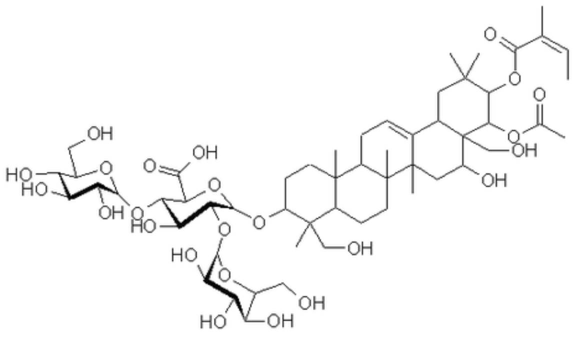

Figure 5.1. General molecular structure of β-aescin.

5.2.2 Surface tension

The dynamic surface tension of a droplet was measured using a pendant droplet analyzer (Theta T200, Biolin Scientific, Sweden). A droplet of ~8 µL was generated at the blunt tip of a 22 G stainless steel (SS) needle at 2 µL/s using an automatic dispenser. Prior to each measurement, the SS needle was cleaned using ethanol and dried with nitrogen. The surface tension was determined from droplet shape analysis, with the Theta software executing an edge-detection routine. The β-aescin concentration in Milli-Q water was varied between 5×10^{-5} wt% and 0.5 wt%. The surface tension was measured for 0.83 h to ensure that the steady-state condition was attained. The influence of droplet evaporation was minimized by increasing the relative humidity in the quartz cuvette and sealing the measurement cell using Parafilm. Small changes in the droplet volume were also compensated by activating the automatic evaporation tool in the Theta software. The feedback loop ensured that the droplet volume was maintained by automatically injecting fluid when the droplet volume diverged by 1 %.

Prior to generating the water droplet, the imaging software was triggered to capture the initial adsorption dynamics. For surface tension measurements the image capture rate was set to 2 fps.

5.2.3 Droplet spreading

Even though the Theta tensiometer had a maximum frame rate of 2,500 fps, the frame rate was too slow to fully capture the details of inviscid droplet spreading. Therefore, a high speed camera (Photron FASTCAM SA5, Photron Ltd., Japan) was used to record droplet spreading at 10,000 fps. The high speed camera was positioned perpendicular to the Theta tensiometer and slightly elevated (< 2°) above the spreading surface. Two LED lights were positioned in front of the quartz cuvette either side of the camera to provide sufficient illumination of the spreading droplet. 10 µL droplets were instantaneously produced at the blunt-tip of a 22 G SS needle. The needle tip was positioned 5.5 mm from the spreading substrate, with the droplet apex (lower edge) ~ 3.5 mm from the spreading substrate. Depending on the system, the droplet was held in position for a pre-determined time to ensure that the interfacial properties (surface tension, surface shear elasticity) had approached near steady-state condition. The droplet hold time for water + β-aescin was 5 min. Once the droplet had aged, the droplet was lowered towards the underlying substrate at 10 mm/min whilst remaining attached to the SS needle. The rate of droplet approach (0.17 mm/s) was maintained beyond droplet contact with the spreading substrate. Since droplet spreading occurred over a few hundredths of a second, this mechanical motion had little effect on the spreading rate, and the droplet always detached from the SS needle during spreading. The captured images were analysed using ImageJ software to measure the droplet spreading diameter and droplet height (centreline) as a function of time. Prior to each measurement, the silicon wafers were cleaned by soaking the substrates in Piranha solution for 2 h, thoroughly rinsing with Milli-Q water and dried with nitrogen.

5.2.4 Interfacial buckling

In order to further assess the interfacial elastic properties, interfacial buckling experiments were conducted. A 10 µL droplet was generated at a rate of 2 µL/s which was performed using the automatic dispenser. To study the interfacial properties, droplets were aged for a period of time from 15 to 300 s and then the droplet volume was withdrawn at a rate of 0.8 µL/s. The effect of withdrawal rate was also considered by aging droplets for 300 s and varying the withdrawal rate from 0.05 to 1 µL/s. Similar to the surface tension experiments, a 10 µL droplet was aged for 5 mins and the droplet volume was abruptly reduced to 5.4 µL at a rate of 0.8 µL/s and allowed to equilibrate at this new volume, similar to the relaxation studies conducted by Rane *et al*..(39) All results are an average of three experiments.

5.2.5 Fluid and interfacial shear rheology

The viscosity of β-aescin solutions and the interfacial shear rheology of the air-water interface were measured using a Discovery Hybrid Rheometer (DHR-2) (TA Instruments, UK). Equivalent β-aescin concentrations as those discussed for surface tension measurements were considered. The concentric cylinder geometry was used to measure the viscosity of the β-aescin solutions, and the geometry was chosen to minimize the surface area to volume ratio, thus ensuring that any contribution from interfacial rheology on the bulk viscosity was negligible. The shear viscoelasticity of the air-aqueous (water + β-aescin) interface was measured using the Double Wall Ring (DWR) geometry. The method of cleaning and set-up have been described in detail elsewhere.(34) It should be noted that the instrument was calibrated using precision mapping and the bearing mode set to soft. The geometry was positioned at the air-aqueous interface and a pre-shear protocol ($\dot{\gamma}$ = 170 s^{-1} for 3 min) was initiated to ensure that the start condition for each experiment remained constant. The time-dependent viscoelasticity was measured by oscillating the DWR at constant strain, 0.05%, and constant frequency, 1 Hz. A strain dependent sweep verified that the oscillation strain remained in the linear viscoelastic region. The *G'* (elastic) and *G"* (viscous) moduli were measured for 30 min, and to minimize the effect of solvent evaporation a Teflon cap was placed over the DWR Delrin trough. All rheology experiments were completed at T = 20 ^{o}C.

5.3 Results and Discussion

The spreading of water (inviscid) droplets is shown in Figure 5.2. The two distinct regimes can be identified as inertial and viscous spreading, with the exponent of spreading decreasing from 0.50 to 0.10, the latter in good agreement with Tanner's law. Using Eq. 5.5, the characteristic time of spreading was calculated to be 8×10^{-3}

s, which identifies the onset of the transition from inertial to viscous spreading, see Figure 5.2. Three repeats are shown in Figure 5.2 and confirm good reproducibility of the spreading dynamics (spreading exponents for each experiment are shown inset).

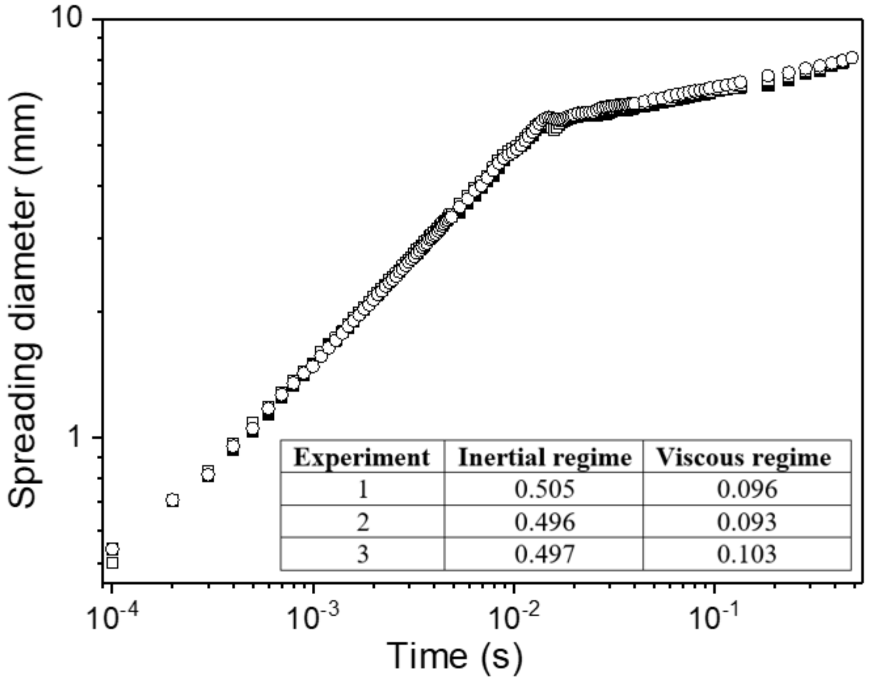

Experiment	Inertial regime	Viscous regime
1	0.505	0.096
2	0.496	0.093
3	0.497	0.103

Figure 5.2. Spreading dynamics of three water droplets deposited on a hydrophilic silicon substrate.

5.3.1 Surface tension

The dynamic surface tension of water + β-aescin was measured to determine the minimum adsorption time required to reach steady-state. Figure 5.3a shows the dependence of surface tension on the β-aescin concentration, with concentrations less than 5 × 10^{-3} wt% resulting in negligible changes to the surface tension ($\gamma_{water} =$ 72.3 mN/m). At concentrations ≥ 5 × 10^{-3} wt%, the surface tension was observed to progressively decrease with increasing β-aescin concentrations up to 5 × 10^{-2} wt%. At higher β-aescin concentrations the adsorption dynamics and apparent surface tension was independent of the concentration, i.e. beyond the critical micelle concentration (CMC) of β-aescin.

The apparent surface tension isotherm is shown in Figure 5.3b. Three additional β-aescin concentrations were also measured such that the CMC could be determined, CMC = 0.2 mM (0.022 wt%), in reasonable agreement with the range of CMCs previously reported by Pekdemir *et al.*(40) CMC = 0.78 mM and Stoyanov *et al.*(38) CMC = 0.071 mM. The order of magnitude difference in the reported CMC may result from differences in the molecular composition and purity of the β-aescin, which is reasonable since β-aescin is a naturally sourced product. The variability in reported CMC values might also be attributed to a non-surface tension force. As will be discussed below, β-aescin forms strongly elastic interfaces and the effect of the resulting deviatoric stresses can deform the droplet, leading to apparent changes in the measured surface tension.(41) As such, we refer to the surface tension as an apparent surface tension.

The slope of the apparent surface tension isotherm can by analysed using the Gibbs equation (Eq. 5.6) to determine the maximum adsorption of β-aescin ($\Gamma_{\max}$) at the air-water interface. In the Gibbs equation, Γ represents the excess solute per unit area at the interface, R the universal gas constant, T the temperature, γ the surface tension, and C the bulk concentration of β-aescin in Milli-Q water. $\Gamma_{\max}$ for β-aescin at the air-water interface was calculated to be 6.59×10^{-6} mol/m^2. From the surface excess the area per molecule (A_i) can be calculated using Eq. 5.7, where N_A is Avogadro's constant, hence, for the β-aescin used in the current study the area per molecule was 0.26 nm^2. Stanimirova *et al.*(42) used molecular dynamics simulations to elucidate the interfacial ordering of β-aescin (air-water) and showed two preferred orientations, i) lay-on configuration (i.e. parallel to the interface) A_i ~ 0.75 nm^2, and ii) end-on configuration (i.e. perpendicular to the interface) A_i ~ 0.26 nm^2. The latter configuration is in good agreement with the calculated area per molecule, hence it is most likely that the end-on configuration is the preferential orientation of β-aescin at the air-water interface.

$$\frac{-d\gamma}{RT} = \Gamma \; dln \; C \tag{5.6}$$

$$A_i = \left(\frac{1}{\Gamma_{max} N_A}\right) \tag{5.7}$$

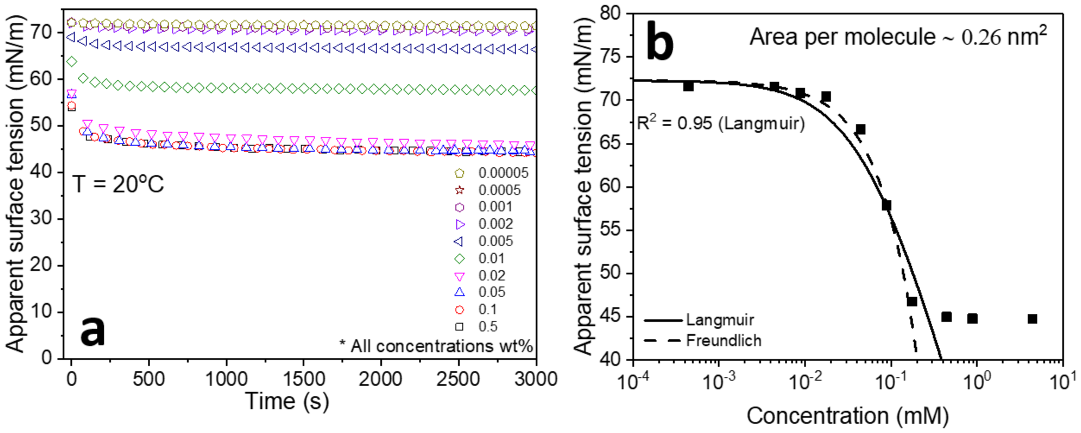

Figure 5.3. a) Dynamic surface tension of water droplets with increasing concentrations of β-aescin. b) Apparent equilibrium surface tensions as a function of the β-aescin concentration.

The apparent surface tension isotherm was fitted to a Langmuir model (Eq. 5.8) with a coefficient of determination equal to 0.95. A slightly better fit to the experimental data was observed using the empirical Freundlich isotherm which may suggest that the adsorbed β-aescin film is slightly heterogeneous, although this has not been confirmed.

$$\gamma = \gamma_a + RT\Gamma_{max} ln(\frac{1}{1+KC}) \qquad (5.8)$$

5.3.2 Fluid and interfacial shear rheology

The primary objective of this work was to isolate the contribution of interfacial shear rheology on droplet spreading, hence a critical concentration of β-aescin was first determined, such that the effect of β-aescin on the interfacial rheology was significant while changes to the bulk fluid viscosity were negligible. The bulk viscosities of β-aescin solutions over the concentration range 5 × 10^{-4} wt% to 0.5 wt% are shown in Figure 5.4a. At β-aescin concentrations ≤ 5 × 10^{-3} wt%, the fluid can be considered to behave as a Newtonian fluid with a measured viscosity equal to that of water. At higher β-aescin concentrations the fluid becomes non-Newtonian (shear thinning), with a fluid viscosity slightly exceeding that of water. For example, at a β-aescin concentration of 0.01 wt% and a shear rate of 40 s^{-1}, the relative viscosity ($\frac{\mu_\beta}{\mu_W}$) was increased by 12% and demonstrated weakly shear thinning behaviour, power-law index = 0.84. The degree of fluid shear thinning was shown to increase slightly at higher β-aescin concentrations, although the fluid rheology displayed little variation at concentrations beyond the CMC.

While the exact shear rate during droplet spreading is not known, the shear rate ($\dot{y}_0$) at droplet impact can be approximated by $\dot{y}_i = \frac{v_i}{D_i}$, where v_i and D_i are the droplet impact velocity and droplet diameter, respectively.(19) In the current study the droplet shear rate at impact was ~ 0.05 s^{-1}. Based on the relative differences in spreading and impact velocities, it is expected that the droplet shear rate during spreading greatly increases. Hence, the difference between the viscosity of Milli-Q water and the shear rate dependent viscosity of 0.01 wt% β-aescin solution can be considered negligible. To assess the importance of equivalent shear thinning behaviour on the droplet spreading dynamics, a comparative study using xanthan gum was also considered. Xanthan gum was chosen due to its ability to structure in solution and consequently affect the bulk fluid viscosity while showing negligible surface activity, thus not affecting the interfacial shear rheology.

For equivalent β-aescin concentrations (bulk rheology), the shear viscoelastic properties of the air-water interface were measured to elucidate the time-dependent build-up of both the viscous (*G”*) and elastic moduli (*G’*). At β-aescin concentrations lower than 5×10^{-3} wt%, the interface remained purely viscous with no measurable elasticity. This is in good agreement with the negligible changes in the air-water surface tension at low β-aescin concentrations (Figure 5.3a), thus suggesting sparse coverage of β-aescin molecules at the air-water interface. Increasing the β-aescin concentration led to the onset of a measureable elasticity ($C = 5 \times 10^{-3}$ wt%), while at higher β-aescin concentrations strongly elastic interfacial films were formed and could be considered solid-like (i.e. $G' > G''$). The critical β-aescin concentration required to develop a solid-like interfacial film was found to be 0.01 wt% but this also corresponded to the onset of a weakly shear thinning fluid, see Figure 5.4a. Following the pre-shear protocol, the aging time required for the air-water interface to become solid-like was less than 30 s (C = 0.01 wt%), and became almost instantaneous (few seconds) at higher β-aescin concentrations. For 0.01 wt% β-aescin in water, the G'/G'' ratio at 5 min aging was ~ 10, confirming the strongly elastic nature of the formed interfacial film.

At 0.01 wt% *β*-aescin, even though the relative viscosity of the bulk fluid had increased by 12% (compared to water at a shear rate of 40 s^{-1}), a significant change in the interfacial shear rheology was observed, transitioning from a purely viscous (water only at $t = 0$) to a solid-like interface that was sufficiently strong to induce an apparent interfacial yield stress of ~ 1.7 x 10^5 Pa. The 2D yield point of the interfacial film was measured via an oscillation stress ramp(43) (Figure B1) following 5 min aging. The critical stress at *G' = G"* was converted to an apparent yield stress by including the interfacial film thickness (5 nm), which was taken to be equivalent to a monolayer thick.(38, 44)

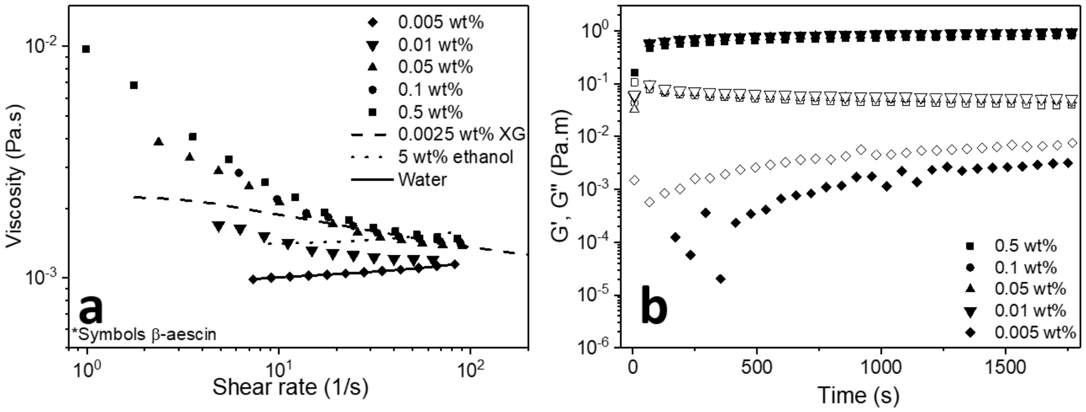

Figure 5.4. a) Fluid viscosity as a function of the β-aescin concentration. Lines represent the rheology of water (solid), water + 5 wt% ethanol (dotted) and water + 0.0025 wt% xanthan gum solution (dashed). b) Interfacial shear viscoelasticity of β-aescin films at the air-water interface as a function of the β-aescin concentration and interfacial aging time. Open symbols = G', closed symbols = G". Oscillation rheology conducted using constant strain, 0.05 % and constant frequency, 1 Hz. All experiments were conducted at T = 20 °C.

5.3.3 Interfacial buckling

The β-aescin forms a film or 'skin' at the interface with elastic properties. When the droplet volume is reduced (by volume withdrawal), droplet curvature is increased, and this creates compressive stresses that cause mechanical instabilities in the interfacial film. (45, 46) Further reducing the droplet volume increases the stress and mechanical instabilities until the droplet 'buckles', *i.e.* the droplet suddenly changes from a Laplacian to a non-Laplacian shape. The critical volume at which the droplet buckles compared to the initial droplet volume (i.e. $t = 0$) gives the buckling ratio, $\frac{V(@\,buckling)}{V(t=0)}$. For this study, the point of buckling was defined as the first image that cannot be fitted to the Laplacian shape. Analysing the images of a buckling droplet, akin to the stick-slip phenomena, the droplet appears to buckle in different regions as a function of time. The changes were very abrupt and easy to identify from the images. The droplet neck appeared to undergo significant buckling.

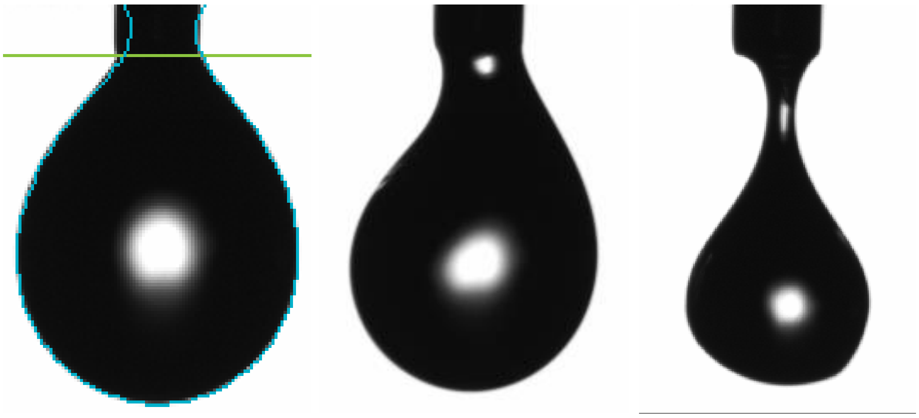

Figure 5.5. 0.01wt % β-aescin stabilized droplet after 5 min aging and during droplet volume withdrawal at 1.0 µL/s a) 1 s before interfacial buckling displaying a Laplacian droplet shape (blue line = laplacian fit), b) first image at interfacial buckling, c) 2 s after droplet buckling showing significant crumpling.

From both the surface tension (Figure 5.3a) and rheology (Figure 5.4b) data, it can be deduced that the *β*-aescin takes approximately 300 s to form a strongly elastic film. Such aging can also be observed by measuring the buckling ratio, Figure 5.6a.

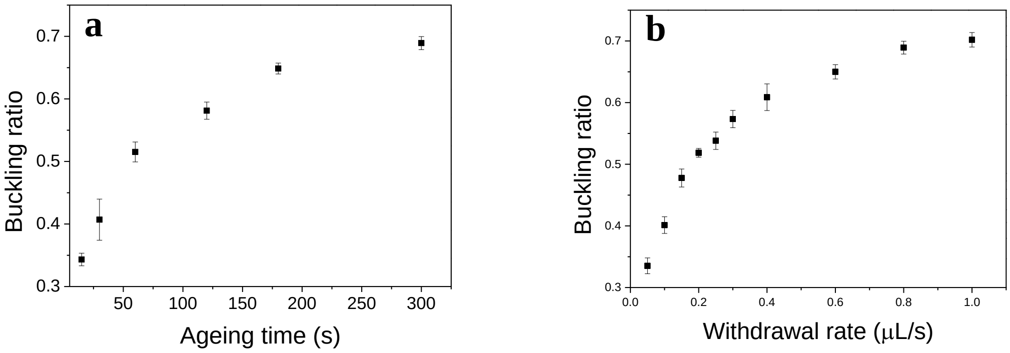

Figure 5.6. a) 10 μL 0.01 wt% β-aescin stabilized droplet was allowed to age before measuring the buckling ratio at different time intervals, fluid withdrawal rate = 0.8 μL/s, b) 10 μL 0.01 wt% β-aescin stabilized droplet aged for 5 mins and the interfacial buckling ratio measured as a function of the withdrawal rate.

Similar to the viscoelastic moduli (Figure 5.4b), the buckling ratio was shown to increase with aging time (Figure 5.6a), confirming that the interfacial film becomes more solid-like. Since the β-aescin is irreversibly adsorbed, during droplet volume reduction, the molecules are not displaced (exchanged) to the bulk fluid. Therefore, the molecules become compressed and the interface eventually buckles to alleviate the compressional force acting on the film, akin to a collapse pressure on a Langmuir trough. Even after very short aging (15 s) the droplet still buckles, but at a low buckling ratio. This result may appear to contradict the interfacial shear rheology data, because an interface can only buckle when in the solid-like state, i.e. G'/G". However, it must be reminded that during droplet volume reduction, the interfacial area reduces accordingly, and since the molecules are irreversibly adsorbed, the “aging effect” is accelerated for a system of decreasing interfacial area.

Interestingly, the buckling ratio is shown to be a function of the fluid volume withdrawal rate (Figure 5.6b). For higher fluid volume withdrawal rates the droplet buckling ratio is higher. It appears that the buckling ratio is reaching an asymptote at higher withdrawal rates. While this phenomena has not be considered in further detail, it may indicate that at lower withdrawal rates, the β-aescin has more time to reorganize in the film, and thus lower droplet volumes are attained before droplet buckling is observed. Such data may be akin to frequency dependent responses measured by a rheometer, i.e. higher frequencies produce stiffer, more elastic responses.

The potential for the interfacial film to reorganize and relax has been demonstrated by a simple droplet volume reduction experiment (Figure 5.7). Following aging for 300 s, the droplet volume was reduced from 10 µL to 5.4 µL. Since the withdrawal rate was 0.8 µL/s, the droplet underwent buckling. As the droplet volume (5.4 µL) was maintained the surface tension appeared to fluctuate slightly before increasing to a new steady-state surface tension. Those slight fluctuations likely result from fitting the buckled droplet and should be ignored. However, eventually the interface appears to reorganize and since the droplet interfacial area is lower that the initial interfacial area, the β-aescin molecules are more tightly packed, leading to a lower surface tension.

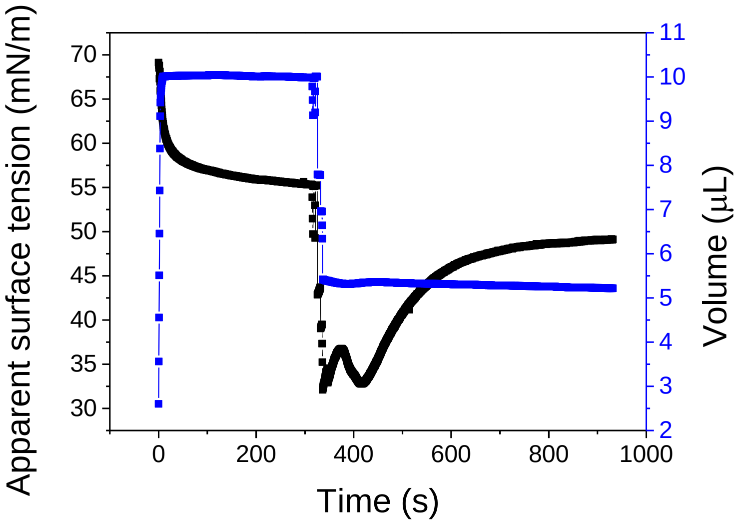

Figure 5.7. a) apparent surface tension during droplet aging (0.01 wt% β-aescin) followed by droplet volume reduction.

5.3.4 Droplet spreading

The spreading dynamics of inviscid droplets without and with interfacial shear elasticity have been compared. The rheology data confirmed that the critical *β*-aescin concentration to generate substantial interfacial shear elasticity but weakly modify the fluid rheology was 0.01 wt%, hence this concentration was considered for the comparison study. Figure 5.8 is a series of images depicting the time-dependent spreading or pure water and water + 0.01 wt% *β*-aescin droplets. For a water droplet (Figure 5.8a), following contact with the spreading substrate, rapid expansion of the contact area was observed with the three-phase contact line moving at ~ 400 mm/s. As the droplet continues to spread, a fluid 'neck' forms between the spreading droplet and the fluid pinned at the tip of the capillary. The fluid neck was observed to rapidly thin, eventually destabilising to separate the spreading droplet from the liquid pinned at the tip of the dispensing capillary.

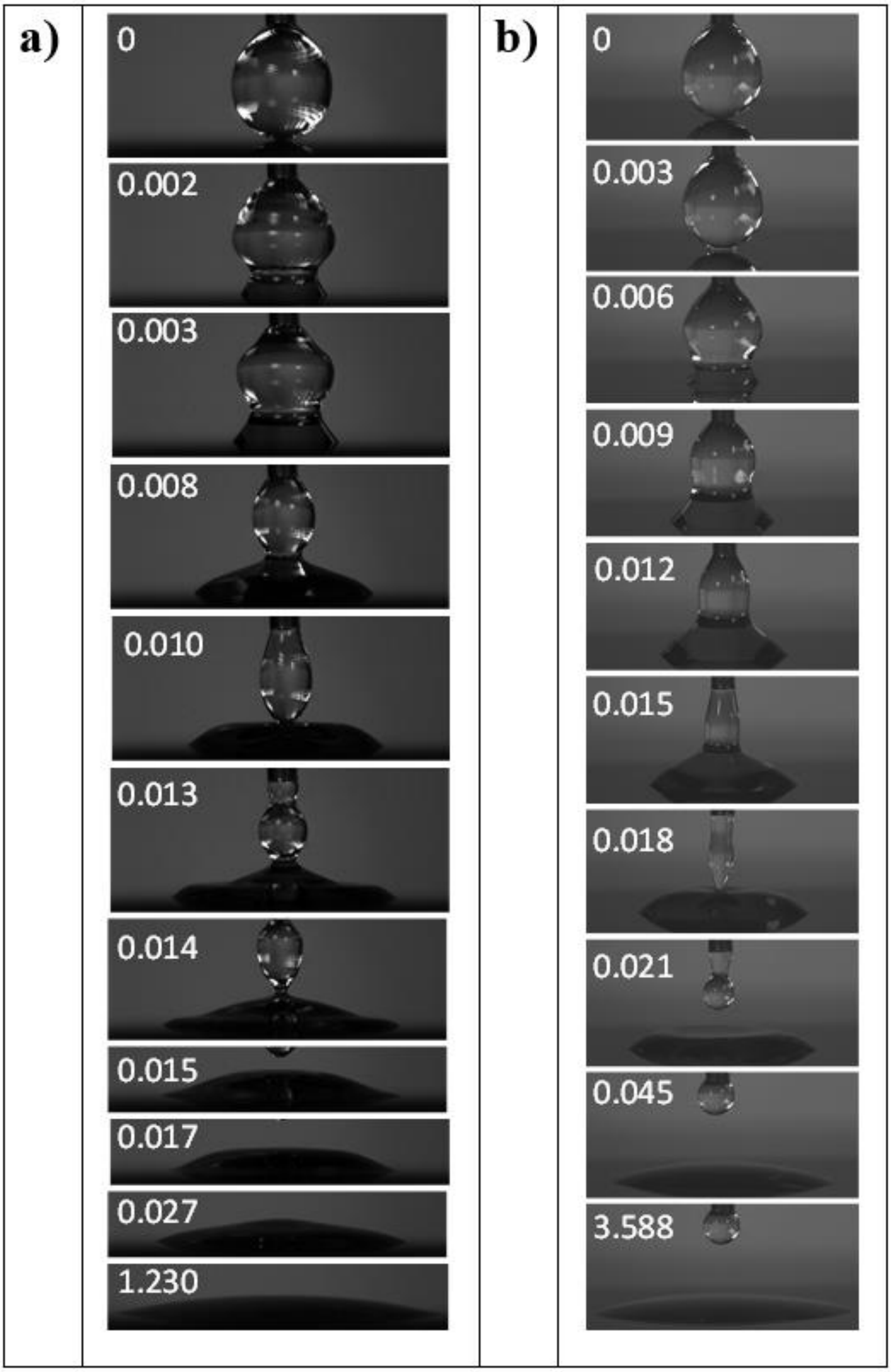

Figure 5.8. Time-dependent sequence of a) water droplet and b) 0.01 wt% β-aescin droplet spreading on a hydrophilic silicon substrate. Droplet spreading times (s) shown inset.

Figure 5.8b shows a similar time sequence for the 0.01 wt% β-aescin droplet spreading on a hydrophilic silicon substrate. The spreading droplet again detaches from the liquid retained at the tip of the dispensing capillary, although it is clear from the image sequence that the formation of the fluid neck and eventual pinch-off is affected by the interfacial rigidity. Indeed, the fluid neck exhibits less deformation than the pure water droplet, retaining an almost cylindrical shape before eventually pinching-off at the apex of the spreading droplet (t ~ 0.018 s).

The spreading dynamics of pure water and water + 0.01 wt% β-aescin are compared in Figure 5.9. Firstly, the spreading dynamics of both fluids exhibit inertial and viscous regimes. While the spreading of water obeys the classical spreading exponents, $t^{0.5}$ and $t^{0.1}$, the water + 0.01 wt% β-aescin droplet appears to exhibit two spreading exponents in the 'conventional' inertial spreading regime. Between $t = 0$ and $t = 5 \times 10^{-4}$ s the droplet spreads with an exponent $t^{1.05}$, slightly reducing to an exponent of $t^{0.61}$ until the viscous spreading regime is reached and the droplet continues to spread with an exponent of $t^{0.11}$. The spreading exponents for all fluids are summarized in Table 5.2. Based on the measured spreading exponents, the presence of β-aescin at the air-water interface accelerates the rate of inertial droplet spreading. To elucidate the contribution of the strong interfacial elasticity to the accelerated spreading, three other fluids were considered for comparison i) 5 wt% ethanol solution, ii) 0.0015wt% glucopyranoside (DG) solution, and iii) 0.0025 wt% xanthan gum (XG) solution. The ethanol and DG fluids were specifically chosen so that the surface tension was 57 mN/m at 20 °C, equivalent to the surface tension of the 0.01 wt% β-aescin solution. Both fluids were purely viscous (shear independent viscosity), although the DG surfactant was selected to mimic the presence of surface active molecules without developing interfacial shear elasticity. XG was selected at the specific concentration to mimic the weakly shear thinning behaviour of the *β*-aescin solution (Figure 5.4a) with no interfacial shear elasticity. As shown in Figure 5.9 and summarized in Table 5.2, all droplets, except *β*-aescin, were observed to spread with equivalent exponents to that of water. Hence, the slight reduction in surface tension, increased fluid viscosity and shear thinning behaviour of the fluid were found to have minimal effect on the spreading exponents, and thus the accelerated inertial spreading of the water + *β*-aescin droplet can be attributed to the strongly elastic interface.

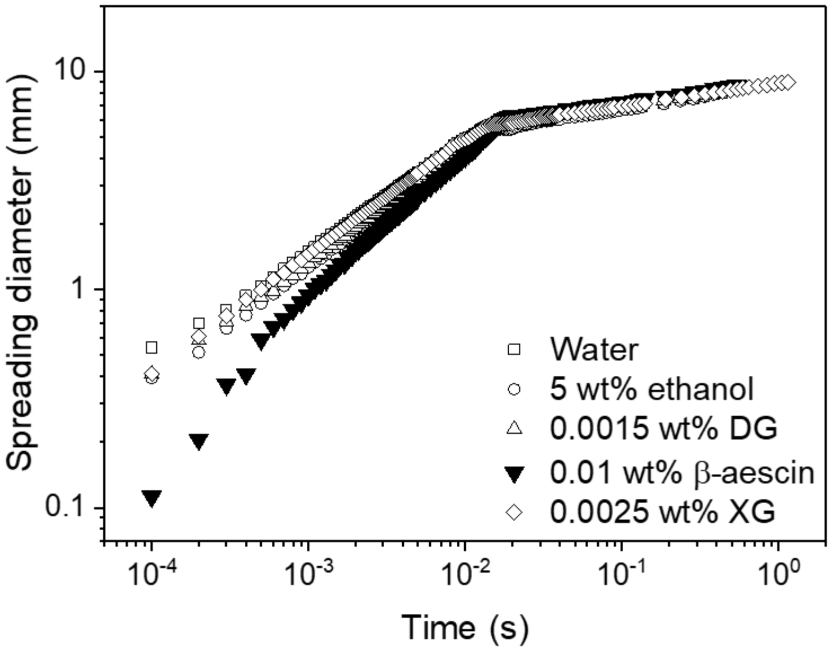

Figure 5.9. Comparison of the droplet spreading dynamics in the inertial and viscous regimes. The droplet volume and the droplet-substrate approach velocity remained constant at 10 μL and 10 mm/min, respectively. The β-aescin and DG droplets were aged for 5 min prior to initiating droplet approach.

From Figure 5.9, it can be seen at $t = 10^{-4}$ s (first captured image of droplet spreading), the initial spreading diameters are equivalent for all droplets with a purely viscous interface, but greatly exceed the initial spreading diameter of the water + 0.01 wt% β-aescin droplet. This variation highlights that the mechanism of droplet spreading is likely different when the droplet interface is strongly elastic. The interfacial shear rheology data confirmed that the interface stabilized by β-aescin exhibits a yield stress, which is able to initially resist droplet spreading upon droplet-substrate contact. However, as the droplet continues to descend towards the substrate, the droplet becomes sufficiently deformed such that the β-aescin stabilized interfacial film ruptures to initiate droplet spreading. This is in contrast to the droplets whose interfaces are purely viscous and instantaneously spread when contacting the substrate. Hence, the rate of droplet spreading is initially retarded by the yield stress interface but once the interfacial film ruptures the droplet spreading rate is indeed accelerated compared to fluids with no interfacial shear elasticity.

The contribution to droplet spreading from the shear elastic interface is evidenced by the interfacial crumpling at $t = 0.0025$ s (Figure 5.10), which is induced by the negative curvature of the droplet compressing the interfacial material. As such, during droplet spreading the elastic interface drives minimization of the negative curvature and alleviates interfacial compression. It is likely that this phenomenon combined with the potential energy liberated at the point of interfacial film rupture contribute to the enhanced rate of droplet spreading in the inertial regime.

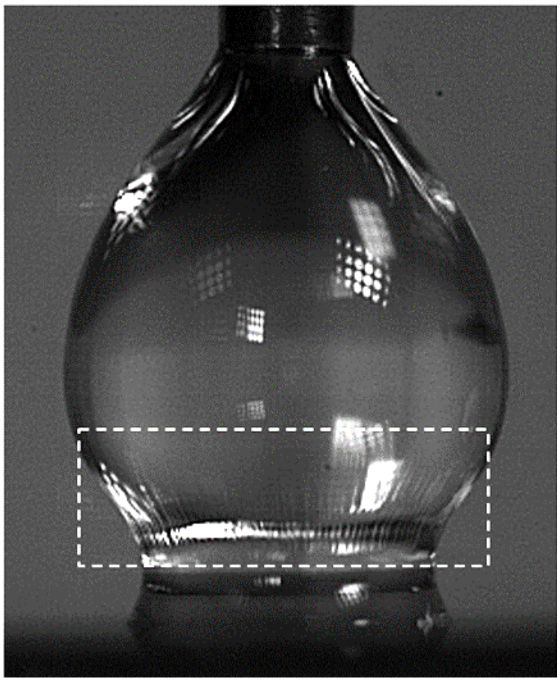

Figure 5.10. Observed interfacial crumpling of a 0.01 wt% β-aescin stabilized droplet during spreading.

Table 5.2. Droplet spreading exponents in the inertial and viscous regimes.

Fluid	**Inertial regime**		**Viscous regime**
0.01 wt% β-aescin	1.05 ± 0.07	0.61 ± 0.02	0.11 ± 0.009
Water	0.50 ± 0.002		0.10 ± 0.005
0.0015 wt% DG	0.52 ± 0.010		0.11 ± 0.005
5 wt% ethanol	0.51 ± 0.001		0.11 ± 0.008
0.0025 wt% XG	0.51 ± 0.009		0.10 ± 0.003

5.3.5 Droplet oscillations

Differences in the damped oscillations of detached droplets were also observed. These oscillations can be modelled by a simple damped oscillation, Eq. 5.9, where $A(t)$ is the droplet peak height, A_0 the initial droplet height, ω the frequency of oscillation, ψ the phase shift and β the dampening coefficient.(47)

$$A\,(t) = A_0 exp(-\beta t)\, sin(\omega t + \psi) \tag{5.9}$$

Figure 5.11 compares the damped oscillation of water droplets without and with 0.01 wt% β-aescin. With the droplets detached from the dispensing capillary the two data sets were superimposed such that the minimum during the first oscillation cycle was aligned ($A(t)$ = 3.5 mm when t = 0.0075 s). In the presence of β-aescin the droplet oscillations were rapidly damped, showing two oscillations within the measurement period compared to the minimum three oscillations for the water-only droplet. Fitting the experimental data to the oscillation damped model, the dampening coefficients for water droplets without and with 0.01 wt% β-aescin were 36 and 58, respectively. The higher dampening coefficient for water + 0.01 wt% β-aescin confirmed that the interfacial shear elasticity was not completely diminished following the rupture (yielding) of the interfacial film to initiate droplet spreading, and the interface remained sufficiently elastic to dampen the bulk oscillation of the droplet. Based on the interfacial rheology data shown in Figure 5.4b, the interfacial elasticity during droplet spreading is not thought to result from a rapidly developing interfacial film, but instead from the residual elasticity of the pre-formed film prior to droplet spreading.

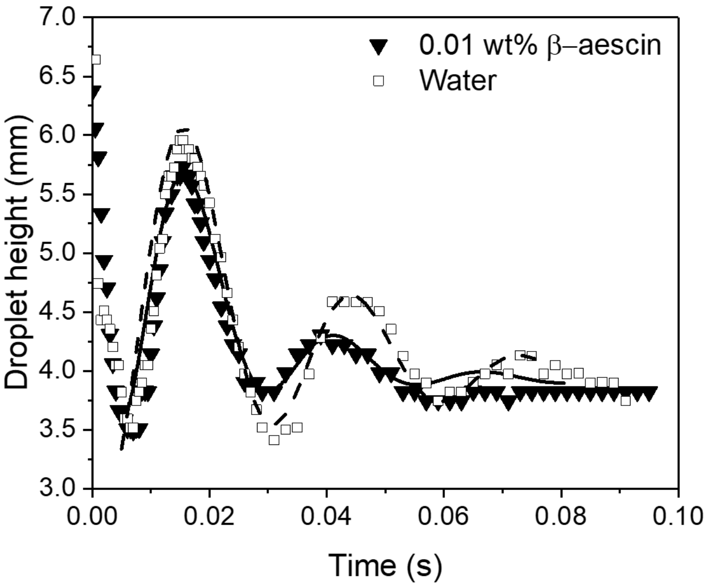

Figure 5.11. Damped oscillations of detached droplets. Experimental data is represented by the symbols and the damped oscillation model ($\mathcal{A}(t) = A_0 exp(-\beta t)\ sin(\omega t + \psi)$) *is represented by the lines (solid and dashed).*

5.3.6 Free droplet spreading

To verify that the droplet-capillary attachment did not influence the observed enhancement in inertial droplet spreading, the spreading experiments were repeated for free droplets. Free droplets were generated using a 22 G capillary positioned 5.5 mm from the spreading substrate, with droplets detached from the capillary by gently tapping the feed tube to the dispensing capillary. Only droplets with circularity greater than 0.8 at the point of droplet-substrate contact were considered and analyzed. Without β-aescin all droplets demonstrated a power-law dependency in the region of 0.5 (inertial regime), with the rate of spreading almost independent of the droplet viscosity and surface tension (5 wt% ethanol, 1.5×10^{-3} wt% DG). However, the droplet spreading profile for water + β-aescin was more complex (Figure 5.12), a result of the apparent droplet spreading prior to interfacial film rupture (droplet deformation [maximum width / height] at t = 0 (Figure 5.12b) and $t = 3.2 \times 10^{-3}$ s (interfacial film rupture) (Figure 5.12c) was 0.83 and 1.28, respectively). Applying the same analysis method as previously described, $t = 0$ was defined as the first contact between the droplet and the substrate. Without β-aescin all droplets exhibited no resistance to spreading, hence the droplets spread at a rate $n' \sim 0.5$. For the water + β-aescin droplet two decay profiles were observed (boundary at $t \leq 3.2 \times 10^{-3}$s, Figure 5.12a). The slower droplet spreading in Region I was attributed to the balance of hydrodynamic forces and interfacial rigidity, with the interfacial elasticity retarding the outward expanding deformation of the droplet. At $t = 3.2 \times 10^{-3}$ s the β-aescin film yields (droplet deformation = 1.28, Figure 5.12c) and the droplet wets the substrate to begin three-phase spreading. In Region II the power-law dependency exceeds all other fluids ($n' = 0.73 \pm 0.02$), again confirming that the shear interfacial elasticity of the β-aescin film accelerates the inertial regime of droplet spreading.

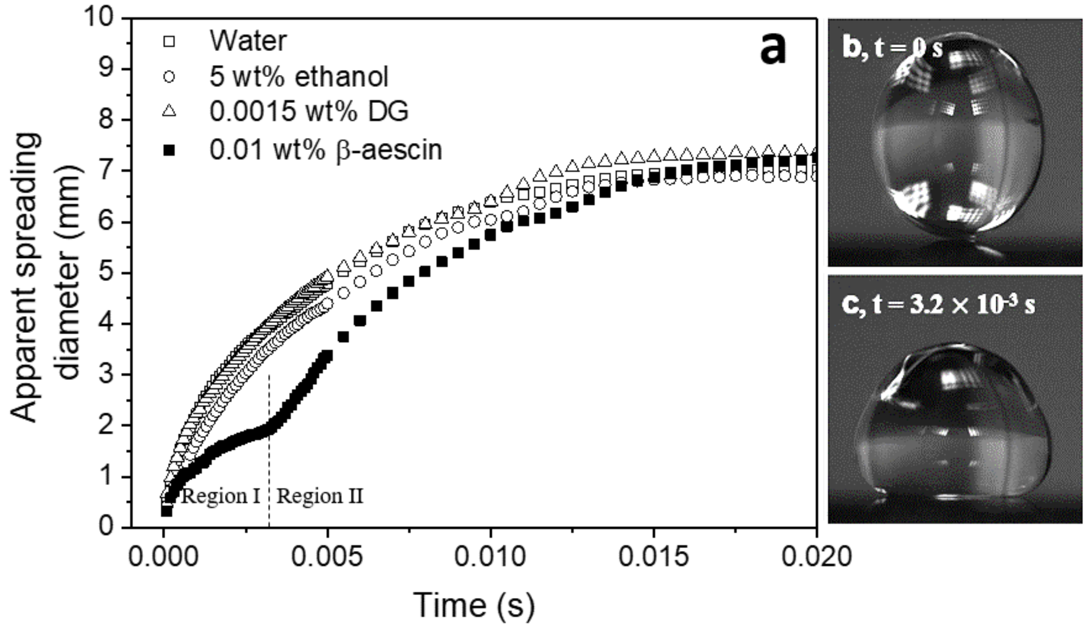

Figure 5.12. a) Spreading dynamics of free droplets (minimum droplet deformation = 0.8). b) Water + 0.01 wt% β-aescin droplet at substrate contact (t = 0 s), droplet deformation (maximum width / height) = 0.83. ***c****) Maximum droplet deformation (1.28) at interfacial film rupture.*

5.4 Conclusion

Accelerated droplet spreading in the inertial regime ($n'_1 = 1.05$, $n'_2 = 0.61$) resulted from the yielding of a strongly elastic interfacial film. A concentration of 0.01 wt% β-aescin was shown to significantly increase the interfacial shear elasticity with minimal effect on the bulk fluid (water) viscosity. β-aescin exhibited a molecular area of ~ 0.26 nm^2 with a preferential orientation at the air-water interface being end-on configuration. The high surface excess led to the formation of a strongly elastic interface, with surface shear moduli of 0.57 Pa.m (G') and 0.09 Pa.m (G'') after 1 min interfacial aging. The β-aescin stabilized water droplet could significantly deform (degree of deformation = 1.28) before the interfacial film ruptured to promote accelerated droplet spreading in the inertial regime. The residual interfacial elasticity also damped the normal oscillations of a detached droplet, exhibiting only two oscillation cycles as compared to more than three for water-only.

This research has demonstrated the ability to modify the inertial regime of droplet spreading by controlling the interfacial shear rheology. Such control may have desirable implications in many droplet-substrate applications. While the inertial regime of droplet spreading can be manipulated, a similar approach to modify the viscous regime of droplet spreading has not yet been achieved, although one can foresee that such control using surface active species could be highly beneficial.

References E

1. DE RUIJTER, M.J., J. DE CONINCK and G. OSHANIN. Droplet Spreading: Partial Wetting Regime Revisited. *Langmuir,* 1999, **15**(6), pp.2209-2216.
2. VELLINGIRI, R., N. SAVVA and S. KALLIADASIS. Droplet spreading on chemically heterogeneous substrates. *Physical Review E,* 2011, **84**(3), p.036305.
3. TANNER, L. The spreading of silicone oil drops on horizontal surfaces. *Journal of Physics D: Applied Physics*, 1979, **12**(9), p.1473.

4. SEAVER, A.E. and J.C. BERG. Spreading of a droplet on a solid surface. *Journal of applied polymer science*, 1994, **52**(3), pp.431-435.
5. DE GENNES, P.G. Wetting: statics and dynamics. *Reviews of modern physics*, 1985, **57**(3), pp.827-863.
6. DAVIS, M.J. and S.H. DAVIS. Droplet spreading: Theory and experiments. *Comptes Rendus Physique*, 2013, **14**(7), pp.629-635.
7. SAWICKI, G. Wetting, Spreading and Adhesion. 1978.
8. EGGERS, J., J.R. LISTER and H.A. STONE. Coalescence of liquid drops. *Journal of Fluid Mechanics*, 1999, **401**, pp.293-310.
9. EDDI, A., K.G. WINKELS and J.H. SNOEIJER. Short time dynamics of viscous drop spreading. *Physics of Fluids*, 2013, **25**(1), p.013102.
10. BIANCE, A.-L., C. CLANET and D. QUÉRÉ. First steps in the spreading of a liquid droplet. *Physical Review E*, 2004, **69**(1), p.016301.
11. BENNETT, T. and D. POULIKAKOS. Splat-quench solidification: estimating the maximum spreading of a droplet impacting a solid surface. *Journal of Materials Science*, 1993, **28**(4), pp.963-970.
12. CAZABAT, A. and M.C. STUART. Dynamics of wetting: effects of surface roughness. *J. Phys. Chem*, 1986, **90**(22), pp.5845-5849.
13. SCHIAFFINO, S. and A.A. SONIN. Molten droplet deposition and solidification at low Weber numbers. *Physics of Fluids*, 1997, **9**(11), pp.3172-3187.
14. LIN, P.A. and A. ORTEGA. The influence of surface tension and equilibrium contact angle on the spreading and receding of water droplets impacting a solid surface. *In: 13th InterSociety Conference on Thermal and Thermomechanical Phenomena in Electronic Systems*, May 30 2012-June 1 2012, 2012, pp.1379-1386.
15. CHEN, L., G.K. AUERNHAMMER and E. BONACCURSO. Short time wetting dynamics on soft surfaces. *Soft Matter*, 2011, **7**(19), pp.9084-9089.
16. STAPELBROEK, B.B.J., H.P. JANSEN, E.S. KOOIJ, J.H. SNOEIJER and A. EDDI. Universal spreading of water drops on complex surfaces. *Soft Matter*, 2014, **10**(15), pp.2641-2648.
17. HONG, J., Y.K. KIM, K.H. KANG, J.M. OH and I.S. KANG. Effects of Drop Size and Viscosity on Spreading Dynamics in DC Electrowetting. *Langmuir*, 2013, **29**(29), pp.9118-9125.
18. MCHALE, G., C. BROWN and N. SAMPARA. Voltage-induced spreading and superspreading of liquids. *Nature communications*, 2013, **4**, p.1605.
19. BOLLEDDULA, D.A. *Droplet impact and spreading of viscous dispersions and volatile solutions*. thesis, University of Washington, 2011.
20. BIRD, J.C., S. MANDRE and H.A. STONE. Short-time dynamics of partial wetting. *Physical review letters*, 2008, **100**(23), p.234501.
21. CHEN, L. and E. BONACCURSO. Effects of surface wettability and liquid viscosity on the dynamic wetting of individual drops. *Physical Review E*, 2014, **90**(2), p.022401.
22. VON BAHR, M., F. TIBERG and V. YAMINSKY. Spreading dynamics of liquids and surfactant solutions on partially wettable hydrophobic substrates. *Colloids and Surfaces A: Physicochemical and Engineering Aspects*, 2001, **193**(1–3), pp.85-96.
23. SVITOVA, T., R.M. HILL and C.J. RADKE. Adsorption layer structures and spreading behavior of aqueous non-ionic surfactants on graphite. *Colloids and Surfaces A: Physicochemical and Engineering Aspects*, 2001, **183–185**, pp.607-620.
24. ROQUES-CARMES, T., V. MATHIEU and A. GIGANTE. Experimental contribution to the understanding of the dynamics of spreading of Newtonian fluids: Effect of volume, viscosity and surfactant. *Journal of colloid and interface science*, 2010, **344**(1), pp.180-197.
25. WINKELS, K.G., J.H. WEIJS, A. EDDI and J.H. SNOEIJER. Initial spreading of low-viscosity drops on partially wetting surfaces. *Physical Review E*, 2012, **85**(5), p.055301.

26. LIANG, Z.-P., X.-D. WANG, D.-J. LEE, X.-F. PENG and A. SU. Spreading dynamics of power-law fluid droplets. *Journal of Physics: Condensed Matter*, 2009, **21**(46), p.464117.
27. RAFAı, S., D. SARKER, V. BERGERON, J. MEUNIER and D. BONN. Superspreading: aqueous surfactant drops spreading on hydrophobic surfaces. *Langmuir*, 2002, **18**(26), pp.10486-10488.
28. DUTSCHK, V. and B. BREITZKE. Spreading characteristics of aqueous surfactant solutions on polymer surfaces. *Tenside Surfactants Detergents*, 2005, **42**(2), pp.82-87.
29. DUTSCHK, V., B. BREITZKE and K. GRUNDKE. Wetting of aqueous surfactant solutions on polymer surfaces. *Tenside, surfactants, detergents*, 2003, **40**(5), pp.250-255.
30. STAROV, V.M., S.R. KOSVINTSEV and M.G. VELARDE. Spreading of Surfactant Solutions over Hydrophobic Substrates. *Journal of colloid and interface science*, 2000, **227**(1), pp.185-190.
31. KUZNICKI, N.P., D. HARBOTTLE, J. MASLIYAH and Z. XU. Dynamic Interactions between a Silica Sphere and Deformable Interfaces in Organic Solvents Studied by Atomic Force Microscopy. *Langmuir*, 2016, **32**(38), pp.9797-9806.
32. KUZNICKI, N.P., D. HARBOTTLE, J.H. MASLIYAH and Z. XU. Probing Mechanical Properties of Water–Crude Oil Interfaces and Colloidal Interactions of Petroleum Emulsions Using Atomic Force Microscopy. *Energy & Fuels*, 2017, **31**(4), pp.3445-3453.
33. BI, J., F. YANG, D. HARBOTTLE, E. PENSINI, P. TCHOUKOV, S.B. SIMON, J. SJÖBLOM, T. DABROS, J. CZARNECKI and Q. LIU. Interfacial layer properties of a polyaromatic compound and its role in stabilizing water-in-oil emulsions. *Langmuir*, 2015, **31**(38), pp.10382-10391.
34. HARBOTTLE, D., Q. CHEN, K. MOORTHY, L. WANG, S. XU, Q. LIU, J. SJOBLOM and Z. XU. Problematic Stabilizing Films in Petroleum Emulsions: Shear Rheological Response of Viscoelastic Asphaltene Films and the Effect on Drop Coalescence. *Langmuir*, 2014, **30**(23), pp.6730-6738.
35. BONN, D., J. EGGERS, J. INDEKEU, J. MEUNIER and E. ROLLEY. Wetting and spreading. *Reviews of modern physics*, 2009, **81**(2), p.739.
36. KOVALCHUK, N.M., A. BARTON, A. TRYBALA and V. STAROV. Surfactant Enhanced Spreading: Catanionic Mixture. *Colloids and Interface Science Communications*, 2014, **1**, pp.1-5.
37. LEISKE, D.L., C. MONTEUX, M. SENCHYNA, H.A. KETELSON and G.G. FULLER. Influence of surface rheology on dynamic wetting of droplets coated with insoluble surfactants. *Soft Matter*, 2011, **7**(17), pp.7747-7753.
38. GOLEMANOV, K., S. TCHOLAKOVA, N. DENKOV, E. PELAN and S.D. STOYANOV. Remarkably high surface visco-elasticity of adsorption layers of triterpenoid saponins. *Soft Matter*, 2013, **9**(24), pp.5738-5752.
39. PAUCHARD, V., J.P. RANE and S. BANERJEE. Asphaltene-laden interfaces form soft glassy layers in contraction experiments: A mechanism for coalescence blocking. *Langmuir*, 2014, **30**(43), pp.12795-12803.
40. PEKDEMIR, T., Y. ISHIGAMI and H. UCHIYAMA. Characterization of aescin as a biosurfactant for environmental remediation. *Journal of Surfactants and detergents*, 1999, **2**(3), pp.337-341.
41. YEUNG, A., T. DABROS and J. MASLIYAH. Dissipative Interfaces and Departures from the Young−Laplace Equation. *Langmuir*, 1997, **13**(24), pp.6597-6606.
42. STANIMIROVA, R., K. MARINOVA, S. TCHOLAKOVA, N. DENKOV, S. STOYANOV and E. PELAN. Surface rheology of saponin adsorption layers. *Langmuir*, 2011, **27**(20), pp.12486-12498.
43. ZHANG, H., K. YU, O.J. CAYRE and D. HARBOTTLE. Interfacial particle dynamics: One and two step yielding in colloidal glass. *Langmuir*, 2016, **32**(50), pp.13472-13481.

44. LORENT, J.H., J. QUETIN-LECLERCQ and M.-P. MINGEOT-LECLERCQ. The amphiphilic nature of saponins and their effects on artificial and biological membranes and potential consequences for red blood and cancer cells. *Organic & biomolecular chemistry*, 2014, **12**(44), pp.8803-8822.
45. DATTA, S.S., H.C. SHUM and D.A. WEITZ. Controlled Buckling and Crumpling of Nanoparticle-Coated Droplets. *Langmuir*, 2010, **26**(24), pp.18612-18616.
46. KING, H., R.D. SCHROLL, B. DAVIDOVITCH and N. MENON. Elastic sheet on a liquid drop reveals wrinkling and crumpling as distinct symmetry-breaking instabilities. *Proceedings of the National Academy of Sciences of the United States of America*, 2012, **109**(25), pp.9716-9720.
47. ATA, S. The detachment of particles from coalescing bubble pairs. *Journal of colloid and interface science*, 2009, **338**(2), pp.558-565.

Chapter 6: Conclusions and Future Work

The droplet spreading dynamics on solid surfaces were studied in this project. Comprehensive investigations have been carried out to understand the effects of various parameters on droplet spreading dynamics. The conclusions of this thesis and the recommendations for the future research are summarised in this chapter. The following conclusions are drawn from this research work:

6.1 Conclusions

6.1.1 Droplet spreading dynamics: CH_3- and NH_2-terminated PDMS oil droplet spreading in air

The spreading dynamics of viscous droplets were investigated using CH_3- and NH_2-terminated PDMS oil of viscosities ranging from 9.9 to 12710 mPa·s. Droplet spreading radii were measured using a pendant drop analyser. The comparison of the spreading behaviour of the different viscous oils showed that increasing the oil droplet viscosity slows down the spreading dynamics. The three most commonly used models (*i.e.* Tanner, de Gennes and Seaver and Berg models) were unable to effectively fit the data for the entire viscosity range. The Seaver & Berg model was more appropriate to fit the data of low viscosity oils due to its cylindrical disk approximation. Conversely, the Tanner and de Gennes models were more appropriate to fit the data for higher viscosity oils due to their spherical cap approximation. A master curve could be created by dividing the spreading time by the droplet viscosity. The central region of the master curve had a power law gradient of 0.1; hence showing further agreement with Tanner's law. The spreading dynamics were enhanced with increasing impact velocity (experimentally increased by increasing the droplet release height). The spreading dynamics were also affected by droplet shape, with very viscous oils showing a liquid tail that altered spreading dynamics. NH_2-terminated PDMS oils were shown to have slower spreading dynamics than CH_3-terminated PDMS oils, possibly caused by an increased molecular orientation at the surface-droplet and air-droplet interfaces.

6.1.2 Oil droplet spreading in aqueous environments

The PDMS oils, previously studied in Chapter 3, were also used to investigate underwater droplet spreading dynamics. Water and PDMS oil densities closely matched each other causing droplet ballooning. To counter this problem, D_2O was used as it has a higher density than the studied PDMS oils. Using D_2O meant that an inverted system was needed as the oil droplets rose, due to their lower density. The spreading radius was measured with time and recorded *via* a pendant drop analyser as for the previous study. The influence of the spreading surface wettability was first studied, where silicon surfaces were silanised for various times to exhibit water-in-air contact angles of 0, 30, 65 and 100°. Increasing the hydrophobicity allowed the droplets to spread to a larger extent, smaller induction times were recorded with quicker spreading rates, due to the increase in hydrophobic-hydrophobic interactions possible. The spreading dynamics of the droplets were shown to fit MKT and HD theories, with a slight preference to MKT. The empirical Wang model provided the best fit and was used to fit all data to effectively compare spreading rates.

A gradual increase in the concentration of an anionic surfactant (SDS) led to slower spreading dynamics and decreased the extent of spreading because the surfactant adsorbed at the surface interface and reduced the effective hydrophobicity. The increase in SDS concentration also led to higher induction times as the Marangoni flow increased the TLF drainage time. Increasing the droplet viscosity caused a decrease in spreading dynamics as expected. Interestingly, the induction times were shorter because droplets deformed less at the interface. NH_2-terminated oils exhibited a larger extent of spreading on the silicone surfaces compared to the CH_3-terminated. However, dynamics were slightly slower (similarly to droplet spreading in air) and also believed to come from an increased ordering of the molecules at the surface-droplet and water-droplet interfaces.

Finally, the silicon wafers were spin coated with cellulose to create a rougher surface with an RMS value of approximately 0.6. These surfaces prevented the wetting of both the CH_3- and NH_2-terminated PDMS oils. This absence of wetting is believed to come from the increased surface roughness, which physically increases the effective hydrophilicity of the surfaces, as well as from the absorption of water by the cellulose fibres (hygroscopicity), which chemically increases the effective hydrophilicity.

6.1.3 Accelerated spreading of inviscid droplets prompted by the yielding of strongly elastic interfacial films

The β-aescin was shown to exhibit a high interfacial shear elasticity. A strongly elastic film formed at the liquid-air interface for β-aescin solutions of concentrations close and above the CMC. Moreover, β-aescin solutions of higher concentrations exhibited higher bulk viscosities with a more pronounced shear thinning behaviour. However, a bulk viscosity increase would affect spreading dynamics. Hence, a concentration of 0.01 wt% *β*-aescin was selected to maximise interfacial shear elasticity whilst minimising bulk fluid viscosity. Surface rheology reached equilibrium after 5 mins ageing, and the film had an interfacial yield stress of approximately 1.7×10^5 Pa. The studied range of *β*-aescin concentrations allowed plotting of a surface tension isotherm, and calculating the molecular area. The obtained value of *ca.* 0.26 nm^2 suggests an air-water interface end-on configuration.

Droplet spreading experiments were then recorded on a high-speed camera that allowed a higher frame rate of 10,000 FPS. The droplet spreading dynamics of the 0.01 wt% *β*-aescin aqueous solution were compared to: i) water, ii) 5 wt% ethanol solution, iii) 0.0015 wt% DG solution and iv) 0.0025 wt% XG solution, to check for possible effects coming from the solvent, the surface tension, the surfactant or the shear thinning properties respectively. Hence, the ethanol and DG concentrations were chosen with a surface tension of 57 mN/m at 20°C, identical to the 0.01 wt% *β*-aescin solution. All the four control solutions exhibited the expected spreading exponents of 0.5 (inertial spreading) and 0.1 (viscous spreading). The 0.01 wt% *β*-aescin solutions, whilst exhibiting the same viscous regime, exhibited enhanced spreading dynamics in the inertial regime characterised by an initial exponent of 1.05 during the first 5×10^{-4} s which then reduced to 0.61. The enhanced spreading dynamics observed for the 0.01 wt% *β*-aescin solution were shown to arise from the strong elastic film and were also corroborated with free droplet spreading. The variation of the droplet height during spreading experiments also showed that the elastic film dampened the oscillations of the droplet.

6.2 Future Work

Although the effects of various parameters on droplet spreading dynamics have been studied, there are still significant areas for further investigation. A few have been chosen to highlight key areas from the work undertaken in this study.

6.2.1 Droplet spreading dynamics: CH_3- and NH_2-terminated PDMS oil droplet spreading in air

Whilst the master curves provide an alternate simple method to predict droplet spreading dynamics, this may not be true of all oils of varying viscosity. The spreading curves of the different PDMS oils aligned well and the central region exhibited a gradient of 0.1, as predicted by both Tanner's and Seaver & Berg's model. A similar systematic study to try forming a master curve for oils of varying surface tension would prove interesting. A central region fitting to a power law $t^{0.1}$ would show further corroboration of the spreading laws.

Further research into the difference in spreading dynamics due to terminating group would also prove interesting. Confirming that OH-terminated PDMS groups have slower spreading dynamics than the NH_2-terminated oils could highlight the effect of terminating group polarizability. This effect could be further investigated by changing the hydrophobicity of the spreading surfaces (by similarly coating with silane) as the influence of the terminating groups may be reduced when surface hydrophobicity is increased. Using PDMS oils with NH_2 (or OH) groups along the polymer backbone rather than as the terminating groups would help understanding the spatial importance of the polarizable group along the PDMS chains.

6.2.2 Oil droplet spreading in aqueous environments

Droplet spreading dynamics under water were investigated with an in-house built rig. Parameters such as oil viscosity, surface hydrophobicity, surfactant concentration, surface roughness and terminating group polarizability were varied. As for the study of droplet spreading dynamics in air, it would be interesting to investigate the effects of the droplet release height using different length stoppers, and those of the impact velocities by injecting the continuous phase into the rig (it would detach the droplet; hence increasing the impact velocity). Such capabilities were available on the rig but could not be used during the project due to time limitations.

The lack of spreading of CH_3-terminated PDMS oils on cellulose highlighted the effects of roughness on hydrophilic surfaces. The fact that the NH_2-terminated PDMS oil did not spread either was surprising, as such oils had previously shown to spread on hydrophilic silane surfaces. It would be interesting to further investigate the effects of roughness, hydrophobicity of rough surfaces, surface hygroscopicity and surface porosity. Preliminary experiments with a CH_3-terminated PDMS oil spreading on TMSCellulose (rough hydrophobic surface) were conducted as seen in Figure 6.1.

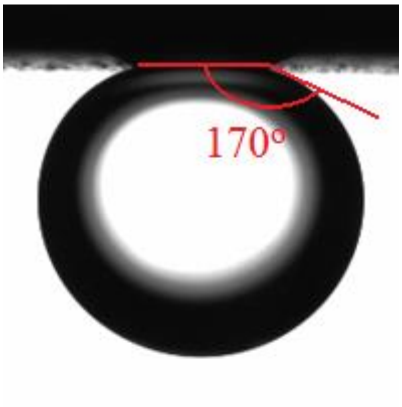

Figure 6.1. Spreading of a 1000 mPa·s CH_3*-terminated PDMS droplet on a TMSCellulose surface.*

As seen in Figure 6.1, the CH_3-terminated PDMS oil does not spread on the more hydrophobic TMSCellulose surface either. However, it is not clear whether the droplet does not spread due to the surface roughness (physical effect), or the hygroscopicity (chemical effect), or a combination of both. A systematic study would determine the individual effects of each of these variables. Moreover, many real examples of cellulose surfaces, such as clothes, have a complicated network of fibres which introduce different levels of porosity to the surface. The effects of surface porosity would thus also be interesting to study. Initial experiments investigating the effects of glass frit porosity have been conducted. Glass frits with 26.4 % porosity were silanised to have either hydrophilic (30° water-in-air CA) or hydrophobic (100° water-in-air CA) properties. A 1000-mPa.s CH_3-terminated PDMS droplet was placed on the surface and the droplet volume was recorded over time as shown in Figure 6.2 and Table 6.1.

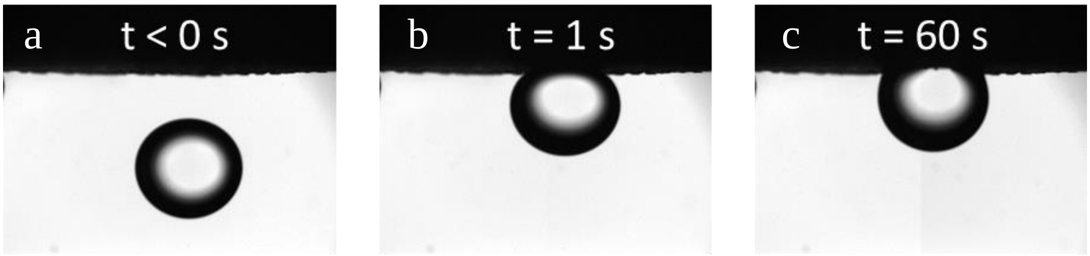

Hydrophobic porous surface

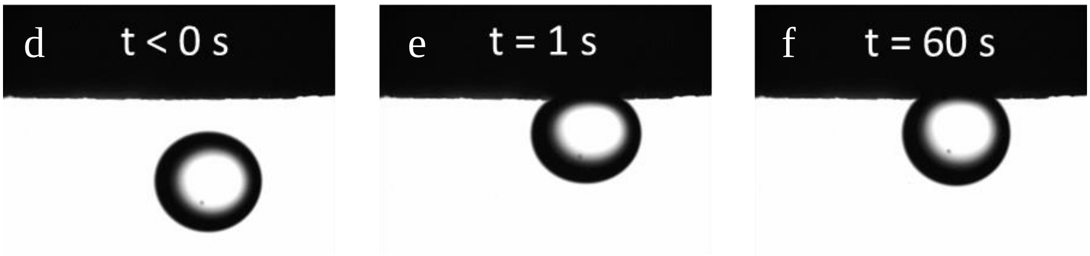

Hydrophilic porous surface

Figure 6.2. Spreading of a 1000 mPa·s CH_3-terminated PDMS droplet on a hydrophobic porous glass frit (a-c) and a hydrophilic porous glass frit (d-f) at various time intervals.

Table 6.1. Contact angles and volumes of a 1000 mPa·s CH_3-terminated PDMS droplet on both hydrophobic and hydrophilic porous surfaces.

Surface	**Water-in-air CA (deg)**	**Oil-in-water CA (deg)**	**Volume at t = 0 s (µL)**	**Volume at t = 60 s (µL)**	**Volume change (%)**
Hydrophobic	100	112	23.9	23.05	-0.036
Hydrophilic	30	130	24.6	24.4	-0.008

As seen in Figure 6.2 and Table 6.1, the CH_3-terminated PDMS droplet spreads more on the hydrophobic surface. Indeed, after 1 min spreading, the volume of the droplet has reduced by approximately 5 times more than the droplet spreading on a hydrophilic surface. The surface needs to be hydrophobic for the oil to adsorb into the surface porous holes. Whilst the effects of porosity on droplet spreading have been reported in the literature, a study of the combined effects of porosity and hygroscopicity would help understanding PDMS spreading on cellulose surfaces.

Increasing the concentration of an anionic surfactant, SDS, showed a reduction in the extent of spreading on hydrophobic surfaces and reduced droplet spreading dynamics. The surfactant molecules were able to sit at the interface and effectively reduce the surface hydrophobicity. It would be interesting to establish if the opposite was also true for hydrophilic surfaces, after which using a positive surfactant could also result in interesting behaviour. Silicone and cellulose surfaces have are negative and so a positive surfactant may increase the hydrophobicity of hydrophilic surfaces more successfully.

6.2.3 Accelerated spreading of inviscid droplets prompted by the yielding of strongly elastic interfacial films

The presence of a strong elastic film at the air-liquid interface enhanced droplet spreading with spreading exponents of 1.05 followed by 0.61, instead of the expected 0.5. This is believed to be due to a combination of added elastic energy after film breakage and the pressure of the film (caused by the droplet curvature) promoting faster spreading dynamics. It would be interesting to further investigate how interfacial elasticity affects spreading dynamics. For example, saponins (or similar molecules that form elastic interfaces) with stronger and weaker elastic interfaces could be used to see how the spreading exponents are influenced. A more thorough understanding may lead to an altered Tanner's law that would incorporate interfacial elasticity effects. The diffusion and/or the rearrangement of molecules at the surface may also play an important part in enhancing droplet spreading dynamics. Other interfacially elastic molecules can also be used to investigate the contribution of both diffusion and rearrangement dynamics on droplet spreading.

Appendix A

A.1 Design and optimisation of the water cell

The PDMS and H_2O are closely matched in density, with the PDMS being only slightly less dense, this means there is a real risk of the droplet ballooning in size. The design of the water cell needs to be inverted whilst giving control to the user over the droplet size that can be generated. One method would to be to generate a flow from the continuous phase (H_2O) which would shear the PDMS oil and enable droplets of different size to be generated. With that in mind a design has been made, shown in Figure A1a, along with photos of the finished products in Figure A1b and c.

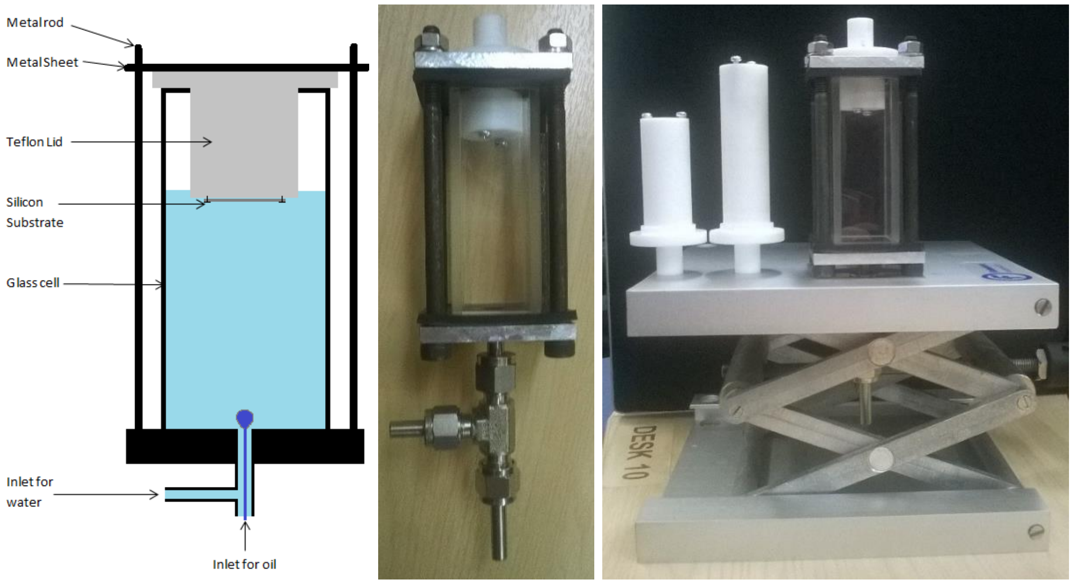

Figure A1. a) Original design for the water cell design, b) The finished product, c) the water cell with extra Teflon lids and the stage.

A straight needle will be used, it will be coming from below so that the needle is upside down. The inlet for the needle will be stoppered by a bung, different needle gauges will allow different sized droplets ensuring droplet size diversity. The inlet for the continuous phase (H_2O) will be attached to tubing which is attached to a syringe pump, this can be programmed to have different flows and, therefore different shear rates. The silicon substrate wafer will be affixed to the bottom of a Teflon lid with two screws holding the wafer in place. Several Teflon lids with different lengths will be used, this allows droplet velocity to be investigated by altering the distance between needle and surface. The structure is held together with four rods which screw down to ensure there is no leakage of water.

Figure A1b shows the finished product, due to workshop limitations the inlet tube for the oil needle was much longer than originally thought, and this meant that the needles required were 3.5 inches long. In order to further reduce the risk of leaking and to ensure the glass was not shattered a neoprene black rubber sheet was placed between the glass and metal plates. The Teflon lid was placed on top of the metal plate, they were made to ensure a height of 6cm, 0.6 cm and 3cm (in order to correspond with the droplet heights from Chapter 3). The wafers would need to be cut to a square shape of length 14 mm in order to sit between the screws. As the camera is at a fixed height and the three Teflon lids would mean the surface was at different heights, a hole was drilled into a jack in order to raise the surface to the correct height. The water cell fit perfectly at this height as can be seen in Figure A1c.

As this water cell was designed and built in-house several tests were done in order to optimise the design and to make sure it worked. The first issue was that there was a slow leak at the bottom of the glass, although this was slow any change in flow could have an effect on the droplet velocity. Also, it would not be possible to measure the droplet spreading over an hour as the water line fell below the surface after a couple of minutes. This was very easy to fix; applying silicon oil on the outside of the glass (and cleaning it off the glass so that a clear window was still present) stopped the leaking of the water almost completely. This would need to be re-applied for each experiment. Another issue was that there was a very low rate of successful drops hitting the wafer surface. As seen below in Figure A2 the droplet often hit the screw or missed the surface entirely.

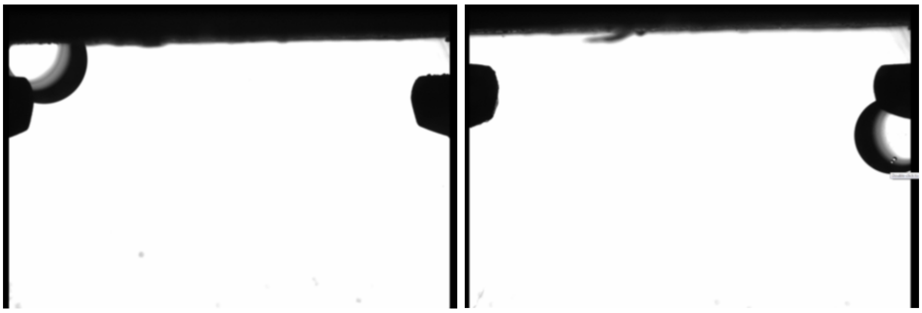

Figure A2. the droplet not always hit the surface but often missed or hit the screw

As can be seen in Figure A2 the droplet often hit the needle, or in fact completely missed the surface, this would make the experiment less reproducible. There were two main reasons as to why the droplets were set off course i) the longer needle made it more difficult to centrally align, generating different amounts of shear on either side of the droplet, ii) the oils wick the needle, meaning there could be different amount of droplet surface area surrounding the needle, again creating different amounts of shear on the side of the droplet, shown below in Figure A3. This uneven distribution of shear results in the droplet not detaching and flowing straight but veering off and missing the surface.

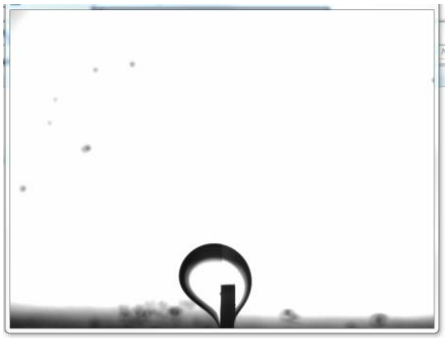

Figure A3. Wicking of the oil on the needle means there is an uneven distribution of shear around the droplet of CH_3-terminated 1000 mPa·s PDMS.

The first problem is fixed fairly easily, a small length of string is wound around the needle and comes through either side of the water cell, between the rubber and metal. This holds the needle centrally and can be manually manipulated, it is also held in place once the metal rods are tightened. The second issue is harder to solve; cleaning the needle with piranha solution does work in stopping the CH_3-terminated PDMS from wicking, however the NH_2-terminated oil seems impervious to making either hydrophilic or hydrophobic needles. Measuring the two PDMS oils' interfacial tensions in D_2O had no wicking issues – this could be an alternative to avoid wicking. However, as the density difference is much larger, then the droplets generated will be much smaller which needs to be taken into account.

A syringe pump was used as it should generate a constant flow, firstly CH_3-terminated PDMS at 1000 mPa·s was used to form two droplets of different sizes 10 µL and 6.5 µL. The volumetric flow was varied in order to determine the critical flow rate of the syringe pump required to detach the droplets. The higher the volumetric flow used the more air bubbles introduced and the more the droplet deviated from its central path. The effect was less the closer to the critical volumetric flow, Figure A4a and b shows two droplets at 10 and 6.5 µL after detaching from the needle under their measured critical velocities 77.5 and 84.6 mL/min, respectively.

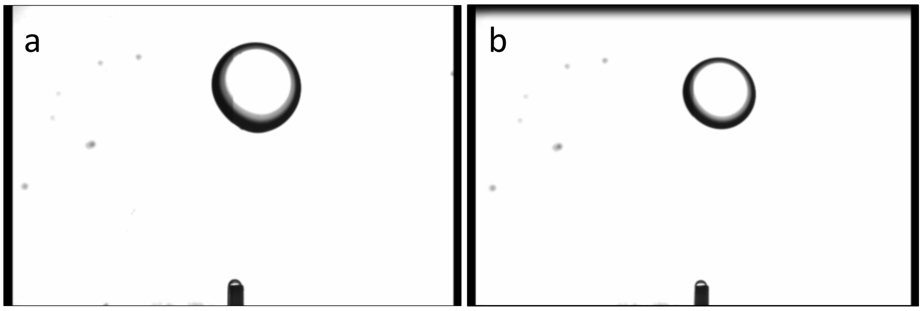

Figure A4. a) a 10 µL droplet detached at a speed of 77.5 mL/min and b) a 6.5 µL droplet detached at a speed of 84.6 mL/min.

A larger droplet has a lower critical volumetric flow, this is because it has a larger surface area that is affected by the shear rate generated by the continuous phase. The closer the velocity to the critical volumetric flow the better for the CH_3-terminated PDMS, however, the NH_2-terminated PDMS is impossible to work with in these conditions. The flow of the continuous phase causes the oils to stream and break up, a single droplet detachment was not possible. Even at the critical volumetric flow for the CH_3-terminated PDMS there are air droplets entering the cell. After soaking all elements of the water cell in water and sonicating, there are still air bubbles. Another problem is that with the flow used to detach the droplets from the needle, there is a significant amount of energy when the droplet reaches the surface, causing it to rebound and roll, which prevents it from spreading on the surface. There are significant problems using flow to detach the droplets, but the surface tension experiments in the present study had shown that droplets of smaller sizes could be generated and would spontaneously detach in a D_2O environment. Therefore in order to i) prevent wicking, ii) prevent streaming of the NH_2-terminated PDMS and iii) prevent air bubbles affecting the system and to iv) minimise rebounding and rolling of droplets no flow will be used, instead droplets will be generated to a maximum size before detachment in a D_2O environment.

A.2 Oscillation strain sweep

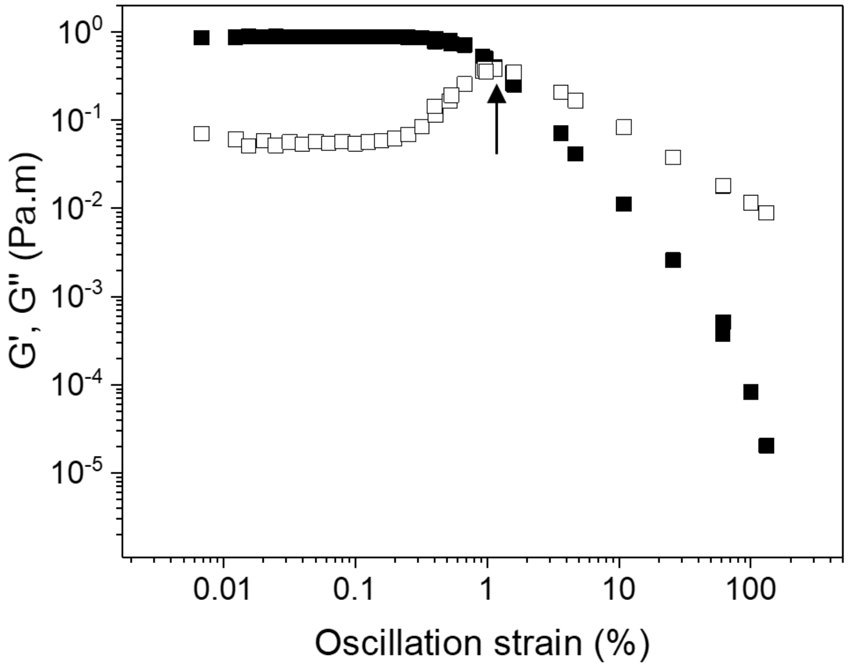

Figure A5. Oscillation strain sweep of an air-water interface stabilized by 0.01 wt% β-aescin following 5 min ageing. The yield point (indicated by the arrow) was taken as the crossover point of G' and G".

A.3 Dodecyl surface tension

The dynamic surface tension experimental technique developed for the *β*-aescin and discussed in Section 5.3.1 can also be applied to the DG surfactant. DG solutions of various concentrations were tested to identify the DG concentration corresponding to an equilibrium surface tension of 57 mN/m (i.e. identical to the equilibrium surface tension of 0.01 wt% *β*-aescin solution), and to ensure the equilibrium surface tensions were reached within 5 minutes (i.e. the DG droplets would be aged for 5 minutes, like the β-aescin droplets, to ensure differences were not an effect of the ageing time). This set of measurements also allowed plotting an isotherm which could then be fitted to extract numerical values for molecular area and the adsorption constant. Dynamic surface tension data can be seen in Figure A6a and equilibrium surface tension *versus* concentration data are shown in Figure A6b.

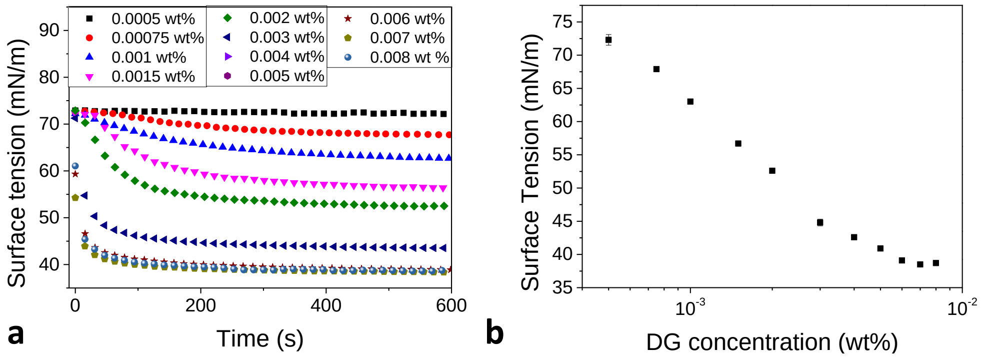

Figure A6. a) dynamic surface tension of DG solutions of various concentrations; each curve is an average of the data collected for 3 droplets; b) equilibrium surface tensions for the various DG concentrations.

As seen in Figure A6a the 0.0015 wt% DG solution is appropriate for comparison to the 0.01 wt% β-aescin solution as it has a similar equilibrium surface tension of 57 mN/m. Using the same technique as that for the β-aescin, the CMC was calculated to be 0.16 mM; which is comparable to literature data such as Lopez *et al*,(1) who calculated a CMC value of 0.18 mM. Using the Gibbs isotherm, the molecular concentration was calculated as 3.47 x 10^{18} m^{-2}; corresponding to a molecular area of 0.29 nm^2 which is similar to the size of a β-aescin molecule. Using the Langmuir isotherm (Section 5.3.1), a maximum molecular concentration of 3.81 x 10^{18} m^{-2} can also be calculated, which corresponds to a molecular area of 0.26 nm^2. The adsorption constant was calculated to be 65.2 M^{-2}; showing slightly slower diffusion rates than the *β*-aescin molecules.

A.4 Development of the method for bulk rheology measurements

Finding an appropriate method to investigate bulk rheology properties, Section 5.2.4, proved to be more complex than expected and is hence worth mentioning. A cone-and-plate geometry was first used. The results obtained for three selected *β*-aescin concentrations can be seen in Figure A7 and show that the studied solutions have a shear-thinning behaviour.

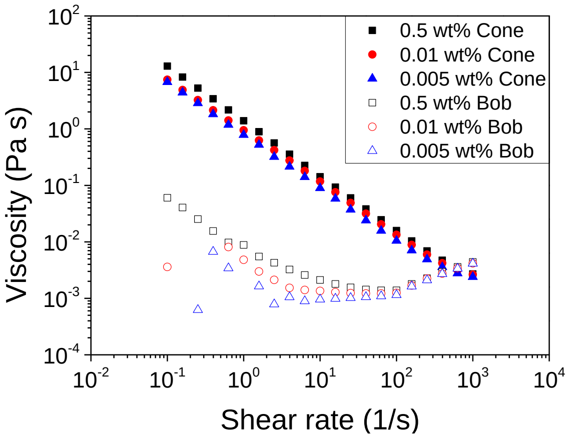

Figure A7. The viscosity of three β-aescin solutions (0.005 wt%, 0.01 wt% and 0.5 wt%) measured using both a cone-and-plate (closed symbols) and a bob-and-cup (open symbols).

The data obtained with the cone-and-plate geometry (Figure B6) showed very little difference in shear-thinning behaviour when *β*-aescin concentration was varied. Literature data(2, 3) had shown that *β*-aescin preferentially sits at an air-water interface and has a fast diffusion rate. Furthermore, solutions of concentrations below 0.01 wt%

had not shown any significant interfacial shear elasticity (Figure 5.4b) or surface tension changes (Figure 5.3a), however were exhibiting near-identical bulk viscosity values. When using a cone-and-plate geometry, to load the sample on the rheometer a large droplet was placed directly on the centre of the plate before the cone was lowered into position. No matter how quickly the cone was lowered, there was time for the saponin to diffuse to the air-water interface and begin to form a film. The author suggests that once the cone is lowered, a film covers the underside of the cone; which would provide significant structuring to the liquid and would potentially cause artefacts in the measurements.

Using a bob-and-cup geometry could potentially negate this. With the bob already in the experimental position, the liquid was added to the cup to a height above the bob. The sample was added in a way that would prevent bubbles forming as they could also interfere with the experiment. The experiments were run in the same way as for the cone-and-plate experiments, other than the changed geometry and sample loading method. The result can also be seen in Figure A7. The bulk rheology data collected using the bob-and-cup geometry shows a less pronounced shear-thinning behaviour. The least concentrated solution exhibits a nearly Newtonian behaviour in the medium range of studied shear rates, the lowest shear rates still provided very scattered data.

A further systematic study was conducted to see whether the equilibrating time (6 s) and the averaging time (30 s) were appropriate for the stress range. Fixed stresses were applied to the solution for 5 mins to study the time-dependence of the viscosity across the studied range of stresses, the results shown in Figure A8.

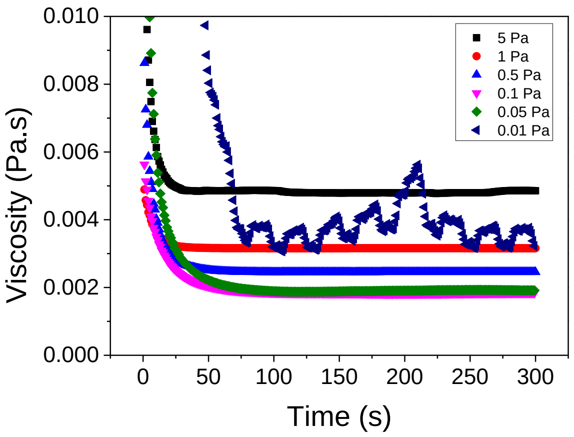

Figure A8. Time evolution of the viscosity of a 0.5 wt% β-aescin solution measured for various shear stresses.

For stresses below 0.01 Pa (data not shown), no steady-state viscosity can be achieved as the measurements are performed too close to the low limits of the instrument. Such a steady state flow is still not achieved at 0.01 Pa (See Figure B7) as the measured viscosity oscillates with time. Data collected from 0.05 Pa exhibit a constant viscosity with time after approximately 100 s. This steady-state viscosity is identical at both 0.05 and 0.1 Pa, and increases for higher stress values because of inertial effects. From this preliminary study, the equilibrium time (*i.e.* time during which the stress is applied to achieve the steady-state flow) and the averaging time (*i.e.* the time during which the viscosity is measured and averaged to give a single data point on the viscosity curve such as the ones shown in Figure B6 and Figure 5.4a) were both set to 200 s.

References F

1. LÓPEZ, O., M. CÓCERA, J.L. PARRA and A. DE LA MAZA. Influence of the alkyl chain length of alkyl glucosides on their ability to solubilize phosphatidylcholine liposomes. *Colloids and Surfaces A: Physicochemical and Engineering Aspects*, 2001, **193**(1), pp.221-229.
2. GOLEMANOV, K., S. TCHOLAKOVA, N. DENKOV, E. PELAN and S.D. STOYANOV. Remarkably high surface visco-elasticity of adsorption layers of triterpenoid saponins. *Soft Matter*, 2013, **9**(24), pp.5738-5752.
3. PAGUREVA, N., S. TCHOLAKOVA, K. GOLEMANOV, N. DENKOV, E. PELAN and S.D. STOYANOV. Surface properties of adsorption layers formed from triterpenoid and steroid saponins. *Colloids and Surfaces A: Physicochemical and Engineering Aspects*, 2016, **491**, pp.18-28.